De bepaling van lokale warmteoverdrachtscoëfficiënten
en vineffectiviteit voor longitudinale vinnen
door middel van het inverse conductieprobleem en thermografie

Using the Inverse Heat Conduction Problem and Thermography
for the Determination of Local Heat Transfer Coefficients
and Fin Effectiveness for Longitudinal Fins

Arnout Willockx

Promotor: prof. dr. ir. M. De Paepe
Proefschrift ingediend tot het behalen van de graad van
Doctor in de Ingenieurswetenschappen: Werktuigkunde-Elektrotechniek

Vakgroep Mechanica van Stroming, Warmte en Verbranding
Voorzitter: prof. dr. ir. R. Sierens
Faculteit Ingenieurswetenschappen
Academiejaar 2009 - 2010

UNIVERSITEIT
GENT

ISBN 978-90-8578-311-4
NUR 961
Wettelijk depot: D/2009/10.500/69

Universiteit Gent
Faculteit Ingenieurswetenschappen
Vakgroep Mechanica van Stroming, Warmte en Verbranding

Promotor: Prof. dr. ir. Michel De Paepe

Universiteit Gent
Faculteit Ingenieurswetenschappen

Vakgroep Mechanica van Stroming, Warmte en Verbranding
Sint-Pietersnieuwstraat 41, 9000 Gent, België

Tel.: +32-9-264.32.88
Fax.: +32-9-264.35.759

Department of Flow, Heat and Combustion Mechanics

Proefschrift tot het behalen van de graad van
Doctor in de Ingenieurswetenschappen:
Werktuigkunde-Elektrotechniek
Academiejaar 2008-2009

Dankwoord

De laatste loodjes wegen het zwaarst, zegt men, iets wat ik aan den lijve ondervonden heb. Een andere toepasselijke 'In De Gloria'-levenswijsheid is 'Langzaam bereikt de slak de ark'. Nu de ark eindelijk voor me oprijst, is het tijd om terug te blikken op de vier en een half jaar lange reis naar dit doctoraat. Daar hoort een passend dankwoordje bij, want alleen had ik dit avontuur nooit tot een goed einde gebracht. Vele mensen hebben geprobeerd me met hun steun en raad steeds op de goede weg te houden, een weg bezaaid met heel wat hindernissen. In de eerste plaats bedank ik mijn promotor, Michel. Als startende professor gaf jij mij de kans om een verlengstuk te breien aan mijn studies. We begaven ons beiden op onbekend terrein. Je gaf me de vrijheid om mijn eigen weg in de onderzoekswereld te zoeken, maar niet zonder in te grijpen als ik op een doodlopend spoor dreigde te geraken. Je zorgde er steeds voor dat ik de nodige financiën en andere hulpmiddelen ter beschikking kreeg om het onderzoek zo goed mogelijk uit te voeren, ook als de financiële middelen van de groep beperkt waren. Er kwam meermaals een wit konijn uit je toverhoed. Je gaf me de mogelijkheid mijn werk te presenteren op internationale conferenties, en dit in alle uithoeken van de wereld. Zo kon ik mijn horizon verbreden, en niet enkel op academisch niveau. Het globetrottervirus in mij werd sterk aangewakkerd, daar ben ik dankbaar voor. Want op deze manier draaide het doctoraat niet enkel rond wetenschappelijk gehakketak, maar gaf het me ook levenservaring en opende nieuwe werelden. Hierbij zou ik ook Gilbert willen bedanken. Jij overbrugde mij in het eerste jaar en plaveide zo de weg naar een solidere positie. Je maakte me wegwijs in de wereld van koeling van elektronica en natuurlijke convectie. Je bracht me kennis bij over infrarood thermografie en stelde een windtunnel ter beschikking. Ook al was ik de laatste jaren niet meer actief aanwezig in je groep, toch kon ik met mijn vragen steeds bij je terecht en verruimde je mijn inzicht in de zaken.

Een promotor beschikt ook niet over alle kennis in het universum, waardoor ik wel eens in uitzichtloze situaties leek terecht te komen, maar dan boden andere mensen een uitweg. Benny, dank je voor de vele hulp en uitleg over inverse problemen en optimalisatie. Je vertaalde ingewikkelde wiskundige methoden van Chinees naar Nederlands (al was het soms nog een dialect voor mij). Je stond steeds paraat om mogelijke problemen samen te bekijken en me nieuwe inzichten en opties aan te bieden. Je hebt me veel bijgebracht en enkele binnenwegen getoond

om tijd uit te sparen. Je maakte altijd tijd voor mij, waarvoor mijn oprechte appreciatie, te meer omdat je hier geen enkele verplichting toe had. Ik ben ook Jan een dankwoord verschuldigd, voor de inzichten en raad die hij me gaf over CFD. Zo kom ik bij Werner terecht, al sinds jaren een goede vriend, die bedreven is in optimalisatietechnieken en beeldverwerking, kennis die hij met veel plezier met me deelde, ook na de werkuren in een iets minder academische omgeving. Ook Bart en Stéphane mag ik niet vergeten, die belangeloos hun peperdure apparatuur ter beschikking stelden, zonder hierop enige tol te heffen. Pjotr, Cosmin en Octavio, jullie wil ik zeker bedanken voor de hulp en technische kennis die jullie me bijbrachten tijdens mijn eerste jaar.

Experimenteel onderzoek kan je niet doen zonder de hulp van ervaren technici, hetgeen Patrick en Robert zeker zijn. Ze vinden overal een oplossing voor, soms uit onverwachte hoek, en behouden steeds een nuchtere kijk. Ik wil hen van harte bedanken voor de vele hulp en technisch inzicht bij de opbouw van de proefstand. Als mijn computer weer eens moeilijk deed, of het zelfs begaf, dan was er altijd Yves, die in sneltempo deze problemen van de baan hielp. Dank je Yves, je hebt me meermaals uit de nood geholpen. Patricia verdient ook een schouderklopje voor haar puik administratief werk.

Dan zijn er de collega's, de reisgezellen zeg maar. Christophe, Hendrik-Jan en Hugo, jullie zijn meer dan gewoon bureaugenoten. Jullie stonden altijd klaar met raad en daad om mijn talloze probleempjes te helpen oplossen, of slecht geschreven doctoraatsteksten te verbeteren ;-). Maar jullie zorgden er vooral voor dat ik steeds met een glimlach op het werk zat, ook op de mindere dagen. De sfeer op het bureau zat steeds goed en de vele ontspannende, soms absurde conversaties maakten zelfs het saaiste werk weer draaglijk en zorgden voor veel hilariteit en gelach ('het luide bureau'). Het was fijn om samen een pint te pakken, te quizzen, naar de film of een optreden te gaan, ja zelfs samen op reis te gaan (wat is Reykyavik toch een bruisende stad ...). Het was me een waar genoegen jullie als collega's te hebben, ik kon het slechter getroffen hebben. Jullie lachten zelfs (al dan niet oprecht) om al mijn stomme mopjes, een zeldzame kwaliteit. Ik mag natuurlijk Sebastian niet vergeten. Hoewel hij niet fysisch op ons bureau zat en een mindere drinker is, toch hoort hij er ook bij, dankzij de vele aangename middagpauzes en verhelderende quizavonden. Ook de laatste aanwinsten van onze onderzoeksgroep, Marnix en Henk, wil ik bedanken voor hun bijdrage tot de gemoedelijke sfeer en het in stand houden van het hoge zevergehalte. Ook de overige collega's van de vakgroep: Reni, 'Tiny', Wasan en alle andere, bedankt voor de losse babbels in het keukentje, de gezellige bieravonden en de aangename sfeer in onze gang. Ook Bart wil ik bedanken, wiens deur steeds open stond, niet enkel voor vragen over CFD, maar ook voor een voetbalpraatje. Dat ging zelfs verder dan een praatje, want ik keek ook uit naar de jaarlijkse voetbalmatchen met ons ploegje, samen met Jan en Roger.

Als je meer dan vier jaar werkt aan een doctoraat, zit je uiteraard niet altijd op bureau. Het is een lange onderneming, en daarvoor heb je ook de nodige ontspanning en steun naast het werk nodig. Daarom wil ik ook mijn familie bedanken, en in de eerste plaats mijn ouders, voor de vele steun die ik van jullie kreeg. Bedankt

voor de mentaliteit die jullie me bijbrachten om steeds door te zetten en het beste uit mezelf proberen te halen. Een extra dikke dankjewel voor de ondersteuning die jullie me gaven in de laatste zware maanden. Op die manier zorgden jullie ervoor dat ik mij volledig op mijn werk kon toeleggen. Maar ook mijn broer en zussen wil ik bedanken, voor het medeleven en de interesse. Aan ontspanning had ik ook geen gebrek de laatste jaren. Zo wil ik graag mijn ploegmaten van onze zaalvoetbalclub Lazio Lede bedanken. We hebben de laatste jaren vele mooie momenten meegemaakt en enkele unieke prestaties geleverd, zowel op als naast het veld, en dat gaf me steeds de nodige energie en hield me scherp. Ik wil ook Gert en Jeroen bedanken, jullie twee zijn heel goede vrienden. Jullie staan steeds klaar om te zwanzen (mensen zeggen dat we dat soms doen ;-)), een pintje of wijntje te drinken en te luisteren als het nodig is. Jullie verdienen dus ook een plaats in dit dankwoord, al was het maar om naar mijn gezaag over dat doctoraat te luisteren.

Tenslotte wil ik mijn beste vriendin Stéphanie bedanken. Stéphanie, jij verdient een apart plaatsje in dit dankwoord. Jij bent voor mij de drijvende kracht geweest de laatste drie jaar, zonder jou had ik dit doctoraat nooit afgewerkt. Je was altijd een luisterend oor en een uitlaatklep voor mij. De tientallen concerten, prachtige reizen, ontelbare film- en muziekavonden, gesprekken en diverse zotte uitspattingen maakten het leven aangenaam en gaven me veel kracht om door te zetten. Jij hebt me leren relaxen en relativeren. En op de moeilijkste momenten was je er steeds voor me. Dankzij jou heb ik doorgezet en het einddoel bereikt. Zo zijn deze jaren van mijn doctoraat jaren die ik nooit meer zal vergeten.

Gent, augustus 2009
Arnout Willockx

Table of Contents

List of Figures

List of Tables

Nomenclature

a	Thermal diffusivity	m^2/s
A	Area	m^2
B	Camera calibration constant	–
Bi	Biot Number	–
c	Specific heat capacity	J/kgK
C_1	First radiation constant	–
C_2	Second radiation constant	–
d	Thickness (of wall or fin)	m
e	Hemispherical emissive power	W/m^2
E	Emitted radiated energy	W
F	Focal distance	m
F_p	Fin pitch	m
h	Heat transfer coefficient	W/m^2K
$\tilde{h}$	Estimated heat transfer coefficient	W/m^2K
H	Fin height	m
J	Funcional	–
k	Thermal Conductivity	W/mK
L	Fin length	m
M	Number of measurement points	–
n	Normal	
Nu	Nusselt Number	–
P	Search direction	–
Pr	Prandtl number: ratio of kinematic viscosity and thermal diffusivity	–
PR	Fin performance ratio	–
q	Heat flux	W/m^2
Q	Heat transfer rate	W
R	Thermal resistance	m^2K/W
Re	Reynolds number, the subscript refers to the chosen reference length L_{ref}	–
Ri	Richardson number	–
S	Surface	–
T	Temperature	K
ΔT	Temperature variation	K
U	Camera output signal	–
V_f	View factor	–
v	Velocity	m/s
x	Spatial coordinate, horizontal sense	m
y	Spatial coordinate, vertical sense	m
Y	Measured temperature	K

Greek Symbols

α	Viewing camera angle	
β	Step size in the SDM and CGM	–
γ	Conjugate coefficient used in the CGM	–
δ	Direac Function	–
ϵ	Emissivity	–
η	Fin efficiency	–
ζ	Fin effectiveness	–
θ	Louver angle	$^\circ$
λ	Lagrange multiplier and regularization parameter	–
μ	Dynamic viscosity	Pas
ν	Kinematic viscosity	m^2/s
χ	Stopping criterion	–
ρ	Density	kg/m^3
ϱ	Reflectivity	–
σ	Standard deviation	–
σ_c	Stefan-Boltzmann constant	W/m^2K^4
τ	Transmittance	–
Ω	Numerical domain	–

Superscripts

n	Index for the iteration number during CGM and SDM

Subscripts

air	Airside property
amb	Ambient property
b	Blackbody
cal	Calculated
conv	Convection
d	Related to the fin thickness
f	Fin
H	Horizontal
i	Index for an array of elements
id	Ideal, related to the fin having infinitely high thermal conductivity
L	Related to the fin length
m	Index for the measured temperature array
max	Maximum value
meas	Measured
obj	Object property
prim	Primary surface
prom	Promatec
ref	Reference value
surf	Surface
tot	Total
V	Vertical
wall	Wall property
x	The value in the X-direction
∞	Undisturbed free stream value

Acronyms

CFD	Computational Fluid Dynamics
CGM	Conjugate Gradient Method
FEM	Finite Element Method
FOV	Field of View
FVM	Finite Volume Method
IEA	International Energy Agency
IHCP	Inverse Heat Conduction Problem
IHTP	Inverse Heat Transfer Problem
IR	Infrared
LW	Long wave
SDM	Steepest Descent Method
SW	Short wave
VMM	Variable Metric Method

Nederlandse samenvatting –Summary in Dutch–

Warmteoverdracht is een fysisch proces waarbij energie wordt uitgewisseld. Het komt onder meer voor bij de productie van elektriciteit, de klimatisatie van gebouwen, het bereiden van maaltijden, ... De laatste jaren streeft men bij warmteoverdracht naar energetische efficiëntie. Dat is niet onbegrijpelijk. Het energieverbruik is immers exponentieel toegenomen en deze trend zal zich voortzetten. Daarom tracht men warmteoverdrachtsprocessen te verbeteren. Tegelijk streeft men naar miniaturisatie. Deze trend valt vooral in de elektronica op: desktops, laptops, dvd-spelers, mp3-spelers en televisies worden steeds dunner en/of kleiner. De combinatie van miniaturisatie met steeds krachtiger en snellere elektronica zorgt ervoor dat de energiedichtheid van elektronische componenten (chips, processors,...) aanzienlijk toeneemt. Om deze componenten te voeden zijn grote hoeveelheden elektrische energie nodig. Die wordt omgezet in warmte die de kleine oppervlakten niet kunnen dissiperen zodat grote warmtefluxen ontstaan. Om oververhitting (en dus falen) van elektronische componenten te voorkomen is een efficiënte warmteafvoer noodzakelijk. Ondanks de ontwikkeling van nieuwe koelmethodes om hoge vermogenfluxen te dissiperen blijft de meest gebruikte, goedkoopste en vrijwel universeel toepasbare methode voor het koelen van elektronica lucht als koelmiddel hanteren in combinatie met een vinblok ('heat sink'). Het vinblok staat op de elektronische en zorgt voor een betere verspreiding van de warmte en een groter warmtewisselend oppervlak. Meestal is een vinblok opgebouwd uit longitudinale vinnen. Aanpassingen aan de vinvorm kunnen de warmtewisseling laten toenemen zonder dat hiervoor een groter vinvolume nodig is.

Dit doctoraatsproefschrift is specifiek gericht naar longitudinale vinnen. In eerste inastantie is er een meetmethodiek ontwikkeld die het mogelijk maakt om zowel de prestatie van longitudinale vinnen te bepalen als de mogelijke prestatieverbetering door aanpassingen aan de vinvorm. Deze techniek verschaft niet alleen een globale waardebeoordeling aan de hand van een performantieparameter, maar maakt het tevens mogelijk om lokale warmteoverdrachteffecten te bestuderen. In dit werk wordt de meettechniek toegepast op longitudinale vinnen voor koelen van elektronica maar hij is uitbreidbaar naar andere vintypen. Hoofdstuk 1 bestudeert het bestaande onderzoek naar longitudinale vinnen en naar lokale warmteoverdrachtscoëfficiënten. Het aantal studies is beperkt en bovendien zijn deze studies vaak onnauwkeurig. Daarnaast presenteert hoofdstuk 1 een onderzoek naar de verschillende vinprestatie indicatoren. Een algemene conclusie is dat het wijd-

verspreide concept vinefficiëntie misleidend is en eigenlijk een slechte indicator is voor de vinprestatie. Toch wordt vaak gestreefd naar een zo hoog mogelijke vinefficiëntie, als zou die de maximale warmteoverdracht garanderen. Een betere, meer betrouwbare parameter is de vineffectiviteit, of de prestatieratio die er van afgeleid is. Een hoge vineffectiviteit stemt daadwerkelijk overeen met een betere warmteoverdracht. Daarom is er in dit werk gekozen om vineffectiviteit te gebruiken als evaluatieparameter. De meetmethodiek moet dus naast lokale warmteoverdrachtscoëfficiënten ook vineffectiviteit kunnen bepalen. Om beide doelen te bereiken moet de verdeling van de warmtefluxen door een vin gekend zijn. Aangezien het niet evident is om warmtefluxen te meten, is het meer gebruikelijk om temperaturen te meten en aan de hand van deze temperatuurverdeling de warmtefluxen te bepalen. Deze aanpak vereist twee zaken: een meettechniek om temperatuurverdelingen nauwkeurig op te meten en een numerieke methode om de warmtefluxverdeling uit deze temperatuurmetingen te bepalen.

Het tweede hoofdstuk ontwikkelt deze numerieke methode. Het bepalen van warmtefluxen uit temperaturen staat beter bekend als het invers conductieprobleem. Het is een invers probleem omdat de aanpak omgekeerd tewerkgaat: in een direct probleem gelden warmtefluxen als randvoorwaarden en wordt daaruit het temperatuurveld bepaald, bij een invers conductieprobleem is de oplossing gekend (het temperatuurveld) en bepaalt men daaruit de randvoorwaarden (de warmtefluxen). Een inleidende literatuurstudie toont aan dat inverse conductieproblemen slecht geponeerd zijn en dus meerdere oplossingen kunnen hebben. Daarom worden er speciale wiskundige methodes gebruikt om een stabiele, fysisch correcte, oplossing te bekomen. Er zijn vele verschillende oplossingsmethoden terug te vinden in de literatuur, die allen steunen op de minimalisatie van een temperatuurfunctie. Het hoofdstuk verstrekt vervolgens een overzicht van de gebruikte technieken en de verschillende types inverse conductieproblemen. Het type invers conductieprobleem bestudeerd in dit werk is driedimensionaal, lineair en stationair. Op basis van het overzicht van de verschillende numerieke technieken wordt de meest geschikte methode gekozen. Twee methodes komen in aanmerking: de steepest descent method (SDM) en de conjugate gradient method (CGM). In het hoofdstuk zijn de volledige oplossingsalgoritmen te vinden voor deze vergelijkbare technieken.

Hoofdstuk 3 past beide oplossingsmethoden ontwikkeld in hoofdstuk 2 toe op enkele numerieke testcases. Deze bestaan uit een rechthoekige longitudinale vin die een vlak primair oppervlak gedeeltelijk bedekt. De vinwanden en het primair oppervlak krijgen verschillende profielen voor warmteoverdrachtscoëfficiënten opgelegd. Met deze randvoorwaarden wordt een temperatuurprofiel berekend op dezelfde oppervlakken. Deze temperatuurprofielen worden beschouwd als perfecte temperatuurmetingen en zijn de randvoorwaarden van het inverse conductieprobleem. Het inverse conductieprobleem wordt opgelost zowel met SDM als met CGM. Hierbij wordt ook de invloed van meetfouten op de opgemeten temperatuurprofielen nagegaan, voor twee verschillende meetnauwkeurigheden: 0.1°C en 0.5°C. SDM en CGM blijken vergelijkbare resultaten op te leveren op het gebied van nauwkeurigheid, maar CGM convergeert veel sneller dan SDM. Het intro-

duceren van meetfouten op de temperatuurmetingen geeft vergelijkbare resultaten met het ideale geval van exacte temperatuurmetingen. Enkel de afwijkingen op de randen nemen aanzienlijk toe. Het opvoeren van de meetfout van 0.1°C naar 0.5°C zorgt niet voor de verwachte drastische verminderde nauwkeurigheid van de geschatte profielen. De resultaten zijn zelfs vergelijkbaar met de resultaten zonder meetfout. Daaruit blijkt dat de oplossingsmethoden niet te gevoelig zijn aan ruis en dus geschikt zijn om experimentele meetdata te verwerken. Vanwege de snellere convergentie werd er gekozen om CGM te gebruiken als oplossingsmethode.

De numerieke oplossingsmethode om warmtefluxen uit temperatuurmetingen te bepalen staat nu op punt. Vervolgens ontwikkelt hoofdstuk 4 de meettechniek. Daarbij wordt gekozen voor infrarood thermografie die als voordeel heeft dat het een contactloze meetmethode is zodat het temperatuurveld en meetobject niet verstoord worden door het uitvoeren van de meting. Bovendien biedt thermografie de mogelijkheid volledige temperatuurprofielen vast te leggen met één meting. Het eerste deel van het hoofdstuk licht enkele basisbegrippen van straling en thermografie toe, werkt kalibratiemethodes uit en past die toe. Op de parameters die de invallende stralingsenergie bepalen en op de cameraspecifieke eigenschappen wordt een foutenanalyse uitgevoerd, wat resulteert in een onzekerheid over de gemeten temperatuurwaarden. Het tweede deel behandelt de gebruikte meetopstelling. Eerst worden de dimensies van de bestudeerde vinnen bepaald op basis van de Reynolds analogie en gegevens uit de literatuur. Daarna wordt de opbouw van de proefstand beschreven. Die maakt gebruik van een lagesnelheidswindtunnel om de omgevingscondities in te stellen en het Reynoldsgetal (Re) te variëren, zodat de invloed van Re op de vineffectiviteit en het lokale warmteoverdrachtscoëfficiëntprofiel kan bestudeerd worden. Er wordt een warmtebron onderaan de vin geplaatst, in combinatie met een guard heater om ongecontroleerde warmteverliezen te beperken. Het vermogen van de warmtebron wordt bepaald op basis van de temperatuur waarop de vin moet staan om zo nauwkeurig mogelijke metingen met de infrarood camera te kunnen uitvoeren. Er worden diverse vinvormen bestudeerd: volle rechthoekige longitudinale vinnen en geperforeerde vinnen met een verschillend aantal perforaties.

Het laatste hoofdstuk voert een data reductie uit presenteert de resultaten. De temperatuurfoto's, opgemeten met de infrarood camera tijdens de experimenten, worden omgezet naar een matrix met de temperatuurwaarden. Deze matrix valt in te lezen als randvoorwaarde van het inverse conductieprobleem. Dit probleem wordt vervolgens opgelost met de ontwikkelde oplossingsmethode gebaseerd op CGM. Zo worden dan de lokale warmtefluxen en de vineffectiviteit bekomen. De resultaten voor de rechthoekige longitudinale vinnen stemmen overeen met wat de literatuur voorspelde. De lokale warmteoverdrachtscoëfficiënten geven de verwachte trends aan, en tonen zelfs de invloed van een hoefijzerwervel aan de vinbasis. De resultaten van de vineffectiviteit zijn te onnauwkeurig om sluitende conclusies te trekken. De resultaten voor de geperforeerde vinnen demonstreren de invloed van de perforaties en van het herstarten van de grenslaag: na de perforatie hebben de lokale warmteoverdrachtscoëfficiënten hogere waarden. De vergelijking met waarden uit de literatuur bevestigt de bekomen resultaten. De resultaten

van de vineffectiviteit zijn te onnauwkeurig om sluitende conclusies te trekken. Tot slot trekt hoofdstuk 6 de belangrijkste conclusies maakt het suggesties voor toekomstig onderzoek.

English summary

Heat transfer is a physical process in which energy is exchanged. It occurs in numerous applications, such as production of electricity, building climatisation, food preparation, ... Since energy consumption has increased tremendously in the last decades and this trend will continue, the concept of energy efficiency has become omnipresent. In electronics miniaturization has become a trend. Desktops, laptops, dvd-players, mp3-players, televisions, ... are getting thinner and/or smaller. Together with the increase in work speed and capacity, these small dimensions cause the energy density of electronic components (chips, processors,...) to intensify significantly. As the electric power supply for these components is converted into heat, the component temperature rises. Hence, large amount of electricity are dissipated in a small surface area and cause high heat fluxes in the electronic components. To prevent overheating (and therefore failure) of electronic components, efficient heat removal is necessary. A cheap and almost universally applicable method for the cooling of electronics uses air as coolant in combination with a heat sink. The heat sinks are placed on the electronic component in order to distribute the heat and to create a better heat transfer. A heat sink mostly consists of longitudinal fins. Fin shape adjustments can improve the heat transfer, without the need for an increase in fin volume.

This dissertation is specifically aimed at the research on longitudinal fins. It takes off looking for a measurement method to determine the performance of longitudinal fins as well as possible performance improvements by adjustments to these fins. The developed technique offers a global examination with a performance parameter. Moreover, it creates the possibility to study local heat transfer effects. In this work, the technique is applied to longitudinal fins, specifically fins for the cooling of electronics, but can be extended to other fin types. Chapter one also provides a summary of previous research on longitudinal fins. The number of studies on local heat transfer coefficients is limited and these studies are often inaccurate. A study of different fin performance indicators was also made, which indicated that the widely spread concept of fin efficiency is misleading, and a bad fin performance indicator. Nevertheless, many studies still aim for the highest possible fin efficiency, assuming this would guarantee the maximum heat transfer. A better, more reliable fin performance parameter is the fin effectiveness, or the performance ratio which is derived from it. As high fin effectiveness actually corresponds to a higher heat transfer, fin effectiveness was used as the fin performance indicator in this work. The developed measurement technique should not only be able to determine local heat transfer coefficients, it should also measure the fin ef-

fectiveness. To attain those goals, one has to determine the heat flux distribution in the fin. Normally, one does not measure heat fluxes, but temperatures, that make it possible to calculate the heat flux distribution. This requires a technique to accurately measure temperature profiles, and a numerical method to calculate the heat flux distribution from these measurements.

This numerical method is developed in the second chapter. Determining heat fluxes from temperatures is known as the inverse heat conduction problem. This kind of problem is solved inversely. Whereas in a direct problem heat fluxes are imposed as boundary conditions and the temperature field is calculated from these conditions, in an inverse conduction problem the solution (temperature field) is known and the boundary conditions (heat fluxes) are determined from these temperatures. An introducing literature survey indicates that the inverse conduction problem is ill-posed and that it therefore can have several solutions. To obtain stable, physically correct solutions, mathematical methods are used. The second chapters offers a summary of the solution methods found in literature, which are all based on the minimization of a temperature functional. The inverse heat conduction problem studied in this work is three-dimensional, linear and steady state. Based on the summary of the different numerical techniques the most suitable methods are chosen. Two methods are taken into consideration: the steepest descent method (SDM) and the conjugate gradient method (CGM). Chapter two mathematically develops both of these similar techniques and writes the complete solution algorithm for both of them.

These two solution algorithms are applied to some numerical test cases in chapter 3. The test cases consist of a rectangular longitudinal fin that partly covers a flat primary surface. Different heat transfer coefficient profiles are imposed on the fin walls and the primary surface. Using these boundary conditions, the temperature profiles on the same surfaces are calculated. These temperature profiles are considered as exact temperature measurements and are the boundary conditions for the inverse heat conduction problem. This inverse heat conduction problem is solved with both SDM and CGM. Afterwards, chapter three investigates the influence of measurement errors on the measured temperature profiles for two different measurement accuracies: 0.1°C and 0.5°C. Apparently SDM and CGM have a comparable accuracy, but CGM converges much faster. The introduction of measurement errors gives comparable results as in the ideal case of exact temperature measurements. Only at the edges the deviations increase significantly. Enlarging the measurement error from 0.1°C to 0.5°C does not lead to the expected drastic decrease in accuracy of the estimated profiles. The results are even comparable to the exact results. This indicates that the solution methods are not too sensitive to noise and thus suitable to process experimental measurement data. Relying on the results, CGM was chosen as solution method because of the faster convergence rate.

Chapter 4 develops a measurement method using infrared thermography as measurement technique. Infrared thermography has the advantage that it is a non-contacting method. Thus the temperature field and measurement object are not disturbed by the measurement. Moreover, thermography makes it possible to get

complete temperature profiles with a single measurement. The first part of the chapter explains some basic notions on radiation and thermography. Calibration methods are drawn up and applied. An error analysis is executed on the parameters that determine the incident radiation energy and on the camera specific properties, resulting in an uncertainty for the measured temperature values. The second part of the chapter explains the measurement setup. First the dimensions of the studied fins are determined based on the Reynolds analogy and on data from literature. Subsequently, the composition of the experimental setup is described. A low speed wind tunnel is used to set the environmental conditions and vary the Reynlods number (Re), which allows examining the influence of Re on the fin effectiveness and local heat transfer coefficients. A heat source is placed at the bottom of the fin, in combination with a guard heater to limit uncontrolled temperature losses. The power of the heat source is based on the fin temperature that should be attained to perform the most accurate temperature measurements with the infrared camera. The end of the chapter presents the different fin forms that will be studied: solid rectangular longitudinal fins and perforated fins with various numbers of perforations.

The final chapter accomplishes the data reduction and presents the results. The temperature images, measured with the infrared camera during the experiments, are converted to a matrix with temperature values. This matrix can be used as a boundary condition for the inverse heat conduction problem that is solved with the developed solution method based on CGM. This solution makes it possible to determine the local heat fluxes and fin effectivenesss. The results obtained for the rectangular longitudinal fins agree with data from literature. The local heat transfer coefficients indicate the expected trends, and even show the influence of a horseshoe vortex at the base of the fin. The results for the perforated fins show the influence of the perforations and of restarting the boundary layer: after a perforation higher local heat transfer coefficients are found. The comparison with values from literature confirms the obtained results. The results for fin effectiveness are not accurate enough to draw conclusions for this.

To conclude, chapter 6 presents the most important findings and perspectives for future work.

1 Introduction

1.1 Heat transfer

Heat transfer is all around us: it is intertwined in all aspects of our lives. Some basic examples are:

- preparation (e.g. cooking, baking,...) and conservation (e.g. refrigerator) of food
- production of electricity (e.g. steam production from water to feed steam turbines)
- providing good indoor air quality (temperature and relative humidity control) in houses, buildings and vehicles (e.g. heating, air conditioning,...)
- cooling of electronic equipment to keep it durable and reliable (e.g. televisions, computers,...)
- all kinds of industrial activities and production techniques

These are just a few examples. The amount of energy that is transferred daily worldwide under the form of heat is enormous. Energy consumption worldwide has increased significantly over the last decades, from 8000 Mtoe in 1986 to 10.000 Mtoe in 2001 and almost 12.000 Mtoe in 2006 [1], as is shown in Fig. 1.1. The same graph illustrates that still more than 80 % of this energy production originates from fossil fuels. The associated CO_2 emissions rose with 25 % between

1990 and 2005. Considering the very strong indicators that these man-made greenhouse gasses have an impact on the worlds heat balance (global warming), a strong drive exists to reduce emissions. This drive resulted in the signing of the Kyoto Protocol. An important factor in reducing the CO_2 emission while meeting the increasing energy demand, is a more intensive use of alternative and renewable energy resources, such as solar power, wind power, hydropower, biomass,... energy resources which are CO_2 neutral. However, there is also a second way to reduce the effect of the increasing energy demand: improved energy efficiency. A study of the International Energy Agency (IEA) [1] reports that for 16 IEA-countries, the economical growth is decoupled from the final energy consumption due to improved energy efficiency. Without the improvement of energy efficiency between 1973 and 2005, the energy use in those countries would have been 58 % higher in 2005 than it actually was. The importance of a continuous improvement of energy efficiency explains the need for improving the performance of heat transfer technologies.

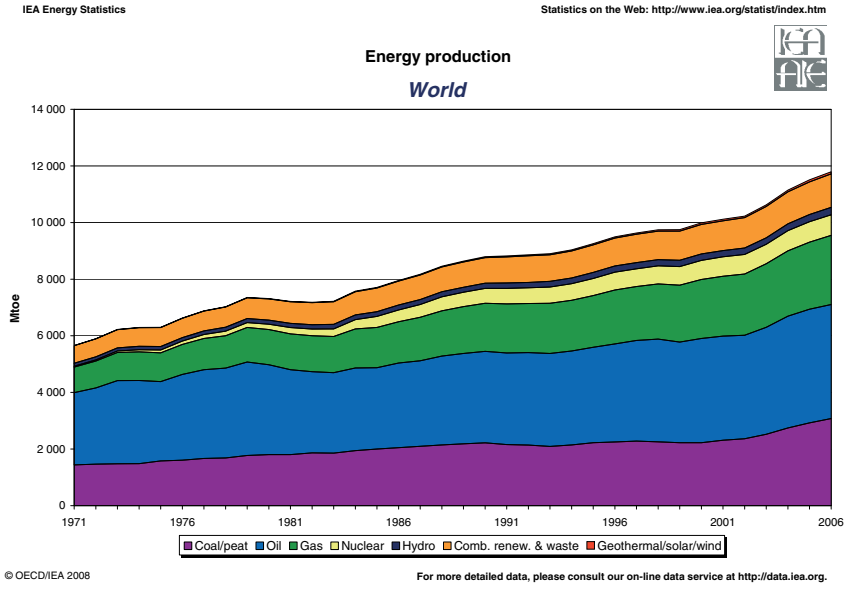

Figure 1.1: The worldwide energy production during the last decades [1]

The same IEA report states also that global electricity consumption increased by 54 % between 1990 and 2005. For household energy demand, appliance energy use is growing very rapidly and has overtaken water heating as the second most important demand after space heating. This can be explained by the high living

standard and large amount of electric appliances per family. A second effect which comes into play is the increasing power density of electronic equipment in the last decades.

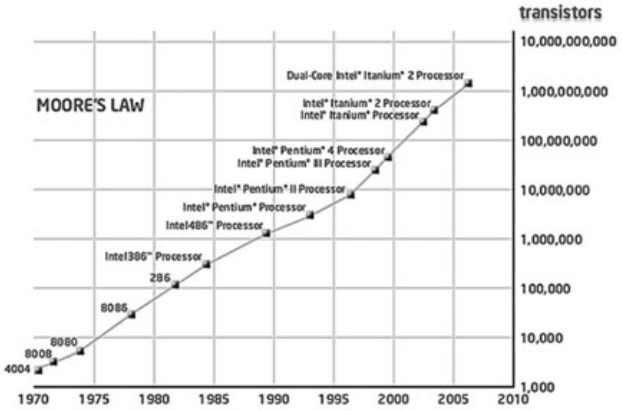

Figure 1.2: The evolution of Intel CPU processors illustrates Moore's law [2]

The increase in power density of electronic components was already predicted in 1965 by Moore [18]. He predicted that the number of transistors on a chip will double about every 18 months. Later he corrected this to every two years. This is known as Moore's law. Figure 1.2 depicts how accurate this law proved to be for Intel processors [2]. This incredible increase in transistor density results in ever increasing applied power per unit volume demands for the electronic packaging. In combination with higher clock rates and an emerging trend of miniaturization, this results in high heat fluxes at chip level. The miniaturization of course is related to increasing the transistor density as well as reducing the power consumption of the individual transistors. The 2005 International Technology Roadmap for Semiconductors (ITRS) indicated a continuing rise of high performance processors from a maximum power of 365 W in 2006 to 515 W by 2011 [19, 20]. This increase in power dissipation and the reduced size creates a growth in power density, which is expected to keep growing in the coming years. The junction temperature on silicon based semiconductors is limited to 100 °C for safe operation. However, lower temperatures are desirable for higher reliability, extended life and lower maintenance costs [21]. High chip temperatures result in thermal failures such as mechanical stresses, thermal fracture and thermal de-bonding. Temperature is the main reason for failure in electronics, as shown in Fig. 1.3 [22]. ITRS predicts a decrease in the maximum allowable junction temperature from 100 °C, currently, to 90 °C by 2011 [20]. Different models of CPU's have different maximum operating temperatures and power consumption, as illustrated in table 1.1 [23]. So there is a

continuous need for development of high performance thermal management solutions to maintain integrated circuit chips at an acceptable junction temperature by heat dissipation. More efficient heat transfer augmentation cooling devices are needed to control the junction temperature. Next to CPUs, there are also Graphical Processing Units (GPU's) found in todays PCs. These are used in high-end applications and often have even higher loads than CPUs. Therefore cooling of electronic equipment is a very active branch of heat transfer investigation [24].

CPU type	Max operating T (°C)	Power dissipation (W)
P IV Extreme 3.46GHz.	68.0	110.0
Pentium M.	100.0	25.0
Athlon XP 2200+.	85.0	67.9

Table 1.1: Some examples of maximum CPU temperatures and power consumption

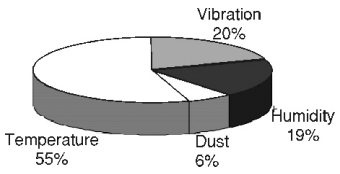

Figure 1.3: Cause for electronic failure

1.2 Basic Heat Transfer

1.2.1 Heat transfer modes

There are three fundamental heat transfer mechanisms: conduction, convection and radiation. The importance or presence of each of these mechanisms depends on the application. For the cooling of electronics, all three heat transfer modes play an important role.

Conduction

Conduction occurs at molecular scale: it is the transport of thermal energy between adjoining molecules due to a temperature gradient. The heat will always flow from a higher temperature to a lower temperature. Conduction appears in solids as well

as in liquids and gases. The heat transfer will not be discussed in detail on a microscopic level, but the effects on a macroscopic level are. The law that describes heat conduction at macroscopic level is called Fourier's law [25]. It is illustrated based on an example of one-dimensional conduction through a solid wall, as depicted in Fig.1.4. The left side of the wall is maintained at a temperature T_1, the right side is at a lower temperature T_2. So there is a temperature gradient over the thickness d of the wall. Heat flows through the wall from the higher temperature T_1 to the lower temperature T_2. Fourier's law states that the heat transfer Q through the wall is proportional to the negative temperature gradient. Often the heat transfer is expressed per unit area, called the heat flux q. The constant of proportionality is the thermal conductivity k of the substance (in this case the wall). So Fourier's law for the example in Fig.1.4 can be written as:

$$q = -k \cdot \frac{dT}{dx} \tag{1.1}$$

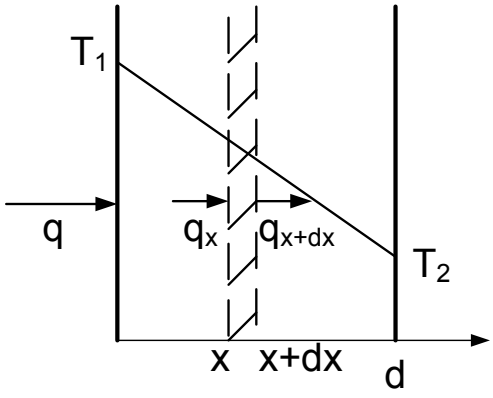

Figure 1.4: One-dimensional conduction through a wall

Conduction is very important for heat transfer through solids. The other heat transfer mechanisms (convection and radiation) do not occur inside opaque solids, but only at the boundary walls of the solid. For transparent solids radiation occurs through solid bodies, even with internal reflections, but this does not apply for this work.

Radiation

Heat transfer by radiation can be viewed in terms of electromagnetic waves. Each object at a temperature higher than 0K will emit this kind of electromagnetic

radiation. The best known example is the solar radiation which heats the earth. The total amount of radiation emitted by an object is proportional to the fourth power of the object temperature (T^4), thus heat radiation increases fast with increasing object temperature. The thermal radiation occurs at a wide range of frequencies. A more extensive introduction to thermal radiation is given in Chapter 4, in which the main concepts and laws are explained. For now only the Stefan-Boltzmann law (Eq.(1.2)) is mentioned, which gives the total amount of heat radiated by a black body at temperature T. The exact definition of a black body is also given in Chapter 4.

$$e = \sigma \cdot T^4 \tag{1.2}$$

with σ the Stefan-Boltzmann constant ($5.67{\times}10^{-8}\mathrm{W/m^2K^4}$) and e the total amount of radiated energy flux.

Convection

Convection is the transport of energy by the bulk motion of a medium. In engineering applications, convection is commonly used to remove heat from a surface to a moving fluid [25]. Convective heat transfer depends on the movement of a fluid, and thus only occurs in liquids and gases. The rate of convective heat transfer is a function of the surface geometry and temperature, fluid temperature, fluid velocity and the thermophysical properties of the fluid. The amount of heat transferred to or from a surface by a fluid flow was first quantified by Sir I. Newton's law of cooling (Eq. (1.3)) expresses that the heat transfer rate is proportional to the surface area and the temperature difference between the surface and the fluid. The proportion factor was called the convective heat transfer coefficient h, which is a function of the flow velocity, the surface size and geometry and the flow and plate temperature.

$$Q = h \cdot A \cdot (T_{\mathrm{surf}} - T_{\mathrm{fluid}}) \tag{1.3}$$

There are two types of convective heat transfer: natural and forced convection. In natural convection the fluid motion is generated by buoyancy forces that result from density differences in the fluid due to temperature gradients. When the fluid is forced to flow over the surface by an external source such as a fan or a pump, it is called forced convection. Although the difference is made, both convection modes can occur simultaneously.

1.2.2 Boundary layers and dimensionless numbers

It is clear that a higher convective heat transfer coefficient h gives a better heat transfer between surface and fluid. The boundary layer concept is important for

the study of convective heat transfer and is applicable for newtonian fluids. There are two types of boundary layers: laminar and turbulent boundary layers, depending on the flow regime (Reynolds number). Only the concept of laminar boundary layer is used in this work and this is illustrated with the example of a laminar air flow at a velocity V_∞ over a horizontal plate at a temperature T_{surf} which is higher than the air temperature T_∞ (Fig.1.5). The hydrodynamic boundary layer is the fluid layer in the immediate vicinity of a surface. The boundary layer is formed by viscous forces: the fluid layer in direct contact with the plate is stationary due to viscous action, and this layer retards the motion of adjoining fluid layer, and this layer retards the next fluid layer, and so on, until the effect becomes negligible. This retardation is associated with shear stresses, thus the hydrodynamic boundary layer is not characterized by temperature gradients. The border of the boundary layer is set where the air velocity V_x is 99% of the free stream velocity V_∞. Coupled with this hydrodynamic boundary layer, there is also thermal boundary layer, in which the temperature varies from T_{surf} at the wall (y = 0) to T_∞. The thermal boundary layer thickness δ_t is defined as the value of y (Fig. 1.5) for which $[(T_{surf} - T)/(T_{surf} - T_\infty)]$ = 0.99. The thermal and hydrodynamic boundary layer are not the same and mostly have a different thickness. For increasing flow velocity, the velocity boundary layer thickness decreases, and the temperature gradient over the thermal boundary layer becomes steeper. The fluid layer in contact with the wall is stationary, thus the heat is transferred through this layer by conduction. Fourier's law then gives:

$$q = -k \cdot \left(\frac{\partial T}{\partial y}\right)\Big|_{y=0} \tag{1.4}$$

in which k is the thermal conductivity of air. By comparison with Newton's law of cooling (Eq.(1.3)), the convection coefficient can also be written as:

$$h = \frac{-k \cdot \left(\frac{\partial T}{\partial y}\right)}{T_{\mathrm{surf}} - T_\infty} \tag{1.5}$$

Thus, by increasing the velocity V, the temperature gradient in the y-direction (Fig.1.5) in the boundary layer becomes steeper, and the convection coefficient h increases. Hence the convective heat transfer coefficient depends on the boundary layer thickness. The boundary layer thickness is not only a function of the fluid velocity, but also of the fluid viscosity and the flow regime: laminar, turbulent or a transition between both. These factors also influence the convective heat transfer. Dimensionless numbers are used in correlations to allow for apt comparisons of different geometries and different flow regimes. The Reynolds number Re (Eq.(1.6)) represents the ratio of inertial to viscous forces within a flow. The classification of laminar and turbulent flow is also based on Re. Therefore Re is used in correlations for forced convective heat transfer. Such correlations often express

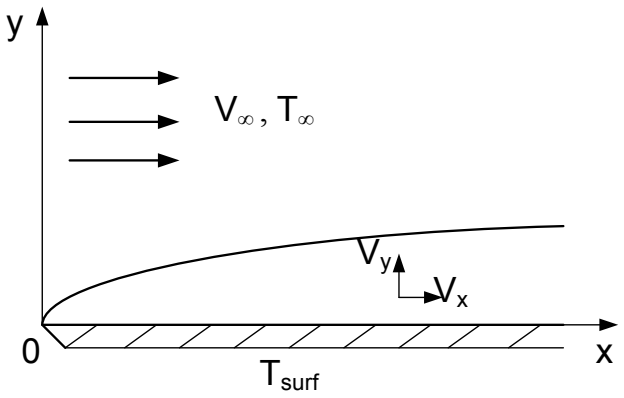

Figure 1.5: Laminar boundary layer for air flow along a horizontal plate

the relation between the hydraulic dimensionless group Re and a dimensionless number that represents the heat transfer: the Nusselt number Nu (Eq.(1.7)). This number represents the ratio of the convective to the conductive heat transfer across a boundary.

$$Re = \frac{\rho \cdot V \cdot L_{\mathrm{ref}}}{\mu} \tag{1.6}$$

$$Nu = \frac{h \cdot L_{\mathrm{ref}}}{k} \tag{1.7}$$

In these dimensionless numbers, L_{ref} is a reference length scale, which should be selected at a dimension relevant to the studied case, e.g. plate length. The velocity V can be either the main inlet velocity or the average velocity in the minimal flow section. The fluid properties (such as density ρ, thermal conductivity k and dynamic viscosity μ) are usually evaluated at mean fluid temperature. Other dimensionless numbers used in this work are:

- Prandtl number Pr (Eq. (1.8)), ratio of kinematic viscosity and thermal diffusivity:

$$Pr = \frac{\mu \cdot c_p}{k} \tag{1.8}$$

- Biot number Bi (Eq. (1.9)) is the ratio of the convective heat transfer coefficient to the thermal conductivity transfer coefficient in a solid body

$$Bi = \frac{h \cdot L_{\mathrm{ref}}}{k_{\mathrm{obj}}} \tag{1.9}$$

1.2.3 Extended surface heat transfer

There are two categories of methods for improving heat transfer: active and passive methods. Active methods require external power to enhance heat transfer, passive methods do not [26]. Fins or extended surfaces are the most common example of a passive method. Fins extend from a primary surface, and thus are also called extended surfaces. They are used with the goal of substantially increasing the heat transfer from the primary surface to the surrounding fluid. This increase in heat transfer is mainly realized by the increase in heat transfer surface area. But fins can also interrupt boundary layers and induce turbulence, which also causes higher convective heat transfer coefficients and thus increases heat transfer [9]. Transferring heat from one object or medium to another is subjected to a heat transfer resistance, which is a summation of resistances. This can be seen in Fig. 1.6, where heat is transferred between two fluids separated by a wall. There are three resistances in this case: convective resistance between fluid 1 and wall, the conductive resistance through the wall and another convective resistance from wall to fluid 2. When transferring heat to air, the air side convective resistance dominates the total resistance and is greater by at least one order of magnitude. Fins reduce the dominant resistance to heat flow across the primary surface by increasing the heat transfer coefficient h and/or increasing the heat transfer area A [21, 27]. The usefulness of a fin is expressed by a fin performance parameter. The commonly used fin performance parameter is the fin efficiency, which is defined as the ratio of heat transferred by a fin to the amount of heat transferred by the same fin if the total fin was at base temperature. Thus fin efficiency expresses the fin performance to an ideal fin of the same form.

The most obvious example of an active method to enhance heat transfer is the increase of flow velocity. An increased flow velocity results in an increased heat transfer coefficient but also in an increased pressure drop and hence in an increase of the fan power consumption. This undesirable effect explains the popularity of the use of fins.

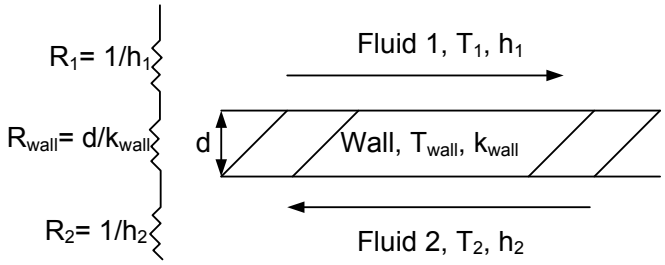

Figure 1.6: Heat resistances during heat transfer

Fins are used in a wide variety of applications. For example: air conditioners, refrigeration systems, domestic applications such as radiators in rooms, radiators in vehicles, internal combustion engines, electronic devices (PCs, power sources, transformers,...), heat exchangers in industry, but also radiating finned surfaces for space heat rejection systems [27, 28]. These are just a few examples of the numerous applications. The cooling of electronics is a very specific application in which the fins mostly take the shape of a heat sink. Heat sinks absorb and dissipate heat from an object at a relatively high temperature using thermal contact. Heat sinks create a larger volume and cause a better spreading of the heat, so the heat fluxes through the larger surface areas of the heat sink drop and as a consequence, the temperature also decreases. For cooling of electronics, a heat sink is an assembly of fins placed on a base plate, which is placed directly on the critical components. In Fig. 1.7 an example of a heat sink commonly used in the cooling of electronics is shown.

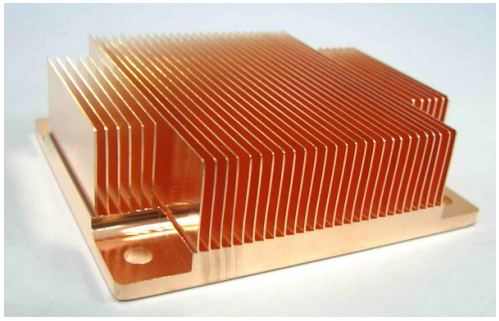

Figure 1.7: Heat sink commonly used to cool electronics

Depending on the situation, different kinds of fins are used. Different factors that influence the choice of fin type are: available volume, weight limitation, amount of heat that needs to be removed, working conditions, ... [29]. Three basic fin types can be distinguished: longitudinal, pin and annular fins [4, 30]. This work focuses on heat sink applications. The most commonly used extended surfaces in heat sinks are longitudinal and pin fins.

1.3 Cooling of electronics

Air cooling remains the most popular method for electronics cooling. It is used for a wide variety of applications: from portable devices to large business systems [22]. Natural convection cooling (sometimes in combination with heat sinks) is used for circuit boards with heat fluxes from 155-1500 $\mathrm{W/m^2}$. It is common in

TV, DVD,... [21]. Forced air convection with heat sinks is used when natural convection becomes insufficient, thus for electronics with higher power dissipation. A classic and well-known example is the cooling of computer processors. However, Lasance [31] stated already in 1995 that the limits of air cooling with heat sink and fin would be reached in the coming years. Copeland [32] gave performance limits for heat sinks and these are almost reached. Notwithstanding this, forced air convection with heat sinks will remain popular for cooling of electronics due to its advantages. Therefore, it remains important to increase the efficiency of the heat sink heat transfer which makes search on new fin forms for heat sinks and high efficiency heat sinks a very active area. Even if this technique is not sufficient anymore to provide cooling for the high end processing units of PC's or workstations due to the increased heat flux, it still has a wide range of applications in electronic equipment containing microprocessors or power handling semiconductors, like TV's, power converters,... The use of heat sinks is common for various reasons:

- ease of maintenance
- passive cooling technique, and if fans are necessary they have a low power consumption
- low production cost
- thermal spread: more uniform temperature in the components
- ease of implementation in the device and relatively low weight
- no special cooling fluid

One of the main constraints in thermal management is the cost: the cooling technology must be cost effective and has to be compatible with the reduction in overall package size [22]. Heat sinks are a passive cooling technique, which have a preference for modules with spatial limitation. Cost effectiveness is the driving force in new designs of electronics, not thermal management. Thermal management of electronics is often studied at the end of the design procedure, which often causes the need for high cooling power. There are of course other possibilities than air cooling. Other kinds of techniques used for cooling of electronics are:

- forced liquid cooling
- natural two-phase flow (heat pipes)
- forced two phase flow (boiling in microchannels)
- refrigeration cooling

- thermoelectric cooling

If these different methods are classified in four categories, according to heat transfer capacity, the graph in Fig. 1.8 is obtained [22]. Liquid cooling is already introduced in electronics cooling for applications with higher heat fluxes. Figure 1.8 shows that this technique increases the cooling limits significantly. The other methods are already in use too, but there is still a lot of research necessary. They often have some constraints, such as higher costs, difficulties to implement in the system, higher power consumption, extra weight, possible leakage,... So, despite the relatively poor thermal properties, air cooling through the use of extended surfaces continues to be used as a coolant for many electronic devices [33].

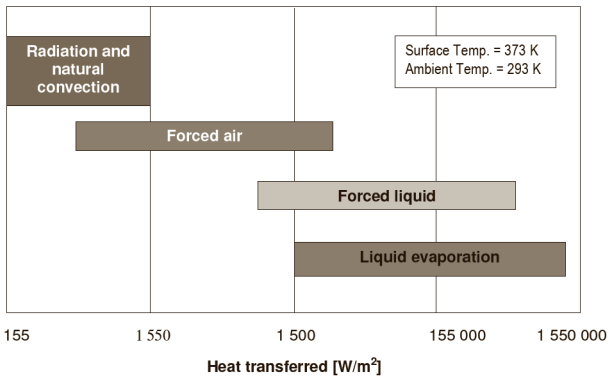

Figure 1.8: Limits of different heat transfer modes for a surface at 80 °C and surroundins at ambient temperature

1.4 Research on longitudinal fins

Longitudinal fins with rectangular cross-sectional area are the most basic, and therefore most commonly used type of fin for heat sinks. They are relatively easy to manufacture [5, 29]. This fin type is also the basic example used in most text books to analyze the heat transfer models of fins [30]. Because of their widespread use, extensive research has been performed on these fins, resulting in a lot of publications in open literature. Initially this research was largely analytical and some experimental work, recently numerical studies are gaining popularity. To study the heat transfer by a fin analytically and obtain the temperature profile along a fin, the

conduction equation needs to be solved. For a two dimensional steady state case, this equation can be simplified to:

$$k \cdot (\frac{\partial^2 T}{\partial x^2} + \frac{\partial^2 T}{\partial y^2}) = 0 \tag{1.10}$$

Certain assumptions were made in order to simplify the solution and clearly define the problem. Harper and Brown [34] were the first to state these assumptions, in 1922 already. These assumptions were later extended by Murray [30] and Gardner [35] and are mentioned here briefly:

1. the heat flow and temperatures in the fin remain constant with time: steady state
2. fin material is homogeneous and temperature invariant.
3. constant and uniform convective heat transfer coefficient on fin side (excluding the fin tip)
4. temperature of the surrounding is uniform.
5. fin thickness is small, compared with its height and length, so that temperature gradients across the fin thickness and heat transfer from the extreme edges of a longitudinal fin may be neglected: one-dimensional conduction
6. uniform fin base temperature
7. no contact resistance between fin base and primary surface
8. no heat sources within the fin itself
9. adiabatic tip: heat transferred through the fin tip is negligible compared with the heat leaving its lateral surfaces
10. heat transfer to or from the fin is proportional to the temperature excess between the fin and surrounding medium

Most extended-surface analyses employ a one-dimensional heat conduction model based on these assumptions. The one-dimensional model with its boundary conditions is shown in Fig. 1.9(a). The x-axis lies along the height of the fin, the y-axis perpendicular to this at the base in the center of the fin. The height is H, the base temperature is T_b and the ambient temperature T_{amb}. The fin is cooled at both sides with a uniform heat transfer coefficient h. Symmetry was used to solve this problem, and it was solved dimensionless. [30]

However, the question can be raised how valid this one-dimensional model is. As argued by Razelos and Georgiou [36], this one-dimensional model is valid if the transverse Biot number is of the order of 0.01 and aspect ratio (height/thickness)

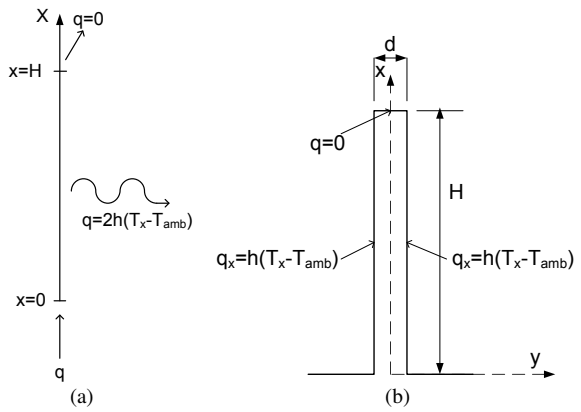

Figure 1.9: The one-dimensional (a) and two-dimensional (b) model of a rectangular longitudinal fin with its boundary conditions

of order 1 [28,30]. The Biot number was defined as the ratio of the convective heat transfer coefficient to the thermal conductivity transfer coefficient, or stated otherwise: the ratio of the fin's thermal resistance (d/k) to the fluid resistance ($1/h$). Thus, the smaller Bi, the smaller the fin's resistance is compared to the fluid resistance. So it seems logical that from a certain value of Bi, the conductive thermal resistance will not influence the heat transfer and thus one-dimensional heat conduction model is acceptable. In the textbook of Kraus et al. [30], the problem in Fig. 1.9(a) is solved as a two-dimensional heat conduction problem described by Lau and Tan [37]. The dissipated heat calculated with this 2-D solution is compared with the 1-D solution of the same problem for different Bi numbers and aspect ratios. For $Bi \leq 0.1$, the maximum error is 1%. This error increases with increasing Bi and also for an aspect ratio > 1. So this confirms Razelos statement that the 1-D assumption is valid for Bi much smaller than 1 ($Bi < 0.1$). However, it should be pointed out that these findings are based on the original assumptions that the temperature boundary conditions are uniform, and that it still needs to be verified if these simplified boundary conditions are applicable or not.

Most analytical studies are based in the Murray-Gardner assumptions, but some of these assumptions do not correspond to real fin conditions, which can lead to oversimplification. There are different cases in which 2-D conduction effects become important and a 2-D solution is necessary: unequal convection coefficients on fin faces, non-uniform base temperature, space-varying heat transfer coefficient, anisotropic materials,... Many studies in literature, analytical as well as experimental, investigate the validity of one or more of the Murray-Gardner assumptions and/or the need for a 2-D solution. A first example is the adiabatic tip

condition. For very long fins this condition will be true, however, the shorter the fin, the more important the heat flow through the tip. The same goes for thick fins, so the fin aspect ratio will also play a role, as will thermal conductivity of the fin material [9]. Huang and Shah [38] performed a two-dimensional study on a rectangular fin with fin tip heat transfer coefficient different from that of the fin faces. They derived an expression for the fin efficiency, and comparison with the 1-D fin efficiency. This study showed again that 2-D effects are negligible for $Bi \ll 1$. Other examples where the influence of fin tip heat transfer is taken into account are Look [39] and Kundu [40]. Harper and Brown [34] introduced the half-thickness rule (HTR) i.e. the solution was calculated for an insulated fin tip, but corrected for the tip heat loss by correcting the height of the fin with half the fin thickness. This correction was done under the assumption that fin tip and faces had the same heat transfer coefficient. Stachiewicz [3] showed experimentally that the heat transfer coefficient on the fin tip is not equal to the mean heat transfer coefficient on the fin faces for forced convection. In case of a rectangular fin, the coefficient on the fin tip can be up to 40% higher [41]. Nevertheless, the fin tip correction is commonly accepted and used [41].

The validity of the assumption of a constant and uniform convective heat transfer coefficient on all fin walls is also widely studied. In many analytical 1-D and 2-D studies, the heat transfer coefficient was the same and uniform for each fin side. However, in reality, this is not the case: the heat transfer coefficient varies over the fin surface, or there is a large difference between the heat transfer coefficients on both fin sides which induces asymmetry. It can be imagined that under these conditions 2-D conduction effects become important. An example of this asymmetric convection coefficient boundary condition is a horizontal fin in natural convection. Look [39] stated that the convection coefficient on the top fin side is twice as large as the convection coefficient on the surface at the downside and solved this as a 2-D conduction problem. Comparison with the 1-D solution shows a significant difference in temperatures, that varies depending on the Biot number and fin tip condition (insulated, at ambient temperature or convection from the tip). For an insulated fin tip, an error of minimum 15% exists between 1-D and 2-D solution, even for $Bi = 0.01$. Razelos and Krikkis [42] contradict this finding. They state that if $Bi \ll 1$, an inequality between the heat transfer coefficients does not need a 2-D analysis. They claim that the dissipated heat in the fin can be calculated using a 1-D model with a Biot number based on the average heat transfer coefficient and after introduction of an equivalent semi-thickness. Although this could give acceptable values for the fin heat dissipation, a 1-D model never accounts for the difference in heat flux distribution between top and bottom surface, or for a calculated temperature difference between both surfaces. However, in both studies [39, 42] it is not clear with which 1-D solution the results are compared, regarding to the heat transfer coefficient values [28, 30].

In these studies, the heat transfer coefficients are still uniform over a fin surface, but have a different value on each surface. However, the existence of a non-uniform convection coefficient has been established theoretically and even observed experimentally [40]. The heat transfer coefficient may vary depending on the fin surface temperature, thermophysical properties, fluid velocity, cross-sectional area,... [43]. In a 2-D model, the possibility of a varying heat transfer coefficient along the fin height can be accounted for. Ma et al. [44] performed a first limited analytical study: the variation of the convection coefficient existed only of two different values with a step between them and this for one specific case of a rectangular fin. They concluded that the 1-D solution with an average h underestimates the dissipated heat. However, this is in contrast with the results for a 1-D fin with constant h that overestimates the dissipated heat compared to the 2-D solution [30]. There are numerous other studies on the influence of varying heat transfer coefficients along the fin height. An old experiment of Ghai [45] showed an increasing heat transfer coefficient towards the fin tip and a minimum at fin base. Gardner [46] searched an expression for the variation of the convection coefficient based on Ghai's experimental results. A monotonically increasing convection coefficient from base to tip was suggested. Most analytical studies consider a convection coefficient variation according to a mathematical law along the fin height: linear [40], power law [47],... Stachiewicz [3] measured convection coefficients on longitudinal constant cross-sectional area fins experimentally. He observed that the film coefficients do not increase monotonically from base to fin tip as suggested earlier, but increase to a maximum at about 50 percent of fin height, then dip and then increase again near the tip (Fig. 1.10). The experiments however lacked accuracy. Sparrow and Acharya [48] reported a decrease in convection coefficient near the fin base and a subsequent increase in the down stream for fins under natural convection, and this for a wide range of conditions. Others defined the variation of the convection coefficient as a function of the local temperature excess (Unal [49], Yeh [50]). The actual nature of the convection coefficient can be obtained by a conjugate analysis of conduction in the fin and convection in the adjacent fluid flow, as Advani and Sukhatme [51] tried. However, the exact nature of variation of local convection coefficients has not been established yet [40].

There are no general conclusions made for space-varying heat transfer coefficients, but only results for very specific cases. Also, these studies are done for heat transfer coefficient variations along the fin height, but no heat transfer variations along the fin length are accounted for. This would require a 3-D model. These effects could be of importance for relatively short fins (similar to the entrance effect in short tubes), so this will again be very case specific. After a study of the earlier research that considered non-uniform convection coefficients, Kraus [30] had concluded that the non-uniformity of convection coefficients has an impact in the heat dissipation rate by fins. This was the conclusion of most investigations

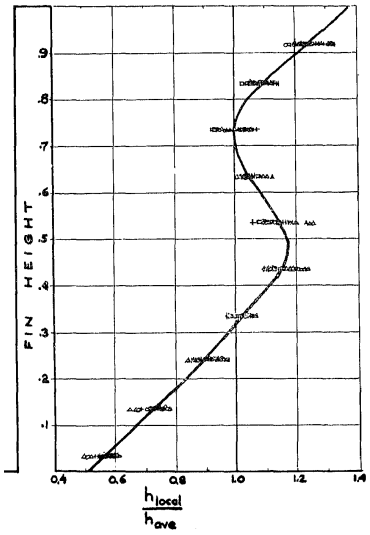

Figure 1.10: The local heat transfer coefficient variation, normalized with respect to the average coefficient, along the fin height as found by Stachiewicz [3]

mentioned. Nnanna et al [43] mentioned an error ranging from negligible up to 50% on the heat transfer rate, depending on the thermal conditions of fin and surroundings, is introduced by using a constant heat transfer coefficient assumption. Stachiewicz [3] concluded that the fin efficiency decreased due to non-uniformity of the convection coefficient. Kundu and Das [40] also found a profound effect on the fin performance.

Another assumption in the standard 1-D model is a uniform fin base temperature. A fin that is attached to a wall will dissipate much more heat than the same area without the fin. So the fin attachment introduces spatial non-uniformities in the wall flux and lowers the base temperature of the fin compared to the unfinned surface. This is called the base temperature depression and it reduces the heat dissipation capability of the fin [28]. So in reality, when the conduction in both fin and primary surface are studied, this base temperature will vary slightly, with the lowest temperature in the center of the fin base and the highest at the edges. This implies again 2-D heat conduction. Sparrow and Hennecke [52] were the first to examine the base temperature depression in detail analytically. They studied a single rectangular fin attached to a thick wall and obtained a solution for the coupled two-dimensional conduction in the fin and wall. Slender fins have less base temperature depression than shorter and thicker fins, for which they found up to 23% for the temperature depression. So the classical assumption that the fin base is at same temperature as the unfinned primary wall can overestimate the heat loss from

the fin significantly. Huang and Shah [38] found that a higher thermal conductivity of the fin, compared to the primary surface results in a larger base temperature depression. Juca and Prata [53] considered the base temperature depression for an array of fins connected to a wall of finite thickness. Only for $Bi \geq 0.1$ a noticeable base temperature depression was found. Suryanarayana [54] analytically solved the problem of a fin assembly on a plate by looking at one half of the fin with one half of interfin spacing, and solved this using finite-difference technique. He compared the results with a one-dimensional heat transfer model, a second model which ignored contact resistance between fin and primary wall and a third model which included thermal resistance of the wall. The heat transfer was overestimated by the 2-D model if the thermal resistance of the wall is ignored, it was underestimated if the thermal resistance was included. Heggs and Stones [55] solved the same arrangement also with a finite difference method, and compared the results with another one-dimensional model. The heat flow calculated in the 2-D model always overestimated the one-dimensional heat flow. They found a maximum error of 20%, which is more pronounced for shorter fins, smaller fin spacing and a thinner primary wall.

Other possible factors that induce 2-D effects and need a 2-D solution are internal heat generations and anisotropic fin materials. The internal heat generation in fins is not considered in this work, and neither are anisotropic fin materials. However, for the latter, one can imagine that if the transverse conductivity of the fin material is considerably smaller than the longitudinal conductivity, this will reduce the heat transfer to the side walls and thus the total heat dissipation and induce 2-D conduction [30].

Finally, Razelos [4] introduces three postulates which have been proven to be correct:

- one-dimensional analysis always overestimates the heat transfer from the fin in comparison to that determined through two-dimensional treatment
- heat transfer for constant thickness fins is always larger compared to heat transfer for any other shape of fin with the same base thickness and height and its borders lying within the boundaries of the constant thickness fin
- for any fin with a heat transfer coefficient that monotonically increases from base to tip, the heat dissipation is overestimated when it is evaluated assuming constant heat transfer coefficient and equal to its average value

This short literature review on fin models shows that depending on the fin dimensions, thermal boundary conditions and thermal conductivity of the material (actually Biot number), a 2-D model is necessary to do accurate predictions on the heat dissipation of the fin. Moreover, if longitudinal fins are limited in length, edge effects also influence the heat transfer in a third dimension. This is even more the

case if not only the global fin performance or heat transfer is studied, but also local heat fluxes and heat transfer phenomena are investigated. Most mentioned studies were done analytically or numerically, very few experimentally, and these often lack accuracy. In this work, a methodology is developed to study the local temperature and local heat transfer coefficients on a surface part of a three dimensional geometry. Longitudinal fins as used in heat sinks are used as test case. These fins are typically limited in height and width. Heat transfer coefficients have a variation over the fin surface, and this both along the height and length of the fin. This variation depends on the fin form, thermal conductivity and thermal properties and velocity of the surrounding fluid. A study on the local convection coefficients makes it possible to predict the heat flux through this particular fin, and can be used to study the fin performance of different fin forms more accurately. The developed methodology is generally applicable to different fin geometries and thus the influence of modifications (such as perforations, dimples, turbulators,...) on the local heat transfer coefficients and fin performance can also be examined.

1.5 Fin optimization

There is continuous research to reduce fin size, weight and cost, but to improve the dissipated heat by the fin. Different techniques are used to reduce size and weight, such as: increasing the ratio of fin heat transfer surface area to fin volume, increasing heat transfer coefficient on the fin walls, using materials of high thermal conductivity,... [29]. The optimum thermal design of fins is a classical heat conduction problem, and has been widely investigated. Two different optimization problems are common [41]:

- Heat dissipation or weight is given, combined with thermal conductivity, base temperature and heat transfer coefficient, and the profile and dimensions of the fin are determined to minimize the weight or maximize the heat dissipation (e.g. Snider and Kraus [56], Kundu and Das [57])
- The profile of the fin is given, and dimensions need to be determined for minimal weight or maximal heat dissipation (e.g. Laor and Kalman [47], Razelos and Look [42])

Most studies on single fin optimization are purely mathematical. For example, Razelos [58] derived mathematically a curved optimal form for a longitudinal fin. For a given profile area for a straight fin the concave parabolic profile (Fig. 1.11) provides the maximum heat dissipation [59]. However, this type of fin would have high manufacturing costs, especially compared to rectangular fins. Sometimes economic restrictions are also used in the optimization. The rectangular fin, common in industrial applications, is a common subject of such optimizations because of its simple profile. Most optimizations are also based on three of

the Murray-Gardner assumptions: 1-D heat conduction, uniform convection heat transfer coefficient, and an insulated fin tip. However, as discussed previously, these assumptions are not always applicable. Fin optimizations that do not consider these assumptions are necessary. Look and Kang [60] did this for rectangular fins with tip heat transfer and different heat transfer coefficients on the fin faces. They used a 2-D fin model. Laor and Kalman [47] performed a numerical study for different shapes of longitudinal fins, spines and annular fins. The optimization was done for maximum heat dissipation for constant mass. The heat transfer coefficients on the fin surface are not assumed constant, but temperature dependent, according to a power law. They also assume the fin tip is either insulated, or has a given a heat transfer value. The optimum fin performance as well as the dimensions were presented. Chung and Iyer [61] took the effects of variable heat transfer coefficients into account. They also found that the optimization for a fin with insulated tip has always a unique solution, but when tip heat loss is considered, the optimum fin design does not have a unique solution anymore. Casarosa and Franco [41] searched the optimum design of a longitudinal fin with constant thickness and different mean heat transfer coefficients on face and tip.

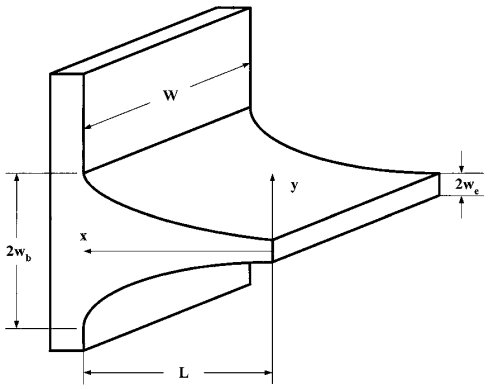

Figure 1.11: A concave parabolic longitudinal fin provides the maximum heat dissipation [4]

Next to individual fin optimizations, there are many studies on optimization of arrays of fins or complete heat sinks, such as the work of Kou et al. [62]. In these studies, the ratio of heat transfer to pressure drop is often used as optimization criterion, which is different from those used for the single fin solution. There are two standard approaches to determine the optimal heat sink design:

- optimize fins individually, so separated from the supporting surface and array of fins. Then it is assumed that the optimum fin arrays are composed of

a number of individually optimized fins.

- the whole array and its supporting surface is optimized: the fin itself, number of fins, interfin spacing,... (e.g. experimental investigation of El-Sayed et al. [24]).

The first technique for optimization of heat sinks is widely used in industry, while the second aims more at advanced technological solutions, e.g. the thermal control of electronic equipment [41].

Aside from the optimization of fin forms to an optimal fin profile or fin dimensions for a given profile, there are also several other studies on improving fin performance or heat dissipation. This improvement is obtained by introducing new fin types or modifying existing designs. Some examples from literature include perforated fins [5, 26, 29, 63] (Fig. 1.12), dimpled fins [6, 64] (Fig. 1.13), ribbed fins [64], composed fin arrays [65], fluted and wavy fins [7] (Fig. 1.14), tree-shaped fins [8] (Fig. 1.15) and dovetail fins [27]. The improvement of the heat transfer by these modifications is based on the manipulation of the boundary layer or inducing local vortices. Decreasing the boundary layer thickness or interruption of the boundary layer increases the heat transfer coefficient.

Next to the well-known rectangular longitudinal fin discussed earlier, a second experimental test case is needed for the validation and application of the methodology developed in this work. The variations in heat flux, heat transfer coefficients and fin performance are determined with the developed method and compared with literature. This would demonstrate the power of this technique.

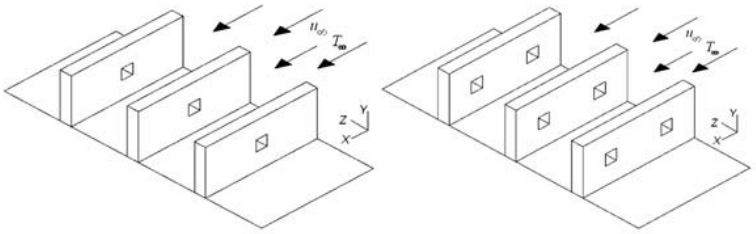

Figure 1.12: Lateral perforated fins [5]

Sikka et al. [7] performed an experimental study on two new fin types different from the conventional longitudinal-plate fins for heat sinks: fluted and wavy fins. The results showed that the two novel designs did not improve the thermal performance significantly. Moreover, these fins are not so easy to manufacture. Therefore, these fin types will not be studied in this work. Almogbel [8] performed a mathematical optimization on tree-like fins with total volume and fin

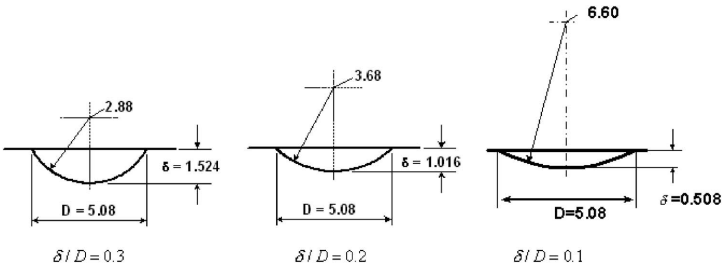

Figure 1.13: Dimples made in fins [6]

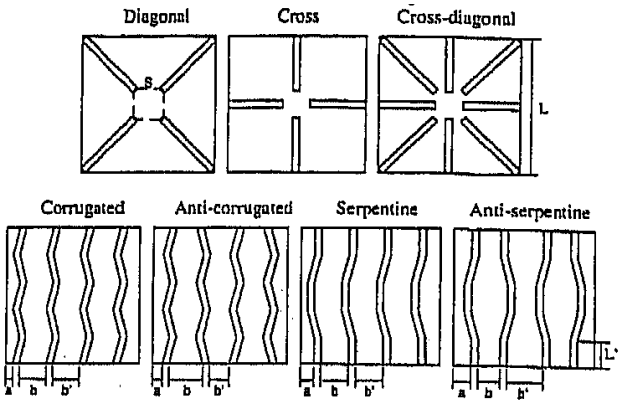

Figure 1.14: Wavy and fluted fins [7]

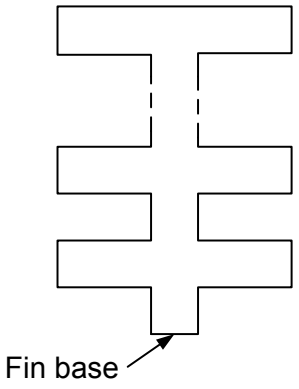

Figure 1.15: A tree-shaped fin [8]

material constraints. Performance increases with the number of pairs of branches, but there is of course a complexity limit. A substantial increase in global conductance was found compared to other optimal designs of the same volume, but an idealization was used in the mathematical model: the heat transfer coefficient was independent of the free flow area shape. Due to the difficulties and costs in construction of the fins and the lack of usable results (only mathematical), this fin is also not suitable as test case. In the work of Brauhnstein et al. [65] composed fin arrays (meaning fins with fins on it) are studied. Despite these fins are used in compact heat exchangers and for the cooling of electronic equipment, there is very little data available on these types of fins. Brauhnstein et al. [65] performed a mathematical optimization, in which the ideal number of branches and length ratio are searched. The optimization is done related to the mass, so the relative heat dissipation is observed, i.e. the ratio of the dissipated heat to the mass of the fin. This optimization is not straightforward, because an increase in number of branches causes also an increase in fin volume if the fin length remains constant. They found that composed fins with up to four junctions perform better than regular ones with the same volume. Again, difficulties in manufacturing and the lack of usable experimental results from papers (only mathematical) prevented that this fin of being chosen as test case.

Wee et al. [64] performed a numerical study with FLUENT [66] in which they studied smooth, dimpled, ribbed, and dimpled and ribbed heat sinks. A heat sink with ribs (under an angle of 45) augmented the heat transfer with 104%, a dimpled heat sink with 63%. On the other hand, the pressure drop for dimpled heat sinks is much lower. A combination of ribs and dimples resulted in no further improvement. This paper contains clear and useful data to use as test case. However, dimpled fins are not easy to implement in the developed methodology. Moreover, the results were obtained for fins in a heat sink array, not for individual fins. Lane and Heggs [27] investigated dovetail fins analytically. A dovetail fin is smaller at the base than at the tip (inverted trapezoidal). The results are aimed at comparing different performance parameters and making performance parameter charts based on an analytical study. They are not suitable as test case.

Finally, research on perforated fins is examined. Al-Essa et al. [29] studied horizontal fins with square perforations for natural convection. This research is not suitable for the experimental setup used in this doctoral thesis. Shaeri et al. performed two studies on perforated longitudinal fins: one with lateral square perforations [5] (Fig.1.12) and one with square perforations along the fin's length [26]. The latter is very difficult, if not impossible, to manufacture. However, their work on lateral square perforations (perpendicular to the fluid flow) is very thorough and detailed and these fins can be readily manufactured. It is a numerical study, but the numerical model and technique has been experimentally validated on other test cases. Their work contains data on the average Nusselt number in function of the

Reynolds (Re) number, and on different fin performance parameters in function of Re-number. The results are compared with the equivalent solid fin, and an increase in total heat transfer and a weight reduction is shown. The number of perforations is varied from one to fifty. The detailed data and ease of manufacturing make this fin type an ideal test case. These results will be discussed in Chapter 5.

1.6 Performance parameters

There has always been searched for a meaningful fin performance indicator. Harper and Brown [34] introduced the fin efficiency idealization and used this concept as a fin performance indicator. Fin efficiency (=η) is defined as the ratio of heat transferred by a fin to the amount of heat transferred by the same fin if the total fin was at base temperature. This definition is shown in Fig. 1.16. This would mean that the fin is made of an ideal material that has infinitely high thermal conductance [30], [17]. However, such a material does not exist and the physics of the problem makes it impossible for the complete fin surface to be at the base temperature T_b. So, with respect to heat flow, the concept of fin efficiency is physically meaningless. Nevertheless, fin efficiency is widely used in design and extensively studied in text books. This popularity is due to the pioneering work of Harper and Brown [34], who presented their results in the form of fin efficiencies in algebraic expressions and design charts. If fin efficiency is used to find optimum fin dimensions for a certain type of fin, one finds that short fins are optimal [9]. The fin temperature is close to the base temperature for the whole fin. However, short fins dissipate and transfer only a small fraction of the maximum possible heat. A fin is a heat transfer enhancer, and thus has the goal to maximize the heat dissipation, preferably with a minimum of weight and material. Also, because fin efficiency compares the real performance of the fin to the performance of an ideal non-existing fin of the same shape, it is difficult to compare the thermal performance of different fin forms. So there is need for a better fin performance indicator.

Heggs [17] states that fin effectiveness is a better performance indicator than fin efficiency. Fin effectiveness is also mentioned in literature and text books (e.g. [30]), but has never been popular. Fin effectiveness is the ratio of the heat transferred by the fin to the heat transferred from the primary surface covered by the fin's base under the same thermal conditions, in the absence of the fin. According to figure 1.17 fin effectiveness ζ is:

$$\zeta = \frac{Q_f}{Q_b} \tag{1.11}$$

The temperature difference between fin surface and surrounding fluid decreases along the fin from base to tip. So there is also a decrease in the driving force for

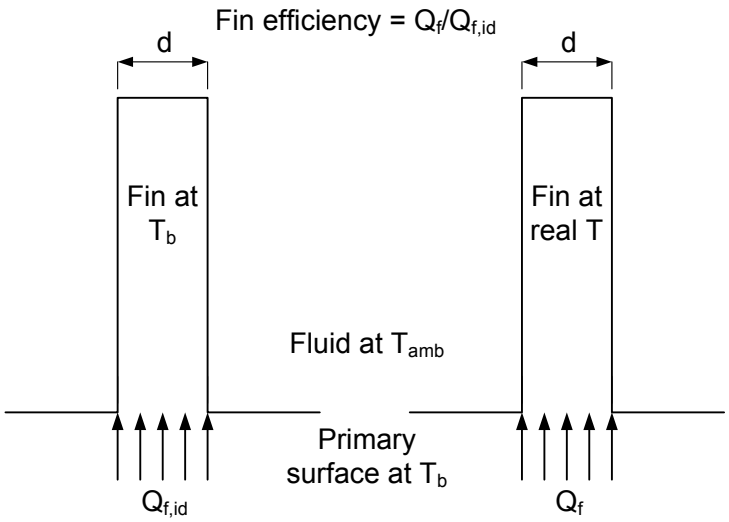

Figure 1.16: The definition of fin efficiency

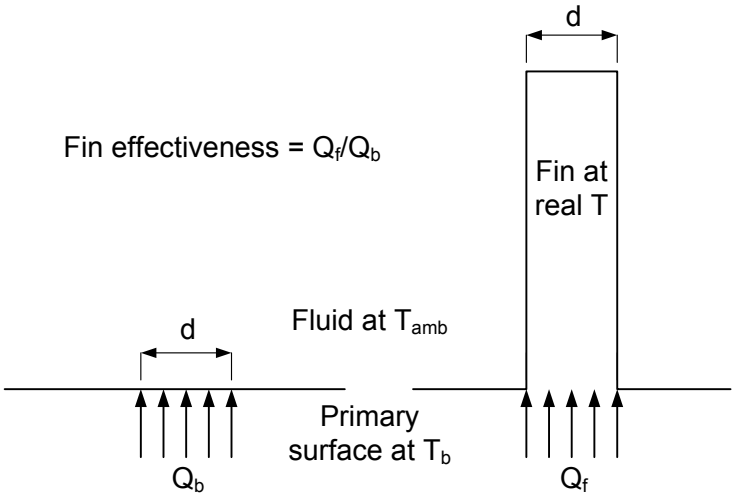

Figure 1.17: The definition of fin effectiveness

heat transfer along the fin height. For an infinitely high fin, the temperature at the fin tip will be the same as the temperature of the surrounding fluid. This infinitely high fin is the upper limit of heat flow through the fin. For fins of constant cross section, this upper limit can be calculated and is given by [17]:

$$Q_{f,\max} = \sqrt{k \cdot A_x \cdot h \cdot A_s} \cdot (T_b - T_\infty) \tag{1.12}$$

A_x is the cross-sectional area of the fin, A_s the perimeter (surface area per unit height), h is the surface averaged convective heat transfer coefficient, T_b is the base temperature and T_∞ is the temperature of the surrounding fluid. If it is assumed that the heat transfer coefficient on the primary surface in absence of the fin is the same as the one on the fin, then the heat transfer rate through the primary surface in absence of the fin is given by:

$$Q_b = h \cdot A_x \cdot (T_b - T_\infty) \tag{1.13}$$

So a maximum fin effectiveness can be defined for a fin with constant cross section:

$$\zeta_{\max} = \sqrt{\frac{k \cdot A_s}{h \cdot A_x}} \tag{1.14}$$

The value of fin effectiveness will always be situated between two boundaries:

$$1 \leq \zeta \leq \zeta_{\max} \tag{1.15}$$

From the definition of fin efficiency, an expression in function of fin effectiveness can be derived:

$$\eta = \frac{Q_f}{Q_{f,\mathrm{id}}} \tag{1.16}$$

$$\begin{aligned} \eta &= \tfrac{Q_f}{Q_{f,\mathrm{id}}} \\ Q_{f,\mathrm{id}} &= h \cdot (A_s \cdot H + A_x) \cdot (T_b - T_\infty) \\ \Rightarrow \eta &= \tfrac{\zeta}{(\frac{H \cdot A_s}{A_x} + 1)} \end{aligned} \tag{1.17}$$

Higher fins (larger H) will have a higher fin effectiveness (as could be expected from the definition of maximum effectiveness), but the fin efficiency decreases with height. This confirms that using fin efficiency as a quantitative measure for performance can result in misleading information, in this case the impression that fins should be relatively short. Another good example of the weakness of fin efficiency was shown in the paper of Brauhnstein et al. [65] concerning composed fin arrays. For composed fin arrays the denominator is not a constant: if the length ratio is kept constant and the number of branches is increased, the denominator

(thus the maximum possible heat dissipation for an ideal fin) will increase linearly with the number of branches, but the nominator will increase more moderately, as a result of the reduction of the base temperature of the farthest fin branches, which is associated with a reduction of their heat dissipation. This shows a problem of fin efficiency i.e. there is no unified reference: different fin forms, even of the same sort, cannot be compared with each other, because each fin is compared to an ideal fin of the exact same form. So graphs and comparison based on fin efficiency for fin arrays with a different number of branches or length ratio is meaningless. When using the fin effectiveness to quantify the fin performance (e.g. for comparison of different types), these problems don't appear; the fin effectiveness indicates the ability to remove heat from the surface. This makes it possible to compare different fin forms with each other and with a standard straight fin of the same dimensions, volume or mass.

It is obvious that fin effectiveness always has to be larger than 1, otherwise the fin would have an insulating effect, and fins are used to increase the heat transfer rate and not to insulate. Fin efficiency on the contrary is always smaller than 1.

In the same study, Heggs [17] gave an expression for the fin effectiveness of a fin with constant cross-section and finite length.

$$\zeta = \zeta_{\max} \cdot \frac{1 + \zeta_{\max} \cdot tanh(\frac{\frac{H \cdot A_s}{A_x}}{\zeta_{\max}})}{\zeta_{\max} + tanh(\frac{\frac{H \cdot A_s}{A_x}}{\zeta_{\max}})} \tag{1.18}$$

This makes it possible to calculate the dissipated heat for these fins, but only if the fin dimensions, the thermal conductivity of the material, base temperature of the fin (or primary surface temperature) and most importantly the heat transfer coefficient are known (in absence of the fin). The determination of the heat transfer coefficient is the least reliable element. Either a uniform heat transfer coefficient is assumed, or the mean heat transfer coefficient based on correlations from literature. Also, all these expressions and calculations of Heggs [17] are based on the one-dimensional heat conduction model through fins. This model is not always accurate enough, as mentioned in a previous paragraph. So the accuracy of predictions of fin heat dissipation based on these expressions can be questioned.

Heggs [17] did not propose the fin effectiveness itself as a fin performance parameter, but he introduced the performance ratio PR, which is defined as

$$PR = \frac{\zeta}{\zeta_{\max}} \tag{1.19}$$

and thus:

$$\frac{1}{\zeta_{\max}} \leq PR \leq 1 \tag{1.20}$$

Heggs also developed an expression for the fin efficiency η as a function of PR and $\zeta_{\max}$. Based on these expressions, he evaluated fin efficiency and maximum effectiveness over the complete range of the performance ratio PR as given by 1.20. He developed a design chart based on these equations: PR can be predicted from fin aspect ratio (ratio of thermal conductivity and half fin thickness) and maximum effectiveness values for constant cross sectional area fins. He published several of these design charts for different fin types e.g. radial rectangular fins [67] and dovetail fins [27]. Some values of PR and efficiency are shown in table 1.2. Fins with a large performance ratio have a wide range of maximum effectiveness $\zeta_{\max}$, but these all appear to have a small fin efficiency. Efficiency increases with decreasing performance ratio. Many designers use a fin efficiency of at least 0.9 as a guideline, but such a fin has only a performance ratio of 0.5, which means that 50% of the maximum possible heat is not dissipated by the fin. This percentage is even lower for higher efficiencies. Although these results are calculated for constant cross-sectional area and with a one-dimensional conduction model, they show a general trend and connection between fin effectiveness and fin efficiency.

Performance Ratio	Max Effectiveness Range	Limiting Efficiency
0.99	>1.101	0.374
0.9	> 1.11	0.611
0.5	>2.00	0.910
0.1	>10.00	0.997

Table 1.2: Performance ratio and corresponding fin efficiency for a fins with constant cross-section according to Heggs [17]

As mentioned, the analysis of Heggs [9, 17] on the PR is based on the 1-D conduction equation with the Murray-Gardner simplifications. However, the adiabatic fin tip condition was omitted. Moreover, the convection coefficient at the tip can be different from the convection coefficient along the sides of the fin in this work. The ratio of the tip convection coefficient to the fin side convection coefficient is also used in the equation to predict the PR. If this convection coefficient ratio is smaller than the maximum calculated fin effectiveness $\zeta_{\max}$, PR is always smaller than 1, but if this ratio is higher than the maximum fin effectiveness, PR is higher than 1. This was proven mathematically for a rectangular fin, but it was also demonstrated for other fin geometries. For fins with $PR > 1$, Kern and Kraus [59] and Razelos [4] recommend not to use a fin, because it has an insulating effect on the base area of the primary surface. This is identical to saying that an effectiveness smaller than 1 or the statement of Razelos and Georgiu [36] that a Biot number larger than 1 has an adverse effect. This is actually a statement about the fin effectiveness: the smaller the Biot number becomes, the higher the fin effectiveness. The value of fin efficiency always lies between 0 and 1, and thus provides no indication whether

a fin is insulating or not. This is another indication of the flaws of fin efficiency as performance indicator. But Heggs [9] also states that a $PR > 1$ (thus a much larger convection coefficient at the tip compared to the fin sides) does not necessarily suggest an insulating fin. Two practical examples are given where this could occur: for condensing and boiling systems. The physical meaning of a $PR > 1$ is caused by an insulating effect along the side of the fin, which is caused by a lower convection coefficient, but more heat is transferred through the fin due to a relatively high heat transfer coefficient at the tip. This phenomenon occurs for short fins in condensing and boiling situations, which is shown in Fig. 1.18.

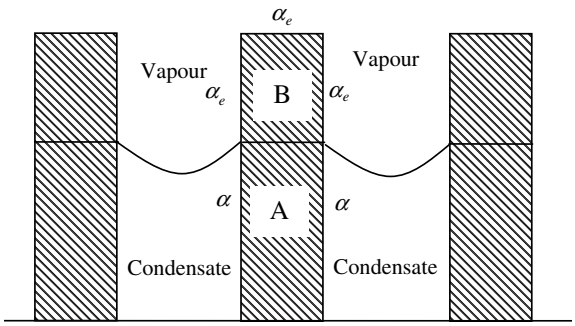

Figure 1.18: Case with $PR > 1$: lower heat transfer coefficient α_e at the fin sides caused by condensate, higher heat transfer coefficient α at the fin tip [9]

Finally Heggs [9] stated that the use of PR and maximum fin effectiveness to evaluate the heat flow through a fin only requires the use of the base area of the fin. This statement is correct for a numerical or mathematical solution, however, it is not evident for experimental research. The heat flux through the fin base cannot be measured without disturbing the heat flow and thermal resistance of the fin. This means that the fin surface needs to be evaluated to experimentally determine the heat flux through the fin. Experimental validation is necessary for short fins, or fins with a limited width, when side effects become more important, and the 1-D solutions become invalid.

1.7 Problem definition and aim

There is a continuous need to improve electronics cooling. The most commonly used cooling technique in electronics remains air cooling with heat sinks. These heat sinks often consist of an assembly of longitudinal fins limited in height and length. There exist numerous studies in open literature on longitudinal fins, but most of these studies are analytical or numerical and are based on a simplified

one-dimensional model. This 1-D assumption is limited in application range, especially for relatively short fins. Some two-dimensional studies are available, but these are based on some simplifying assumptions. There is very little research on local heat transfer coefficient variations over the fin surface, and the existing experimental studies on local heat transfer coefficients lack accuracy. So there is a need for a more detailed study on longitudinal fins without simplifying assumptions, in order to model all effects of the heat transfer. In such a detailed study, local heat transfer coefficients have to be determined, as they provide information on local heat transfer effects and give indications on the way to modify fins (perforations, bumps, fins on fins,...) in order to improve the heat transfer. If fin modifications are applied, local heat transfer coefficients show how these modifications influence the heat transfer.

In this work, a methodology is proposed to evaluate the performance of extended heat surfaces and determine local heat transfer coefficients on the fin surface. This methodology is developed on longitudinal fins, typically used in heat sinks for electronics cooling, but it is expendable to other fin types. Experimental measurements are required in this method. The methodology is thus not solely based on a numerical model and thus does not depend on the simplifications made in the currently used models. The determination of local heat transfer coefficients demands a large amount of measurement points. Heat fluxes cannot be measured accurately, so temperature measurements are done. Local heat transfer coefficients are determined from these measurements, as well as a performance parameter. The literature survey in the introduction showed that the commonly used fin efficiency is not a good fin performance indicator, while fin effectiveness and fin performance ratio are more meaningful indicators. Therefore the choice was made to use fin effectiveness in this work. Fin modifications on the longitudinal fin will be studied using this method. Various examples of such modifications were discussed in the literature survey. Most data was available for longitudinal fins with lateral perforations. These perforated fins will also be used as test case for the developed method.

The local heat transfer coefficient determination is based on temperature measurements on the fin surface. This determination of heat transfer coefficients from temperatures is called the inverse heat conduction problem. This is a mathematical problem that is solved using a numerical optimization method. So actually, the methodology proposed in this work, consists of two parts: a numerical solution algorithm for the inverse heat conduction problem (Chapter 2 and 3) and an experimental part in which fin temperatures are measured and the numerical algorithm is applied to these measurements (Chapter 4 and 5).

2

Inverse Heat Conduction Problem

In this chapter, a numerical solution method is developed to determine the local heat flux distribution in a fin from temperature measurements. The determination of heat fluxes from temperature measurements is called the inverse heat conduction problem (IHCP). First, it is explained why temperatures measurements are used and local heat fluxes cannot be measured. Then it is explained what an IHCP is and which type of IHCP is studied in this work. A literature survey is presented on different IHCP solution methods. The most suitable solution method is selected based on this literature survey. This resulted in two possible solution methods. Both methods are developed mathematically and the implementation of the solution algorithm is presented.

2.1 Introduction

It is very difficult to determine local convection coefficients accurately, or to do accurate local heat flux measurements. However, often the knowledge of the heat flux distribution is indispensable. This is especially so for the design of optimal and efficient heat exchangers [68]. Other applications which benefit from the knowledge of local heat fluxes are the design of mechanical machinery and mechanical processes (e.g. cutting tools [16], drilling [69], engines [70]), design of thermal protection for the reentry of space vehicles [71], various industrial processes (e.g. steel slabs [72], quantitative studies of the heat transfer processes occurring in the industrial applications [13], the heating of a gun barrel [73]),... In

this doctoral thesis, the main application of the study of local heat fluxes is obviously heat transfer enhancement by extended surfaces. The knowledge of these local heat fluxes is necessary to determine the fin effectiveness and fin efficiency more accurately. Moreover, the knowledge of local convection coefficients and local heat fluxes gives information on the heat transfer enhancement mechanisms and more insight in the design of more performant heat transfer enhancers. A third reason for the determination of local heat fluxes is the difficulty of measuring the amount of heat transfer through the fin base - necessary for the calculation of fin effectiveness - without disturbing the heat flux distribution significantly. The heat transfer measurement at the fin base would introduce a thermal resistance between primary surface and fin by the measurement device. Therefore the heat fluxes at the fin base have to be determined indirectly by measuring the heat fluxes through the extended surface and primary surface.

The measurement of local heat transfer coefficients or heat fluxes is a delicate and difficult task. There are several measurement methods:

- heat flux sensors
- local temperature measurements, mostly in solids
- inverse heat conduction problem

Heat flux sensors are seldom used. Heat flux sensors need to be attached to the surface, and give an average value for the heat flux through the sensor surface. Moreover, by attachment of the sensor, an extra thermal resistance is attached to the measurement surface, which influences the measurement and causes a redistribution of the heat flux over the surface. Heat flux sensors are not very accurate: they typically have an accuracy of $\pm 10\%$ [74]. Some sensors have a better accuracy of 5% at ambient temperature, with an increasing error for higher temperatures.

Thermocouples are the most commonly used temperature sensing techniques for monitoring temperatures. Many studies use thermocouples that are embedded in the measurement surface(s) (e.g. plate, fins, heat sinks,...) to determine local heat fluxes [68]. Wu [68] developed a technique to measure local heat fluxes with two thermocouples. This technique is especially useful for high heat fluxes and two phase heat transfer. It is however limited to one-dimensional conduction applications, and is not very useful if a heat flux distribution over a surface needs to be measured. There are of course important downsides to the use of thermocouples. The number of thermocouples that can be imbedded is limited. The presence of thermocouples disturbs the local temperature and the heat flow, due to conduction into the thermocouple and thermocouple wires. This is sometimes called the "fin effect" of thermocouples [75]. The more thermocouples, the larger the disturbance is. This puts also a limit on the spatial reach: it is difficult to get a total distribution of the heat flux over a surface.

Other studies use other temperature measurement techniques to measure temperatures in order to determine heat fluxes. The most well-known is infrared thermography. This technique will be discussed in Chapter 4. Ay [76] used infrared thermography measurements on a plate fin in a plate finned-tube heat exchanger to solve a two-dimensional direct conduction problem with finite difference method and an energy balance method in the plate fin. The error on the local convection coefficient is $\pm 7.5\%$. The measured plate fin is very thin, so that the conduction is two-dimensional. In this case this method works well, but it is not easy to extrapolate it to three-dimensional cases or other two-dimensional cases because the boundary conditions are very critical. Orzechowski [77] determined local heat transfer coefficients on a fin surface for boiling regime. They used thermographic temperature measurements and assumed a power-law correlation between heat transfer coefficient and local wall superheat and then numerically calculated the heat transfer coefficient, with an accuracy of 10%. Freund et al. [78]developed an experimental method to determine local heat fluxes, based on thermography and temperature oscillation by the use of a laser. This is an advanced method, but difficult and expensive to execute, and limited in applications. Another example is the study of El-Sayed et al. [24] who determined local heat transfer coefficients in heat sinks using embedded thermocouples. These are just a few examples of experimental research on local heat transfer coefficients. In recent years, a third technique is becoming more and more popular for identifying local heat fluxes: inverse heat conduction. This technique is mainly used to estimate temperatures or heat fluxes at surfaces that are inaccessible for measurements. The advantage of this method is that experimental studies can be performed under similar conditions and environment as during operation [71]. Inverse methods are very valuable when an operational process is too complicated for direct measurement of physical parameters, or when measuring requires sophisticated or expensive instruments [79]. To solve an inverse heat conduction problem, a mathematical optimization method is required, which uses temperature measurements as input. Based on surface temperatures of a solid object, heat fluxes on one or more surfaces of the object can be estimated. So the need for internal temperature measurements can be omitted. Depending on the temperature measurement technique, the disturbance of the local temperature fields and heat flux distribution is limited or even absent. It also has the advantage that the temperature field in the whole object can be reconstructed based on surface temperature measurements, together with the coupled heat flux distribution. In this work, this technique was developed as a method to determine local heat fluxes on extended surfaces. Fin effectiveness and efficiency are also obtained as a result.

2.2 The Inverse Heat Conduction Problem

Although there are some books [80, 81] and plenty of studies in literature on inverse heat conduction problem (IHCP), this is no common knowledge for heat transfer engineers. This is mainly because it is actually a mathematical optimization problem. Therefore, a small word to introduce the inverse heat conduction problem is at place.

2.2.1 Direct heat conduction

The opposite of the IHCP is a direct conduction problem. In a direct conduction problem the internal and surface temperatures of a solid body are determined for given boundary conditions, thermophysical properties of the solid material and heat sources in the body. This is a well-stated problem, generally known as a heat conduction problem. It is in this form that heat conduction is treated in textbooks [30, 82–84] and education. As this work aims at three-dimensional applications, the direct and inverse heat conduction problem will be treated as three-dimensional. The direct and inverse heat conduction problem will be illustrated on a simple case: a solid cube named Ω of a material with thermal conductivity k, heat capacity c and density ρ. The cube with its boundary conditions are illustrated in Fig.2.1.

The general three-dimensional heat conduction equation is:

- for transient conditions:

$$\frac{\partial^2 T}{\partial x^2} + \frac{\partial^2 T}{\partial y^2} + \frac{\partial^2 T}{\partial z^2} = \frac{1}{a} \cdot \frac{\partial T}{\partial t} \tag{2.1}$$

  with thermal diffusivity a:

$$a = \frac{\rho \cdot c}{k} \tag{2.2}$$

- for steady state conditions:

$$\frac{\partial^2 T}{\partial x^2} + \frac{\partial^2 T}{\partial y^2} + \frac{\partial^2 T}{\partial z^2} = 0 \tag{2.3}$$

This thesis is focused merely on steady state inverse heat conduction problems, so only Eq. (2.3) is of importance. This is also called the Laplace equation. This equation is solved for the cube Ω based on boundary conditions, which are:

- Boundary temperature:

$$T(x, y, z)|_{\mathrm{x}=0} = T_{\mathrm{a}}(y, z) \tag{2.4}$$

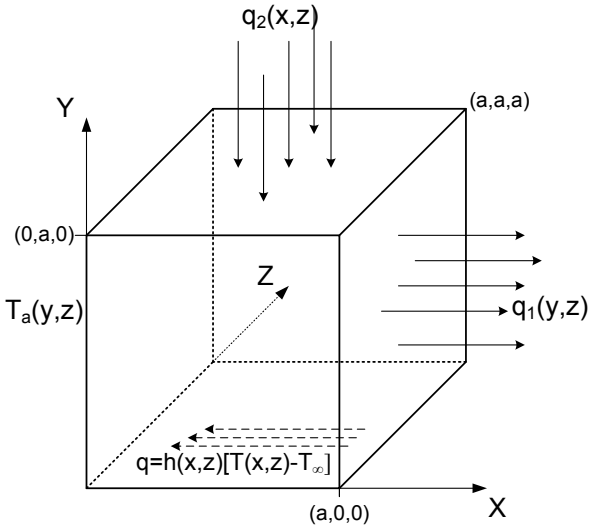

Figure 2.1: Direct heat conduction problem in a cube with diverse boundary conditions

- Outward heat flux:

$$-k \cdot \left(\frac{\partial T}{\partial n}\right)\Big|_{\mathrm{x=a}} = q_1(y,z) \tag{2.5}$$

- Inward heat flux:

$$k \cdot \left(\frac{\partial T}{\partial n}\right)\Big|_{\mathrm{y=a}} = q_2(x,z) \tag{2.6}$$

- Convective heat transfer:

$$-k \cdot \left(\frac{\partial T}{\partial n}\right)\Big|_{\mathrm{y=0}} = h(x,z) \cdot [T(x,z) - T_\infty] \tag{2.7}$$

The two other boundary surfaces are adiabatic, thus boundary heat flux $q = 0$. For the direct problem, the general heat conduction equation (Eq.(2.3)) is solved with the boundary conditions (2.4-2.7) to obtain the temperature field in the cube Ω. This problem is well-posed: it has a unique and stable solution. The direct problem can be solved numerically e.g. by using a finite element method (FEM), finite volume method (FVM), ... Another possible boundary condition that was not used in the example is the radiative heat flux:

Radiative heat transfer:

$$-k \cdot \left(\frac{\partial T}{\partial n}\right) = \sigma\epsilon \cdot \left(T^4 - T_\infty^4\right) \tag{2.8}$$

2.2.2 Inverse heat conduction definition

For an IHCP, experimental temperatures are measured at boundary points and/or interior points of the solid object and subsequently used to estimate unknown boundary conditions at one or more external surfaces of the object [80, 85]. So, the same general conduction equation (Eq. (2.3) or Eq. (2.1)) is valid, but one (or more) of the boundary conditions (2.4-2.8) is unknown. For example, the outward heat flux q_2 is unknown and has to be determined, as shown in Fig.2.2. Some points of the temperature field in the object's interior or on its boundary surfaces are known by measurements: T_1, T_2 and T_3 in Fig.2.2. However, the outward heat flux q_2 cannot be calculated directly from this problem statement, because IHCPs are typically ill-posed. This means that the existence, uniqueness and stability of their solutions cannot be assured [80]. Hence, an IHCP has to be solved using some kind of numerical technique, where the unknown boundary conditions are estimated while minimizing a functional. This functional can be written as:

$$J = \sum_{i=1}^{n} \left[T_{\mathrm{cal,i}} - Y_{\mathrm{i}}\right]^2 \tag{2.9}$$

This functional contains the difference between the measured temperatures Y_{i} and the calculated temperatures $T_{\mathrm{cal,i}}$ at the same coordinates from the IHCP solution. Notice that for transient IHCPs, there is also an initial condition next to the boundary conditions. This initial condition can also be an unknown.

2.2.3 The need for regularization

Temperature measurements contain noise. Inverse problems are ill-posed, which means that the solution to the problem does not depend continuously on the input temperatures [86]. So as a result, direct methods do not give stable approximations of the desired functions. Unless special methods are used, even small perturbations in the measurement data may completely destroy the solution [72, 80]. The exact calculated data from a direct conduction problem will be a perfectly smooth and continuous function at the measurement locations, as expected by the nature of the heat equation. However, for measured data this will not be a smooth function because they contain random error measurements, both in space and time. Therefore ill-posed problems are regularized: replaced by a nearby well-posed problem to obtain a stable solution [87]. A regularization method is based on some approximation process, and seeks to balance the approximation error versus the propagated data error [88]. For example, the least-squares method can be viewed as a very simple form of regularization. In [89], Hadamard was cited: "Any solution of an inverse problem only achieves a compromise between data errors due to measurement noise and deterministic errors resulting from the unavoidable stabilization of the solution. Therefore, the solution quality depends on the algorithm

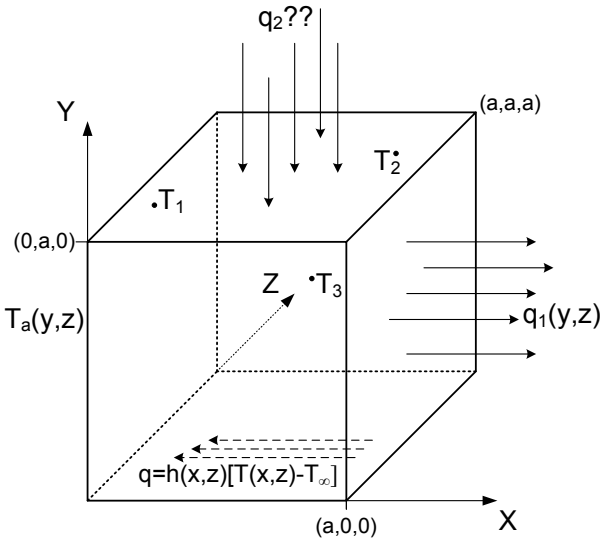

Figure 2.2: Inverse heat conduction problem in a cube with diverse boundary conditions

used and its tuning parameters." So to solve a specific IHCP, it is very important to chose the correct solution algorithm and regularization method to obtain a meaningful and stable solution. There exist different regularization methods, but the most frequently found in literature to solve an IHCP are: Tikhonov regularization and iterative regularization. Regularization involves introducing additional information to the problem to stabilize an ill-posed problem or prevent overfitting. This information is usually of the form of a penalty for complexity, such as restrictions for smoothness. Many regularization techniques correspond to imposing certain prior distributions on model parameters. Tikhonov regularization allows a form of optimal tuning on the sensitivity of the solution to input data errors. It is obtained by a trade-off between the residual norm of the least squares (i.e. the functional J in Eq. (2.9)) and some desirable property resulting from a penalty term on the profile of the solution (e.g. the norm of the solution). So a new functional is created, with a regularization parameter λ and the two previously mentioned terms, for which a new solution needs to be calculated. The new functional is:

$$J = \sum_{i=1}^{n} \left[T_{\mathrm{cal,i}} - Y_{\mathrm{i}}\right]^2 + \lambda \left(\sum_{i=1}^{n} \left[v\right]^2 \right) \tag{2.10}$$

with v: the unknown for which the IHCP is solved (e.g. the heat flux)

This is a Tikhonov regularization of the 0-th order. If the second derivative of

the unknown function is used as penalty term, it is called a Tikhonov regularization of the second order. The zeroth order regularization controls the fluctuations of the profile of the solution, the second order guarantees the smoothness of the solution.

In an iterative regularization no regularization parameter λ has to be determined. The damping of the instability is based on viscous properties of the numerical optimization algorithm. Iterative regularization methods such as gradient methods generate regularizing families of operators. So it is possible to choose a stable approximation of the unknown solution from the corresponding iterative sequence. As the number of iterations increases, an inverse problem solution can worsen, gradually losing its smooth character. Any waviness appearing in the estimated values will gain in strength as fast as the increasing fluctuating errors. Therefore it is suggested to halt the iterative process at a specific iteration. If the iterations are stopped based on the residual criterion, these methods are regularization algorithms, thus they give stable approximate solutions whose accuracy increases steadily as the errors of the input data are reduced. The stopping criterion is thus the regularization parameter and is determined with the discrepancy principle. So a too high stopping criterion would result in a solution in which a significant part of the noise remains, making the solution unphysical. A stopping criterion that is too low can cause removal of relevant parts of the data along with the noise, resulting in a very smooth but false solution.

2.3 Literature survey on IHCP

Various solution methods for diverse IHCPs are found in literature. A short overview is necessary to justify the choice for the method used in this work. Because of the great diversity of IHCPs, a classification of IHCP solution methods used in literature for diverse methods would be a good guide. A classification can be made on the following criteria:

- time condition: transient or steady state problem
- type of mathematical problem: linear or non-linear
  - linear problem: the thermal properties of the material are assumed to be temperature independent
  - non-linear problem: the thermal properties are temperature dependent. This is often assumed if there are large temperature variations in the studied object
- dimension in space: one-, two- or three-dimensional problem
- specification of the unknown parameter: IHCPs can be specified to estimate various unknowns. The different possibilities are the estimation of boundary

heat fluxes, boundary temperatures, internal heat sources or thermal properties of the material

- applied numerical technique: a huge diversity of numerical techniques is used in recent years to solve IHCPs. They each have their advantages and disadvantages for specific applications. The most important examples are:
  - Conjugate Gradient Method (CGM)
  - Steepest Descent Method (SDM)
  - Tikhonov regularization
  - solution procedure based on Boundary Element Method (BEM)
  - Neural Networks
  - Function Specification Method (FSM)
  - Sequential Method
  - ...

A short overview on IHCPs in literature with their applications and accuracies is provided. In order to keep a good overview of the literature survey, it is divided according to the estimated unknown parameter, which is again subdivided for the dimensions of the studied IHCP. As a conclusion, the different techniques will be summarized in Tables 2.2-2.4 with their applications. The best numerical technique for the IHCP in this work is chosen based on this summary.

2.3.1 General solution algorithm

Some works present a general solution method to solve an IHCP for diverse unknown parameters. Alifanov [90] discussed the general solution of a one-dimensional transient IHCP with the Tikhonov regularization algorithm in 1972. Later, Alifanov and Artyukhin [86] discussed the construction of an algorithm to solve a general nonlinear, one-dimensional, transient IHCP. Again, Tikhonov regularization is implemented to obtain stable results.

2.3.2 Estimation of boundary heat flux

There are many solution procedures for one- and two-dimensional IHCP found in literature, but limited studies on three-dimensional IHCPs are available. The solution of a three-dimensional IHCP is very time-consuming and can require large to very large amounts of computer memory depending on the solution method [12].

2.3.2.1 One-dimensional IHCP

Beck et al. [91] compare several solution methods to find an unknown surface heat flux from a transient one-dimensional IHCP. The work is relevant for both linear and nonlinear problems. The unknown heat flux is constant in space but not in time. Seven temperature measurements were taken at one surface to estimate the heat flux, but the average of these temperature measurements was taken as one temperature measurement at each time step, which indicates that the heat flux is only variable in time. The following conclusions were drawn:

- the function specification method (FSM) gives accurate results and is computationally efficient
- the iterative regularization method with conjugate gradient as specified by Alifanov [92] and the zeroth-order Tikhonov regularization method give comparable results. However, the computation time for the Tikhonov regularization is a factor 2 to 4 times larger.
- all three methods give excellent and very similar results

Beck et al. [91] comment on the iterative regularization method (the conjugate gradient method (CGM) in this case). It is a whole domain method, which means that all heat fluxes are simultaneously estimated for all times and/or positions. It has two advantages:

- rigorous mathematical implementation
- very generally applicable

Pourshaghaghy et al. [10] investigated other whole domain solution methods than the CGM to solve transient one-dimensional IHCPs, namely the Variable Metric Method (VMM). Four different versions of VMM are evaluated for accuracy and efficiency in the estimation of a heat flux in an IHCP. These methods have a resemblance with the CGM, but are based on matrix operations. The results with VMM do not show any significant improvement in accuracy, and VMM has the same weakness as all IHCP algorithms: it performs weakly in estimating the heat flux with a sudden or sharp step, as can be seen in Fig.2.3.

Wikstrom et al. [72] proposed a solution for a one-dimensional, nonlinear, transient IHCP, based on three thermocouple measurements inside a steel slab to estimate the surface temperature as well as the surface heat flux. Because of the high oven temperatures and the oxidation of the slab, it was impossible to measure surface temperatures. A Fourrier Transform method was used as solution procedure, which is based on the idea of rewriting the original partial differential equation as a system of ordinary differential equations. Lesnic et al. [93] also analyzed a one-dimensional, linear, unsteady IHCP in a slab. Temperature measurements in

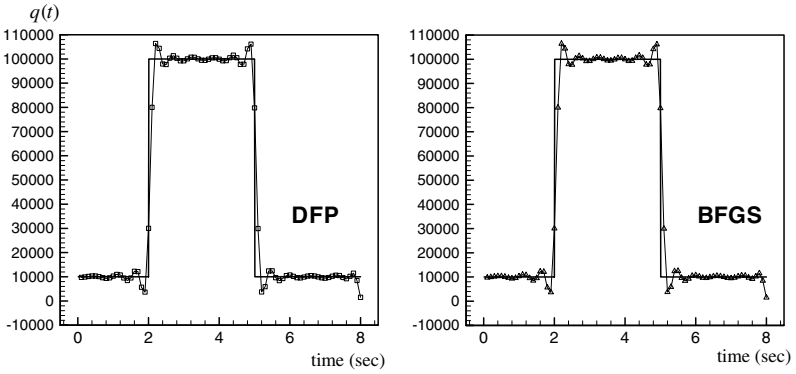

Figure 2.3: Comparison between real and predicted rectangular heat flux (pulse) using non noisy data for two different VMMs [10]

time were taken at an arbitrary location in the slab. The temperature and the heat flux on the inaccessible boundary were determined. The least squares regularization and energy method have been introduced into the boundary element method (BEM) formulation to solve this problem. A good stable estimation of temperature and heat flux was obtained. The constraint which is minimized, depended on a parameter of which the selection was more natural and easier to implement than the choice of the regularization parameter λ.

Deng and Hwang [85] also studied a transient one-dimensional and nonlinear IHCP. They deviated in their solution method from most other studies and used a data fusion technique. Kalman filtering (parametric method) was coupled to a neural network (information theoretic method). A Bayesian regularization method was applied. The proposed method seemed capable to predict the unknown parameters as heat flux and temperature in IHCPs with an acceptable error tolerance. The practical application of the estimation of temperatures and heat fluxes in a multi-layer gun barrel was considered as a one-dimensional transient IHCP by Chen et al. [73]. They developed an algorithm based on a regression model and a Kalman filter.

From these one-dimensional examples it is clear that there exists a wide range of solution techniques for one-dimensional IHCPs.

2.3.2.2 Two-dimensional IHCP

Alifanov and Kerov [92] improved their technique developed on one-dimensional IHCPs [86] to solve a transient two-dimensional IHCP for a hollow cylindrical body. The goal was to recover the unsteady external heat flux on the outside of

the cylinder. They used the conjugate gradient method (CGM) with the discrepancy principle as regularization criterion. The developed CGM algorithm is an iterative regularization technique. They stated that the conjugate gradient method has better characteristics to solve ill-posed inverse problems, compared to the similar steepest descent method (SDM). Prud'homme and Nguyen [94] investigated the iterative regularization character of the CGM. They stated that CGM is one of the most stable algorithms, even without a Tikhonov regularization implemented and proved how the stabilizing effect is built in this iterative minimization process. Next they solved a transient two-dimensional IHCP using the CGM with an implicit control volume approach. The low frequency structure of the heat flux is revealed after only a few iterations, the high frequency components are recovered much later, which is due to the diffusive nature of the equations in the CGM. This makes it possible to obtain an acceptable prediction for an unknown heat flux from noisy data (i.e. the high frequency). Notice that their conclusion was made for a heat flux variation in time. There is no statement made on a variation of the heat flux in space. Yang and Chen [95] applied the CGM to a transient, two-dimensional inverse heat transfer problem (IHTP). This means that both conduction and convection were considered. Both temperature and heat flux were estimated, and excellent results were obtained.

Bahbahani-nia and Kowsary [96] solved a transient, two-dimensional, linear IHCP to estimate an unknown boundary heat flux. A sequential function specification method in combination with the BEM was used. This method is only applicable to transient IHCPs.

While all previously mentioned studies focused on transient IHCPs, Cialkowski et al. [97] investigated a steady state, two-dimensional IHCP. The finite element method (FEM) without the continuity postulate (i.e. continuity of the approximate solution on the neighboring cells) was used as solution method. There can be discontinuity in energy or discontinuity in temperature, but also in entropy production and energy dissipation. Minimizing the discontinuities (multiplied with a factor) forms new criteria for finding the approximate solution of the heat conduction problem. The solution method is based on the minimization of the heat flux difference in the domain, and minimizing the discontinuity was used as regularization. This method gives good results, even better than the Tikhonov regularization, for which it is sometimes difficult to find a proper value for the regularization parameter.

2.3.2.3 Three-dimensional IHCP

Alifanov and Nenarokomov [71] suggested an iterative regularization method to solve a three-dimensional, transient and nonlinear IHCP. They recovered the time and space dependent boundary heat flux at one boundary surface of a three-dimensional shape. However, the studied three-dimensional shapes are simple in form,

they are canonical: slab, cylinder and sphere. The iterative regularization method is based on a gradient method (as the CGM), combined with the principle of the residual minimization. Alifanov's method gives good results in time and space. Mind however that a heat flux distribution in space was limited: it was induced in only one point of the surface, while the largest errors appear at a step change of the heat flux. It was also mentioned that the majority of the solution algorithms for IHCPs are applicable to linear inverse problems, but mostly not to non-linear problems. Haghighi et al. [79] also handled a transient three-dimensional IHCP with the CGM. The unknown boundary heat flux on functionally graded plates was estimated. The authors emphasized the regularizing character of the CGM, and find it a very powerful method to solve an IHCP. FEM was used as solution procedure in the CGM. The IHCP in the functionally graded plate is called three-dimensional but the plate is very thin in the third dimension compared to the other dimensions, and thus seems more like a two-dimensional problem. Another example of the CGM as solution method for three-dimensional IHCPs was illustrated in the work of Chen and Yang [11]. The heat flux at an electronic packaging/heat-sink-assembly interface was estimated, as depicted in Fig.2.4. The problem is treated as linear and transient. The electronic packaging, which was simulated as a rectangular beam, is again a basic three-dimensional shape. A spatial varying sinusoidal three-dimensional heat flux profile had to be estimated at the interface. The results indicate that CGM can reconstruct a spatial varying heat flux of sinusoidal form accurately, even for temperature measurement errors of 2.5%. Some of the results of the latter study are shown in Fig. 2.5. The used calculation grid was more dense were the heat flux is higher, because of the steeper temperature gradients there.

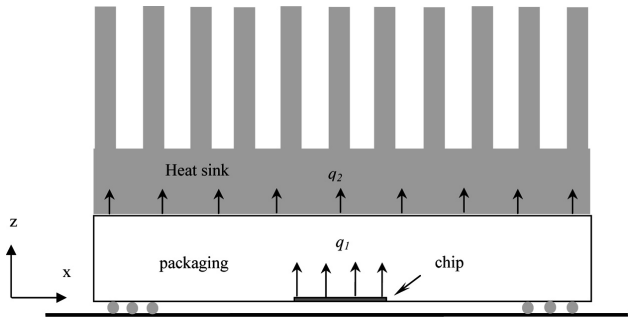

Figure 2.4: Case studied by Chen and Yang [11]. The heat flux q_2 is estimated based on temperature readings in the packaging. Only the IHCP in the packaging was solved

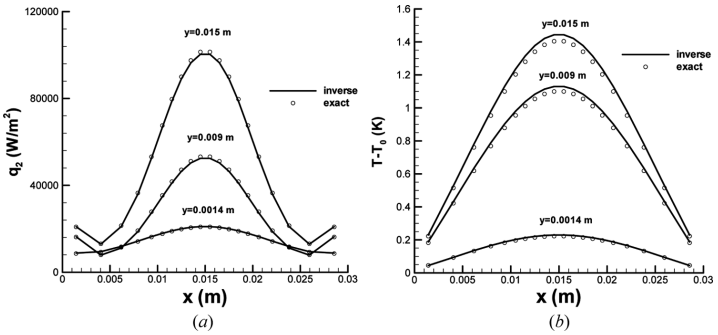

Figure 2.5: Comparison between the exact and inverse heat transfer rates and temperature distributions at the interface for a temperature measurement error of 2.5% [11]

Loulou and Scott [12] chose the CGM to solve a transient nonlinear three-dimensional IHCP, in which severely non-uniform and highly transient heat fluxes had to be reconstructed. They found that the CGM gave relatively correct results (2.4% error on the heat flux for errorless temperature measurements), even for a step change of the heat flux in time. They also emphasized the robustness and stability of the CGM. An example of their results is given in Fig.2.6. Gross et al. [98] considered a three-dimensional IHCP in a falling film experiment. The transient heat flux at the inaccessible film side of a foil is determined from infrared thermography data. The IHCP was also solved with the CGM and gave good results. Heydari and Farhanieh [99] compared the CGM with the Levenberg-Marquardt method (LM) for a transient, linear, three-dimensional IHCP on a hollow cylinder. The gas temperature at the inside of the cylinder was estimated and the conclusion was that CGM performs better than LM for both CPU time and accuracy.

The steepest descent method (SDM) has resemblances with the CGM. Mulcahy et al. [100] used the SDM to solve a transient, three-dimensional IHCP. The heat flux at the inner surface of a tube was reconstructed from temperature measurements on the outer tube surface with an infrared camera. The limited thickness of the tube and the applied boundary conditions simplified the three-dimensionality of the studied case. Satisfying results were obtained, but there was a relatively large error (± 15%) on the calculated heat flux after a sudden step change for the heat flux value in time.

Kim et al. [101] studied a three-dimensional transient IHCP to retrieve a heat flux varying in space and time at one boundary surface. A sequential gradient method was used, combined with a function specification which is used as regularization. The function specification is necessary to get a smooth and stable

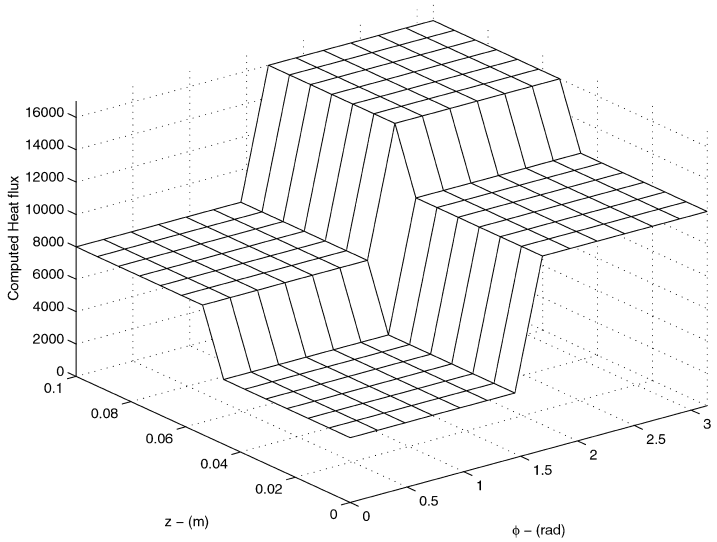

(a)

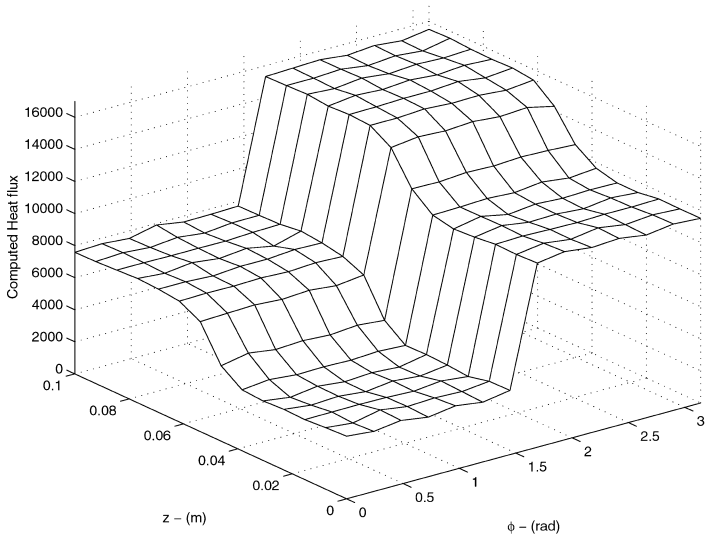

(b)

Figure 2.6: Some results from the work of Loulou and Scott [12]: comparison between the heat flux recovered from exact data (a) and the heat flux recovered from noisy data (b)

solution. It was noted that three-dimensional IHCPs require a lot of temperature readings at one time step because of the large numbers of unknowns. Therefore infrared thermography was used. The studied three-dimensional body was again a relatively basic shape: a beam with small thickness to length ratio. A finite volume method (FVM) was used to solve the partial direct problems in the sequential gradient method. The results showed that discontinuities in heat flux gave larger inaccuracies, but still with an acceptable error. This is thus a promising method to solve inverse problems. Luttich et al. [89] reconstructed time-dependent and spatially unknown heat fluxes for two- and three-dimensional IHCPs. The IHCP is solved in the frequency domain by deriving a state-space model. The solution is based on matrix calculation, so the coefficient matrix of the problem has to be determined. The method has a good performance and can also be applied to steady state problems.

2.3.3 Estimation of heat transfer coefficient

If IHCPs are solved to estimate local heat transfer coefficients at a boundary, this is often done in steady state. The reason for this will be explained later. Chen et al. [13] studied local heat transfer coefficients over a plate fin with a very small thickness using a steady state two-dimensional IHCP. They only performed a very small amount of temperature measurements with thermocouples and divided the fin in seven subregions, each connected to a different temperature measurement (Fig. 2.7). The least squares method coupled with a finite difference method was used as solution method. The heat transfer coefficient was assumed to be constant in each subregion, which is a not so accurate simplification. The results were only used to determine fin efficiency (thus a mean value of heat transfer coefficient is necessary) and the temperature field in the plate fin. Taler [102] estimated heat transfer coefficients at a tube wall. He solved the steady state two-dimensional IHCP with two different methods: Levenberg-Marquardt for a non-linear problem, matrix decomposition for a linear problem. Both methods are suitable to solve the problem and yield very similar results.

2.3.4 Estimation of a heat source

Wang et al. [103] described the SDM and CGM as solution procedures for IHCPs. SDM and CGM are function estimation problems: there is no prior information on the functional form of the estimated quantity. A heat generation source is estimated in a one-dimensional transient IHCP. The numerical test results showed that CGM gives good results for linear as well as nonlinear problems. The largest errors are for sharp peaks or sudden changes in heat generation. CGM was also the subject of the work of Park and Chung [104]. A heat source was estimated in a transient two-dimensional IHCP. Two types of CGM are investigated: the adjoint variable

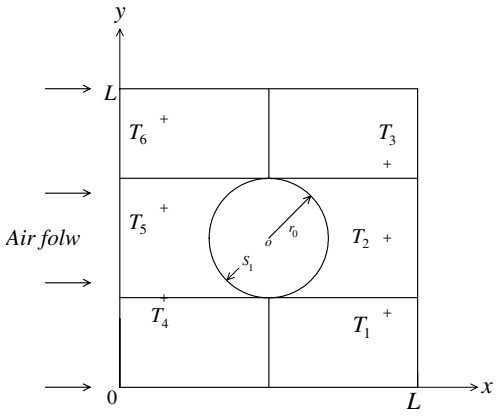

Figure 2.7: The plate fin subdivided in seven subregions with the placement of thermocouples as done by Chen et al. [13]

method and the direct differentiation method (DDM). The adjoint variable method is widespread in literature and most well-known type of CGM. For the DDM, the continuous heat source function is converted into a set of discrete variables with linear basis functions. The number of basis functions used in the DDM defines how many partial differential equations need to be solved, and thus also the calculation time. The adjoint variable method has an advantage in computational time. If there is an error on the temperature measurements, the adjoint variable method shows some oscillatory behavior, but the DDM predicts more accurate profiles (in time) without noisy oscillation. However, it becomes very difficult to use DDM if the number of temperature measurements is high. The number of basis functions depends on the form of the estimated heat flux function: for higher accuracy, the number of basis functions has to be increased. Park and Chung [104] also made an interesting remark concerning the temperature measurement location with regard to the heat source: the more the measurement sensor approaches the heat source location, the higher the accuracy. The sensitivity of the temperature field with respect to the heat source increases as the distance between measurement location and heat source decreases.

Chen et al. [105] solved a transient, two-dimensional IHCP using CGM with the discrepancy principle. The goal was to estimate the unknown heat generation at the interface of cylindrical bars during a friction process. It is actually a three-dimensional problem that was reduced to a two-dimensional by using axisymmetry. Only one internal temperature measurement point was used. The computational grid was denser close to the heat generation surface, because of the steeper temperature gradient. The location of temperature measurements or initial

guess for heat generation had no influence on the solution. Neto and Ozisik [14] proved that the CGM is very efficient method to solve IHCPs. The CGM was used to solve a transient linear two-dimensional IHCP in which a time-dependent line heat source is estimated by one temperature measurement. The heat source is only time-varying, but uniform in space. Accurate results were obtained. They also mention that functions with a step change or sharp corner are generally the most difficult cases to recover with an inverse analysis, as seen in Fig.2.8.

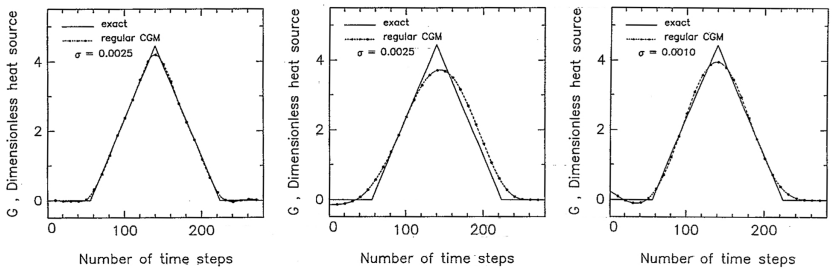

Figure 2.8: Results from Neto and Ozisik [14]. Effects of moving the heat source to the center of the sample and of changing the standard deviation of the measurement errors. Left: source close to the boundary; Center: source at the center; Right: source at the center for smaller temperature measurement error

2.3.5 Estimation of thermal properties

Chen and Lin [106] proposed a hybrid numerical algorithm of the Laplace transform technique and the control-volume method to simultaneously estimate the temperature-dependent thermal conductivity and heat capacity from temperature measurements inside the material using a transient one-dimensional nonlinear inverse calculation. Good estimates of the thermal properties were obtained. Kim et al. [107] converted a transient one-dimensional nonlinear IHCP to a parameter estimation problem that determines the unknown coefficients of the thermal conductivity function. They developed an integral approach to estimate temperature-dependent thermal conductivity without internal measurements. Their approach was verified with several examples. Yang [108] also solved a transient one-dimensional nonlinear IHCP to determine the temperature-dependent thermal conductivity from temperature measurements taken at one boundary. An iterative approach based on a gradient method and linearization method was used to solve a set of nonlinear equations in which the undetermined thermal conductivity is denoted as the unknown. The results confirmed the validity of the proposed method. Huang and Yan [109] used the CGM to simultaneously estimate the temperature-dependent thermal conductivity and heat capacity per unit volume of a material. Excellent

estimations on the thermal properties are obtained when a good initial guess of either thermal conductivity or heat capacity is provided.

2.3.6 Huang's work on SDM and CGM

Examples in open literature of three-dimensional inverse problems for an irregular domain are scarce. Huang published numerous studies on two- and three-dimensional IHCPs. He successfully developed a technique in which an inverse algorithm is coupled with a commercial code by means of data transportation. This is powerful technique to solve general three-dimensional inverse heat transfer problems. Commercial codes can calculate many difficult direct heat conduction problems. If they are coupled with an inverse algorithm, they could be used to solve three-dimensional IHCPs. Huang uses CFX4.2 in all his works. Huang and Tsai [15] solved a linear steady state three-dimensional IHCP using the SDM to reconstruct heat transfer coefficients on the fin walls of a fin and tube heat exchanger (Figure 2.9) from plate fin surface temperature measurements. Although no real temperature measurements were done, he suggested infrared thermography to measure the plate fin surface temperatures. The results showed the difficulty to estimate the local heat transfer coefficients accurately near the tube passage through the plate fin. Some results are shown in Fig.2.10. For a standard deviation of 0.1 °C on the temperature measurements, there is a mean error of 5.92% on the local convection coefficient estimation. This error increases to11.72% for a standard deviation of 0.4°C. This work was extended by Huang and Tsai [110] to a transient three-dimensional IHCP for the same plate fins.

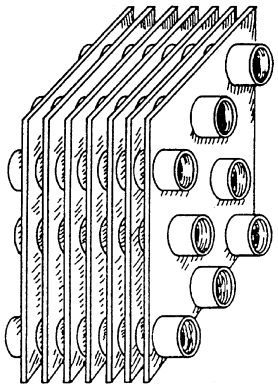

Figure 2.9: A plate fin heat exchanger as studied by Huang and Tsai [15]

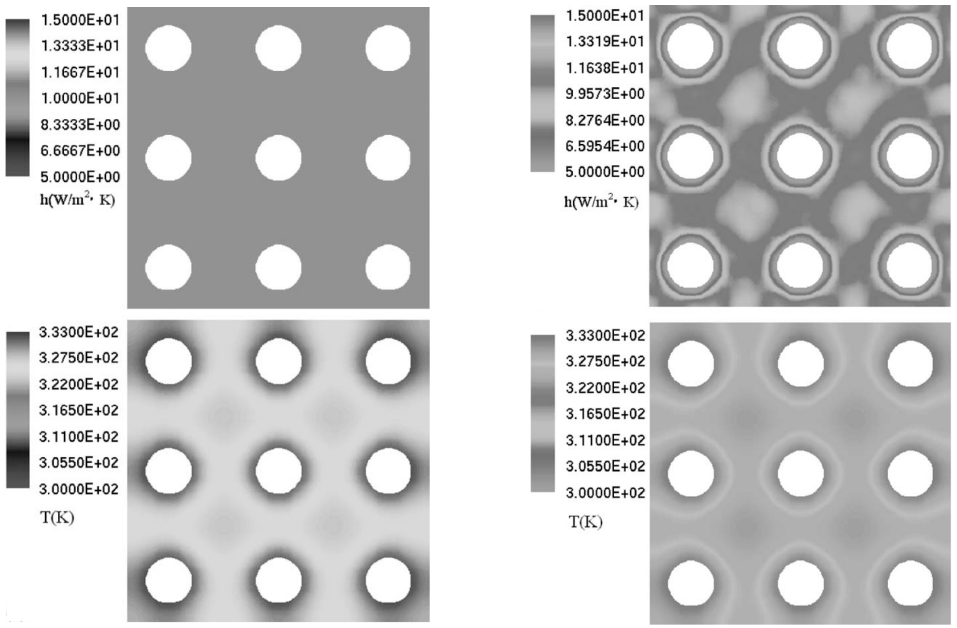

Figure 2.10: Results from Huang and Tsai [15]. (a) the exact values for the heat transfer coefficients (top) and measured temperatures (bottom), (b) the estimated values for the heat transfer coefficients (top) and measured temperatures (bottom) for a standard deviation of σ = 0.1 °C on the measured temperatures

Huang and Wang [111] used the same general method for a linear transient three-dimensional IHCP, in which an unknown boundary heat flux was estimated in a three-dimensional irregular domain of arbitrary, but relatively thin shape. The heat flux was estimated at only one boundary surface. However, this time the CGM was used instead of SDM. Their numerical test cases indicated that the estimates of heat flux are less accurate near locations of discontinuity (in time). For exact temperature values, the average error on the estimated heat flux is 5.2%, but increases to 7.1% for an error of 1% on the measured temperature, and to 8.3% for a temperature error of 2%. Both SDM and CGM proved to be powerful to solve three-dimensional inverse problems.

Huang applied his method with CGM or SDM to solve three-dimensional transient IHCPs to several practical applications. Huang and Lo [16] predicted the heat flux distribution in cutting tools with this method. The heat flux was estimated at three small surfaces of the actual cutting part: surfaces $S_{\mathrm{c}1} - S_{\mathrm{c}3}$ in Fig.2.11. These surfaces are placed orthogonally to each other. The temperature measurements on surfaces $S_{\mathrm{m}1} - S_{\mathrm{m}4}$ are also used in the heat flux estimation. Huang et al. [69] used the SDM again to estimate the applied heat flux on the drilling surface of a drilling tool. SDM was also used to determine the time-dependent heat flux generated in rotor and stator for the high speed electric motor [70]. The accuracy of these three studies are listed in Table 2.1. However, some general remarks on the results of these studies have to be made. The results are very accurate (see table 2.1) even for a sinusoidal varying heat flux or a sudden step in the heat flux. An example of these results is given in Fig.2.12 for the estimation of the heat fluxes on the cutting surfaces $S_{\mathrm{c}1} - S_{\mathrm{c}3}$. The heat flux varies sinusoidal in time and the temperature measurement error is 1%. However, these heat flux variations are only a function of time. For each time step, the space-averaged heat flux at each of the studied boundary surfaces is taken, and these space-averages are used to compare with the exact solution. There is no mention on the accuracy of estimation on the spatial distribution of the heat flux on each surface. The accuracy of his method on the spatial distribution is not checked. It is possible that there is a significant error on local heat flux on each surface (especially near the edges), but that this is not noticeable in the spatial averaged heat flux values. Moreover, the simplest spatial distribution was applied on each surface: a constant heat flux in space. There is no data available on the accuracy of the method for sinusoidal or step functions of the heat flux in function of spatial coordinates. This is an important shortcoming in Huang's work. For the case of the electric motor, there is a significant error of 5.5% on the heat flux estimations for an exact temperature [70]. This is explained by the presence of cooling passages in the motor housing, between the outer surface where the temperatures are measured and the inner surface where the heat fluxes are estimated. These passages block the influence of the internal heat flux on the temperatures measurements on the outer surface. So the surface tempera-

tures are not sensitive enough to the corresponding internal heat fluxes. Therefore it was chosen to work with space-averaged heat flux values over the estimation surface. This gave better results and smaller errors, which are elected in Table 2.1.

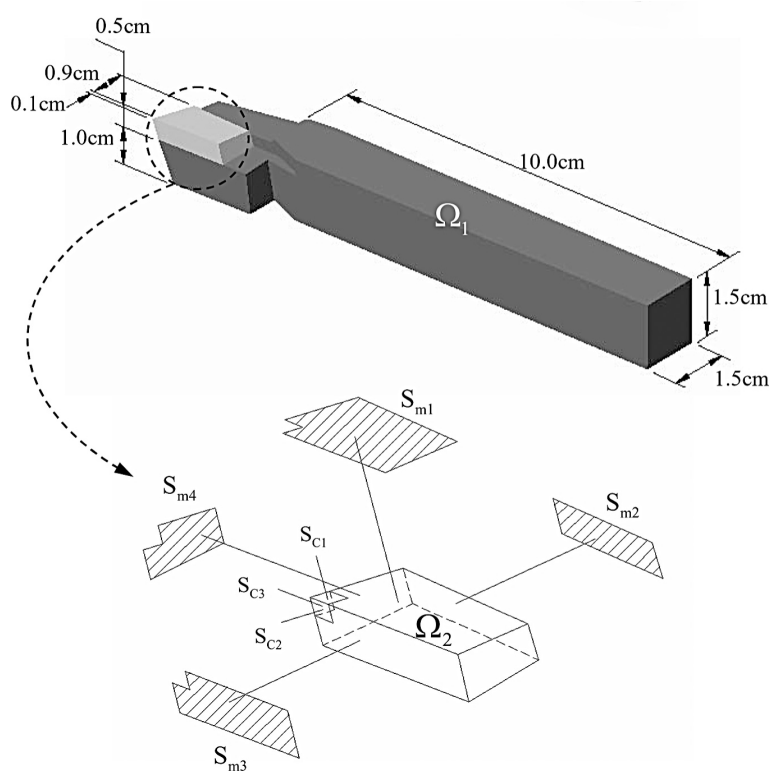

Figure 2.11: The cutting tool studied by Huang and Lo [16]

Huang applied his method also to other inverse problems. Huang and Chen [112] solved an inverse forced convection problem with the CGM. This gave also good results. The following two studies are actually two-dimensional but are placed here as an extension of Huang's work. Huang and Chao [113] applied the method with CGM to an inverse two-dimensional geometry problem: the geometry of a boundary is reconstructed. In this work, the CGM is compared to the Levenberg-Marquardt Method (LMM). CGM needs less computer time than LMM. Also the initial guess does not need to be very accurate for CGM, the number of measurement sensors can be reduced without significant loss of accuracy and it is not very sensitive to measurement errors. However, the estimation of a discontinuity region is not so accurate. In a follow-up paper, Huang and Chen [114] used a boundary element method to solve the inverse geometry prob-

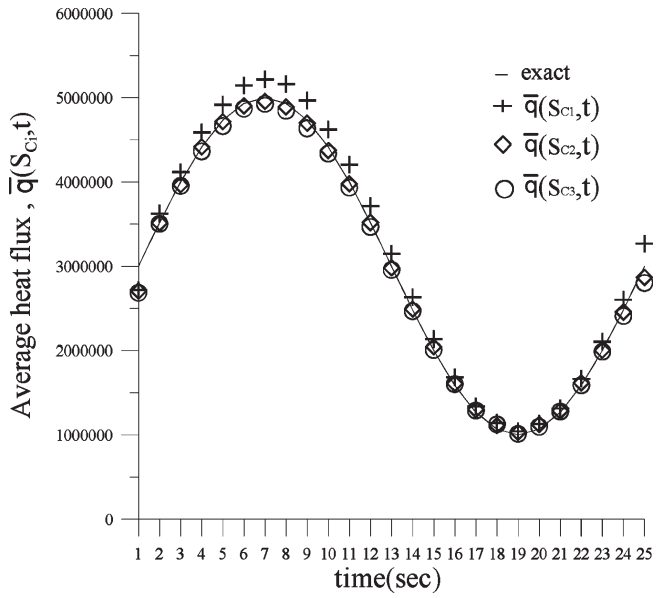

Figure 2.12: Exact and estimated average heat flux values at the three cutting surfaces S_{c1} – S_{c3} for temperature measurement error of 1% [16]

	Cutting [16]	Electric [70]	Drilling [69]
Heat flux error for dT_{meas}=0%	1.0%	0.72%	2.3%
Temperature error for dT_{meas}=0%	0.01%	0.025%	0.1%
Heat flux error for dT_{meas}=1%	5.0%	/	3.4%
Temperature error for dT_{meas}=1%	1.08%	/	0.5%
Heat flux error for dT_{meas}=2.5%	6.71%	3.0%	6.3%
Temperature error for dT_{meas}=2.5%	2.2%	1.3%	1.0%

Table 2.1: The error on the estimated values of heat flux and temperature for three cases studied by Huang

lem. An important conclusion from this work was that it becomes more difficult to estimate the boundary coordinates as the distance between boundaries and sensors increases. This is the corner effect.

2.3.7 Conclusion

The literature survey is summarized in tables 2.2-2.4. Note that most IHCPs are solved for transient conditions. There is only limited literature available on three-dimensional, steady state IHCPs and three-dimensional IHCPs to estimate local heat transfer coefficients. A three-dimensional IHCP is difficult to solve due to the complexity and high computational cost [101]. The SDM and CGM are the most frequently used methods to solve three-dimensional IHCPs and proved to be very powerful and accurate. The CGM is also very suitable for large-scale applications and discretized higher dimensional problems [88]. Especially Huang's general method that combines both techniques with a commercial code, stands out. It has the advantage that it is applicable to irregular domains and can relatively easily be adapted from one geometry to another. It can be adjusted to commercial codes available in the research department. Moreover, developing a numerical method with a house code is very time consuming. Also, infrared thermography measurements lean themselves perfectly as input temperature measurements for this kind of method, as was shown by Huang [15]. A method based on Huang's work seems to be the best choice for investigating local heat transfer coefficients and heat fluxes on extended surfaces in three dimensions.

Ref.	Dimensions	Time condition	Type	Estimated parameter	Method
[90]	1-D	transient	both	general	Tikhonov
[86]	1-D	transient	nonlinear	general	Tikhonov
[73]	1-D	transient	linear	heat flux (+T)	Regression + Kalman
[85]	1-D	transient	nonlinear	heat flux (+T)	Neural network + Kalman
[91]	1-D	transient	both	heat flux	FSM, CGM and Tikhonov
[72]	1-D	transient	nonlinear	heat flux (+T)	Fourrier Transform
[10]	1-D	transient	both	heat flux	VMM
[93]	1-D	transient	linear	heat flux (+T)	BEM
[103]	1-D	transient	both	heat source	CGM
[106]	1-D	transient	nonlinear	thermal conductivity	Laplace Transform
[107]	1-D	transient	nonlinear	thermal conductivity	Integral Approach
[108]	1-D	transient	nonlinear	thermal conductivity	GM

Table 2.2: Overview of the literature for one-dimensional IHCPs

Ref.	Dimensions	Time condition	Type	Estimated parameter	Method
[92]	2-D	transient	both	heat flux	CGM
[97]	2-D	steady	both	heat flux	FEM + Trefftz
[13]	2-D	steady	linear	convection coefficient	FDM + LS
[113]	2-D	transient	/	/	CGM
[105]	2-D	transient	linear	heat source	CGM
[94]	2-D	transient	linear	heat flux	CGM
[104]	2-D	transient	nonlinear	heat source	CGM
[14]	2-D	transient	linear	heat source	CGM
[96]	2-D	transient	linear	heat flux	FSM + BEM
[95]	2-D	transient	linear	heat flux (+T)	CGM
[102]	2-D	transient	both	convection coefficient	LM

Table 2.3: Overview of the literature for two-dimensional IHCPs

Ref.	Dimensions	Time condition	Type	Estimated parameter	Method
[15]	3-D	steady	linear	convection coefficient	SDM
[71]	3-D	transient	nonlinear	heat flux	CGM
[101]	3-D	transient	nonlinear	heat flux	FSM + SGM
[110]	3D	transient	linear	convection coefficient	SDM
[111]	3-D	transient	linear	heat flux	CGM
[16]	3-D	transient	linear	heat flux	SDM
[69]	3-D	transient	linear	heat flux	SDM
[70]	3-D	transient	linear	heat flux	SDM
[79]	3-D	transient	linear	heat flux	CGM
[11]	3-D	transient	linear	heat flux	CGM
[99]	3-D	transient	linear	temperature	CGM and LM
[12]	3-D	transient	nonlinear	heat flux	CGM
[89]	3-D	transient	both	heat flux	Frequency Domain
[98]	3-D	transient	linear	heat flux	CGM

Table 2.4: Overview of the literature for three-dimensional IHCPs

2.4 Problem description: inverse problem in a longitudinal fin

The goal of this work is to develop a methodology to determine fin effectiveness and local heat transfer coefficients/heat fluxes on extended surfaces. It should be applicable to real three-dimensional fin setups, and more specifically to cooling fins for heat sinks and electronics cooling. Therefore the methodology cannot be completely numerical. It has to be validated and be able to process experimental measurements to fin effectiveness and local heat transfer coefficient values. It was already shown that the experimental test cases in this work are limited to longitudinal rectangular fins for heat sinks. The fundamental experimental test case of the longitudinal fin was described in the previous chapter. It consists of a primary surface with a longitudinal fin on it. The fin is observed as a part of a heat sink: there is unfinned primary surface at both sides of the fin for half the fin spacing of a heat sink (Fig. 2.13). The IHCP solution method is based on this fundamental experimental test case. The scaled model with primary surface had the following dimensions (Fig. 2.13):

- fin:
  - length: $0.254\ \mathrm{m}$
  - height: $0.142\ \mathrm{m}$
  - thickness: $0.005\ \mathrm{m}$
- primary surface:
  - length: $0.0254\ \mathrm{m}$
  - height: $0.03\ \mathrm{m}$
  - thickness: $0.025\ \mathrm{m}$

The primary surface and fin are both made out of aluminum with thermal conductivity k. The value of the thermal conductivity will be determined in Chapter 4.

The model of the primary surface with longitudinal fin is the domain Ω in which the IHCP is solved. This domain Ω is shown in Fig.2.14 with the indication of the various boundary surfaces. The boundary conditions imposed on this domain depend on those of the experimental setup. The choice of these boundary conditions was explained in the previous chapter. These boundary conditions are, in consensus with Fig.2.14:

- fin surfaces $S_1 - S_5$: temperatures are measured (with infrared thermogaphy) and local convection coefficients have to be determined

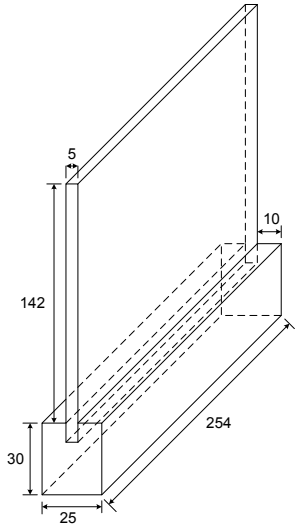

Figure 2.13: Model and dimensions of fin and primary surface

- top of the primary surface S_6 – S_7: same as for S_1 – S_5
- bottom of primary surface S_8: constant heat flux q_0 or heat generation Q_0
- side walls of the primary surface S_9 – S_{12}: adiabatic
- contact surface S_{13}:
  - if primary surface and fin are made out of one piece: coupled
  - if they are separate pieces: contact resistance

In the following, the primary surface and fin are considered as made out of one piece, so the coupled condition is used. The problem with contact resistance will be handled later. Note that the longitudinal fin is thin compared to the length and height and the flow around the fin is assumed symmetric, so the temperature distribution and convection coefficients on the long fin sides S_4 – S_5 can be assumed to be equal. Due to symmetry, the computational domain Ω could be simplified by using a symmetry plane. However, it was chosen not to do this, so that test cases in which the convection coefficient distribution is not symmetric could also be investigated. If the fin form is adjusted, e.g. by introducing perforations in the fin, the symmetric condition will also not hold anymore.

The described problem is a three-dimensional IHCP for which the local heat transfer coefficients or heat fluxes are unknown on 7 surfaces, which are orthog-

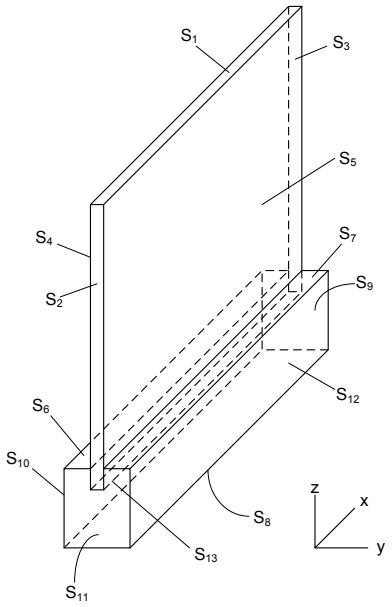

Figure 2.14: Domain with the boundary surfaces

onal to each other when adjacent (Figure 2.14). So the problem is highly three-dimensional and more complex than the three-dimensional problems mentioned in the literature survey. From the literature survey, it was concluded that Huang's method with either SDM or CGM should give the best results to solve the IHCP. It has the advantage that it can be adapted to other fin shapes or test cases due to its communication with a commercial code. So, this method was adapted to solve the described IHCP. The commercial code available in the research department is FLUENT [66], which is a Finite Volume Method code. So Huang's procedure also has to be adjusted to this. The solution procedure of the IHCP for both SDM and CGM are explained in the following paragraphs.

The local convection coefficients $h(S_\mathrm{i})$ on S_1 – S_7 are the unknowns of the IHCP. However, it could also be chosen to determine the unknown heat fluxes $q(S_\mathrm{i})$ on these surfaces, because the surface temperatures are known and thus local convection coefficients $h(S_i)$ can be calculated from the local heat fluxes $q(S_\mathrm{i})$:

$$h(S_\mathrm{i}) = \frac{q(S_\mathrm{i})}{T(S_\mathrm{i}) - T_\infty} \tag{2.11}$$

Note that in this work a short notation is used for functions of $h(S_\mathrm{i})$, e.g.:

$$T_{\mathrm{m}}(h(S_{\mathrm{i}})) = T_{\mathrm{m}}(S_{\mathrm{i}});\ J_{\mathrm{m}}(h(S_{\mathrm{i}})) = J_{\mathrm{m}}(S_{\mathrm{i}});\ P^{n}_{\mathrm{m}}(h(S_{\mathrm{i}})) = P^{n}_{\mathrm{m}}(S_{\mathrm{i}}) \tag{2.12}$$

The IHCP for estimating the unknown $q(S_{\mathrm{i}})$ will be discussed later. The temperature profiles on surfaces S_1–S_7 are measured by infrared thermography. These temperature measurements are denoted as $Y_{\mathrm{m}}(S_{\mathrm{i}})$ (m=1-M_{i}) where M_{i} is the total amount of measurement points over the surface S_{i}. By solving the IHCP, the convection coefficients $h(S_{\mathrm{i}})$ are estimated based on these temperature measurements $Y_{\mathrm{m}}(S_{\mathrm{i}})$, by minimizing the functional:

$$J\left[h(S_{\mathrm{i}})\right] = \sum_{i=1}^{7}\sum_{m=1}^{M_{\mathrm{i}}}\left[T_{\mathrm{m}}(S_{\mathrm{i}}) - Y_{\mathrm{m}}(S_{\mathrm{i}})\right]^2 \tag{2.13}$$

in which $T_{\mathrm{m}}(S_{\mathrm{i}})$ are the computed temperatures at the measurement locations from the direct problem solution with the estimated convection coefficients $h(S_{\mathrm{i}})$.

2.4.1 The direct problem

The IHCP would be a direct problem if the convection coefficients $h(S_{\mathrm{i}})$ at the boundary surfaces S_1 – S_7 are known, instead of the temperatures. Then the temperature field in Ω can be calculated. The direct conduction problem for the domain $\Omega(x, y, z)$ of the primary surface and longitudinal fin is formulated as:

$$\frac{\partial^2 T}{\partial x^2} + \frac{\partial^2 T}{\partial y^2} + \frac{\partial^2 T}{\partial z^2} = 0 \quad \text{in } \Omega(x, y, z) \tag{2.14a}$$

with the following boundary conditions:

$$-k \cdot \frac{\partial T}{\partial n} = h(S_{\mathrm{i}}) \cdot (T - T_{\infty}) \quad \text{on } S_{\mathrm{i}}(i = 1 - 7) \tag{2.14b}$$

$$-k \cdot \frac{\partial T}{\partial n} = 0 \quad \text{on } S_{\mathrm{i}}(i = 9 - 12) \tag{2.14c}$$

$$-k \cdot \frac{\partial T}{\partial n} = q_0 \quad \text{on } S_8 \tag{2.14d}$$

$$-k \cdot \frac{\partial T_{\mathrm{fin}}}{\partial n} = -k \cdot \frac{\partial T_{\mathrm{primary}}}{\partial n} \quad \text{on } S_{13} \tag{2.14e}$$

This direct conduction problem is solved using FLUENT.

2.4.2 Steepest Descent algorithm

The SDM is an iterative algorithm that is used to estimate the local heat transfer coefficients $h(S_\mathrm{i})$ on the boundary surfaces $S_1 - S_7$. The estimation is based on the minimization of the functional J in Eq. (2.13). To start the algorithm an initial guess of $h(S_\mathrm{i})$ is necessary. In each iteration of the SDM, a new value of $h(S_\mathrm{i})$ is calculated based on the previous value, so that the functional J decreases. The new $h(S_\mathrm{i})$ value can generally be written as:

$$h^{n+1}(S_\mathrm{i}) = h^n(S_\mathrm{i}) - \beta^n P^n(S_\mathrm{i}) \quad \text{for } i = 1 - 7 \tag{2.15}$$

with

- β^n: the step size at the n-th iteration
- $P^n(S_\mathrm{i})$: the search direction at the n-th iteration

The step size β^n is a constant value, and the same for each element of the function $h(S_\mathrm{i})$. In discretized form, the search direction $P^n(S_\mathrm{i})$ is a vector of the same dimension as $h(S_\mathrm{i})$, and this vector gives the direction in which the step is taken. For the SDM, the search direction, also known as the direction of descent, is identical to the gradient direction of the minimization functional J (Eq. (2.13)) [115]:

$$P^n(S_\mathrm{i}) = J'^n[h(S_\mathrm{i})] \quad \text{for } i = 1 - 7 \tag{2.16}$$

That is why the steepest descent method is also called the gradient method. Note that $J'^n(S_\mathrm{i})$is the derivative of J to the function h, not S_i. Once the new convection coefficient $h^{n+1}(S_\mathrm{i})$ is calculated, the direct problem from the previous paragraph is solved with this new value to calculate the temperatures $T_\mathrm{m}(S_\mathrm{i})$ at the boundary surfaces $S_1 - S_7$ and the functional J (Eq. (2.13)) is evaluated again. This iteration process is repeated until the functional J drops below a certain value. This is the basic algorithm of SDM. There is no guarantee that a proposed value of J will be attained, it is possible that SDM stops at a higher value. Therefore the functional J is monitored during the iteration process to check the convergence and find possible stagnation of J. In case the proposed stopping criterion is not reached, a less accurate solution is obtained.

Of course, the step size and search direction have to be determined. These two values are determined by solving two partial direct problems: the sensitivity problem and the adjoint problem. Thus the SDM transforms the IHCP into the solution of three problems: the direct problem, the sensitivity problem and the adjoint problem. These three problems can be observed as direct heat conduction problems which have a unique solution.

2.4.2.1 The sensitivity problem

The construction of the sensitivity problem is based on perturbation analysis. If the local convection coefficient $h(S_\mathrm{i})$ is varied with Δh, then the temperature field T in the domain Ω is perturbed to $T + \Delta$T. So the direct problem 2.14 becomes:

$$\frac{\partial^2(T+\Delta T)}{\partial x^2} + \frac{\partial^2(T+\Delta T)}{\partial y^2} + \frac{\partial^2(T+\Delta T)}{\partial z^2} = 0 \quad \text{in } \Omega(x,y,z) \tag{2.17a}$$

with the following boundary conditions:

$$-k \cdot \frac{\partial(T+\Delta T)}{\partial n} = h \cdot (T - T_\infty) + h\Delta T + \Delta h \cdot (T - T_\infty) + \Delta h \cdot [(T+\Delta T) - T_\infty] + \Delta h \Delta T \quad \text{on } S_\mathrm{i}\,(i = 1-7) \tag{2.17b}$$

$$-k \cdot \frac{\partial(T+\Delta T)}{\partial n} = 0 \quad \text{on } S_\mathrm{i}(i = 9-12) \tag{2.17c}$$

$$-k \cdot \frac{\partial(T+\Delta T)}{\partial n} = q_0 \quad \text{on } S_8 \tag{2.17d}$$

$$-k \cdot \frac{\partial(T+\Delta T)_\mathrm{fin}}{\partial n} = -k \cdot \frac{\partial(T+\Delta T)_\mathrm{primary}}{\partial n} \quad \text{on } S_{13} \tag{2.17e}$$

If the original direct problem 2.14 is subtracted from this newly found direct problem for the convection coefficients $h + \Delta h$, and second order terms are neglected (such as $\Delta h \cdot \Delta T$ for boundary condition 2.17b), then a new direct problem is obtained. This problem expresses the sensitivity of the solution (i.e. the temperature field) to a variation of the estimated convection coefficients $h(S_\mathrm{i})$. This is called the sensitivity problem for the sensitivity function ΔT, and is formulated as:

$$\frac{\partial^2 \Delta T}{\partial x^2} + \frac{\partial^2 \Delta T}{\partial y^2} + \frac{\partial^2 \Delta T}{\partial z^2} = 0 \quad \text{in } \Omega(x,y,z) \tag{2.18a}$$

with the following boundary conditions:

$$-k \cdot \frac{\partial \Delta T}{\partial n} = h(S_\mathrm{i})\Delta T + \Delta h(S_\mathrm{i})\,(T - T_\infty) \quad \text{on } S_\mathrm{i}(i = 1-7) \tag{2.18b}$$

$$-k \cdot \frac{\partial \Delta T}{\partial n} = 0 \quad \text{on } S_\mathrm{i}(i = 9-12) \tag{2.18c}$$

$$-k \cdot \frac{\partial \Delta T}{\partial n} = 0 \quad \text{on } S_8 \tag{2.18d}$$

$$-k \cdot \frac{\partial \Delta T_{\text{fin}}}{\partial n} = -k \cdot \frac{\partial \Delta T_{\text{primary}}}{\partial n} \quad \text{on } S_{13} \tag{2.18e}$$

This sensitivity problem is a direct heat conduction problem and can be solved with FLUENT to calculate the sensitivity function ΔT in Ω. The boundary condition on the surfaces $S_1 - S_7$ is implemented in FLUENT as a heat flux boundary condition in which the heat flux is specified by a user defined function (UDF) equal to the right hand side of Eq. (2.18b). For this boundary condition, the values Δh_{i} are necessary. These are equal to the search direction P_{i}^n, which are determined by solving the adjoint problem (following paragraph 2.4.2.2). The constant heat flux boundary condition in the direct problem becomes an adiabatic one in the sensitivity problem. The step size β^n from Eq. (2.15) is determined from the sensitivity function ΔT. If the functional J (Eq. (2.13))is rewritten for iteration n+1, thus for the new h^{n+1} with Eq. (2.15), it becomes:

$$J\left[h^{n+1}(S_{\text{i}})\right] = \sum_{i=1}^{7} \sum_{m=1}^{M_{\text{i}}} \left[T_{\text{m}}\left(S_{\text{i}}; h^n - \beta^n P^n\right) - Y_{\text{m}}(S_{\text{i}})\right]^2 \tag{2.19}$$

The temperature $T_{\text{m}}\left(h^n - \beta^n P^n\right)$ can be linearized by a Taylor expansion of the first order, then the expression of the functional J from Eq.(2.19) becomes:

$$J\left[h^{n+1}(S_{\text{i}})\right] = \sum_{i=1}^{7} \sum_{m=1}^{M_{\text{i}}} \left[T_{\text{m}}\left(S_{\text{i}}; h^n\right) - \beta^n \Delta T_{\text{m}}\left(S_{\text{i}}; P^n\right) - Y_{\text{m}}(S_{\text{i}})\right]^2 \tag{2.20}$$

In this expression, $T_{\text{m}}(S_{\text{i}}; h^n)$ is the solution of the direct problem (Eq. (2.14)) in which the estimated heat transfer coefficient h^n is used on the boundary surfaces $S_1 - S_7$. The sensitivity functions $\Delta T_{\text{m}}(S_{\text{i}}; P^n)$ are the solution of the sensitivity problem (Eq. (2.18)) in which $\Delta h = P^n$ in boundary condition 2.18b. Thus, to determine Δh, the adjoint problem has to be solved first. Notice that the index m indicates that only the values of the solution at the temperature measurement locations are taken. Now, the step size β^n is the only unknown in the expression 2.20 for functional J. The goal of the SDM algorithm is to estimate heat transfer coefficients $h(S_{\text{i}})$ so that the functional J is minimized. So β^n should minimize the functional J. This means that the first derivative of J to the search step β^n should be zero:

$$\frac{\partial J\left[h^{n+1}(S_{\text{i}})\right]}{\partial \beta^n} = 0 \tag{2.21}$$

By applying this to Eq. (2.20), an expression for step size β^n is found:

$$\beta^n = \frac{\sum_{i=1}^{7} \sum_{m=1}^{M_{\text{i}}} \left[T_{\text{m}}\left(S_{\text{i}}; h^n\right) - Y_{\text{m}}(S_{\text{i}})\right] \Delta T_{\text{m}}(S_{\text{i}})}{\sum_{i=1}^{7} \sum_{m=1}^{M_{\text{i}}} \left[\Delta T_{\text{m}}\left(S_{\text{i}}; h^n\right)\right]^2} \tag{2.22}$$

The first unknown, the step size β^n, for Eq. (2.15) is found. Note that step size cannot be determined if the nominator of Eq. (2.22) becomes zero, which would mean that the solution method runs into problems. However, the nominator is unlikely to become zero, as a perturbation Δh_{i} would always cause perturbations ΔT_{i} so that $\sum_{m=1}^{M} \left[\Delta T_{\mathrm{m}}\left(S_{\mathrm{i}}; h^n\right)\right]^2 \neq 0$. The use of a sensitivity problem to determine the step size is not that common, but it is quite advantageous for this problem as shown in the literature survey (section 2.3).

2.4.2.2 The adjoint problem

The adjoint problem is obtained by introducing a Lagrange multiplier λ. Lagrange multipliers are used to find the extrema of a function, subject to a constraint. So actually, the Lagrange multiplier is used here to provide regularization of the IHCP solution. The direct heat conduction equation (Eq. (2.14a)) is multiplied by the Lagrange multiplier $\lambda(\Omega)$, and this expression is integrated over the space domain Ω. Then, this is added to the right hand side of the expression for the functional J (Eq.(2.13). So a new expression for the functional $J\left[h(S_{\mathrm{i}})\right]$ is obtained:

$$\begin{aligned} J\left[h(S_{\mathrm{i}})\right] &= \sum_{i=1}^{7}\sum_{m=1}^{M_{\mathrm{i}}}\left[T_{\mathrm{m}}(S_{\mathrm{i}}) - Y_{\mathrm{m}}(S_{\mathrm{i}})\right]^2 + \int_{\Omega}\left[\lambda(\Omega)\times\nabla^2 T\right]\mathrm{d}\Omega \\ &= \int_{S_{\mathrm{i}}}\left[T_{\mathrm{m}}(S_{\mathrm{i}}) - Y_{\mathrm{m}}(S_{\mathrm{i}})\right]^2\delta(x-x_{\mathrm{m}})\delta(y-y_{\mathrm{m}})\mathrm{d}x\mathrm{d}y + \\ &\quad \int_{S_{\mathrm{j}}}\left[T_{\mathrm{m}}(S_{\mathrm{j}}) - Y_{\mathrm{m}}(S_{\mathrm{j}})\right]^2\delta(x-x_{\mathrm{m}})\delta(z-z_{\mathrm{m}})\mathrm{d}x\mathrm{d}z + \\ &\quad \int_{S_{\mathrm{k}}}\left[T_{\mathrm{m}}(S_{\mathrm{k}}) - Y_{\mathrm{m}}(S_{\mathrm{k}})\right]^2\delta(y-y_{\mathrm{m}})\delta(z-z_{\mathrm{m}})\mathrm{d}y\mathrm{d}z + \\ &\quad \int_{\Omega}\left[\lambda(\Omega)\times\nabla^2 T\right]\mathrm{d}\Omega \\ &\quad \text{for } \Omega(x,y,z) \;\; and \;\; i = 1,6,7; j = 4,5; k = 2,3 \end{aligned} \tag{2.23}$$

in which the delta function is introduced to obtain the integral form of the summation. This is a long expression. For the rest of the work, a shorter notation is used for Eq.(2.23):

$$\begin{aligned} J\left[h(S_{\mathrm{i}})\right] &= \int_{S_{\mathrm{i}}}\left[T_{\mathrm{m}}(S_{\mathrm{i}}) - Y_{\mathrm{m}}(S_{\mathrm{i}})\right]^2\delta(x-x_{\mathrm{m}})\delta(y-y_{\mathrm{m}})\delta(z-z_{\mathrm{m}})\mathrm{d}S_{\mathrm{i}} + \\ &\quad \int_{\Omega}\left[\lambda(\Omega)\times\nabla^2 T\right]\mathrm{d}\Omega \quad \text{for } \Omega(x,y,z) \;\text{ and } i = 1-7 \end{aligned} \tag{2.24}$$

The expression of the minimization functional J is modified by using Eq. (2.14a) as a constraint. The new expression (Eq. (2.24)) can be compared with Eq. (2.10) in the section about regularization. The constraint added to the minimization is the second order derivative of the temperature function T. So the smoothness

of the temperature function is guaranteed. The perturbation technique is applied again. A variation ΔJ of the functional J is obtained by perturbing the heat transfer coefficients h with Δh and the temperature T with ΔT. Then expression 2.24 modifies into an expression for $J + \Delta J$. By subtracting Eq. (2.24) from the expression for $J + \Delta J$ and neglecting second order terms (e.g. ΔT^2), an expression for ΔJ is found:

$$\Delta J\left[h(S_\mathrm{i})\right] = \int_{S_\mathrm{i}} 2\left[T_\mathrm{m}(S_\mathrm{i}) - Y_\mathrm{m}(S_\mathrm{i})\right]\Delta T(S_\mathrm{i})\delta(x-x_\mathrm{m})\delta(y-y_\mathrm{m})\delta(z-z_\mathrm{m})\mathrm{d}S_\mathrm{i} + \int_\Omega \left[\lambda(\Omega)\times\nabla^2\Delta T\right]\mathrm{d}\Omega \quad \text{in } \Omega(x,y,z) \text{ and } i = 1-7 \tag{2.25}$$

The domain integral in Eq. (2.25) can be reformulated using Green's second identity. Green's second identity for this domain states:

$$\int_\Omega \left[\lambda\nabla^2\Delta T - \Delta T\nabla^2\lambda\right]\mathrm{d}\Omega = \int_S \left[\lambda\frac{\partial\Delta T}{\partial n} - \Delta T\frac{\partial\lambda}{\partial n}\right]\mathrm{d}S \tag{2.26}$$

So a new expression for ΔJ is:

$$\Delta J\left[h(S_\mathrm{i})\right] = \int_{S_\mathrm{i}} 2\left[T_\mathrm{m}(S_\mathrm{i}) - Y_\mathrm{m}(S_\mathrm{i})\right]\Delta T(S_\mathrm{i})\delta(x-x_\mathrm{m})\delta(y-y_\mathrm{m})\delta(z-z_\mathrm{m})\mathrm{d}S_\mathrm{i} + \int_\Omega \left[\Delta T\nabla^2\lambda\right]\mathrm{d}\Omega + \int_{S_\mathrm{j}} \left[\lambda\frac{\partial\Delta T}{\partial n} - \Delta T\frac{\partial\lambda}{\partial n}\right]\mathrm{d}S_\mathrm{i} \quad \text{for } i = 1-7\,;\; j = 1-12 \tag{2.27}$$

If the sensitivity problem equation as well as its boundary conditions (2.18a-2.18e) are applied to the expression 2.27, and ΔJ is allowed to go to zero, then the adjoint problem formulation is obtained. The integrands containing ΔT vanished by using the sensitivity boundary conditions. The adjoint problem is used to determine the Lagrange multiplier $\lambda(\Omega)$:

$$\frac{\partial^2\lambda}{\partial x^2} + \frac{\partial^2\lambda}{\partial y^2} + \frac{\partial^2\lambda}{\partial z^2} = 0 \quad \text{in } \Omega(x,y,z) \tag{2.28a}$$

with the following boundary conditions:

$$-k\cdot\frac{\partial\lambda}{\partial n} = h(S_\mathrm{i})\lambda - 2k\left[T(S_\mathrm{i}) - Y(S_\mathrm{i})\right]\delta(x-x_\mathrm{m})\delta(y-y_\mathrm{m})\delta(z-z_\mathrm{m}) \quad \text{for } i = 1-7 \tag{2.28b}$$

$$-k \cdot \frac{\partial \lambda}{\partial n} = 0 \quad \text{on } S_{\mathrm{i}} (i = 9 - 12) \tag{2.28c}$$

$$-k \cdot \frac{\partial \lambda}{\partial n} = 0 \quad \text{on } S_8 \tag{2.28d}$$

$$-k \cdot \frac{\lambda_{\mathrm{fin}}}{\partial n} = -k \cdot \frac{\lambda_{\mathrm{primary}}}{\partial n} \quad \text{on } S_{13} \tag{2.28e}$$

The adjoint problem has also the form of a direct heat conduction problem and is solved with FLUENT. The results give $\lambda(\Omega)$. The boundary condition on the surfaces $S_1 - S_7$ is implemented in FLUENT as a heat flux boundary condition in which the heat flux is specified by a UDF equal to the right hand side of Eq. (2.28b). The constant heat flux boundary condition in the direct problem has become an adiabatic one in the adjoint problem. For the solution λ of the adjoint problem, the functional ΔJ (Eq. (2.27)) is evaluated. The following expression with integral terms is left:

$$\Delta J\,[h(S_{\mathrm{i}})] = \int_{S_{\mathrm{i}}} \frac{\lambda}{k}\,[T(S_{\mathrm{i}}) - T_\infty]\,\Delta h(S_{\mathrm{i}})\mathrm{d}S_{\mathrm{i}} \quad \text{for } i = 1 - 7 \tag{2.29}$$

From the definition [15], the functional increment ΔJ can also be written as:

$$\Delta J\,[h(S_{\mathrm{i}})] = \int_{S_{\mathrm{i}}} J'(S_{\mathrm{i}})\Delta h(S_{\mathrm{i}})\mathrm{d}S_{\mathrm{i}} \quad \text{for } i = 1 - 7 \tag{2.30}$$

By comparing Eq. (2.29) with Eq. (2.30), an expression for the gradient of the functional J is found:

$$J'\,[h(S_{\mathrm{i}})] = \frac{\lambda}{k}\,[T(S_{\mathrm{i}}) - T_\infty] \quad \text{for } i = 1 - 7 \tag{2.31}$$

As mentioned earlier, for SDM, the search direction is the gradient of the functional J, thus

$$P^n(S_{\mathrm{i}}) = J'^n(S_{\mathrm{i}}) \quad \text{for } i = 1 - 7$$

So, by solving the adjoint problem, a solution for the regularizing Lagrange multiplier $\lambda(\Omega)$ is found, which is used to determine the gradient J' of the functional and thus the search direction P^n.

2.4.2.3 Actual algorithm

So by solving the sensitivity and adjoint problem, step size β^n and search direction P^n are found. This means that the new convection coefficient $h^{n+1}(S_{\mathrm{i}})$ can be determined from the previous one with Eq.(2.32).

$$h^{n+1}(S_\mathrm{i}) = h^n(S_\mathrm{i}) - \beta^n P^n(S_\mathrm{i}) \quad \text{for } i = 1-7 \tag{2.32}$$

The estimated convection coefficients $h^n(S_\mathrm{i})$ are assumed accurate enough if the functional $J\left[h^n(S_\mathrm{i})\right]$ drops below a certain value ϵ. When temperature measurements from an experiment are used, the measurement data $Y_\mathrm{m}(S_\mathrm{i})$ will contain measurement errors. Therefore, the functional J is not expected to reach zero. For data containing measurement errors, the discrepancy principle is used as stopping criterion. If the standard deviation σ of the measurements is assumed to be a constant, a good convergence criterion is [116]:

$$J\left[h(S_\mathrm{i})\right] < M\sigma^2 \tag{2.33}$$

The algorithm can be summarized as follows, if the convection coefficients $h^n(S_\mathrm{i})$ are known, or an initial guess is made:

1. The direct problem (Eqs. 2.14 is solved with FLUENT with the estimated convection coefficients $h^n(S_\mathrm{i})$
2. The convergence criterion (Eq. (2.33)) is checked. If the stopping criterion is satisfied, $h^n(S_\mathrm{i})$ is the solution of the IHCP, otherwise the algorithm continues
3. The adjoint problem (Eq. (2.28) is solved with FLUENT to determine λ
4. J' is calculated with Eq. (2.31) and thus the search direction P^n
5. The variation of the convection coefficient $h(S_\mathrm{i})$ is $\Delta h = P^n$. With this Δh, the sensitivity problem is solved using FLUENT to obtain ΔT
6. β^n is calculated with ΔT according to Eq.(2.22).
7. A new $h^{n+1}(S_\mathrm{i})$ is computed with Eq. (2.32) and the algorithm restarts

2.4.2.4 Implementation SDM algorithm with FLUENT

No code has to be written to solve the direct conduction problems, because the commercial code FLUENT was used for this. However, it is not possible to implement an algorithm directly into FLUENT. Therefore the SDM algorithm is programmed in C. This program is able to communicate with FLUENT. This means that the program has to provide the necessary input data to solve the direct, sensitivity and adjoint problem. Subsequently, the necessary solution data needs to be transported back to the SDM algorithm program. The main program that controls the SDM algorithm communicates with FLUENT through journal files. These are text files in which the actions that have to be performed in FLUENT are written one by one. These journal files are written by the main program. There is only one

journal file for each iteration of the algorithm. Thus FLUENT is addressed only once during an iteration of the SDM algorithm. The direct, adjoint and sensitivity problem are solved successively in FLUENT. Intermediary calculations, such as Eq.(2.31) for the search direction P^n after the adjoint problem and Eq. (2.22) for the step size after the sensitivity problem, are executed in FLUENT by using UDFs. These UDFs are also written in C and initialized in FLUENT using the journal files. So at the end of one iteration, new convection coefficients $h^{n+1}(S_\mathrm{i})$ are determined by using UDFs in FLUENT. The new $h^{n+1}(S_\mathrm{i})$ is also written to an UDF, which can be accessed again by FLUENT in the next iteration. After each iteration, all the data present in the FLUENT calculation is also written to a FLUENT data file, so it can still be accessed once the algorithm has finished. So the code consists of the following:

- The main program: this controls the iterations of the algorithms, makes journal files and opens and closes FLUENT
- Journal files: these control the operations executed in FLUENT, step by step. The journal files are generated by the main program
- FLUENT 6.2.16: solves the actual three direct conduction problems and intermediate calculations of the SDM algorithm in the following order: the direct problem, stopping criterion value, adjoint problem, search direction P^n, sensitivity problem, step size β, new value $h^{n+1}(S_\mathrm{i})$.
- UDF file: in this file, all the UDFs are programmed that FLUENT needs to perform the calculations of the SDM algorithm

2.4.3 Conjugate Gradient algorithm

The CGM algorithm works in the same way as the SDM. The CGM was also used by Huang, but for transient IHCPs [111]. The sensitivity, adjoint and direct problem are exactly the same as for the SDM. The only difference between CGM and SDM lies in the determination of the search direction P^n. The search direction is not the gradient of the functional J anymore, as for the SDM. Now the search direction is a conjugate of the gradient direction of functional J at the current iteration n and the search direction P^{n-1} of the previous iteration n-1. There is a relative weight between both terms of the search direction, indicated by the conjugate coefficient γ^n.

$$P^n(S_\mathrm{i}) = J'^n(S_\mathrm{i}) + \gamma^n P^{n-1}(S_\mathrm{i}) \quad \text{for } i = 1-7 \tag{2.34}$$

The conjugate coefficient is defined as:

$$\gamma^n = \frac{\int_{S_\mathrm{i}} \left(J'^n\right)^2 \mathrm{d}S_\mathrm{i}}{\int_{S_\mathrm{i}} \left(J'^{n-1}\right)^2 \mathrm{d}S_\mathrm{i}} \quad \text{for } i = 1-7 \tag{2.35}$$

and

$$\gamma^0 = 0$$

The determination of the new search direction P^n depends also on the previous iteration, which was not the case for the SDM. Note that for $\gamma^n = 0$ the search direction becomes the gradient direction J' again, thus the SDM is obtained again. The conjugate search direction should cause a faster convergence to the solution of the CGM. The CGM always converges, as was guaranteed by Lasdon et al. [117]. It is assumed that CGM always converges. This assumption was based on the solution of some numerical experiments using the CGM solution method with different initial values. The CGM converged and gave the same results for different initial values. The search direction P^n of the CGM is found by determining the gradient direction J'^n and keeping the gradient direction of the previous iteration P^{n-1}. Also, the step size β^n is found in the exact same way as for the SDM. Thus the CGM algorithm can be implemented the same as the SDM if the calculation for the search direction P^n is adjusted.

2.4.4 SDM and CGM for heat flux estimation

Instead of estimating the heat transfer coefficients $h(S_\mathrm{i})$ on surfaces $S_1 - S_7$ (Fig. 2.14), it is also possible to estimate the heat fluxes $q(S_\mathrm{i})$ on $S_1 - S_7$. This means that now a new heat flux $q^{n+1}(S_\mathrm{i})$ will be determined from the previous one with the iterative equation (Eq.(2.36)):

$$q^{n+1}(S_\mathrm{i}) = q^n(S_\mathrm{i}) - \beta^n P^n(S_\mathrm{i}) \quad \text{for } i = 1-7 \tag{2.36}$$

The search step β^n is still determined from ΔT after the sensitivity problem is solved, and the search direction $P^n(S_\mathrm{i})$ from the adjoint problem. However, the direct, sensitivity and adjoint problem are changed in the boundary conditions. They are now reformulated, at least for the boundary conditions on surface $S_1 - S_7$. These boundary conditions are for the heat flux condition:

- For the direct problem:

$$-k \cdot \frac{\partial T}{\partial n} = q(S_\mathrm{i}) \quad \text{on } S_\mathrm{i} (i = 1-7) \tag{2.37}$$

- For the sensitivity problem:

$$-k \cdot \frac{\partial \Delta T}{\partial n} = \Delta q \quad \text{on } S_\mathrm{i} (i = 1-7) \tag{2.38}$$

- For the adjoint problem:

$$-k\cdot\frac{\partial\lambda}{\partial n} = -2k\left[T(S_\mathrm{i}) - Y(S_\mathrm{i})\right]\delta(x-x_\mathrm{m})\delta(y-y_\mathrm{m})\delta(z-z_\mathrm{m}) \;\text{ on } S_\mathrm{i}(i = 1-7) \tag{2.39}$$

As the step size β^n is calculated from the solution ΔT of the sensitivity equation, nothing changes for the formulation of the step size:

$$\beta^n = \frac{\sum_{i=1}^{7}\sum_{m=1}^{M_\mathrm{i}}\left[T_\mathrm{m}\left(S_\mathrm{i};h^n\right) - Y_\mathrm{m}(S_\mathrm{i})\right]\Delta T_\mathrm{m}(S_\mathrm{i})}{\sum_{i=1}^{7}\sum_{m=1}^{M_\mathrm{i}}\left[\Delta T_\mathrm{m}\left(S_\mathrm{i};h^n\right)\right]^2}$$

However, the determination of the gradient of the functional, $J'\left[q(S_\mathrm{i})\right]$ is changed. This could be expected because the boundary condition of sensitivity and adjoint problem on surface $S_1 - S_7$ have changed. The variation ΔJ of the functional is still defined by Eq. (2.25), but the change of the boundary conditions caused the term which remains in ΔJ after solving the adjoint problem to change. The expression that remains for ΔJ is:

$$\Delta J\left[q(S_\mathrm{i})\right] = \int_{S_\mathrm{i}} -\frac{\lambda}{k}\Delta q(S_\mathrm{i})\mathrm{d}S_\mathrm{i} \;\text{ for } i = 1-7 \tag{2.40}$$

Again, with:

$$\Delta J\left[q(S_\mathrm{i})\right] = \int_{S_\mathrm{i}} J'(S_\mathrm{i})\Delta q(S_\mathrm{i})\mathrm{d}S_\mathrm{i} \;\text{ for } i = 1-7 \tag{2.41}$$

the expression for the gradient of the functional J becomes:

$$J'\left[q(S_\mathrm{i})\right] = -\frac{\lambda(S_\mathrm{i})}{k} \;\text{ for } i = 1-7 \tag{2.42}$$

2.4.5 IHCP for thermal resistance estimation

An IHCP cannot only be used to estimate heat fluxes or heat transfer coefficients on boundary surfaces from measured temperature values on these boundary surfaces. As mentioned in the literature survey, heat generation rates, temperatures and thermal properties can also be estimated, and this for boundary surfaces as well as internal points. Besides this, a thermal contact resistance R can also be estimated [118]. A thermal contact resistance occurs at the interface between two solid bodies, such as at the contact surface S_{13} between the fin base and the primary surface (Fig. 2.14 and Fig.2.15). If the fin and primary surface are made as one entity, there is no contact resistance at S_{13} and the boundary condition at S_{13} is formulated as continuous in heat flux and temperature (Eq.(2.14e)). However, if the fin and primary surface are separate entitities that are connected to each other (e.g. by welding, thermal paste,...) there is a contact resistance R introduced at S_{13}, even if the fin and primary surface are made of the same material. The heat

flux remains constant at the thermal resistance surface, but there is a discontinuity in temperature over the contact surface S_{13}. In the following equations, the subscript $l = 1$ refers to the primary surface side of the contact surface, and $l = 2$ to the fin side (Fig. 2.15). The following direct conduction problem is considered:

- surfaces $S_1 - S_7$ are cooled by convection with a convective heat transfer coefficient $h(S_\mathrm{i})$
- a constant heat flux q_0 is imposed at surface S_8
- surfaces $S_9 - S_{12}$ are adiabatic
- there is a thermal contact resistance $R(S_{13})$ at surface S_{13}

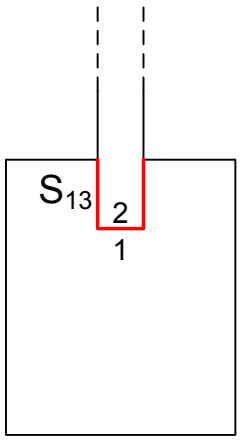

Figure 2.15: The contact resistance surface S_{13} between fin base and primary surface

This direct problem is formulated as:

$$\frac{\partial^2 T}{\partial x^2} + \frac{\partial^2 T}{\partial y^2} + \frac{\partial^2 T}{\partial z^2} = 0 \quad \text{in } \Omega(x, y, z) \tag{2.43a}$$

with the following boundary conditions:

$$-k \cdot \frac{\partial T}{\partial n} = h(S_\mathrm{i}) \cdot (T - T_\infty) \quad \text{on } S_\mathrm{i}(i = 1 - 7) \tag{2.43b}$$

$$-k \cdot \frac{\partial T}{\partial n} = 0 \quad \text{on } S_\mathrm{i}(i = 9 - 12) \tag{2.43c}$$

$$-k \cdot \frac{\partial T}{\partial n} = q_0 \quad \text{on } S_8 \tag{2.43d}$$

$$-k \cdot \frac{\partial T_1}{\partial n} = -k \cdot \frac{\partial T_2}{\partial n} \quad \text{on } S_{13} \tag{2.43e}$$

$$-k \cdot \frac{\partial T_1}{\partial n} = \frac{T_1 - T_2}{R(S_{13})} \quad \text{on } S_{13} \tag{2.43f}$$

Previously, the heat transfer coefficients $h(S_\mathrm{i})$ on $S_1 - S_7$ were assumed unknown and were estimated solving the IHCP. In this case, the heat transfer coefficients $h(S_\mathrm{i})$ are known, but the thermal contact resistance $R(S_{13})$ has to be estimated, thus the IHCP is solved for $R(S_{13})$. The estimation of $R(S_{13})$ is based on temperature measurements on surfaces $S_1 - S_7$. In this IHCP, the estimates are not situated on the same surfaces as the temperature measurements. Although the estimated parameter is situated on another surface than $S_1 - S_7$, the minimization functional J for the solution of the IHCP remains the same as previously defined (see section 2.4.2):

$$J\left[R(S_{13})\right] = \sum_{i=1}^{7} \sum_{m=1}^{M_\mathrm{i}} \left[T_\mathrm{m}(S_\mathrm{i}) - Y_\mathrm{m}(S_\mathrm{i})\right]^2 \tag{2.44}$$

The IHCP is solved in the same way as previously done for the heat transfer coefficient estimation: a new thermal resistance $R^{n+1}(S_{13})$ is determined from the previous one with the iterative equation (Eq.(2.45)):

$$R^{n+1}(S_{13}) = R^n(S_{13}) - \beta^n P^n(S_{13}) \tag{2.45}$$

The search step β^n is still determined from ΔT after the sensitivity problem is solved, and the search direction $P^n(S_{13})$ from the adjoint problem. The sensitivity and adjoint problem are changed in the boundary conditions. They are now reformulated, at least for the boundary conditions on surfaces $S_1 - S_7$ and S_{13}. These boundary conditions are for the sensitivity problem (constructed from the perturbation of the thermal resistance $R(S_{13})$ with ΔR, and consequently T with ΔT):

$$-k \cdot \frac{\partial \Delta T}{\partial n} = h(S_\mathrm{i})\Delta T \quad \text{on } S_\mathrm{i}(i = 1 - 7) \tag{2.46}$$

$$-k \cdot \frac{\partial \Delta T_1}{\partial n} = -k \cdot \frac{\partial \Delta T_2}{\partial n} \quad \text{on } S_{13} \tag{2.47}$$

$$\begin{aligned} -k \cdot \frac{\partial \Delta T_1}{\partial n} &= \frac{(T_1 + \Delta T_1) - (T_2 + \Delta T_2)}{R(S_{13}) + \Delta R} \\ &= \frac{\Delta T_1 - \Delta T_2}{R(S_{13})} - \Delta R \cdot \frac{T_1 - T_2}{R^2(S_{13})} \quad \text{on } S_{13} \end{aligned} \tag{2.48}$$

In Eq.(2.48) the Taylor expansion of $1/(R+\Delta R)$ is used.

The adjoint problem is constructed the same way as in section 2.4.2.2, using the Lagrange multiplier λ and Green's second identity. The adjusted boundary conditions for the adjoint problem are:

$$-k\cdot\frac{\partial\lambda}{\partial n} = h\cdot\lambda - 2k\left[T(S_\mathrm{i}) - Y(S_\mathrm{i})\right]\delta(x-x_\mathrm{m})\delta(y-y_\mathrm{m})\delta(z-z_\mathrm{m}) \quad \text{on } S_\mathrm{i}(i=1-7) \tag{2.49}$$

$$-k\cdot\frac{\partial\lambda_1}{\partial n} = -k\cdot\frac{\partial\lambda_2}{\partial n} \quad \text{on } S_{13} \tag{2.50}$$

$$-k\cdot\frac{\partial\lambda_1}{\partial n} = \frac{\lambda_1-\lambda_2}{R(S_{13})} \quad \text{on } S_{13} \tag{2.51}$$

The step size β^n is calculated from the solution ΔT of the sensitivity equation. Nothing changes for the formulation of the step size:

$$\beta^n = \frac{\sum_{i=1}^{7}\sum_{m=1}^{M_\mathrm{i}}\left[T_\mathrm{m}\left(S_\mathrm{i};h^n\right) - Y_\mathrm{m}(S_\mathrm{i})\right]\Delta T_\mathrm{m}(S_\mathrm{i})}{\sum_{i=1}^{7}\sum_{m=1}^{M_\mathrm{i}}\left[\Delta T_\mathrm{m}\left(S_\mathrm{i};h^n\right)\right]^2}$$

The determination of the gradient of the functional (and thus the search direction), $J'\left[R(S_{13})\right]$ is different, because this is determined at the surface S_{13} on which the contact resistance is estimated and depends on this estimated value. The expression that remains for the variation ΔJ of the functional, after solving the adjoint problem, is:

$$\Delta J\left[R(S_{13})\right] = \int_{S_{13}}\frac{\Delta R}{R^2(S_{13})}\frac{\lambda_1-\lambda_2}{k}\cdot(T_1-T_2)\mathrm{d}S_{13} \tag{2.52}$$

and with:

$$\Delta J\left[R(S_{13})\right] = \int_{S_{13}} J'(S_{13})\Delta R(S_{13})\mathrm{d}S_{13} \tag{2.53}$$

the expression for the gradient of the functional J becomes:

$$J'\left[R(S_{13})\right] = \frac{1}{R^2(S_{13})}\frac{\lambda_1-\lambda_2}{k}\cdot(T_1-T_2) \tag{2.54}$$

The calculation of the search direction P^n from J' depends on whether CGM (Eq.(2.34)) or SDM (Eq.(2.16) is used. The description of the solution algorithm in section 2.4.2.3 applies also to this IHCP.

A thermal contact resistance cannot be set as an input in FLUENT. A contact resistance can be defined as:

$$R = \frac{d}{k} \tag{2.55}$$

with d the thickness of contact interface and k the thermal conductivity of the interface material. In order to simulate a spatial varying contact resistance in FLUENT, the thermal conductivity is made spatially variable using a UDF while the interface thickness is kept constant.

3
Numerical Results

The two developed solution methods, CGM and SDM, from Chapter 2 are applied to various numerical test cases in this chapter. Four different cases of local heat transfer coefficients are studied for a rectangular longitudinal fin: an uniform heat transfer coefficient, a linearly varying profile along the fin length, a linearly varying profile along the fin height and an exponentially varying profile along the fin length. These cases are studied for different temperature measurement accuracies: exact temperatures (no temperature error), a temperature measurement error of 0.1°C and a temperature error of 0.5°C. The accuracy of both methods is examined, as is the convergence rate. Based on these results, the best of both methods is chosen. Finally, this method is also applied to a numerical test case for the estimation of a thermal contact resistance.

3.1 SDM vs CGM

The accuracy and validity of the SDM and CGM are checked for the model of fin and primary surfaces (Fig. 2.14). To this end a numerical experiment is executed. This means that the temperatures $Y_m(S_i)$ on boundary surface S_1 – S_7 are not experimentally measured, but are replaced with numerically simulated temperatures. The simulated temperatures are obtained by solving the direct heat conduction problem (Eq. (2.14)) with a given convection coefficient profile on surfaces $S_1 - S_7$. These temperatures are denoted as $Y_{m,ex}$. For the comparison between the SDM and CGM, the influence of the measurement error is also taken into account.

The comparison is done for three different measurement errors:

- dY_m = 0°C: it is assumed that there are no measurement errors on the simulated temperatures.
- dY_m = 0.1°C: there is a random error added to the exact simulated temperatures. Random values from the normal distribution around zero with a standard deviation of $\sigma = \frac{dY_m}{2}$ are generated and added to $Y_{m,ex}$
- dY_m = 0.5°C: these temperatures are constructed in the same way as for dY_m = 0.1°C

The comparison between SDM and CGM is made for four different convection coefficient profiles, with varying complexity. The comparison is based on two criteria:

- accuracy of the solution
- convergence speed

The numerical grid for the model consists of 247500 cells. The number of cells on the fin side is equal to the number of pixels (thus measurement points) of the thermographic camera, which will be used later on in the actual experiments. This means that each cell corresponds to a pixel or measurement point. On the seven surfaces together, there are 61750 measurement points (=M in Eq. (2.13)). The large amount of measurement points can cause long calculation times before convergence is obtained.

3.1.1 Uniform heat transfer coefficient

A uniform heat transfer coefficient of $h(S_i)$ = 40 $\mathrm{W/m^2K}$ on surface $S_1 - S_7$ was set as boundary condition for the numerical experiment. The boundary conditions on the other surfaces were set as described in the direct heat conduction problem (Eq. (2.14)). The heat flux q_0 at surface S_8 is set at 2000 $\mathrm{W/m^2}$. The temperature field at surface $S_1 - S_7$ obtained by solving this direct heat conduction problem is used as exact measurements $Y_{m,ex}$. This temperature field is shown in Fig. 3.1. This figure shows a three-dimensional view of the studied fin and primary surface, on which four evaluation lines are added. These lines are used to allow for a more detailed evaluation and interpretation of the results. Plots of the estimated heat transfer coefficients and the associated relative error along these lines give a more detailed view on the accuracy of both SDM and CGM. The location of these lines is (Fig. 3.1):

- L_1: at the front surface S_5 along the length of the fin, halfway the height of the fin (z = 0.072 m)

- L_2: at the primary surface S_7 along the length of the fin, halfway the thickness of the primary surface (y = -0.005 m)
- L_3: at the front surface S_5 along the height of the fin, halfway the length (x = 0.125 m)
- L_4: at the primary surface S_7 along the thickness of the fin, halfway the length (x = 0.125 m)

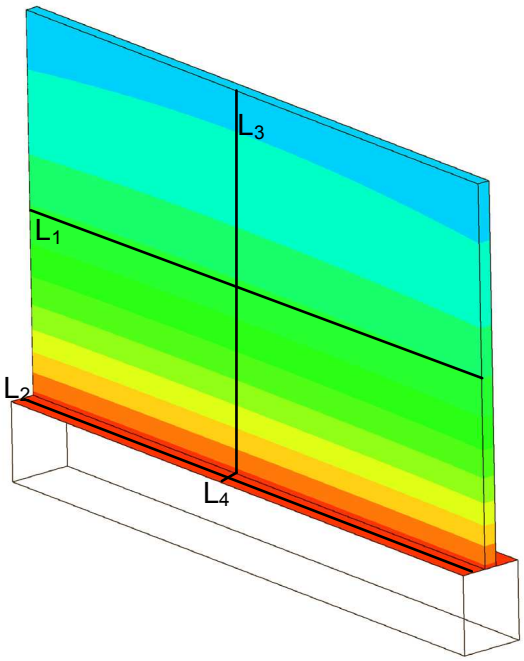

Figure 3.1: Three-dimensional plot of the exact temperature field for a constant convection coefficient h = 40 $\mathrm{W/m^2K}$, and the four evaluation lines in the model

Next to these line plots, the results are also shown in two-dimensional color plots, which give a good global overview of the results on the different surfaces for the IHCP solution. They can be used to indicate critical areas in the model i.e. where large errors occur. These 2-D plots show the front surface S_5 of the fin and a top view of the primary surfaces S_6 – S_7 and the fin tip surface S_1. The only surfaces that cannot be seen on these plots are the back surface S_4 of the fin, and the side surface S_2 – S_3. However, the back surface has the exact same result as the front surface, due to symmetry, and it was found that the side surfaces are an extension of the conditions at the edges of the front surface. The resulting 2D plot

of the simulated exact temperatures $Y_{m,ex}$ is shown in Fig. 3.2. In the following discussion, the exact value of the heat transfer coefficient $h(S_i)$ on S_1 – S_7 is denoted as h_i and the estimated value is denoted as $\tilde{h}_i$. Note also that all 2D-plots of relative errors are dimensionless, thus not in percentage.

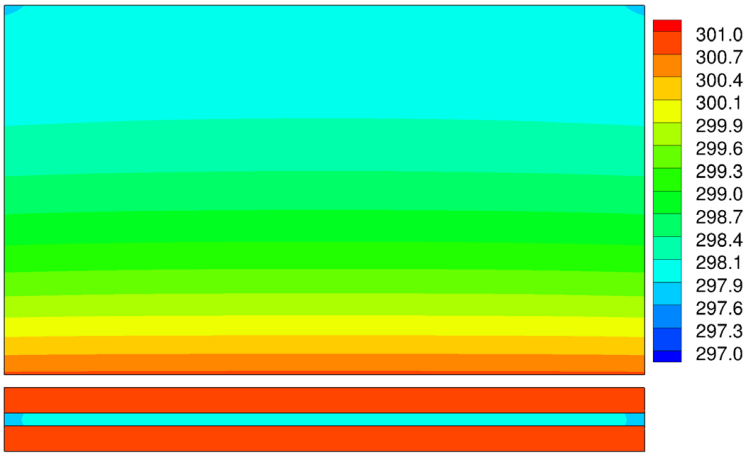

Figure 3.2: Two-dimensional plot of the exact temperature field for a constant convection coefficient h = 40 $\mathrm{W/m^2K}$

3.1.1.1 Exact measurement data: σ=0

Since the measured temperatures are assumed errorless, σ is zero in the stopping criterion (Eq. (2.33)). This means that the iterative solution algorithms of SDM and CGM only have to stop when the function J (Eq. (2.13)) attains complete zero. Of course, this will never happen. Therefore the convergence criterion is set at $\chi = 0.01$. A convergence criterion of 0.01 means that the mean error on each temperature measurement point is $8 \cdot 10^{-4}$ (from Eq.(2.33)). This is far beyond the accuracy of any temperature measurement apparatus. The convergence of SDM and CGM are plotted in Fig.3.3. CGM converges much faster than the SDM. CGM drops below the stopping criterion after 25 iterations, SDM needs 86 iterations. During the first ten steps, the convergence rate of SDM and CGM is very alike, but CGM keeps converging fast while SDM converges much slower when the functional J approaches the stopping criterion (Fig. 3.3). Both algorithms give good results in reconstructing the uniform local convection coefficient h_i = 40$\mathrm{W/m^2K}$. The values of the estimated $\tilde{h}_i$ are situated between 39 and 41$\mathrm{W/m^2K}$ (Fig. 3.4).

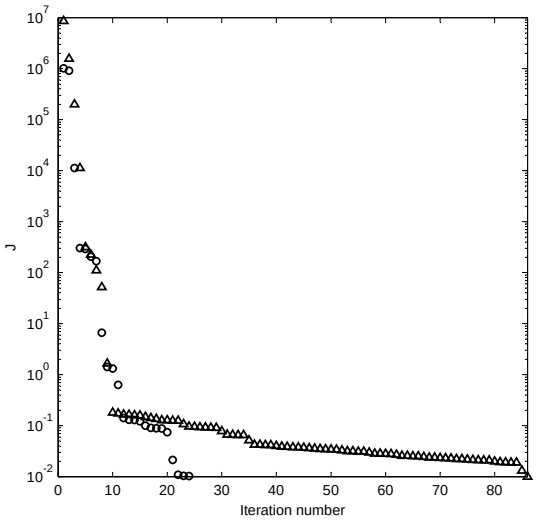

Figure 3.3: Convergency of SDM (Δ) and CGM ($\circ$) for uniform value of h = 40 $\mathrm{W/m^2K}$ for σ=0K for $Y_m(S_i)$

The relative error on $\tilde{h}_i$ is plotted in Fig. 3.5 and Fig. 3.6. It is obvious that $\tilde{h}_i$ contains a wiggle along the fin height: alternating areas of positive and negative relative errors on h_i. The largest error is attained on the primary surfaces S_6 – S_7, but it is still smaller than 1% for the CGM and 1.4% for the SDM. For the SDM, the error on the fin near the base is 0.8%, and it decreases quickly to -0.8% along the height, and then slowly increases to an error of 0.2% and ends at an error of 0.1% near the tip. For CGM, it fluctuates from 0.4% to -0.8% and then back to 0.4% to finish at -0.2% at the fin tip (Fig. 3.6(b)). So it seems that the error on $\tilde{h}_i$ follows a damped sinusoidal variation along the height of the fin. This fluctuation only appears along the fin height (Fig. 3.6(a)). The larger error on $\tilde{h}_i$ at the primary surface is a consequence of the difference in amount of measurement points on fin and primary surface: 57000 on the fin and 4400 on the primary surface. SDM and CGM are whole-domain solution methods: this means that all the components of the unknown heat transfer coefficients are estimated at once. Hence the calculation of the search step size and direction for each unknown, and thus the new $\tilde{h}_i$, is based on all previous estimates in the domain. The number of estimates on the fin (57000) dominates the estimates on the primary surface (4400) and thus the determination of the new search step size and direction. The temperature at the base is always higher than the fin temperature, but due to the dominance of the $\tilde{h}_i$ on the fin, a whole domain method has difficulties to accurately estimate the

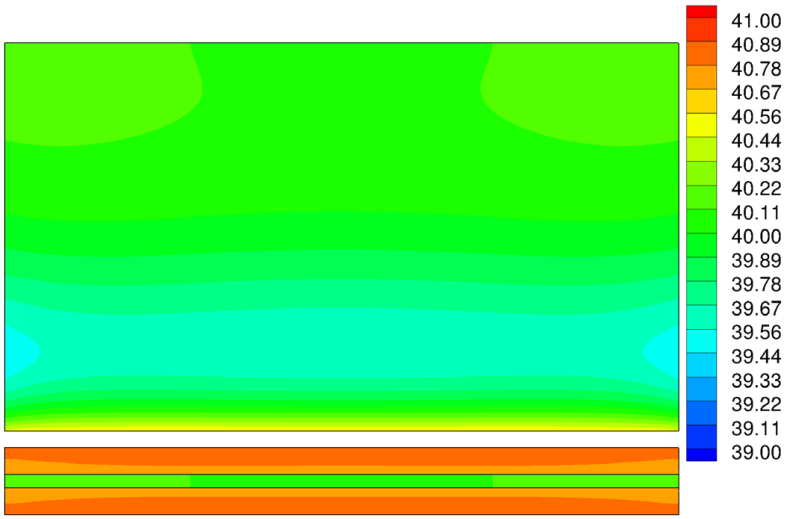

(a)

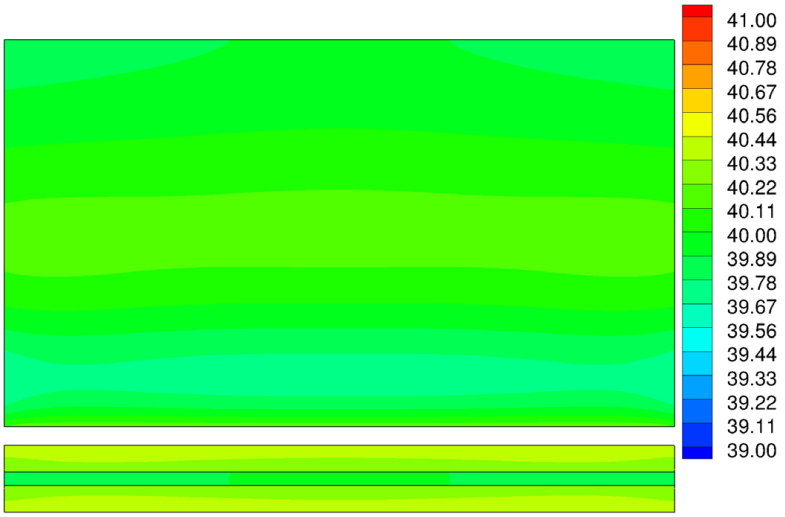

(b)

Figure 3.4: 2-D plot of the estimated $\tilde{h}_i$ (in $\mathrm{W/m^2K}$) from solving the IHCP for an exact uniform value of h = 40 $\mathrm{W/m^2K}$. (a) SDM solution ; (b) CGM solution

$\tilde{h}_i$ on the primary surface. The smoothness of the profile was guaranteed by the addition of regularization to CGM and SDM. The error near the bottom of the fin is flattened out to the top by this smoothness.

The fluctuation of $\tilde{h}_i$ round the exact h_i indicates that the average value of the estimated $\tilde{h}$ has a much smaller error than the local $\tilde{h}_i$. The average value $\tilde{h}_{avg}$ is calculated as:

$$\tilde{h}_{avg} = \frac{\left[\sum_{i=1}^{M} \tilde{h}_i\right]}{M} \tag{3.1}$$

in which M is the number of measurement cells on the boundary surfaces. If the average is taken for one surface only, M is the number of cells on that surface, otherwise M is the amount of cells on all seven surface $S_1 - S_7$ together, i.e. 61750. In the same way, the average exact value h_{avg} is calculated. The relative error on $\tilde{h}_{avg}$ compared to the exact average heat transfer coefficient h_{avg} is also calculated and denoted as $ERRh$. The mean values $\tilde{h}_{avg}$ and ERRh for the fin tip S_1, surface S_5, and primary surface S_7 are listed in Table 3.1, for both SDM and CGM. These mean values have very small, negligible errors, which means that despite some larger errors on the local heat transfer coefficients h_i, the fluctuation on these errors results in a mean value which is very accurate. As expected from the local $\tilde{h}_i$, the largest error occurs at the primary surfaces, and is considerably higher for SDM. An accurate average heat transfer coefficient estimation indicates an accurate fin effectiveness estimation. The results for fin effectiveness will be discussed later.

	SDM		CGM	
	$\tilde{h}_{avg}$ ($\mathrm{W/m^2K}$)	ERRh (%)	$\tilde{h}_{avg}$ ($\mathrm{W/m^2K}$)	ERRh (%)
Fin tip S_1	40.12	0.29	39.87	-0.32
Front S_5	39.9	-0.15	39.93	-0.05
Primary S_6	40.22	1.97	39.77	0.81

Table 3.1: The average values $\tilde{h}_{avg}$ and ERRh for the IHCP solution for an uniform value of h = 40 $\mathrm{W/m^2K}$ with σ=0K

Notice from Fig. 3.6(b) that the SDM solution is a more damped sinusoid than the CGM solution, which has a higher frequency and higher amplitudes. However, CGM swirls closer around the exact solution and hence it gives better average values. Figure 3.7 shows the results for SDM and CGM after 10 iterations. The solution has not converged yet but has already obtained a low value for the functional J, i.e. J=1. One can notice that the relative errors on the local $\tilde{h}_i$ are still large, and compared to the converged solution the estimated value round the exact solution has a lower frequency, but a much higher amplitude, thus larger relative error. So, by converging further, the amplitude of the sinusoidal (i.e. the error) decreases, but the frequency increases.

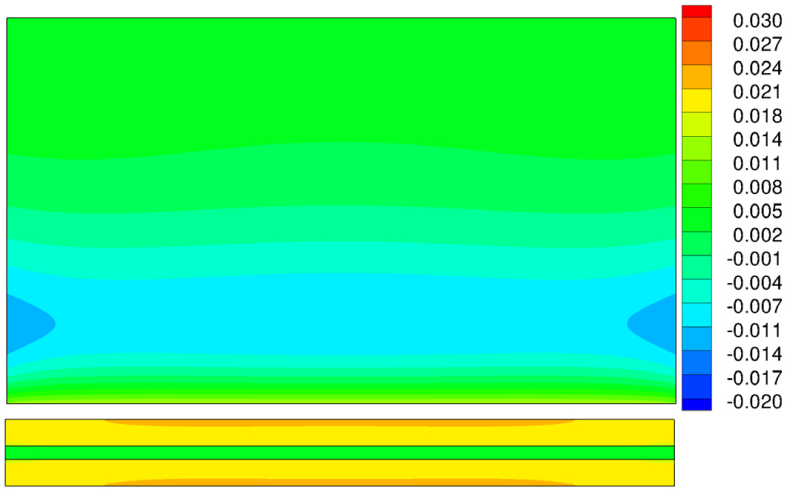

(a)

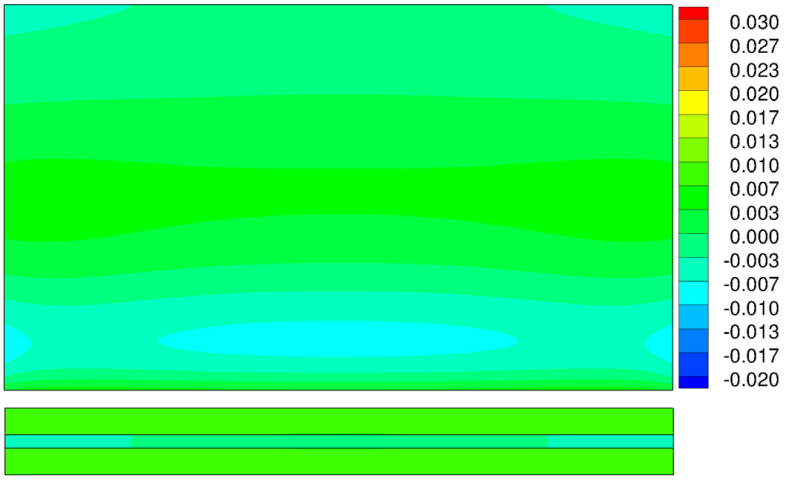

(b)

Figure 3.5: 2-D plot of the relative error on the estimated $\tilde{h}_i$ from solving the IHCP for an exact uniform value of h = 40 $\mathrm{W/m^2K}$. (a) SDM solution ; (b) CGM solution

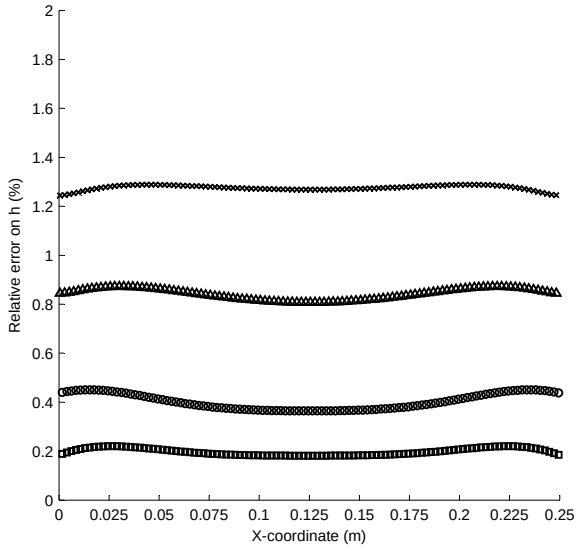

(a) □: SDM at L_1 ; ○: CGM at L_1 ; ×: SDM at L_2 ; Δ: CGM at L_2

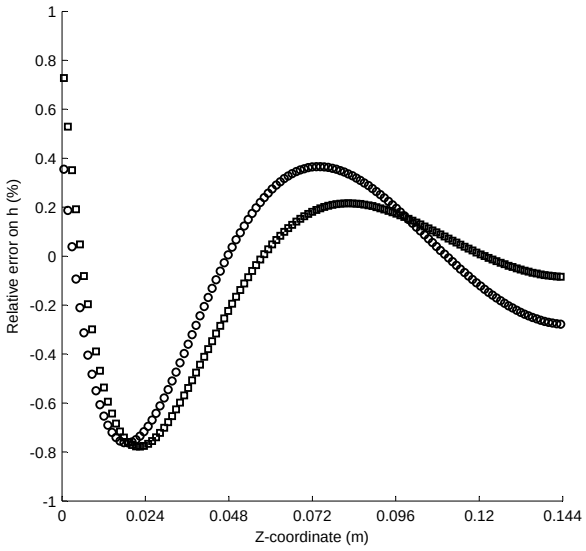

(b) □: SDM at L_3 ; ○: CGM at L_3

Figure 3.6: Relative error on $\tilde{h}_i$ for an uniform value of h = 40 $\mathrm{W/m^2K}$ with σ=0K, plotted along the evaluation lines $L_1 - L_3$.

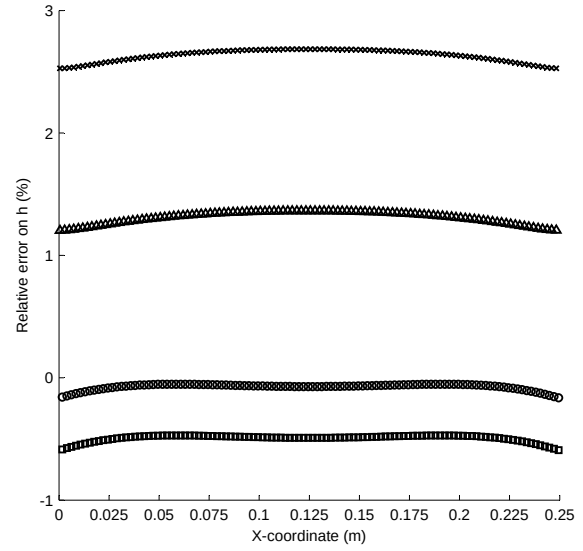

(a) □: SDM at L_1 ; ○: CGM at L_1 ; ×: SDM at L_2 ; △: CGM at L_2

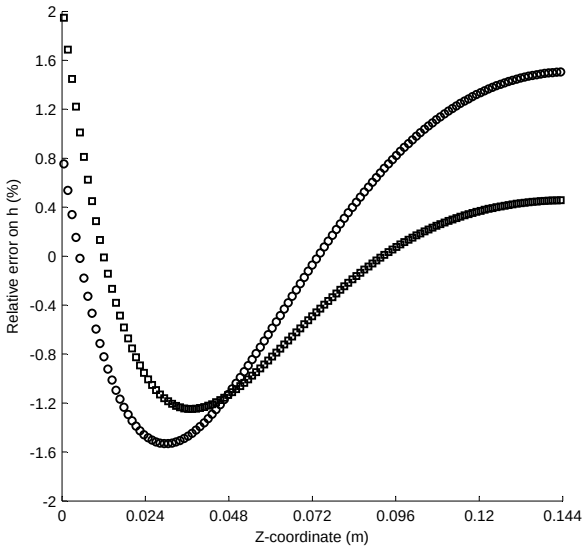

(b) □: SDM at L_3 ; ○: CGM at L_3

Figure 3.7: Relative error on $\tilde{h}_i$ after 10 iterations for an uniform value of h = 40 $\mathrm{W/m^2K}$ with σ=0K, plotted along evaluation lines $L_1 - L_3$

The estimated temperature values are very accurate: the relative errors are smaller than $3 \cdot 10^{-4}$ %. These errors are comparable for SDM and CGM.

3.1.1.2 Temperature measurement error: $dY_m = 0.1K$ or σ=0.05

The measured temperature field $Y_m S_i$ with an accuracy of 0.1°C is plotted in Fig.3.8 to show the change of the temperature field: the imposed temperature error gives a more erratic pattern. The measured temperatures have an accuracy of 0.1°C, which means a standard deviation σ = 0.05°C, and thus the convergence criterion (Eq. (2.33)) becomes χ = 154. The addition of noise to the measured temperature data $Y_m(S_i)$ will cause larger errors for $\tilde{h}_i$, and it could cause non-physical solutions. Therefore, the regularization was applied in the solution procedure of SDM and CGM. The regularization parameter is the stopping criterion. So by stopping the iterations on time, it is prevented that the regularization term becomes too important, and reduces the accuracy of the solution. Both SDM and CGM converge after 10 iterations.

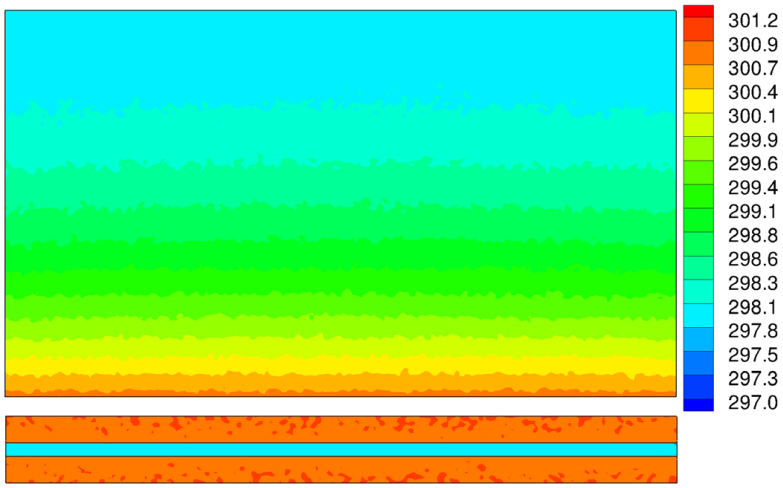

Figure 3.8: 2-D plot of measured temperatures $Y_m(S_i)$ (in K) with σ=0.05K for the numerical experiment with a uniform heat transfer coefficient profile

Plots of $\tilde{h}_i$ show no extra useful information compared to the plots of the relative errors, therefore the results are discussed for the plots on the relative error on $\tilde{h}_i$ (Figures 3.9-3.11). Both algorithms give good results in reconstructing the uniform local convection coefficient h_i. The values of the estimated $\tilde{h}_i$ are still situated between 39 and 41 $\mathrm{W/m^2K}$. The wiggle $\tilde{h}_i$ along the fin height has reduced

, due to the increase in the stopping criterion (Fig. 3.10(b)). The frequency of the wiggle has dropped, but this resulted in a larger amplitude, and thus larger error. The wiggle for the relative error along the fin height varies between 1.5% and -1%, with the largest error at the fin base. The error is even larger at the primary surface (2.8% for the SDM, and 2.6% for the CGM) (Figures 3.10 - 3.11). Again, it seems as if areas of positive and negative relative errors will compensate each other to attain a more precise mean value for $\tilde{h}_{avg}$.

The temperature is reconstructed very accurately with both methods: the largest relative error on the temperature values is 0.06%.

The mean values $\tilde{h}_{avg}$ and the error ERRh on $\tilde{h}_{avg}$ are listed in Table 3.2 for both SDM and CGM for various surfaces. These mean values are still accurate, but the error has increased compared to the case without noise, especially on the primary surface. The mean error on $\tilde{h}_{avg}$ for the primary surface is larger than 2%, and results in an overestimation of heat transfer through the primary surface. This will have consequences for the determination of the fin effectiveness. However, ERRh on the fin surfaces S_1 – S_5 is much smaller. As the total surface area of the primary surface is only 7% of the fin surface area, the accuracy of the heat dissipated in the fin will dominate the accuracy of the fin effectiveness. The results for fin effectiveness are listed and discussed at the end of this chapter. All these errors remain very small and have only a small influence on the heat transfer distribution. An evaluation of the influence of these errors on the determination of the fin effectiveness is made later in this chapter. CGM and SDM give comparable results, but as in the previous case with σ = 0K, the CGM solution is a bit more accurate.

	SDM		CGM	
	$\tilde{h}_{avg}$ ($\mathrm{W/m^2K}$)	ERRh (%)	$\tilde{h}_{avg}$ ($\mathrm{W/m^2K}$)	ERRh (%)
Fin tip S_1	40.21	0.52	40.24	-0.59
Front S_5	39.87	-0.22	39.88	-0.18
Primary S_6	40.47	2.58	40.38	2.35

Table 3.2: The average values for $\tilde{h}$ and ERRh for an uniform value of h = 40 $\mathrm{W/m^2K}$with σ=0.05K

3.1.1.3 Temperature measurement error: dY_m = 0.5°C or σ=0.25

The imposed temperatures have an accuracy of 0.5°C, which means a standard deviation σ = 0.25°C, and thus the convergence criterion (Eq. (2.33)) becomes considerably larger: χ = 3859. Both methods have comparable convergence speed: SDM converges after 9 iterations, CGM after 12 iterations. The measured temperature field $Y_m(S_i)$ becomes very erratic for this measurement error (Fig. 3.12).

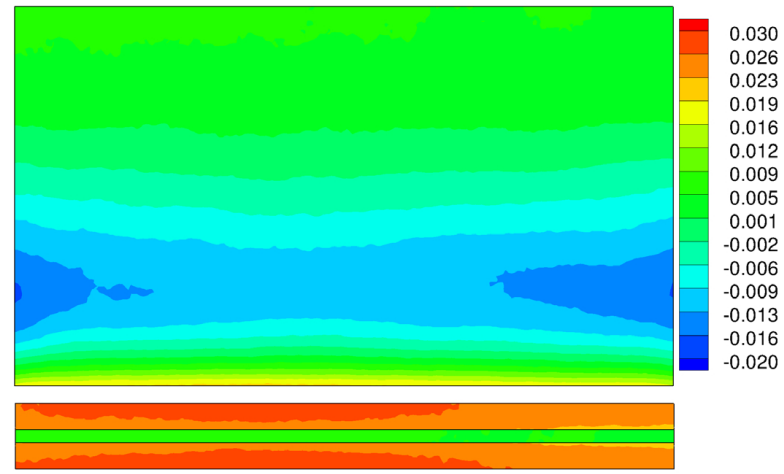

(a)

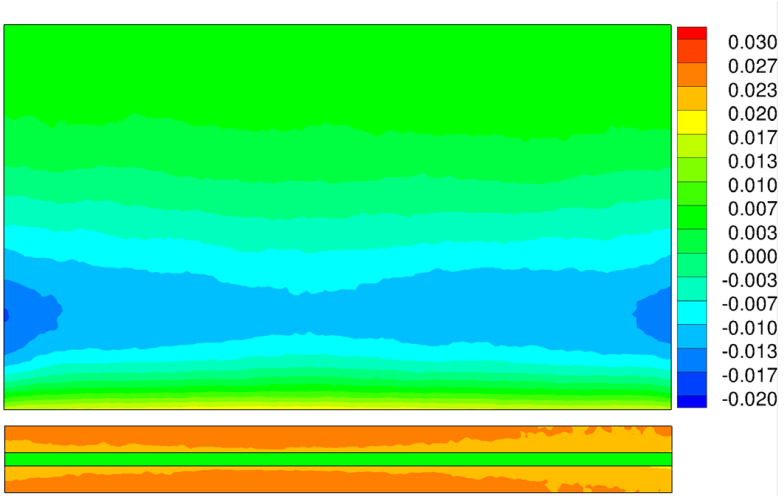

(b)

Figure 3.9: 2-D plot of the relative error on the estimated $\tilde{h}_i$ from solving the IHCP for an uniform value of h = 40 $\mathrm{W/m^2K}$with σ=0.05K for $Y_m(S_i)$. (a) SDM solution ; (b) CGM solution

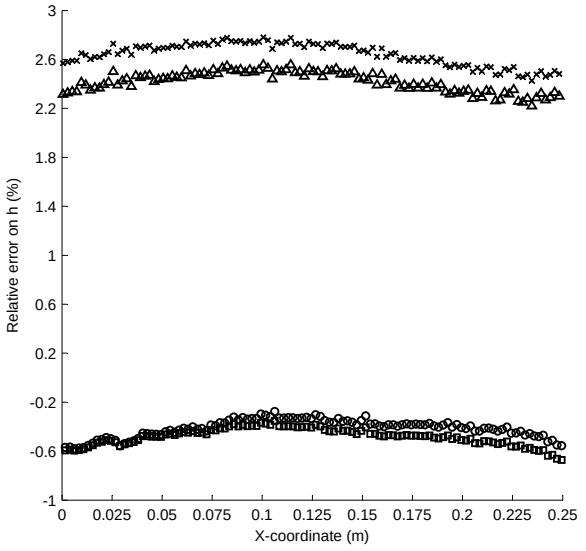

(a) □: SDM at L_1 ; ○: CGM at L_1 ; ×: SDM at L_2 ; △: CGM at L_2

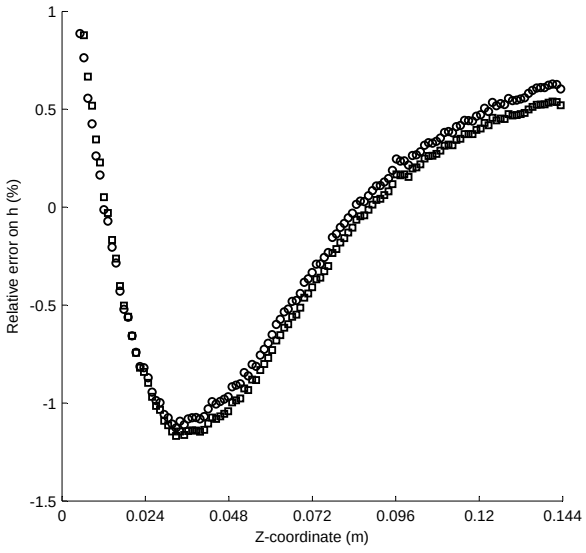

(b) □: SDM at L_3 ; ○: CGM at L_3

Figure 3.10: Relative error on $\tilde{h}_i$ for an uniform value of h = 40 $\mathrm{W/m^2K}$ for σ=0.05K for $Y_m(S_i)$, plotted along the evaluation lines $L_1 - L_3$

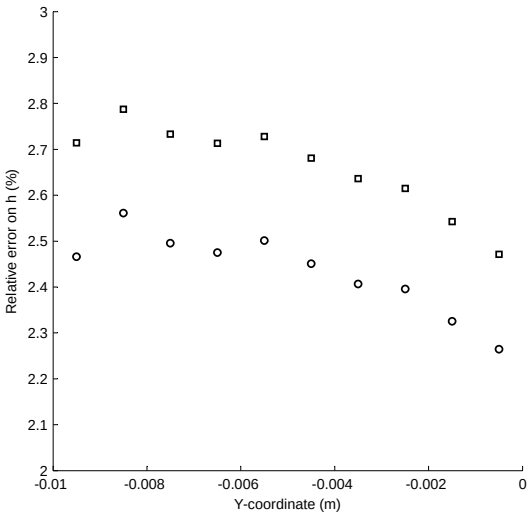

Figure 3.11: Relative error on $\tilde{h}_i$ for an uniform value of h = 40 $\mathrm{W/m^2K}$ for σ=0.05K for $Y_m(S_i)$; □: SDM at L_4 ; ∘: CGM at L_4

The larger error on the measured temperature data $Y_m(S_i)$ should increase the errors for $\tilde{h}_i$.

The results of the relative errors on $\tilde{h}_i$ are plotted in Figures 3.13-3.15. The accuracy of the solution with SDM is compared with the CGM solution in more detail in Fig.3.14. The accuracy of the results does not deteriorate very much compared to the results for σ = 0.05, in spite of the large temperature measurement error. Both algorithms give similar results. The error on the primary surfaces remains the largest: 2.5%-2/8%, but this is of the same order of magnitude as for σ=0.05K. The maximum error along the fin height has increased from 1.2% for σ=0.05K to 2% for σ=0.25K (Fig.3.14(b)). The wiggle $\tilde{h}_i$ along the fin height has the same form as for σ=0.05 but it has a larger amplitude. The influence of the large temperature measurement error can be seen in the results of Fig. 3.14: the estimated $\tilde{h}_i$ do not form a continuously smooth curve anymore, there is more scattering on the estimated values. Nevertheless the trend of the local h_i variation can still be easily deduced.

The mean values $\tilde{h}_{avg}$ and ERRh are given in Table 3.3, for both SDM and CGM. The mean values for CGM deteriorated on the fin tip, where there is an error of almost 1%, which is still accurate. There is no noticeable decrease in accuracy on the other fin surfaces and primary surface. For SDM, the accuracy deteriorated slightly for the fin surface S_5 (from 0.22% to 0.54%). Overall, the

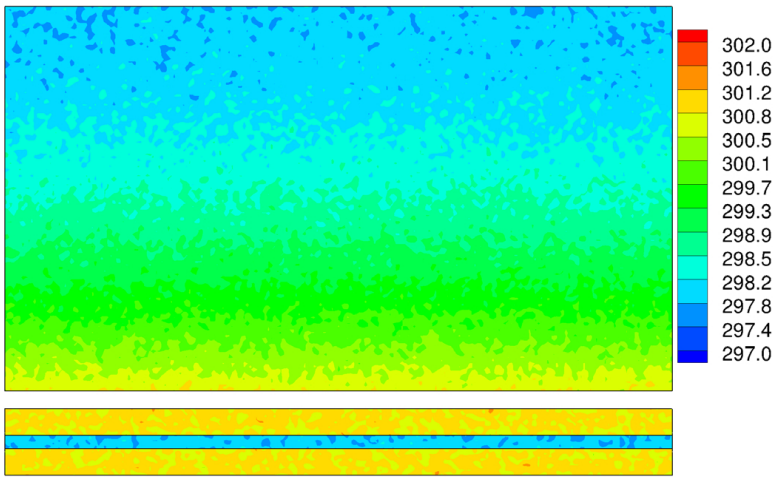

Figure 3.12: 2-D plot of imposed temperatures $Y_m(S_i)$ (in K) with σ=0.25K

accuracy of the local and mean heat transfer coefficients is more than acceptable, even for a relatively inaccurate temperature measurement of 0.5K.

	SDM		CGM	
	$\tilde{h}_{avg}$ ($\mathrm{W/m^2K}$)	ERRh (%)	$\tilde{h}_{avg}$ ($\mathrm{W/m^2K}$)	ERRh (%)
Fin tip S_1	40.11	0.27	40.38	0.945
Front S_5	39.74	-0.54	39.88	-0.19
Primary S_6	40.43	2.5	40.32	2.22

Table 3.3: The average values for $\tilde{h}$ and ERRh for an uniform value of h = 40 $\mathrm{W/m^2K}$with σ=0.25K for $Y_m(S_i)$

3.1.2 Linear increase in heat transfer coefficient along the fin length

3.1.2.1 Exact measurement data: σ=0

Both SDM and CGM give very good results for reconstructing a uniform heat transfer coefficient on different surfaces. But the question remains how do they perform for a variation of the heat transfer coefficient. This is investigated in the following paragraphs. First a heat transfer coefficient which varies linearly along the fin length is studied: from 10 $\mathrm{W/m^2K}$ on the left fin surface S_2 to 40 $\mathrm{W/m^2K}$

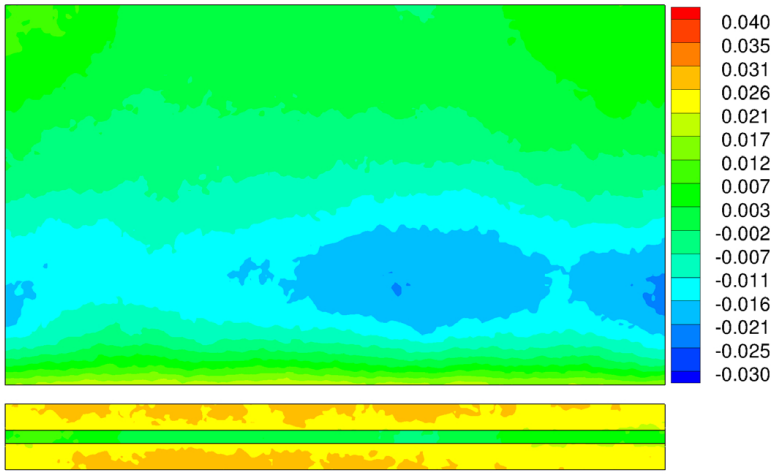

(a)

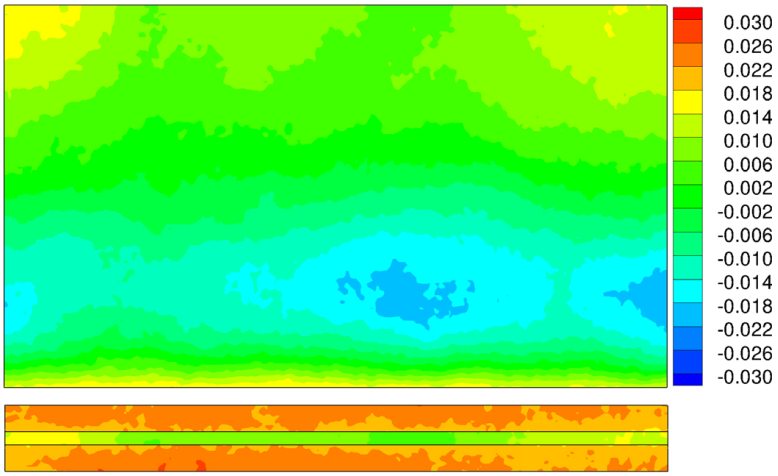

(b)

Figure 3.13: 2-D plot of the relative error on the estimated $\tilde{h}_i$ from solving the IHCP for an uniform value of h = 40 $\mathrm{W/m^2K}$with σ=0.25K. (a) SDM solution ; (b) CGM solution

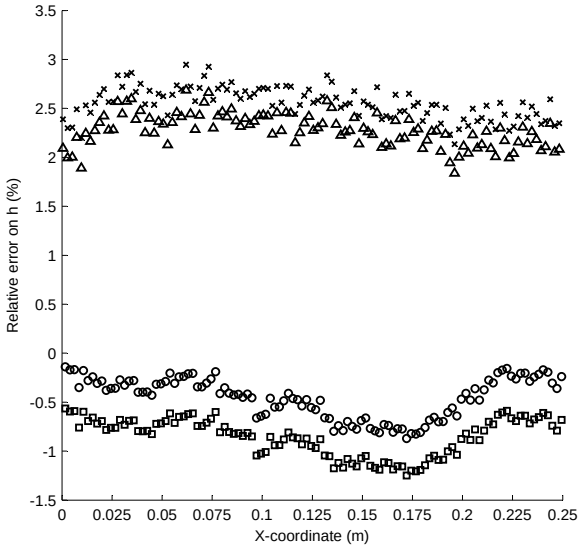

(a) □: SDM at L_1 ; ○: CGM at L_1 ; ×: SDM at L_2 ; △: CGM at L_2

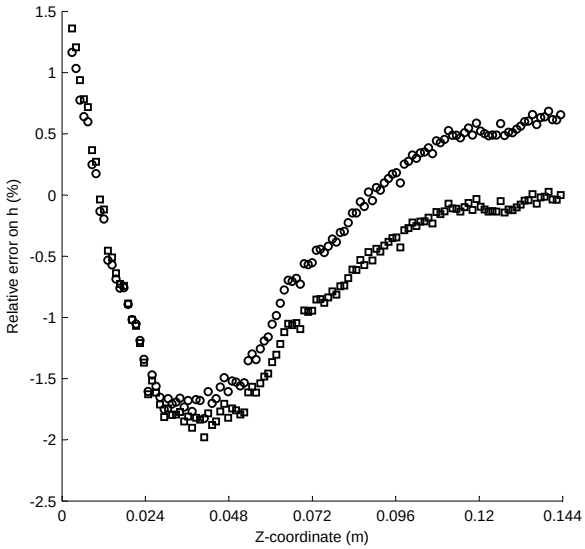

(b) □: SDM at L_3 ; ○: CGM at L_3

Figure 3.14: Relative error on $\tilde{h}_i$ for an uniform value of h = 40 $\mathrm{W/m^2K}$ with σ=0.25K, plotted along the evaluation lines $L_1 - L_3$

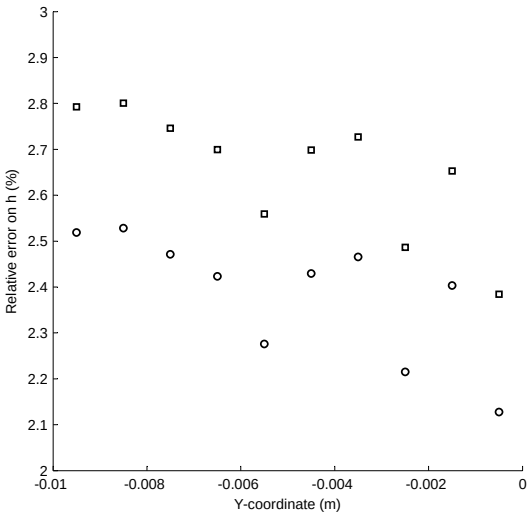

Figure 3.15: Relative error on $\tilde{h}_i$ for an uniform value of h = 40 $\mathrm{W/m^2K}$ with σ=0.25K □: SDM at L_4 ; ∘: CGM at L_4

at the right fin surface S_3. The same heat transfer coefficient profile is imposed on the primary surfaces S_6 – S_7. The heat transfer coefficient profile h_i is shown in Fig. 3.16(a). These h_i are used as boundary condition in the direct heat conduction problem of Eq. (2.14). The resulting simulated temperature measurement profile for $Y_m(S_i)$ is plotted in Fig. 3.17.

It is assumed that the imposed measured temperatures $Y_m(S_i)$ are exact, thus σ=0. These temperatures are used for the minimization of the functional J (Eq. (2.13)). The stopping criterion is set at χ=0.01. SDM converges after 236 iterations, CGM converges much faster with only 100 iterations. The resulting estimated $\tilde{h}_i$ are plotted for SDM in Fig. 3.16(b). The solution with CGM is very similar and is not plotted for this reason. The results along the four evaluation lines L_1 – L_3 given in Fig. 3.18 show more detail. Fig. 3.19 gives the relative error on $\tilde{h}_i$ in a 2-D plot for the SDM and CGM solution. The detailed graphs along the evaluation lineas are shown in Fig. 3.20.

Both solution methods show the exact same trend, as expected. The estimated $\tilde{h}_i$ has the largest error at the edges of the boundary surfaces. On the front fin surface S_4, the largest relative error is situated at the left side: 5% (SDM) or 10% (CGM)(Fig. 3.20(a) and Fig. 3.19(b)). The exact h_i is the lowest, i.e. 10 $\mathrm{W/m^2K}$ at this left side and Fig. 3.18(a) indicates that the absolute errors on the left side are as large as the absolute errors at the right side of the fin. So actually, an error

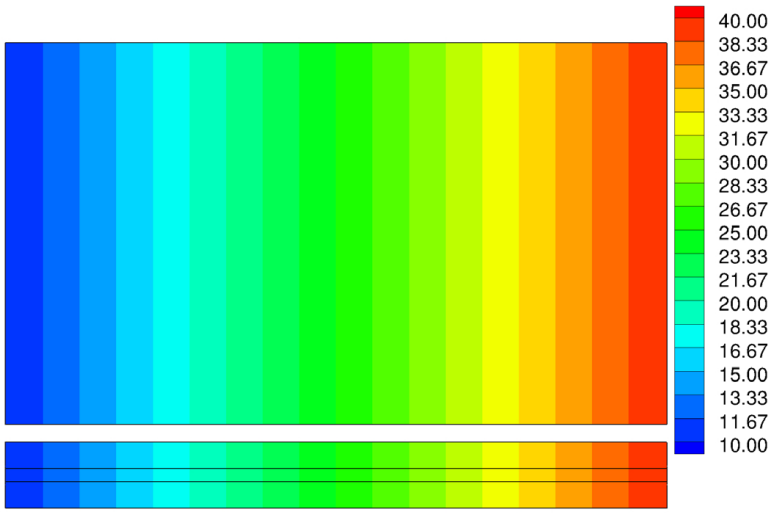

(a)

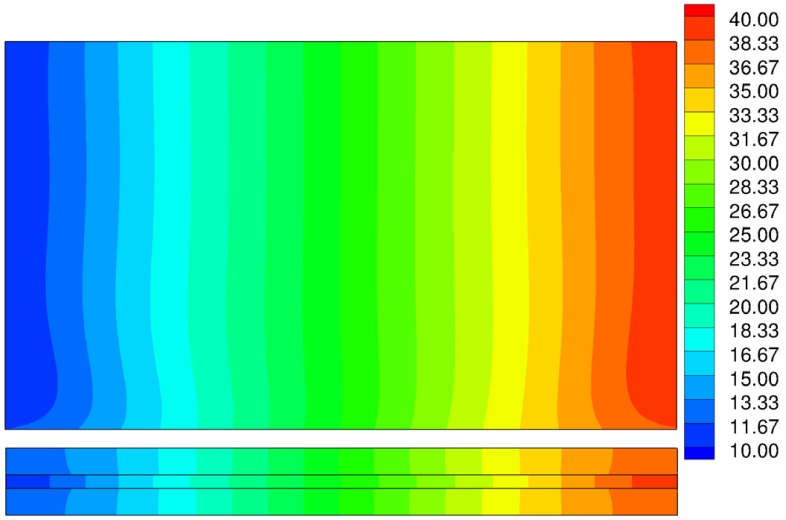

(b)

Figure 3.16: 2-D plots of the exact h_i (a) and the estimated $\tilde{h}_i$ from solving the IHCP wit SDM (b) for the linearly varying exact heat transfer coefficient

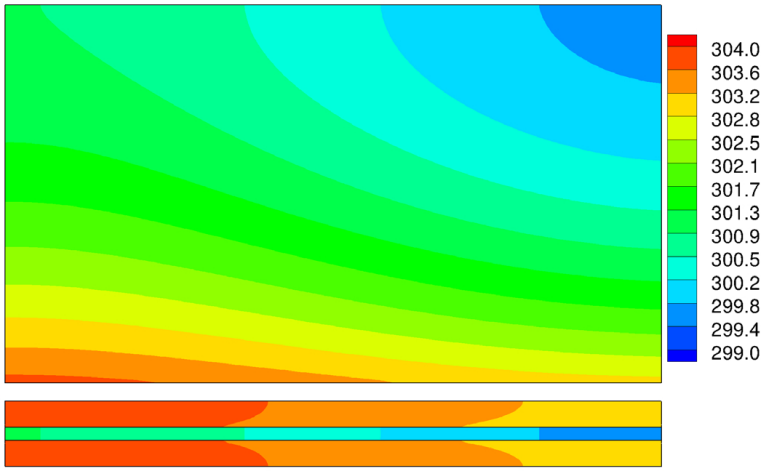

Figure 3.17: 2-D plot of the measured temperature profile $Y_m(S_i)$ for the linearly varying exact heat transfer coefficient

of 10% on a h_i value of 10 $\mathrm{W/m^2K}$ is only an absolute error of 1 $\mathrm{W/m^2K}$. This large error occurs only for the first 5 to 10 cells, depending on the fin height. This is less than 5% of the number of fin cells along the fin length. Figure 3.18(b) and Fig. 3.19 show that the relative error along the fin height is much smaller, except at the left fin side. The largest error occurs again at the fin base, near the primary surface, but is much smaller than the error at the fin sides ($< 1\%$). The error near the fin tip is the smallest: for SDM there is almost no noticeable error ($< 0.1\%$). SDM seems to give more accurate results than the CGM: the wiggle is smaller, both in frequency and amplitude, and even disappears near the fin tip (Fig. 3.20(b)).

The same can be concluded for the estimated $\tilde{h}_i$ along the primary surface length, except that the relative errors are much larger there, up to 24% (SDM) and 36% (CGM) at the left side (Fig.3.20(a)). But again, this is only for a few cells, i.e. less than 15% of the cells has a relative error > 4%, and they all are situated at the left and right edge.

The mean relative error on $\tilde{h}_i$ (thus ERRh) is listed in Table 3.4 for different surfaces. These mean values are surprisingly accurate for both CGM and SDM. While SDM seems to perform slightly better on the estimation of the local $\tilde{h}_i$, CGM is more accurate for the mean values, yet these differences are negligible. This accurate prediction confirms again the idea that the oscillations of the estimated $\tilde{h}_i$ around the exact h_i compensates itself on each surface, which results in

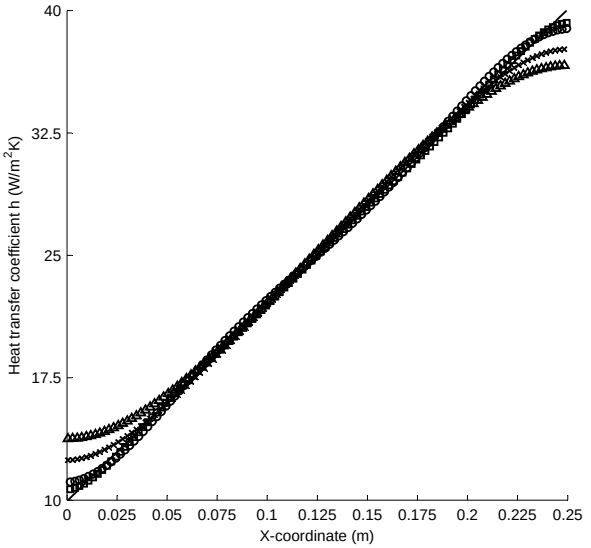

(a) □: SDM at L_1 ; ○: CGM at L_1 ; ×: SDM at L_2 ; Δ: CGM at L_2

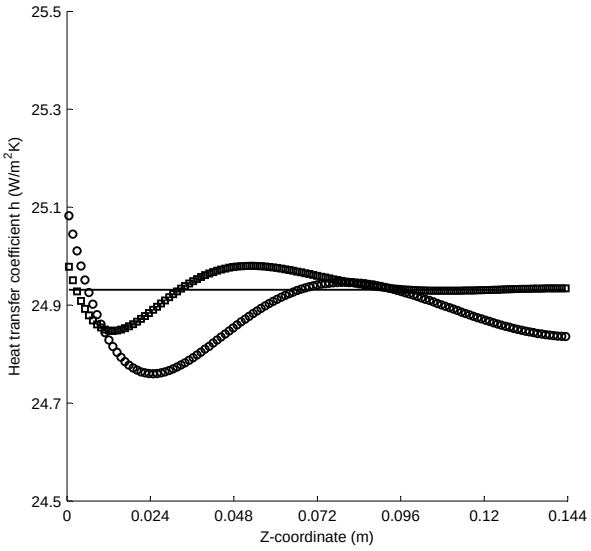

(b) □: SDM at L_3 ; ○: CGM at L_3

Figure 3.18: Estimated $\tilde{h}_i$ for linear varying h_i along the fin length with σ=0K for $Y_m(S_i)$, plotted along the evaluation lines $L_1 - L_3$

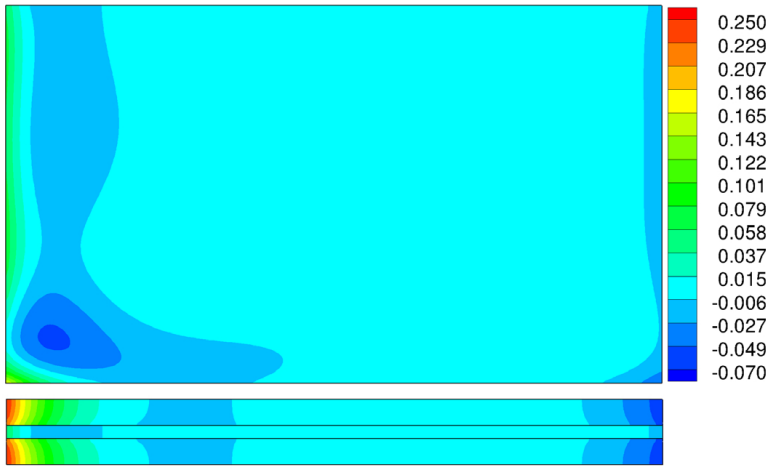

(a)

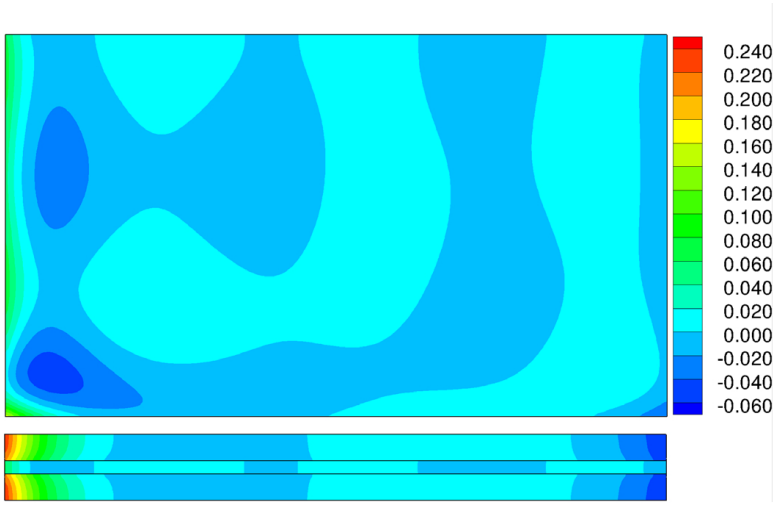

(b)

Figure 3.19: 2-D plot of the relative error on estimated $\tilde{h}_i$ for linear varying h_i along the fin length with σ=0 (a) SDM solution ; (b) CGM solution

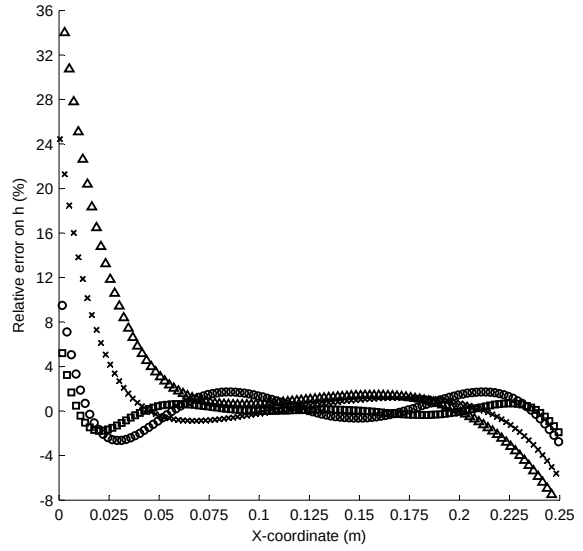

(a) □: SDM at L_1 ; ○: CGM at L_1 ; ×: SDM at L_2 ; △: CGM at L_2

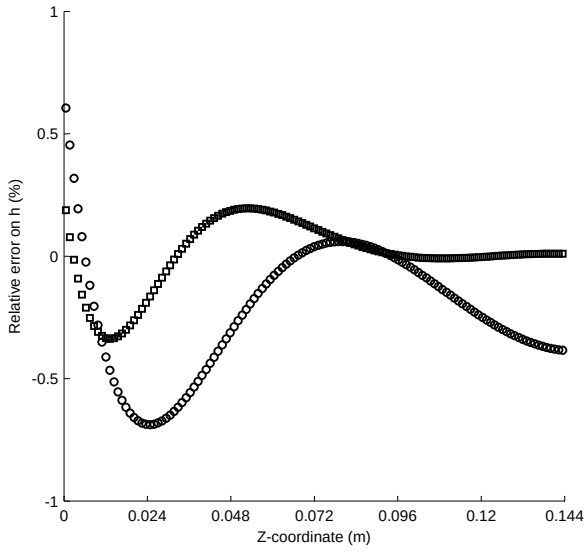

(b) □: SDM at L_3 ; ○: CGM at L_3

Figure 3.20: Relative error on $\tilde{h}_i$ for linear varying h_i along the fin length with σ=0K for $Y_m(S_i)$, plotted along the evaluation lines $L_1 - L_3$

accurate mean heat transfer coefficients and heat fluxes on all the boundary surfaces. This is beneficial to determine the fin effectiveness.

		SDM	CGM
	h_{avg} ($\mathrm{W/m^2K}$)	ERRh (%)	ERRh (%)
Fin tip S_1	25	0.04	0.13
Front S_5	24.97	-0.02	-0.01
Primary S_6	24.65	0.35	0.22

Table 3.4: The average values for ERRh (in %) for a linearly varying heat transfer coefficient along the fin length with σ=0K.

3.1.2.2 Temperature measurement error: dY_m = 0.1°C or σ=0.05

The measured temperatures are assumed to have an accuracy of 0.1°C, which means a standard deviation σ = 0.05°C: the convergence criterion becomes χ = 154. For this test case SDM converges after 30 iterations and CGM after 21 iterations.

The solution of estimated $\tilde{h}_i$ is again similar for SDM and CGM. A 2-D plot is shown in Fig. 3.21. The results along the four evaluation lines $L_1 - L_3$ show more detail (Fig. 3.22). Figure 3.23 gives the relative error on $\tilde{h}_i$ in a 2-D plot for the SDM solution. The 2-D plot for CGM is similar and is not shown. Moreover, line plots along $L_1 - L_3$ give more insight in the accuracy of both methods, especially near the edges, where the errors are the largest (Fig. 3.24).

The results are the same as for σ=0, and the same remarks can be made, only the errors have increased. The largest error on $\tilde{h}_i$ at the left side (for an exact h_i is 10 $\mathrm{W/m^2K}$) has increased: 10% (SDM) or 12% (CGM) (Figures 3.23-3.24(a)). Figure 3.24(a) indicates that this large error is only present for the first 30% of the cells along the fin length (whereas this was only 5% of the cells for accurate temperature measurements). For the other 70% of the cells, the relative error is $< 5\%$. This illustrates the influence of the increasing temperature measurement error: the global trend of h_i variation is still reconstructed, however the errors that occurred for exact temperature measurements increase, especially near the edges. The relative error along the fin height is even smaller: it has only increased with 1% along L_3 (Fig 3.22(b)).

Notice that for the SDM solution This error at the fin base, near the primary surface, is much smaller than the error at the fin sides ($< 1\%$). The error near the fin tip is now much smaller for the CGM solution than for the SDM solution, which is in contrast with the case with σ = 0. A possible explanation is that the SDM solution has converged already too far, or not far enough. It is more difficult to evaluate the convergence for SDM due to the slow convergence rate near the

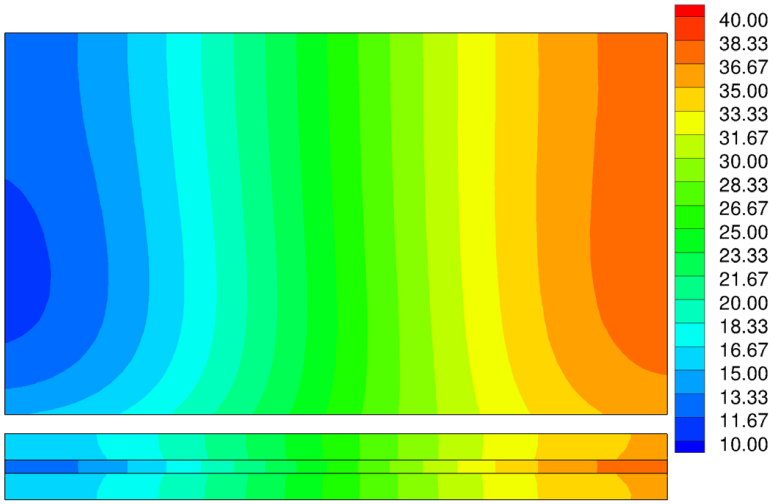

Figure 3.21: 2-D plot of the estimated $\tilde{h}_i$ for the solution with SDM for linear varying h_i along the fin length with σ=0.05K.

convergence criterion. For the error on $\tilde{h}_i$ along the length of the primary surface, the same as for the fin can be concluded, but the relative errors are much larger there at the left side, up to 60% (SDM) and 47% (CGM) (Fig.3.24(a)). But again, this is only the case for a few cells: less than 30% of the cells has a relative error > 5%, and they all are situated at the left and right edge. The results show that the SDM is less accurate than the CGM near the edges.

The mean relative error on $\tilde{h}_i$ is listed in Table 3.5, for SDM and CGM and for different surfaces. For both CGM and SDM these mean values are accurate for the fin. However, the ERRh on the primary surfaces has increased to 4.5% for CGM, and 6.8% for SDM. So CGM performs better than SDM, as well for the mean values as for the local values of the estimated $\tilde{h}_i$. SDM seems to have more problems than CGM to accurately estimate the heat transfer coefficients on the primary surface.

3.1.2.3 Temperature measurement error: dY_m = 0.5°C or σ=0.25

As mentioned in paragraph 3.1.1.3, the convergence criterion becomes χ = 3859 for temperature measurements with a standard deviation of σ = 0.25. SDM converges after 30 iterations, but CGM already after 12 iterations for this test case. The 2-D plots of the resulting estimated $\tilde{h}_i$ are very similar as for the case with σ = 0.25 and do not provide any extra information. Therefore they are not given.

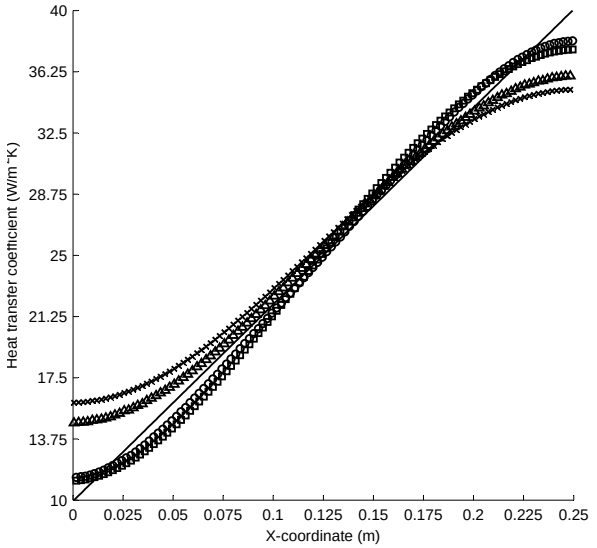

(a) □: SDM at L_1 ; ○: CGM at L_1 ; ×: SDM at L_2 ; △: CGM at L_2

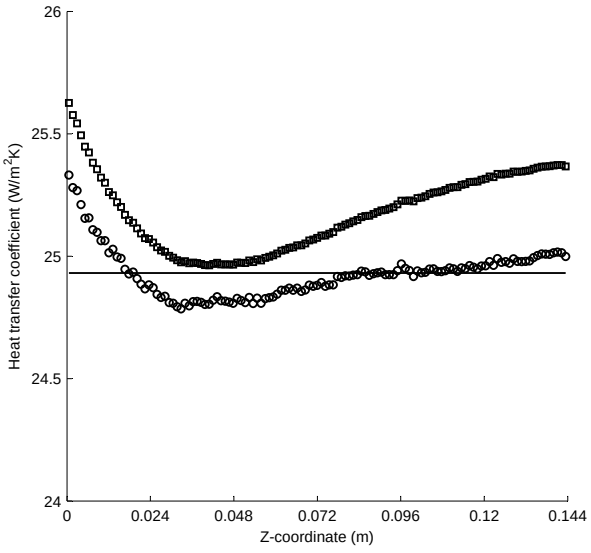

(b) ○: CGM at L_3

Figure 3.22: Estimated $\tilde{h}_i$ for linear varying h_i along the fin length with σ=0.05K for $Y_m(S_i)$, plotted along the evaluation lines L_1 – L_3

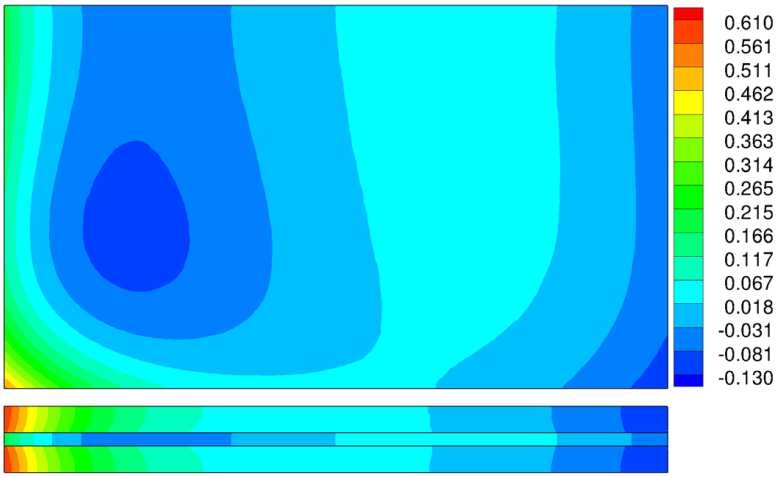

Figure 3.23: 2-D plot of the relative error on estimated $\tilde{h}_i$ for the solution with SDM for linear varying h_i along the fin length with σ=0.05K for $Y_m(S_i)$

		SDM	CGM
	h_{avg} (W/m^{2}K)	ERRh (%)	ERRh (%)
Fin tip S_1	25	0.31	0.37
Front S_5	24.97	-0.24	-0.18
Primary S_6	24.65	2.74	1.73

Table 3.5: The average values for ERRh (in %) for a linearly varying heat transfer coefficient along the fin length with σ=0.05K.

However, the line plots of $\tilde{h}_i$ along the four evaluation lines L_1 – L_3 given in Fig.3.25 provide more detail. The 2-D plots of the relative error on $\tilde{h}_i$ are shown in Fig.3.26 for both the CGM and SDM solution. The detailed graphs of the relative errors along the evaluation lineas are shown in Fig.3.27.

The results have the same trend as for σ=0.05K only the errors are larger. The same remarks as in the previous case hence can be made. The largest errors for the estimated $\tilde{h}_i$ at the front surface S_4 have not increased: 10% (SDM) or 13% (CGM) at the left side (Fig. 3.27(a)-3.26). Figure 3.27(a) shows that this large error is only present for the first 30% of the cells along the fin length. For the other 70%, the relative error is < 6%. The error over the center of the fin however increased slightly (± 1%). Figure 3.25(b) and Fig 3.26 show that the relative error along the fin height has remained practically the same as for σ = 0.05. The main

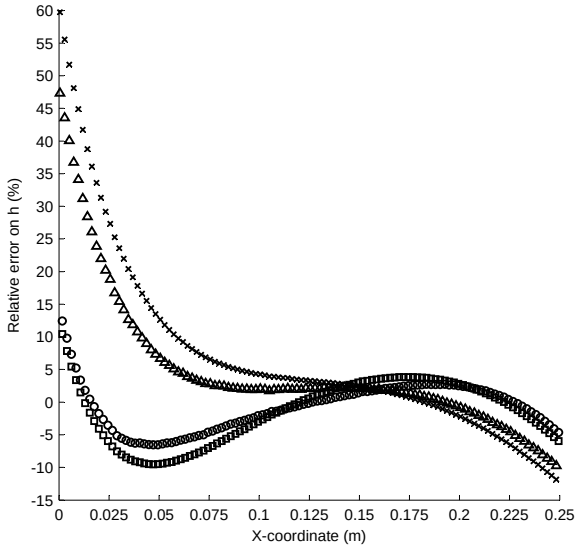

(a) □: SDM at L_1 ; ○: CGM at L_1 ; ×: SDM at L_2 ; △: CGM at L_2

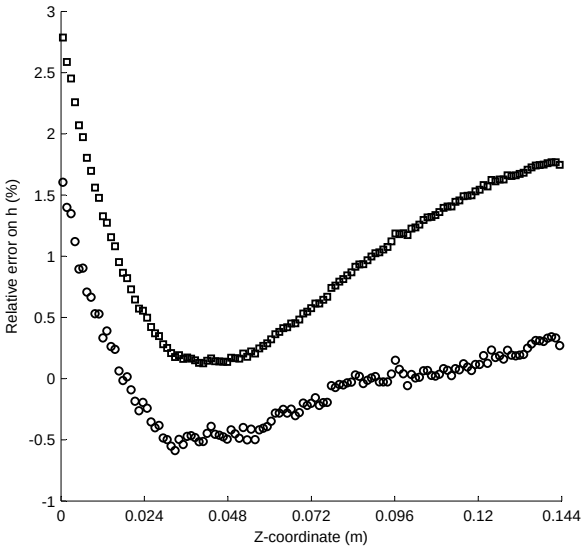

(b) □: SDM at L_3 ; ○: CGM at L_3

Figure 3.24: Relative error on $\tilde{h}_i$ for linear varying h_i along the fin length with σ=0.05K for $Y_m(S_i)$, plotted along the evaluation lines $L_1 - L_3$

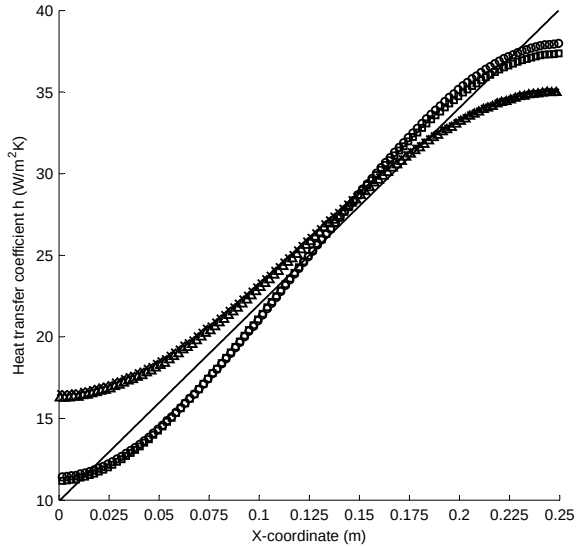

(a) □: SDM at L_1 ; ○: CGM at L_1 ; ×: SDM at L_2 ; △: CGM at L_2

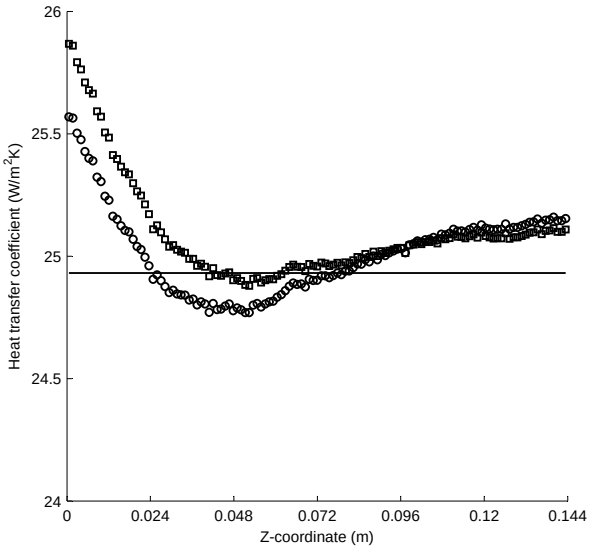

(b) □: SDM at L_3 ; ○: CGM at L_3

Figure 3.25: Estimated $\tilde{h}_i$ for linear varying h_i along the fin length with σ=0.25K for $Y_m(S_i)$, plotted along the evaluation lines L_1 – L_3

difference is the scattering of the data as was also observed for the cases with a uniform heat transfer coefficient. This scattering of the data induces no extra error that has to be taken into account, as it is much smaller than the error induced by the wiggle in the solution. The error near the fin tip is now very similar for the CGM and SDM. The error patterns are very much alike on all surfaces for SDM and CGM, contrary to what was found for the previous case with σ=0.05. So it is very likely that the SDM solution for σ=0.05 was not the best: it needed to converge further. This is a downside for the SDM. Due to the slow convergence near the stopping criterion, the chance of stopping too early increases, whereas for CGM this risk does not exist due to the better convergence near the stopping criterion.

The relative errors on $\tilde{h}_i$ along the length of the primary surface at the left side have increased up to 65% for SDM and CGM. (Fig.3.27(a)). After 30% of the cells along the fin length, this error drops below 10% and stays below 10%. But keep in mind that these large relative errors are for the smallest heat transfer coefficients, which are situated at the left fin side. The error over the primary surface is more important for the SDM than for CGM as was also the case in the previous test cases. Figure 3.26 shows that the combination of the larger errors near the fin left side and the primary surface seem to affect the lower left corner of the fin surfaces $S_4 - S_5$. There is a small zone where the error reaches 30%, which is much higher than the 13% obtained for the rest of the left side of the fin. Yet this zone is very small: it stretches out over less than 10% of the fin height. This effect was also noticeable for temperature measurement errors of σ=0.05. Figure 3.21 and Fig. 3.25 show that the trend of the variation of the local convection coefficients h_i is reconstructed by both CGM and SDM.

The mean relative error on $\tilde{h}_i$ is listed in Table 3.6, for SDM and CGM for various surfaces. The mean values are again accurate for the fin surfaces, especially for the CGM were there is no difference with the results for σ=0.05. SDM however experiences a decrease in accuracy: the mean error on the front fin surface S_5 became three times as large as for σ=0.05. It is still limited to 0.65%, but given the larger surface that is affected by this error, it is not negligible anymore. The ERRh on the primary surfaces has increased to almost 3% for CGM, and 4% for SDM. Because of the small area on which this error occurs, it is still acceptable.

		SDM	CGM
	h_{avg} ($\mathrm{W/m^2K}$)	ERRh (%)	ERRh (%)
Fin tip S_1	25	-0.84	0.55
Front S_5	24.97	-0.65	-0.1
Primary S_6	24.65	3.81	2.81

Table 3.6: The average values for ERRh (in %) for a linearly varying heat transfer coefficient along the fin length with σ=0.25K.

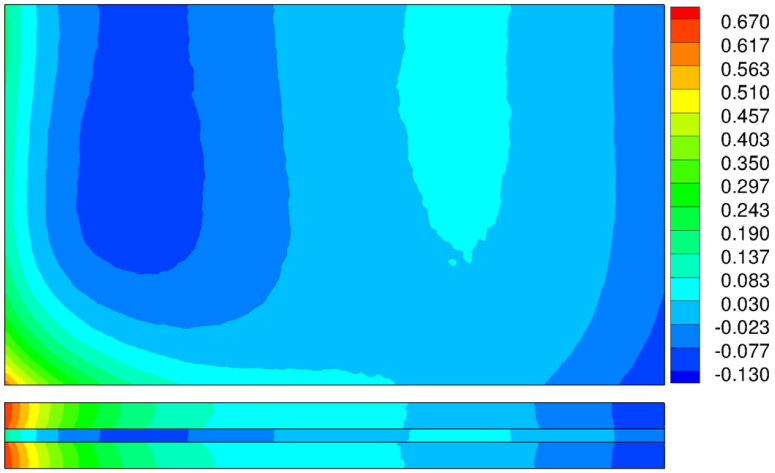

(a)

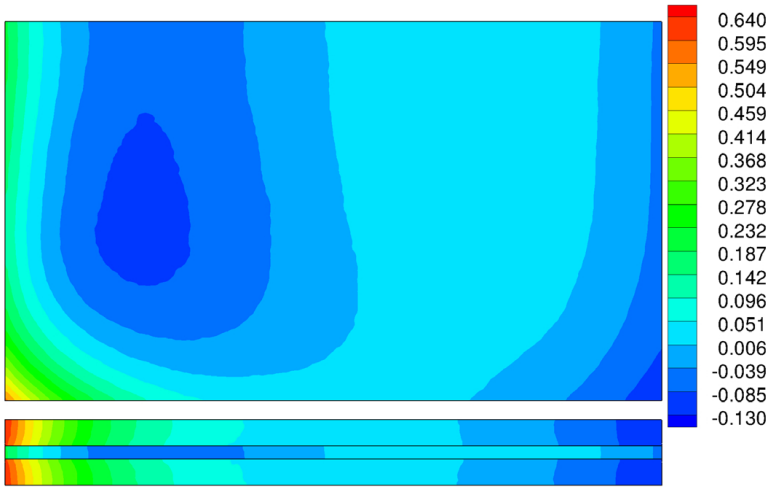

(b)

Figure 3.26: 2-D plot of the relative error on estimated $\tilde{h}_i$ for the solution of linear varying h_i along the fin length with σ=0.25K. (a) SDM solution ; (b) CGM solution

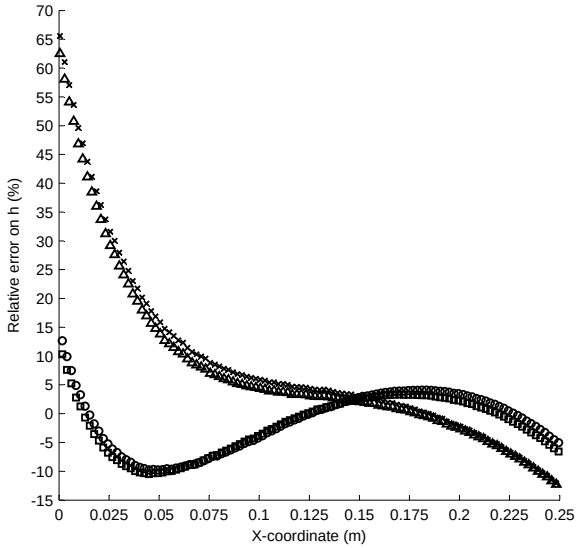

(a) □: SDM at L_1 ; ○: CGM at L_1 ; ×: SDM at L_2 ; △: CGM at L_2

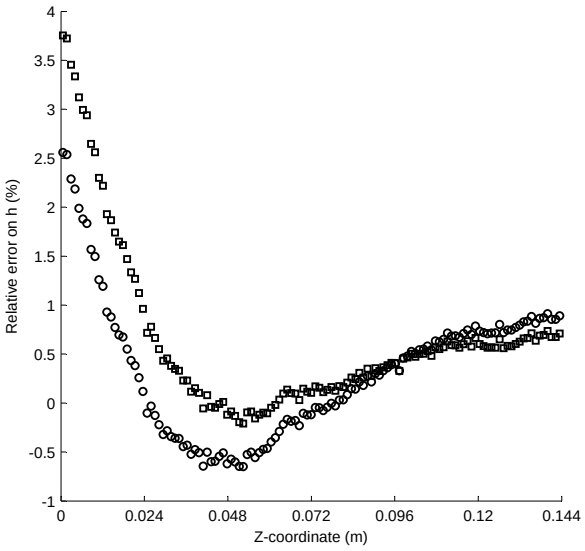

(b) □: SDM at L_3 ; ○: CGM at L_3

Figure 3.27: Relative error on $\tilde{h}_i$ for linear varying h_i along the fin length with σ=0.25K for $Y_m(S_i)$, plotted along the evaluation lines $L_1 - L_3$

3.1.3 Linear variation of heat transfer coefficients along fin height

3.1.3.1 Exact measurement data: σ=0

Previously, a linearly varying heat transfer coefficient h_i along the fin length showed generally acceptable results. Yet the heat transfer coefficient can also vary along the fin height, and along the width of the primary surface. For this reason a heat transfer coefficient which varies linearly along the fin height is now studied. The imposed profile varies from 10 $\mathrm{W/m^2K}$ on the fin tip to 40 $\mathrm{W/m^2K}$ at the base of the fin, and this for all the fin surfaces S_1 – S_5. The heat transfer coefficient on the primary surface varies linearly along the width: from 40 $\mathrm{W/m^2K}$ near the fin base to 30 $\mathrm{W/m^2K}$ at the outside of the primary surface. The imposed heat transfer coefficient profile h_i is shown in Fig. 3.28. These h_i are used as boundary condition in the direct heat conduction problem of Eq. (2.14). The resulting simulated temperature measurement profile calculated from this direct problem are the temperatures $Y_m(S_i)$.

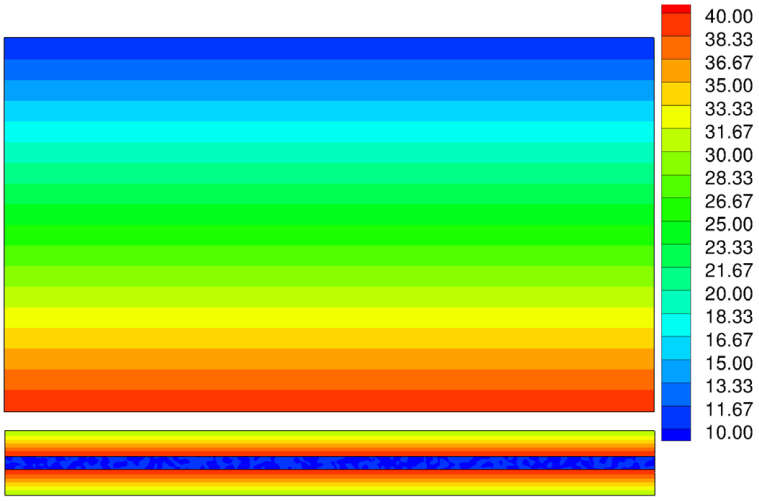

Figure 3.28: 2-D plot of the linearly varying exact heat transfer coefficient h_i (in $\mathrm{W/m^2K}$) along the fin height

It is assumed that the imposed temperatures $Y_m(S_i)$ are exact, thus σ=0. The stopping criterion is set at χ=0.01. SDM converges after 120 iterations, CGM converges much faster with only 30 iterations. Note that the convergence criterion of 0.01 is not attained: both methods stagnate at a residual value of 0.14. Although the $\tilde{h}_i$ are still updated for each iteration beyond the stagnation point, converged

solution is assumed at the stagnation value. Updates beyond this point are only due to regularization and can introduce non-physical solutions.

The resulting estimated $\tilde{h}_i$ are plotted in Fig. 3.29. The results along the four evaluation lines L_1 – L_4 show more details (Fig. 3.30). Figure 3.32(a) gives the relative error on $\tilde{h}_i$ in a 2-D plot. The detailed graphs along the evaluation lines are shown in Fig. 3.33.

Both solution methods show the exact same trend for the solution. The estimated $\tilde{h}_i$ has the largest relative error on the primary surfaces S_6 – S_7, at the fin tip S_1 and near the fin tip on the other fin surfaces S_4 – S_5. The largest relative error on the front fin surface S_4 is 20% for SDM and CGM. It is not surprising that the largest relative error is near the fin tip, because of the lower exact h_i, i.e. 10 $\mathrm{W/m^2K}$ (Fig. 3.30(b) and Fig. 3.29). Figure 3.18(b) indicates that the absolute errors near the fin tip are as large as the absolute errors near the fin base, but the relative error is larger due to the difference in the absolute value of h_i. The same result was found for a linearly varying heat transfer coefficient along the fin length. The relative error along the fin length is much smaller, even at the left and right fin side (Fig. 3.30(a) and Fig. 3.32). So it seems that the largest errors occur in the direction of the largest variation of the heat transfer coefficient h_i, and this always near the edges.

The large error near the fin tip is only applicable for the first 10 cell rows. This is only 8% of the number of boundary fin cells. The largest errors occur again at the fin base, near the primary surface. The heat transfer coefficient varies along the width of the primary surface, but nor SDM nor CGM seem to be able to capture this linear variation. They both reconstruct a uniform value of 38 $\mathrm{W/m^2K}$ over the width of S_6 – S_7 (Fig.3.31). The mean value of the varying heat transfer coefficient on the primary surface is 35 $\mathrm{W/m^2K}$, which is an error of 2.8%. This explains also the large relative error at the outer edge of the primary surface: the imposed h_i is 30 $\mathrm{W/m^2K}$, and the estimated $\tilde{h}_i$ has the uniform value of 38 $\mathrm{W/m^2K}$. The reason that a variation of heat flux cannot be reconstructed at the primary surface is the low number of measurement points at S_4 – S_5 compared to the amount of measurement points at the fin surfaces along the width (only 10 cells). This makes it unable for a whole domain method to reconstruct variations along the width at these surfaces, and a mean value is calculated. This could be solved by reducing the amount of measurement points on the fin surface used in the solution algorithm, or by increasing the number of cells along the width of the primary surface.

The mean relative error on $\tilde{h}_i$ (thus ERRh) is listed in Table 3.7 for various surfaces. These mean values show same result for CGM as for SDM. As expected from the local results, the error on the primary surface has become significant, even for exact temperature measurements (σ=0). This was not the case in previous tests. The error on the mean h_{avg} on the fin tip is quite large, but this is for a low absolute value h_{avg} of 10 $\mathrm{W/m^2K}$.

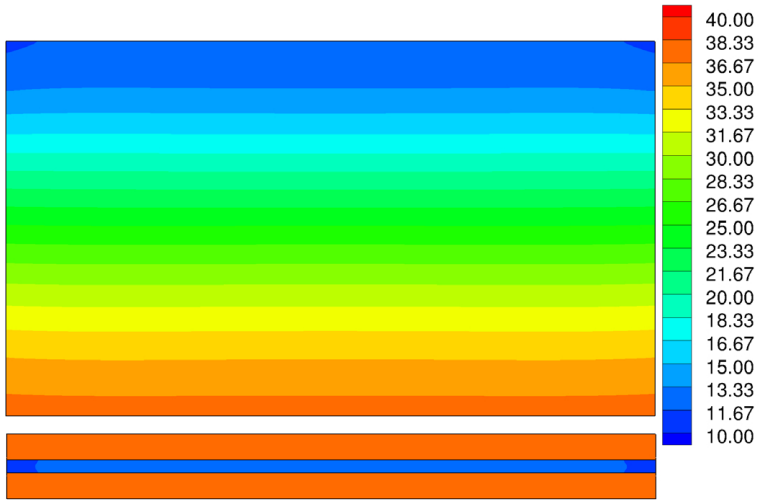

(a)

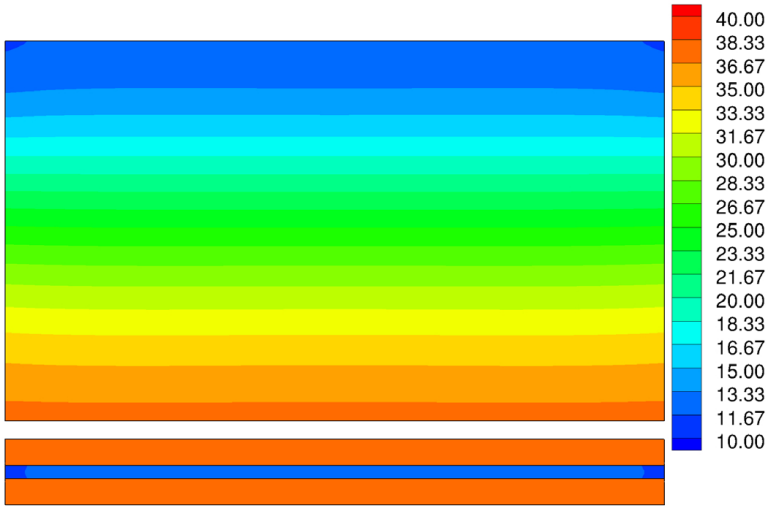

(b)

Figure 3.29: 2-D plot of the estimated $\tilde{h}_i$ for the solution of a linearly varying h_i along the fin height with σ=0K. (a) SDM solution ; (b) CGM solution

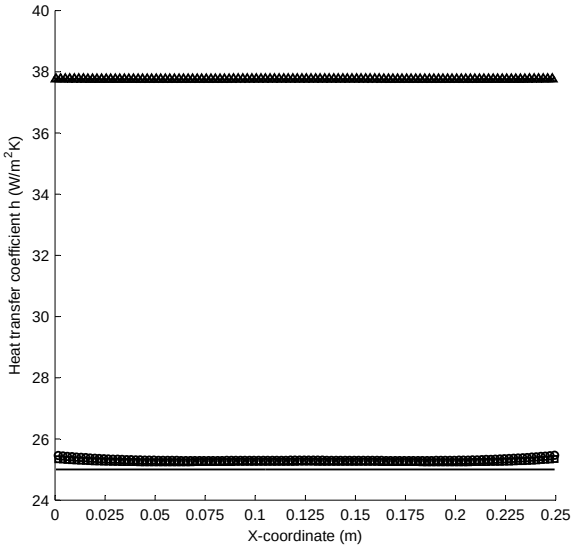

(a) □: SDM at L_1 ; ○: CGM at L_1 ; ×: SDM at L_2 ; Δ: CGM at L_2

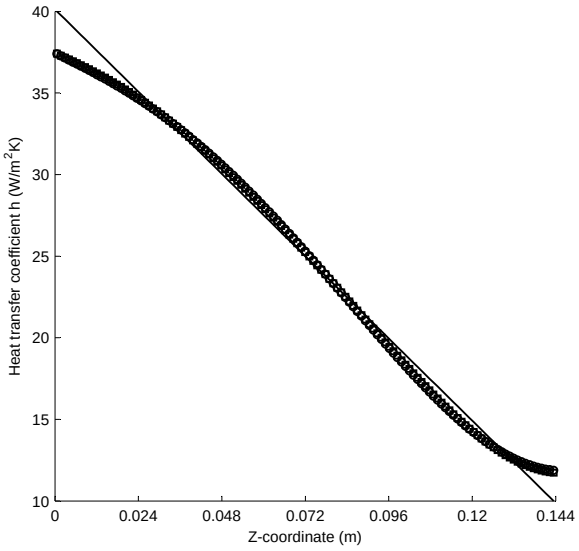

(b) □: SDM at L_3 ; ○: CGM at L_3

Figure 3.30: Estimated $\tilde{h}_i$ for linear varying h_i along the fin height with σ=0K for $Y_m(S_i)$, plotted along the evaluation lines $L_1 - L_3$

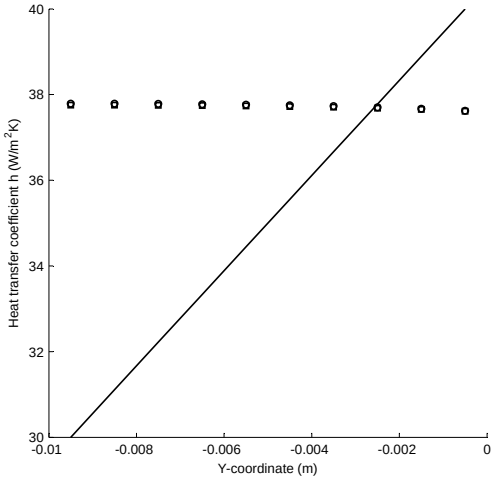

Figure 3.31: Estimated $\tilde{h}_i$ for linear varying h_i along the fin height for σ=0K for $Y_m(S_i)$; □: SDM at L_4 ; ∘: CGM at L_4

		SDM	CGM
	h_{avg} ($\mathrm{W/m^2K}$)	ERRh (%)	ERRh (%)
Fin tip S_1	10	17.4	19.06
Front S_5	24.95	-0.87	-0.93
Primary S_6	34.45	7.96	8.27

Table 3.7: The average values for ERRh for a linearly varying heat transfer coefficient along the fin height with σ=0K.

3.1.3.2 Temperature measurement error: dY_m = 0.1°C or σ=0.05

Neither SDM nor CGM reaches the convergence criterion of χ = 154 for temperature measurement accuracies of 0.1°C: SDM stagnates at 155.4 after 81 iterations, CGM stagnates at the same residual after 20 iterations. The results for SDM and CGM are very similar. The resulting estimated $\tilde{h}_i$ of the CGM solution is plotted in Fig. 3.35(a), and the relative error on $\tilde{h}_i$ in Fig. 3.35(b). The results along the four evaluation lines L_1 – L_4 for the relative error on $\tilde{h}_i$ show more details (Fig. 3.36).

The solution shows the same trend as for the case with σ = 0, so for a discussion on these results is referred to the previous paragraph for the test case with σ = 0. The only difference with the solution for σ = 0 is that some scattering

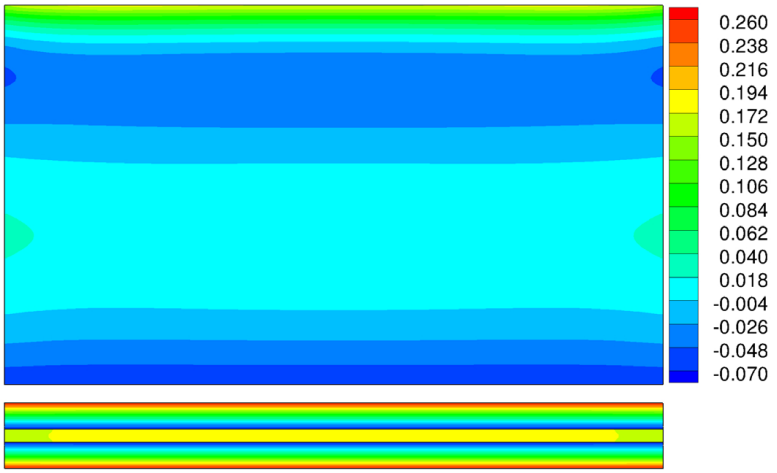

(a)

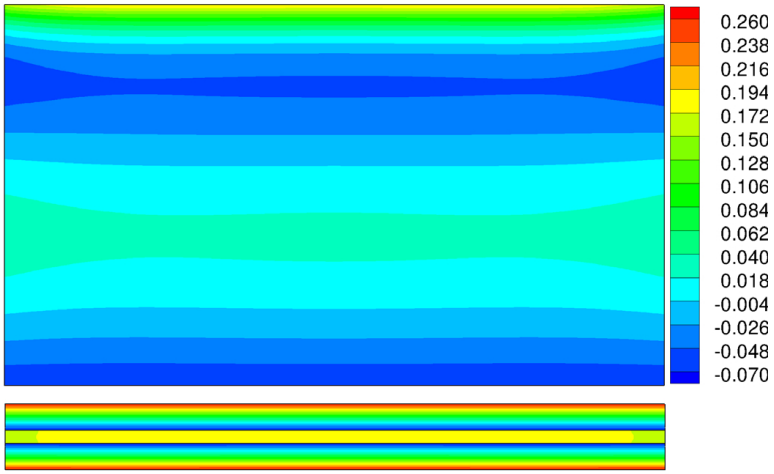

(b)

Figure 3.32: 2-D plot of relative error on the estimated $\tilde{h}_i$ for the solution of a linearly varying h_i along the fin height with σ=0K. (a) SDM solution ; (b) CGM solution

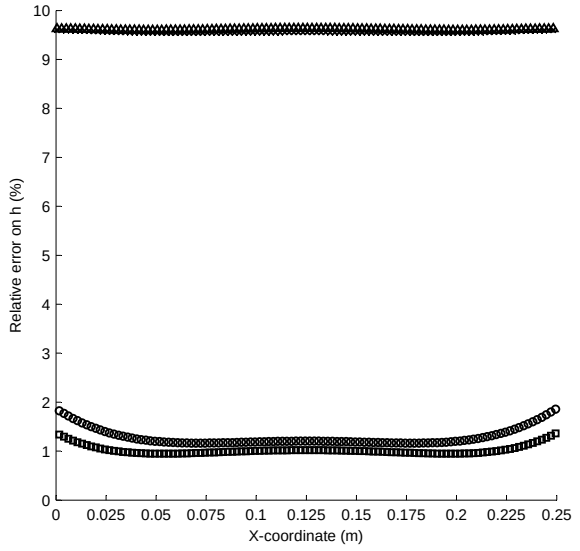

(a) □: SDM at L_1 ; ○: CGM at L_1 ; ×: SDM at L_2 ; △: CGM at L_2

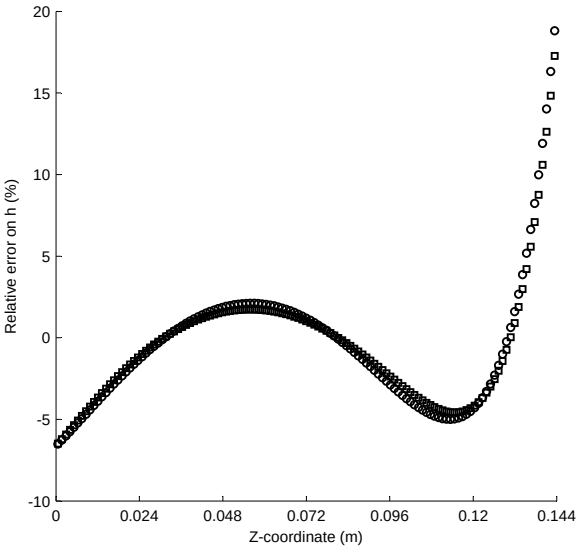

(b) □: SDM at L_3 ; ○: CGM at L_3

Figure 3.33: Relative error on $\tilde{h}_i$ for linear varying h_i along the fin height with σ=0K for $Y_m(S_i)$, plotted along the evaluation lines $L_1 - L_3$

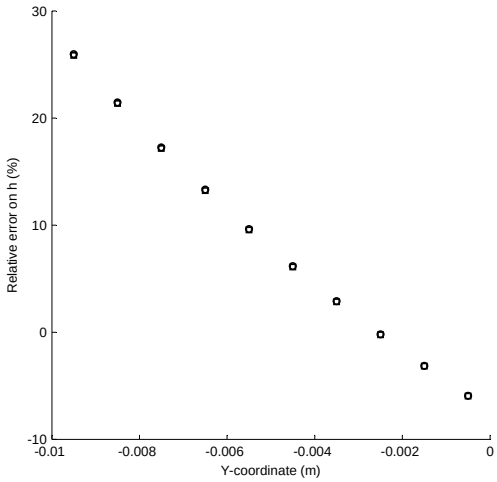

Figure 3.34: Relative error on $\tilde{h}_i$ for linear varying h_i along the fin height for σ=0K for $Y_m(S_i)$; □: SDM at L_4 ; ∘: CGM at L_4

of the order of 1% is added to the estimated $\tilde{h}_i$. This is small compared to the error already present for the estimates based on exact temperature measurements. Hence, the solution for less accurate temperature measurements does not worsen considerably for both SDM and CGM. The same conclusion was found for temperature measurements with an accuracy of 0.5°C (σ = 0.25): the solution still has the same trend, but the scatter on the estimated $\tilde{h}_i$ has increased again. The results for σ = 0.25 are not shown or discussed, because they do not provide a better insight.

The mean relative error on $\tilde{h}_i$ is listed in Table 3.8 for various surfaces. It is remarkable that the mean values decreased for the CGM solution, and this for all surface. The mean values $\tilde{h}_avg$ of the SDM solution slightly increased, but this increase in error is negligible.

		SDM	CGM
	h_{avg} (W/m^{2}K)	ERRh (%)	ERRh (%)
Fin tip S_1	10	18.85	18.11
Front S_5	24.95	-0.88	-0.83
Primary S_6	34.45	8.27	7.71

Table 3.8: The average values for ERRh for a linearly varying heat transfer coefficient along the fin height with σ=0.05K.

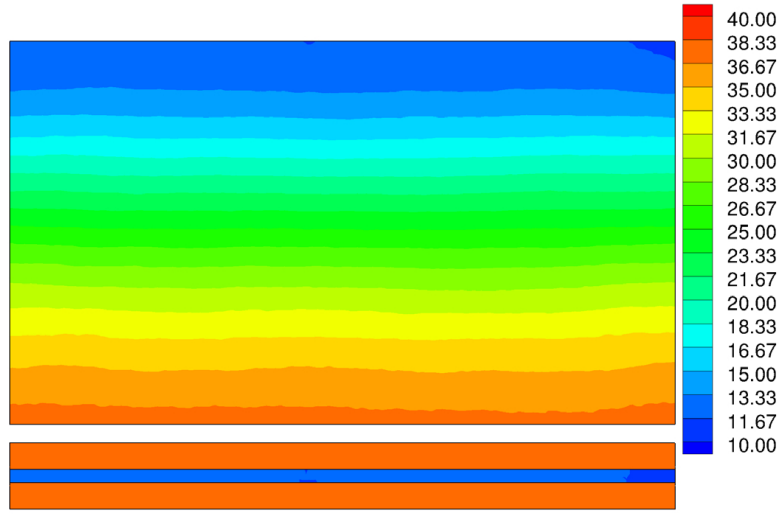

(a)

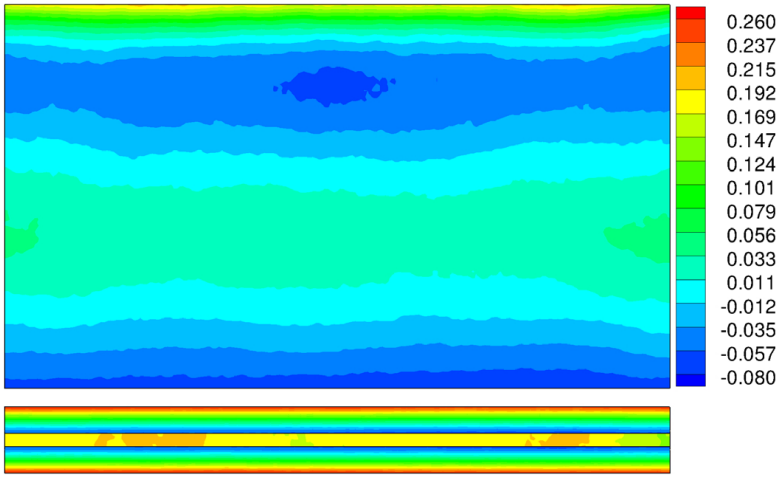

(b)

Figure 3.35: 2-D plot of the CGM solution for the IHCP with linearly varying h_i along the fin height with σ=0.05K. (a) estimated $\tilde{h}_i$; (b) relative error on $\tilde{h}_i$

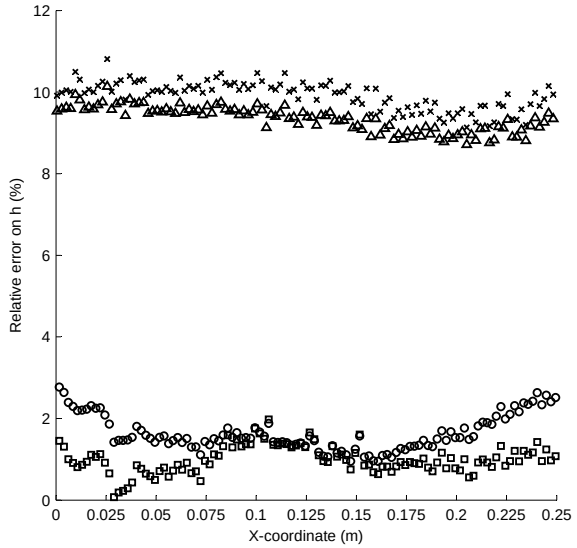

(a) □: SDM at L_1 ; ○: CGM at L_1 ; ×: SDM at L_2 ; △: CGM at L_2

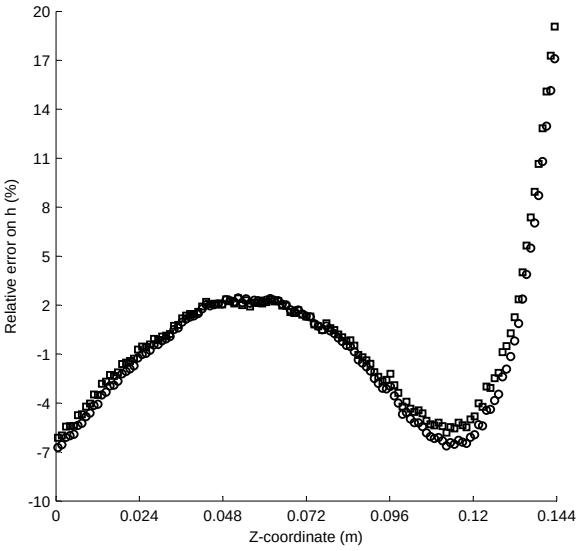

(b) □: SDM at L_3 ; ○: CGM at L_3

Figure 3.36: Relative error on $\tilde{h}_i$ for linear varying h_i along the fin height with σ=0.05K plotted along the evaluation lines $L_1 - L_3$

3.1.4 Exponential variation along fin length

This heat transfer coefficient profile is based on the boundary layer thickness for a given air speed along the fin, yet only a variation along the fin length is considered. The heat transfer coefficient profile h_i is shown in Fig.3.37. The air flow goes from the left to the right of the fin.

3.1.4.1 Exact measurement data: σ=0

There is a high peak of the heat transfer coefficient at the left side of the fin, where the boundary layer begins to build up. The exponential profile of the exact h_i is plotted in Fig. 3.37. The steep peak of $100\mathrm{W/m^2K}$ at the left side is clearly visible in the line plot along the fin length (Fig. 3.38(a)). This high value drops very sharply to $20\mathrm{W/m^2K}$ over just 10 cells and then steadily decreases to $6\mathrm{W/m^2K}$ at the right side. This is a difficult test case for a whole domain method: h_i has a peak value between 50 and $100\mathrm{W/m^2K}$ in less than 2% of the fin surface cells, and h_i is much lower (10% of the peak value) in 80% of the fin cells. Even though exact temperatures are used (σ=0), the stopping criterion was set at χ=1, which is much higher than χ=0.01 in the previous studies. Even for this higher convergence criterion, both methods needed long calculation times: CGM converged only after 560 iterations, and SDM took such a long convergence time that the calculation was stopped before the convergence criterion was attained. Therefore a different h_i-profile was used for SDM with a peak value of only $55\mathrm{W/m^2K}$. SDM reached a residual value of 170 after 400 iterations. At this rate of convergence, the residual would only drop below the convergence criterion of 1 after more than 2500 iterations. Therefore the SDM solution was stopped after 400 iterations for J=170, which corresponds to a temperature error of 0.1°C on the estimated temperatures. This indicates that both algorithms, but especially SDM, have difficulties to accurately reconstruct this kind of profile.

The resulting estimated $\tilde{h}_i$ are plotted in Fig. 3.40. The results along the four evaluation lines L_1 – L_4 show more details (Fig. 3.38). The detailed graphs for the relative error on $\tilde{h}_i$ along the evaluation lines are shown in Fig. 3.41.There are no 2D-plots shown for the relative error because these do not give any extra information compared to the line plots.

It is clear from Fig. 3.38 and Fig. 3.41 that the SDM solution has not converged as far as the CGM solution, and that the SDM solution gives bad results in reconstructing the peak at the left side. Therefore, only the CGM solution will be discussed. Figure 3.38(a) and Fig. 3.40 show that CGM reconstructs the trend of h_i variation, but swirls around the exact solution. CGM also estimates a peak at the left side, but reaches only a value of $60\mathrm{W/m^2K}$ and the peak is not so steep. This is actually not so bad, since the the highest h_i-value of $100\mathrm{W/m^2K}$ is only imposed on less than 0.5% of the cells. Figure 3.41(a) represents the relative errors

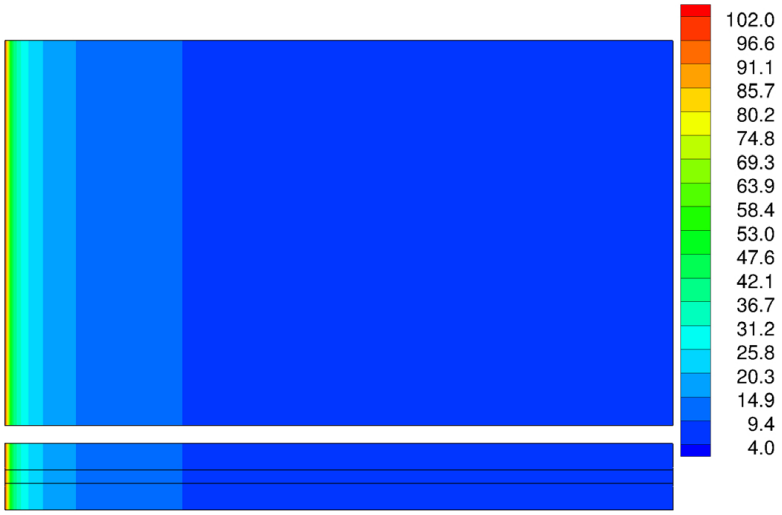

Figure 3.37: 2-D plot of the exponentially varying exact heat transfer coefficient h_i (in $\mathrm{W/m^2K}$) along the fin length

on $\tilde{h}_i$ and shows the oscillation more clearly. This was never found for the previously studied profiles, in which these large errors only appeared near the edges. The higher oscillation amplitude at the left side is induced by the steep gradient for h_i which is difficult to reconstruct for a whole-domain method. Important relative errors are obtained over the entire length of the fin, but this result should be nuanced: the high relative errors between 60% and -30% occur only at the first 10% (x=0-0.05m) of the fin length for the higher h_i values, but then the error decreases rapidly to 15% (for x=0.05m) and keeps oscillating between 10% and -10% till the end of the fin (x=0.25m). The values of the exact h_i between x=0.05-0.25m are smaller than $10\mathrm{W/m^2K}$. The variation of the error along the fin height is limited and does not show these oscillations (Fig. 3.41(b)). The large oscillations round the exact solution are thus introduced by the peak value. It was found by investigating the solution at previous iterations that the frequency of this oscillation was lower, but that it had a larger amplitude. This can be illustrated with the SDM solution (Fig. 3.41(a)): the iteration process was stopped at a higher residual, and the result oscillates just over one period with a constantly large amplitude. By converging deeper, the estimated $\tilde{h}_i$ approaches the exact h_i (smaller error amplitude) but it starts oscillating round the exact solution. This oscillation is likely due to the regularization that is added to the solution procedure: this guarantees a smooth solution, but can also induce the oscillation. If only the plots of relative error on

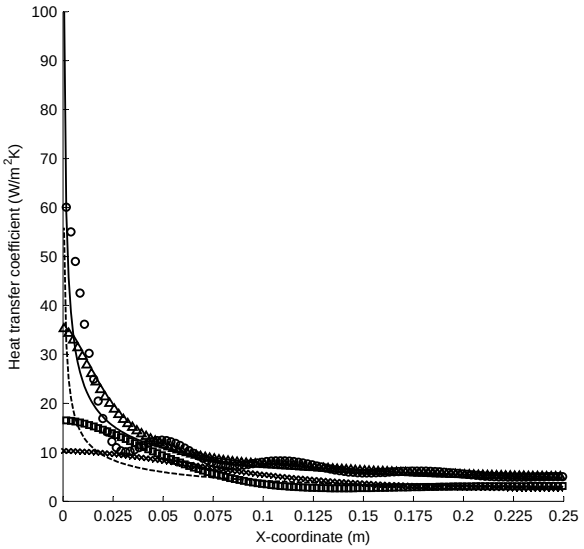

(a) □: SDM at L_1 ; ○: CGM at L_1 ; ×: SDM at L_2 ; Δ: CGM at L_2 ; −: exact solution CGM ; −−: exact solution SDM

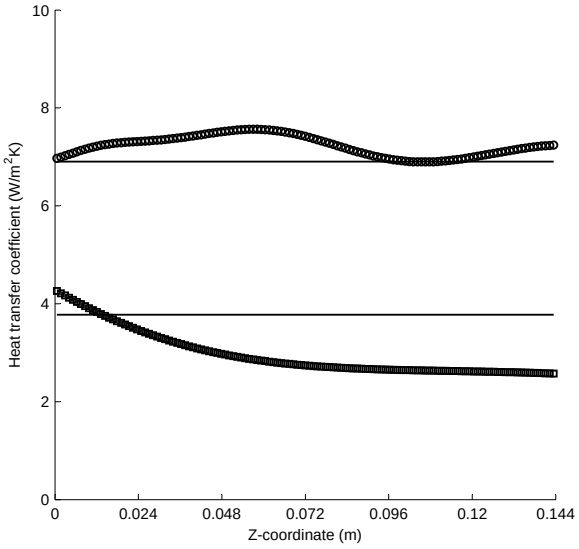

(b) □: SDM at L_3 ; ○: CGM at L_3

Figure 3.38: Estimated $\tilde{h}_i$ for exponentially varying h_i along the fin length with σ=0K, plotted along the evaluation lines $L_1 - L_3$

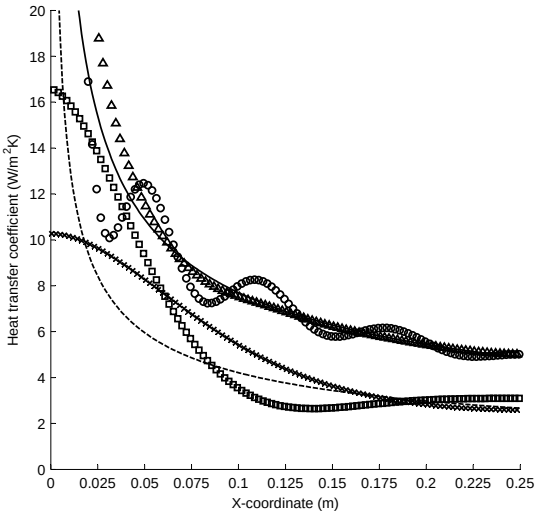

(a) □: SDM at L_1 ; ○: CGM at L_1 ; ×: SDM at L_2 ; Δ: CGM at L_2 ; −: exact solution CGM ; −−: exact solution SDM

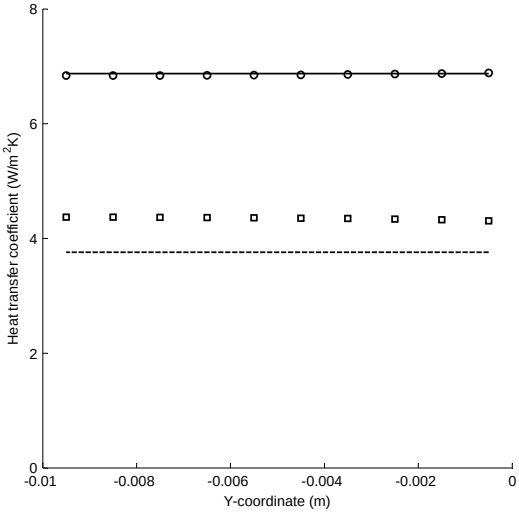

(b) □: SDM at L_4 ; ○: CGM at L_4

Figure 3.39: Estimated $\tilde{h}_i$ for exponentially varying h_i along the fin length with σ=0K, plotted along the evaluation lines L_1 and L_3 on a smaller scale, and along L_4

$\tilde{h}_i$ were studied (Fig. 3.41), a wrong conclusion could be drawn as were the CGM solution unsufficient. However, Fig. 3.38 and Fig. 3.40 indicate that CGM gives an acceptable reconstruction of the imposed heat transfer coefficient profile, and that the absolute errors are limited.

It is remarkable that the oscillation on the primary surface is much smaller: there is no high frequency oscillation, and the imposed h_i-profile near the right side is estimated accurately. However, the estimate of amplitude of the peak value near the left is less accurate.

The mean relative error on $\tilde{h}_i$ (ERRh) is listed in Table 3.9 for various surfaces. These mean values show that the SDM solution did not converge far enough: it has considerably larger errors than CGM. Also for CGM the error on the mean $\tilde{h}_{avg}$ has increased significantly for the fin surfaces compared to the other test cases: from less than 1% to 4%. The accuracy on the mean $\tilde{h}_{avg}$ for the primary surface on the other hand has improved. The effect of this on the fin effectiveness is discussed later.

		SDM	CGM
	h_{avg} ($\mathrm{W/m^2K}$)	ERRh (%)	ERRh (%)
Fin tip S_1	9.54	6	2.96
Front S_5	9.53	7.17	4.12
Primary S_6	9.41	1.97	0.35

Table 3.9: The average values for ERRh for an exponentially varying heat transfer coefficient along the fin length with σ=0K.

3.1.4.2 Temperature measurement error: dY_m = 0.5°C or σ=0.25

The discussion of the influence of the temperature measurement accuracy on the IHCP solution will be limited to the case of a temperature measurement error of 0.5°C, because this produces the largest error on $\tilde{h}_i$. The CGM reaches the convergence criterion χ = 3859 after 59 iterations, SDM after 490 iterations. The results for SDM and CGM are similar to the previous case with exact temperature measurements. The resulting estimated $\tilde{h}_i$ of the CGM solution is plotted in Fig. 3.42(a), and the relative error on $\tilde{h}_i$ in Fig. 3.42(b). The 2D-plots of the SDM solution are not shown, as the results is largely the same as for the previous case (σ = $0K$) (Fig. 3.43): even the relative errors on $\tilde{h}_i$ for the SDM solution remain the same (Fig. 3.44). This is not surprising, as the SDM solution for the exact temperature measurements was only converged to a residual of 170, which corresponds to a temperature measurement accuracy of 0.1°C.

For a detailed discussion on the results is referred to the previous paragraph, as the solution shows the same general trend as for the case with σ = 0. The large

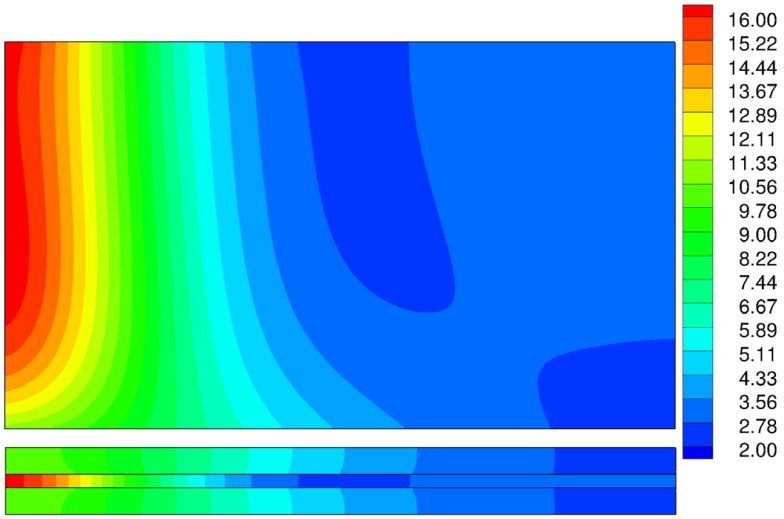

(a)

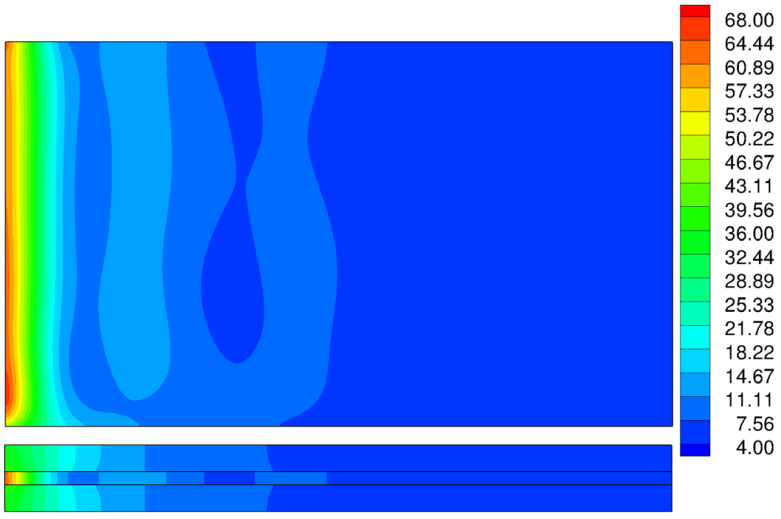

(b)

Figure 3.40: 2-D plot of the estimated $\tilde{h}_i$ for the solution of an exponentially varying h_i along the fin length with σ=0K. (a) SDM solution ; (b) CGM solution

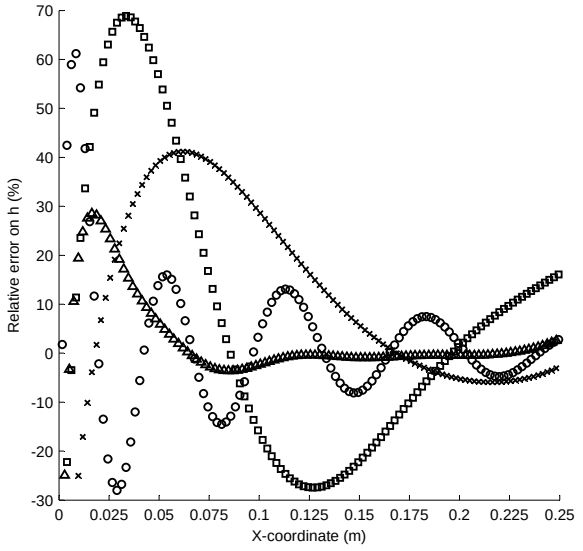

(a) □: SDM at L_1 ; ○: CGM at L_1 ; ×: SDM at L_2 ; △: CGM at L_2

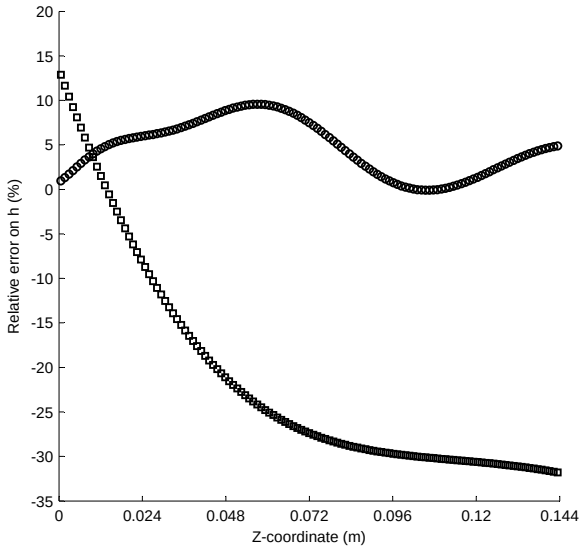

(b) □: SDM at L_3 ; ○: CGM at L_3

Figure 3.41: Relative error on $\tilde{h}_i$ for exponentially varying h_i along the fin length with σ=0K, plotted along the evaluation lines $L_1 - L_3$

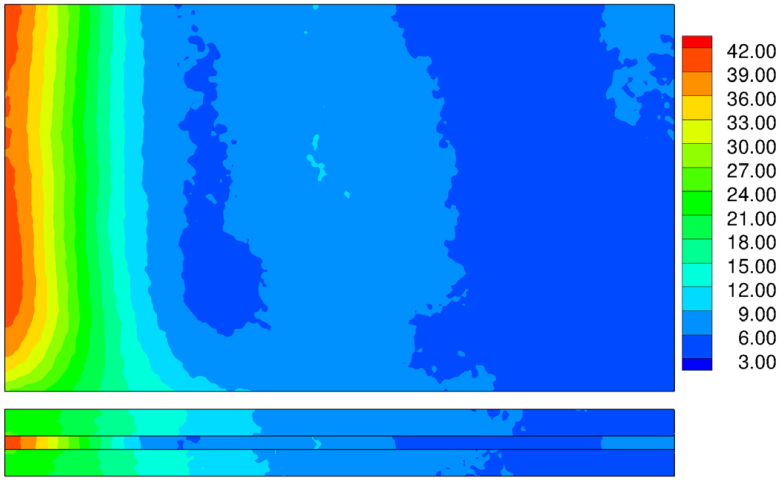

(a)

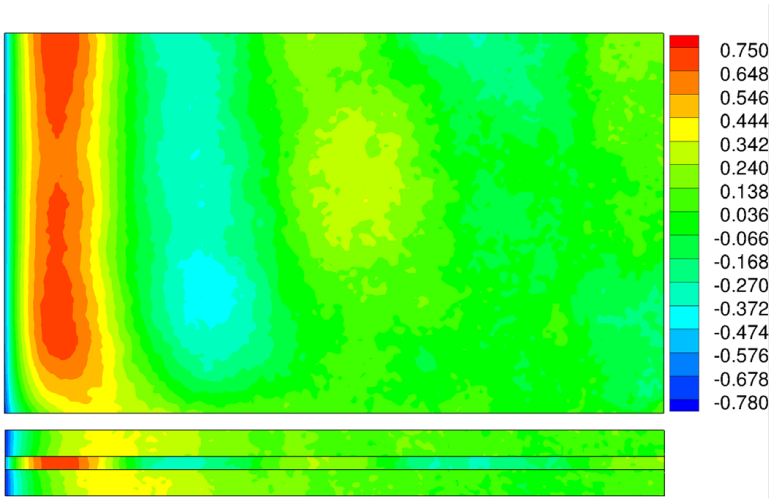

(b)

Figure 3.42: 2-D plot of the CGM solution for the IHCP with exponentially varying h_i along the fin height with σ=0.25K. (a) estimated $\tilde{h}_i$; (b) relative error on $\tilde{h}_i$

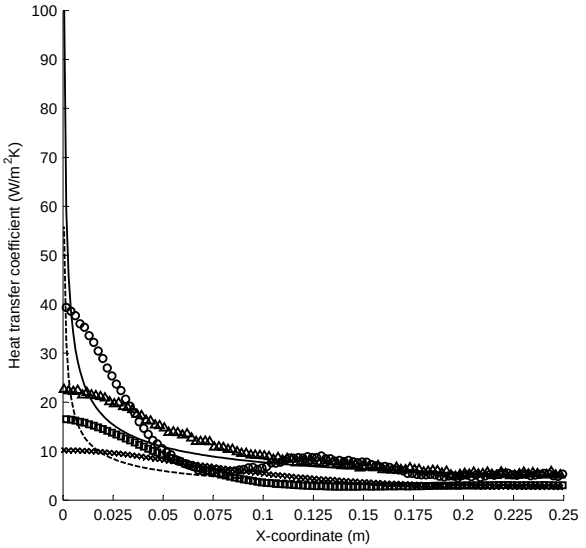

(a) □: SDM at L_1 ; ○: CGM at L_1 ; ×: SDM at L_2 ; Δ: CGM at L_2

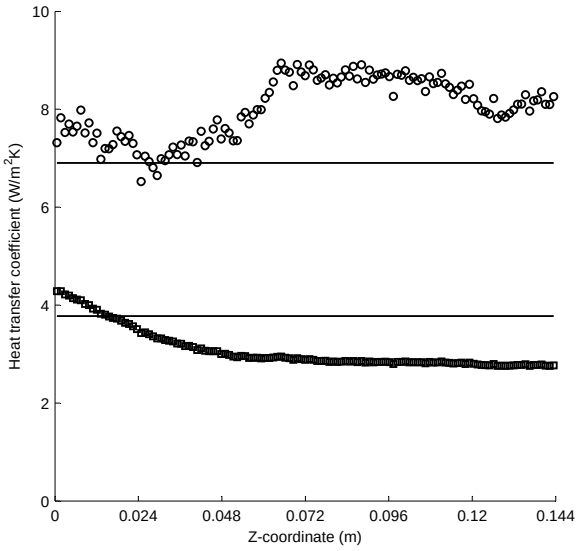

(b) □: SDM at L_3 ; ○: CGM at L_3

Figure 3.43: Estimated $\tilde{h}_i$ for exponentially varying h_i along the fin length with σ=0.25K, plotted along the evaluation lines $L_1 - L_3$

temperature measurement error deteriorates the accuracy of the CGM solution: scattering is added to the estimated $\tilde{h}_i$, which is very distinct for the right half of the fin because of the low heat transfer coefficients ($h_i < 8\mathrm{W/m^2K}$). The large temperature measurement error causes a less accurate reconstruction of the peak value: $40\mathrm{W/m^2K}$ compared to $60\mathrm{W/m^2K}$ for $\sigma = 0$. The oscillation of the estimated $\tilde{h}_i$ round the exact solution has a smaller frequency, but the larger errors of more than 30% occurs for the complete left side of the fin, compared to only 20% of the fin surface for $\sigma = 0$ (Fig. 3.44(a)). Figures 3.44(b) and 3.43(b) show that an error of 30% halfway the fin length corresponds to an absolute error of $2\mathrm{W/m^2K}$. Notwithstanding these large relative errors, the absolute errors are limited for $\tilde{h}_i$ which are not in the peak. The general form of the heat transfer coefficient profile is reconstructed with the CGM, even for considerable temperature measurement errors (0.5°C). The peak is reconstructed, but it is difficult to estimate the exact value of this peak as it only applies to a very limited amount of cells (less than 2%).

The mean relative error on $\tilde{h}_i$ is listed in Table 3.10 for various surfaces. The mean values for the SDM solution did not increase much, but ERRh increased for CGM and attained the same order of magnitude as the SDM solution. The smallest error occurs again at the primary surface.

		SDM	CGM
	h_{avg} ($\mathrm{W/m^2K}$)	ERRh (%)	ERRh (%)
Fin tip S_1	9.54	6.58	6.08
Front S_5	9.53	7.15	6.1
Primary S_6	9.41	5.26	2.29

Table 3.10: The average values for ERRh for a linearly varying heat transfer coefficient along the fin height with σ=0.05K.

3.1.5 Simulated convection coefficient profile with FLUENT

This heat transfer coefficient profile is based on a numerical simulation from a full CFD model in FLUENT: the air flow around the fin is modeled. The air flow was set at 1 $\mathrm{m/s}$. As the results should be independent of the boundary positions, the air entrance and exit section should be sufficiently far from the fin surfaces. Based on [5] the entrance and exit region were placed at 20 times the fin thickness from the fin. The side boundary conditions were set as symmetry planes at a distance of 20 times the fin thickness from the fin walls. Air was modeled as an ideal gas and the viscous laminar model was used as the Re-number is situated in the laminar flow regime. This case was calculated for exact measurement data (σ=0). Only the CGM solution was discussed in this paragraph as this gave the best results in

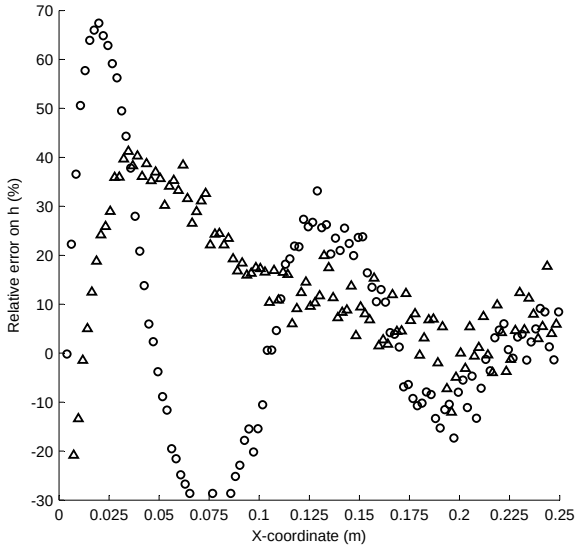

(a) ○: CGM at L_1 ; Δ: CGM at L_2

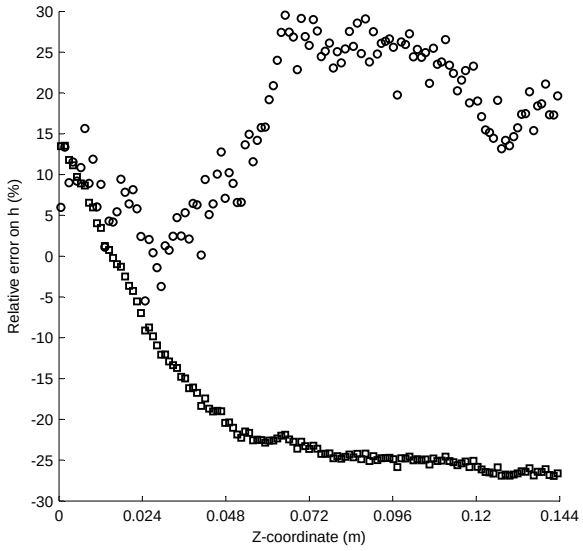

(b) □: SDM at L_3 ; ○: CGM at L_3

Figure 3.44: Relative error on $\tilde{h}_i$ for exponentially varying h_i along the fin length with σ=0.25K plotted along the evaluation lines $L_1 - L_3$

the previous test cases.

The heat transfer coefficient profile h_i obtained from the CFD calculation is shown in Fig.3.45. The air flow goes from the left to the right of the fin. There is a high, small peak of the heat transfer coefficient at the left side of the fin, where the boundary layer begins to build up. The steep peak of over 20 $\mathrm{W/m^2K}$ at the left side is clearly visible in the line plot along the fin length (Fig. 3.46(a)). This high value drops very sharply to 3 $\mathrm{W/m^2K}$ after which there is a small oscillation: a sharp increase to 5 $\mathrm{W/m^2K}$ followed by a steep drop to 4 $\mathrm{W/m^2K}$ which is maintained over a few cells. This seems very strange but can be explained after investigating the flow pattern around the fin. The starting boundary layer at the front of the fin seperates immediately and there is a recirculation zone, which causes the drop of the heat transfer coefficient. This recirculation zone exists of two recirculations which causes the oscillation in h_i. This recirculation appears only for 25 mm(one tenth of the fin length) which corresponds to the observed h_i-profile. After this recirculation zone there is a boundary layer reacttachment which causes the increase in h_i (Fig. 3.46(a)). The boundary layer is built up giving a steady decrease of h_i. There is a small increase in h_i again for the last $10\mathrm{mm}$ of the fin due to boundary layer thinning near the trailing edge. The variation of h_i along the fin height halfway the fin length (Fig. 3.46(b)) is very unsteady and oscillates around a mean value of 5 $\mathrm{W/m^2K}$. These oscillations are caused by a variation in boundary layer seperation and reattachment along the fin height at the leading edge.

This is a difficult test case for a whole domain method due to the numerous variations over small fin areas. Especially the steep drop in h_i at the leading edge and the oscillations due to the recirculation zone are very difficult to reconstruct as these variations appear for a very small part of the fin area and cause small fin temperature variations in that area (due to the high conductivity of the aluminum). The IHCP solution was evaluated for two stopping criteria: χ=1 and χ=10. This is much higher than χ=0.01 in the previous test cases. Even for this higher convergence criterion, CGM needed long calculation times: 300 iterations for χ=10, 1200 iterations for χ=1.

The resulting estimated $\tilde{h}_i$ are plotted in Fig. 3.48 for J = 1. The results along the three evaluation lines L_1 – L_3 show more details for both J = 10 and J = 1 (Figures 3.46-3.47). There are no 2D-plots shown for the relative error because these do not give any extra information compared to the line plots.

It is clear from Figures 3.46-3.47 that the solution for J = 10 has not converged as far as the solution for J = 1. The solution for J = 10 along L_1 does not reconstruct the h_i variation in detail. It shows a peak at the leading edge followed by a drop (boundary layer seperation) and a small increase (flow reattachment) but this increase is not distinct, and the location for the dip due to the seperation is not correct. However, for the IHCP solution at J = 1, the dip due to boundary layer

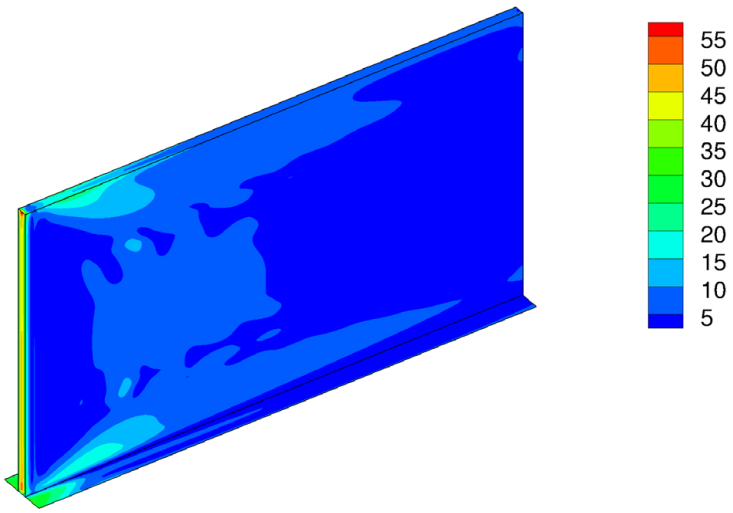

Figure 3.45: 3-D plot of the numercically simulated exact heat transfer coefficient h_i (in $\mathrm{W/m^2K}$) for an air velocity of $1\mathrm{m/s}$

seperation is more distinct and at the correct position, as is the increase of h_i due to boundary layer reattachment. The peak at the leading edge is also reconstructed. Thus the general trend is reconstructed, only smaller variations over small areas are not reconstructed, as they do not have enough influence on the temperature profile. The same can be concluded for the solution along the fin height line L_3. The IHCP solution along L_2 on the primary surface also reconstructs the correct h_i profile, but there is an inaccuracy on the position of the curve inflexion point and the steep gradient of h_i near the leading edge. It can be concluded from comparison between the solution for J = 10 and J = 1 that an IHCP solution needs to be converged far enough in order to reconstruct profiles with more unsteady variations and very small variations are difficult or even impossible to reconstruct. Figure 3.47 shows that the estimated $\tilde{h}_i$ starts to swirl around the exact solution the more iterations are performed, but these oscillations have a very small amplitude. The relative error on the estimated $\tilde{h}_i$ for the solution with J = 1 is shown in Fig. 3.49. The relative error along L_1 is smaller than 10% for 80% of the cells and becomes very large (up to 100%) for only a few cells near the steep gradient and recirculation zone at the leading edge. This large relative error applies to small h_i values of 5 $\mathrm{W/m^2K}$. A similar conclusion can be drawn for the relative errors on h_i along the fin height (L_3): the relative error is smaller than 15% for more than 80% of the cells and the larger errors occur at variations with a steep gradient over a small fin area. So

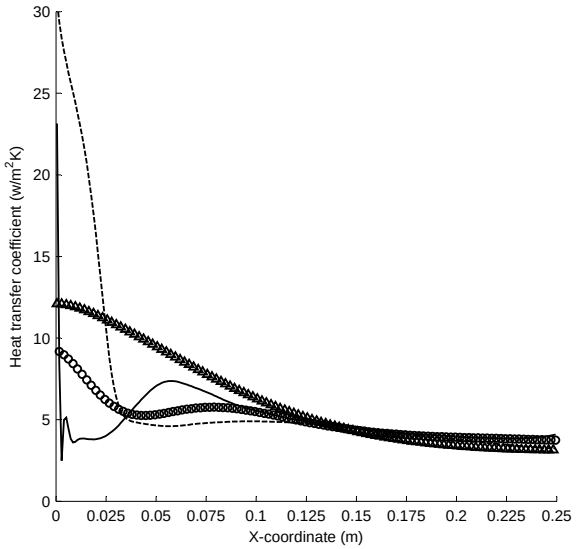

(a) ∘: CGM at L_1 ; Δ: CGM at L_2 ; $-$: exact solution at L_1 ; $--$: exact solution at L_2

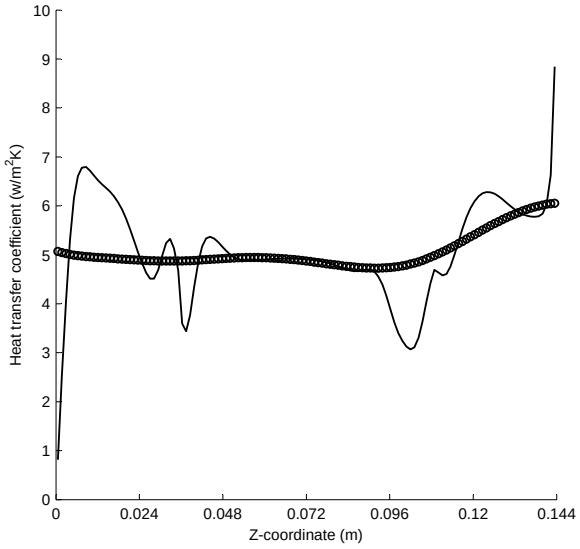

(b) ∘: CGM at L_3; $-$: exact solution at L_3

Figure 3.46: Estimated $\tilde{h}_i$ for the numerically simulated h_i for air velocity of $1\mathrm{m/s}$ with σ=0 plotted along evaluation lines $L_1 - L_3$ for $J = 10$

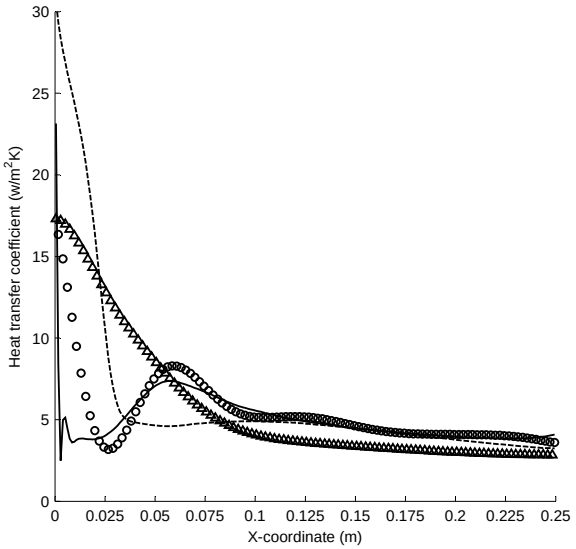

(a) ∘: CGM at L_1 ; Δ: CGM at L_2 ; $-$: exact solution at L_1 ; $--$: exact solution at L_2

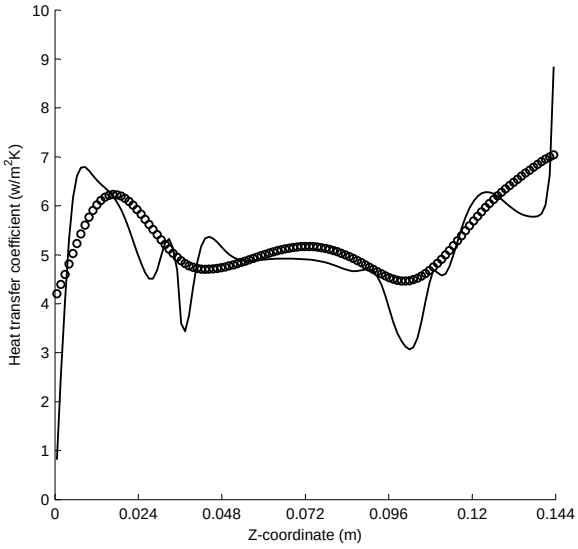

(b) ∘: CGM at L_3; $-$: exact solution at L_3

Figure 3.47: Estimated $\tilde{h}_i$ for the numerically simulated h_i for air velocity of $1\mathrm{m/s}$ with σ=0K, plotted along evaluation lines $L_1 - L_3$ for $J = 1$

CGM gives good results for a realistic heat transfer coefficient profile calculated from CFD simulations. Moreover, the mean value of the convection coefficients over the fin surface is 5 $\mathrm{W/m^2K}$ which is much smaller than the average h_i of 25 $\mathrm{W/m^2K}$ in the previous test cases. Thus CGM also gives good solutions for smaller heat transfer coefficients.

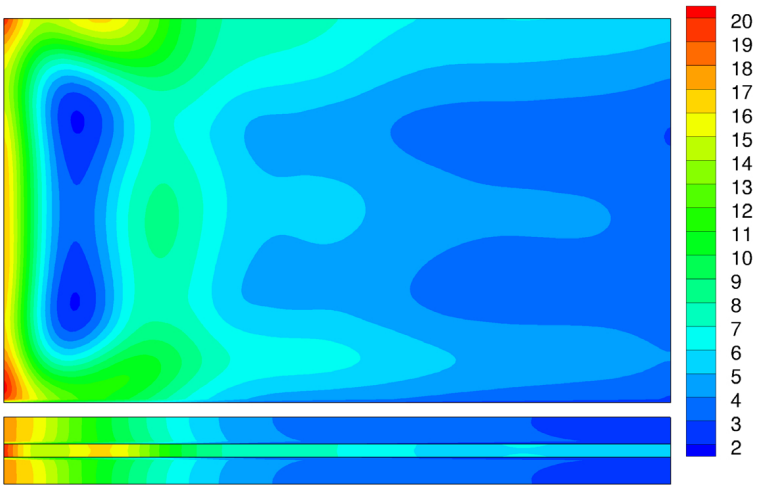

Figure 3.48: 2-D plot of the estimated $\tilde{h}_i$ for the numerically simulated h_i for air velocity of $1\mathrm{m/s}$ with σ=0K and for J = 1

The mean relative error on $\tilde{h}_i$ (ERRh) is listed in Table 3.11 for various surfaces. These mean values show that CGM gives a good estimation of the mean h_{avg} for the fin front surface and primary surface.

	h_{avg} ($\mathrm{W/m^2K}$)	ERRh (%)
Fin tip S_1	9.52	19.8
Front S_5	5.42	6.3
Primary S_6	6.91	10.1

Table 3.11: The average values for ERRh the numerically simulated h_i for air velocity of $1\mathrm{m/s}$ with σ=0K

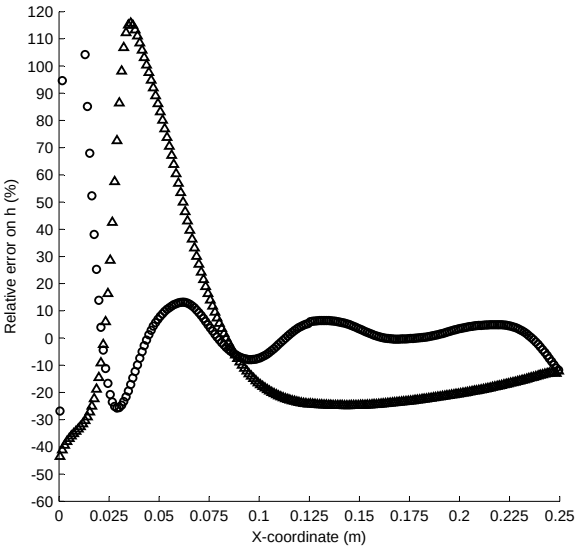

(a) ∘: CGM at L_1 ; Δ: CGM at L_2 ; $-$: exact solution at L_1 ; $--$: exact solution at L_2

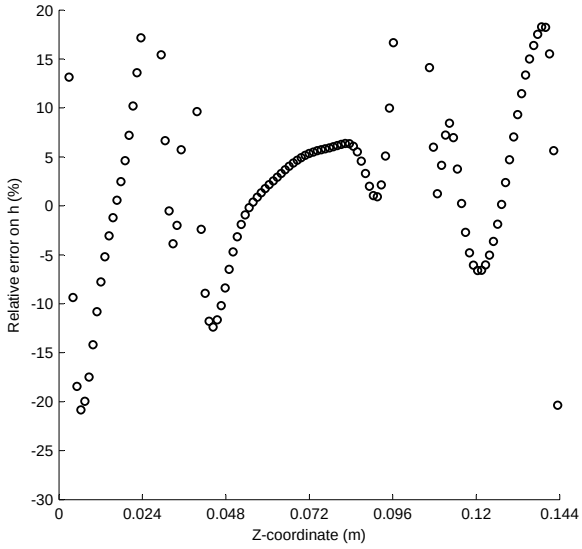

(b) ∘: CGM at L_3; $-$: exact solution at L_3

Figure 3.49: Relative error on $\tilde{h}_i$ for the numerically simulated h_i for air velocity of $1\mathrm{m/s}$ with σ=0K, plotted along evaluation lines $L_1 - L_3$ for J = 1

3.1.6 Validity of CGM solution for larger heat transfer coefficients

3.1.6.1 Linear increase in heat transfer coefficients along the fin length from 200 $\mathrm{W/m^2K}$ to 300 $\mathrm{W/m^2K}$ with σ=0

The previous test cases show that the solution method with CGM and SDM gives good results for fin heat transfer problems with a mean h_{avg} value of 25 $\mathrm{W/m^2K}$ and 5 $\mathrm{W/m^2K}$. So the validity is checked for a limited range of Re-numbers. There is no certainty that this solution method still has the same performance for higher Re-numbers (thus higher h_i and h_{avg}) without any modifications. Therefore a test case with a much higher h_{avg} = $250\mathrm{W/m^2K}$ is investigated. A linearly varying heat transfer coefficient profile was used: from 200 $\mathrm{W/m^2K}$ on the right fin surface S_3 to 300 $\mathrm{W/m^2K}$ at the right fin surface S_2. For this test case only the line plots along L_1 – L_3 are shown (Figures 3.50-3.51).

The results in Fig. 3.50 show that the estimated $\tilde{h}_i$ with CGM are very accurate along the fin length and fin height. The relative error is smaller than 0.5% ((Fig. 3.51). This is a much better result than for the numerical test case with a mean heat transfer coefficient h_{avg} = 25 $\mathrm{W/m^2K}$. An accurate interpretation of this result is necessary. The increase in accuracy of the estimations with CGM is not necessarily due to the larger heat transfer coefficients, but mainly due to the variation of the fin temperature. As a larger h_{avg} is applied, a higher heat flux is applied at the bottom surface S_8 so that a noticeable temperature variation over the fin surface is obtained. This higher heat flux gives a larger temperature variation over the fin surface than for the case of h_{avg} = $25\mathrm{W/m^2K}$ (Fig. 3.52). The IHCP solution depends on these temperature variations. The larger the fin temperature variations are, the better the accuracy of the IHCP solution. So the main reason for the increase in accuracy for a numerical test case with a larger mean heat transfer coefficient is the larger temperature variation over the fin surface. Nevertheless, these results show that the application range of the solution method is independent of the Reynolds number.

3.1.7 Results: h_i estimation vs q_i estimation

It was mentioned in section 2.4.4 that the IHCP can also be solved for heat flux estimations $\tilde{q}_i$ instead of heat transfer coefficients $\tilde{h}_i$. Due to the difference in calculating the search step size and direction, the solution for $\tilde{q}_i$ estimation could give different results with regard to stability and accuracy. The comparison is made for the most difficult test case: exponentially varying heat transfer coefficient along the fin length. Exact temperature measurements were assumed (σ = 0, convergence criterion set at 1). CGM was used as solution method for both cases. The CGM method for $\tilde{q}_i$ estimations converged after 293 iterations, and for $\tilde{h}_i$ estimations after 560 iterations. The method for flux estimation is clearly faster. The

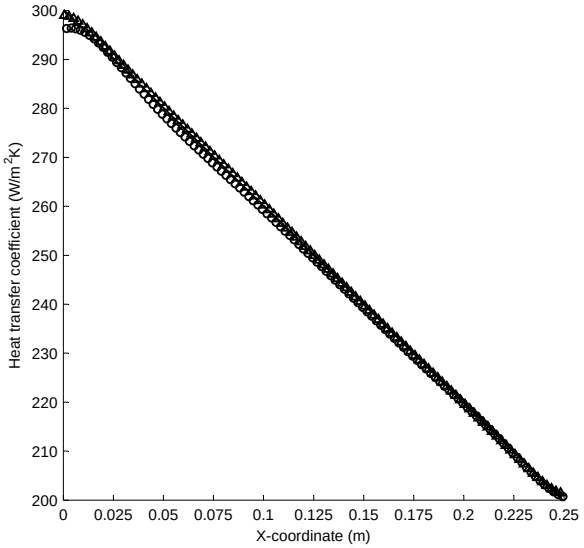

(a) ∘: CGM at L_1 ; Δ: CGM at L_2

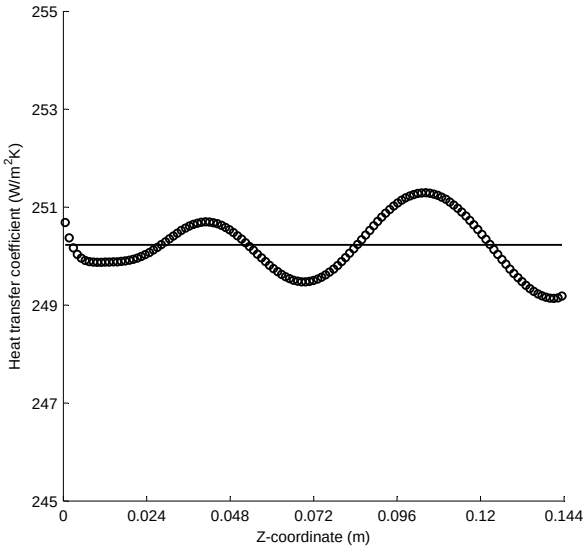

(b) ∘: CGM at L_3

Figure 3.50: Estimated $\tilde{h}_i$ for a linearly varying heat transfer coefficient profile from 200$\mathrm{W/m^2K}$ to 300 $\mathrm{W/m^2K}$ plotted along the evaluation lines $L_1 - L_3$

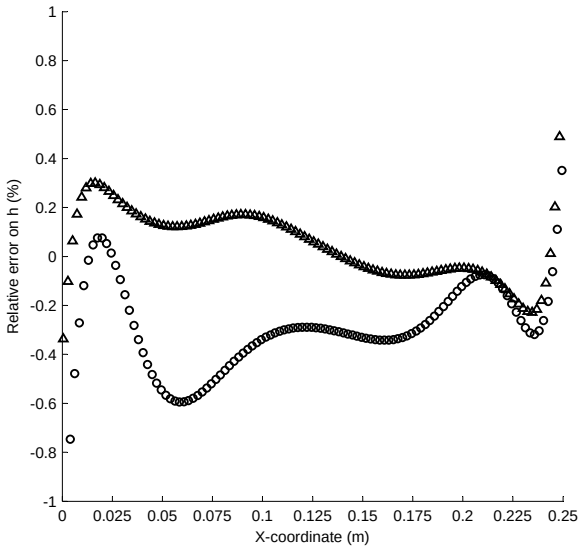

(a) ∘: CGM at L_1 ; Δ: CGM at L_2

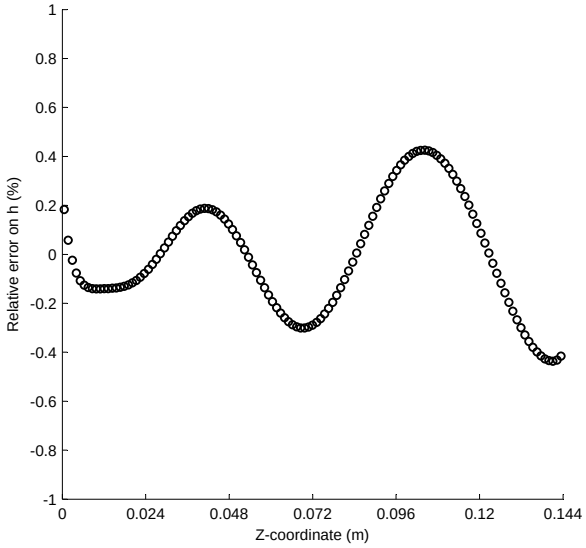

(b) ∘: CGM at L_3

Figure 3.51: Relative error on $\tilde{h}_i$ for a linearly varying heat transfer coefficient profile from 200$\mathrm{W/m^2K}$to 300 $\mathrm{W/m^2K}$plotted along the evaluation lines $L_1 - L_3$

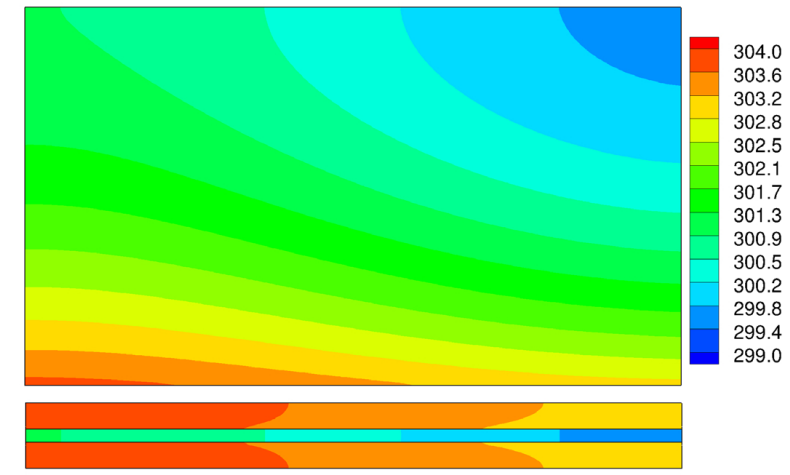

(a)

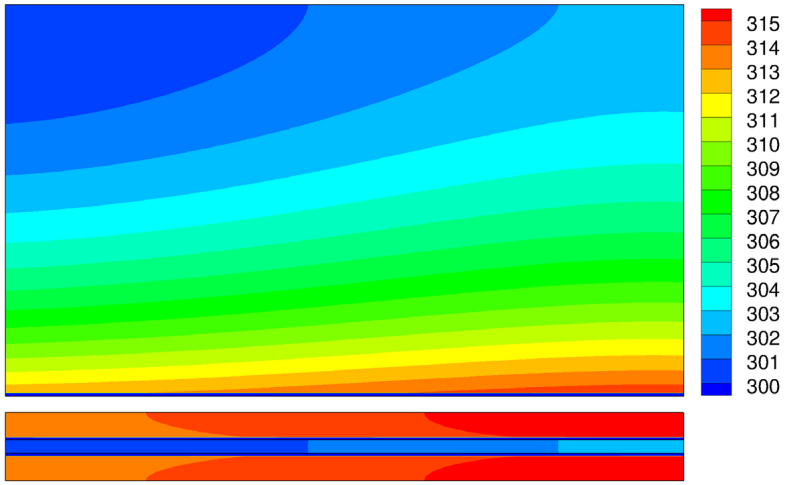

(b)

Figure 3.52: 2-D plot of the temperature profiles for a linearly varying h_i along the fin length (a) h_{avg} = $25\mathrm{W/m^2K}$; (b) h_{avg} = $250\mathrm{W/m^2K}$

comparison between both solutions is shown in Figures 3.53-3.54.

There is no need for a long discussion, because the results are clear: there is no significant difference in accuracy between the solution method for $\tilde{h}_i$ and $\tilde{q}_i$ estimation. The solution for $\tilde{q}_i$ converges faster, so logically the solution method for $\tilde{q}_i$ estimation would be chosen. However, there is a complication. The solution method for the IHCP is based on FLUENT to solve the direct, adjoint and sensitivity method. FLUENT is a finite volume method and the heat balance has to be closed for each iteration i.e. the amount of heat that enters the fin and primary surface has to leave it also when steady calculations are performed. If a convection coefficient profile is used as boundary condition, FLUENT can adjust the temperature field to obtain a closed heat balance. However, when heat fluxes q_i are set as boundary conditions, the heat balance cannot be changed by FLUENT by adjusting the temperature field. Also, this problem is underdefined, there is a need for a temperature boundary condition to get a well defined problem. Therefore one of the measured temperature surfaces S_1 – S_7 has to be set as a temperature boundary condition instead of a heat flux boundary condition. If this is done, FLUENT can solve the problem and will close the heat balance over the temperature surface. In the first few iterations this will lead to high positive and negative heat fluxes in this surface, depending on the accuracy of the initially guessed $\tilde{q}_i$. In order to obtain a good accuracy with this method, a well considered choice for the temperature surface has to be made. It was found that the surface with the lowest heat flux gave the best results as temperature boundary condition. However, there still remains a large error near the edges of this surface, and there is no rule for the choice of this surface in real conditions. Therefore the solution method using $\tilde{q}_i$ estimates was not used in this work, because it leads to more assumptions, and the use of $\tilde{h}_i$ estimations creates a straightforward problem.

This conclusion applies for steady state problems only. Transient IHCPs can easily be solved using $\tilde{q}_i$ estimates, as the heat dissipation in the fin is then considered.

3.2 Results for fin effectiveness

The fin effectiveness is also calculated for each of the previously discussed cases of this chapter. The fin has a width of $5\mathrm{mm}$ for a primary surface of $25\mathrm{mm}$ thick. Thus the primary surface area taken by the fin is 1/5 of the total primary surface area. The heat flux on the primary surface is uniform in absence of the fin, and thus 1/5 of the imposed heat at the bottom of the primary surface flows through the primary surface area on which the fin will be placed. This is $2.5\mathrm{W}$ for a total heat generation of $12.5\mathrm{W}$. For each imposed heat transfer coefficient profile the exact fin effectiveness ζ_{ex} is calculated. Afterwards, the fin effectiveness is calculated from the IHCP solutions for different temperature measurement accuracies: σ = 0,

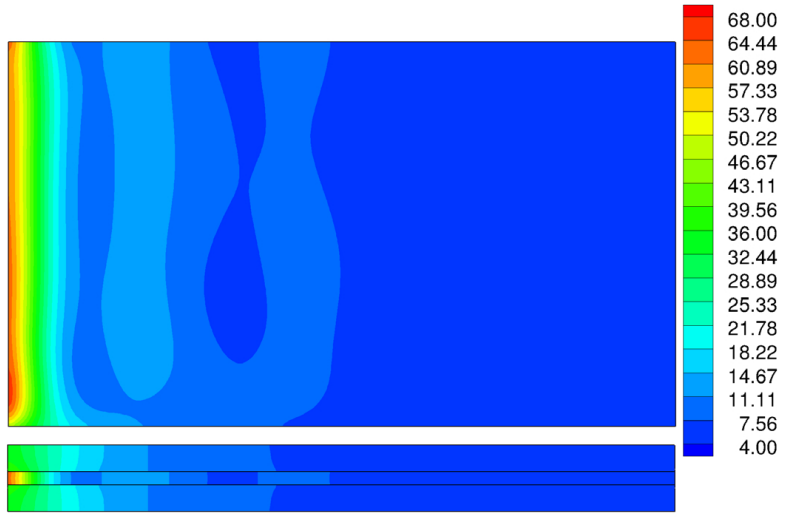

(a)

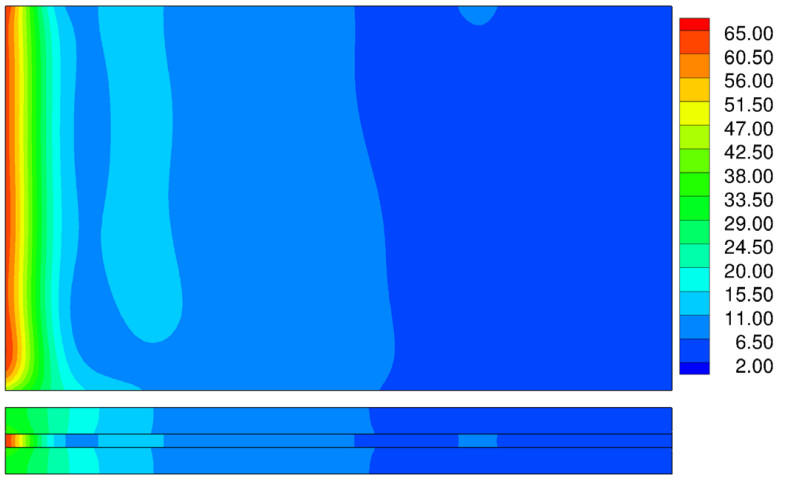

(b)

Figure 3.53: 2-D plot of the estimated $\tilde{h}_i$ for the solution of an exponentially varying h_i along the fin length with σ=0K. (a) $\tilde{h}_i$ solution ; (b) $\tilde{q}_i$ solution

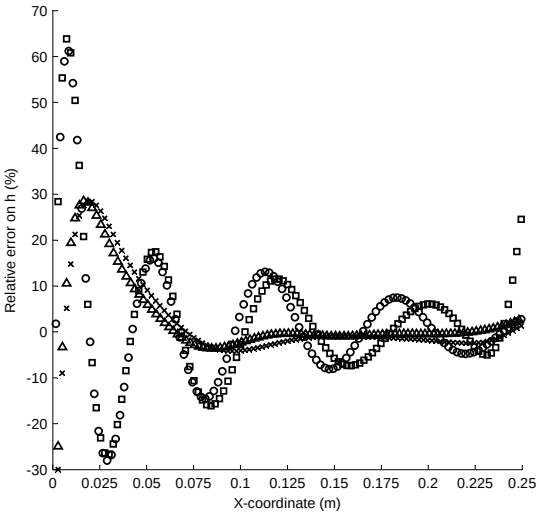

(a) □: $\tilde{q}_i$ solution at L_1 ; ○: $\tilde{h}_i$ at L_1 ; ×: $\tilde{q}_i$ solution at L_2 ; Δ: $\tilde{h}_i$ solution at L_2

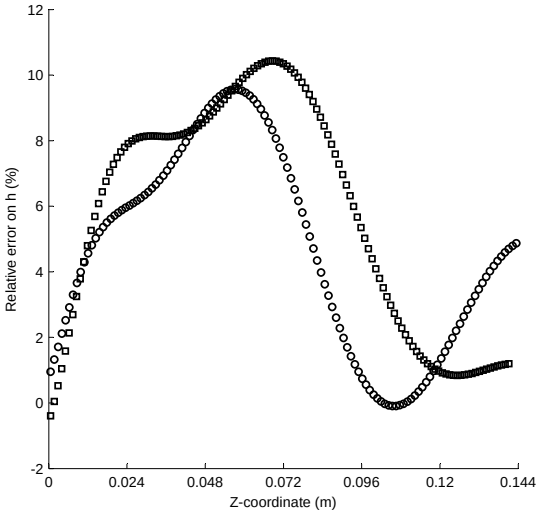

(b) □: SDM at L_3 ; ○: CGM at L_3

Figure 3.54: Relative error on estimated $\tilde{h}_i$ for exponentially varying h_i along the fin length with σ=0K, plotted along evaluation lines $L_1 - L_3$

σ = 0.05 and σ = 0.25. This makes it possible to estimate the accuracy of the fin effectiveness determination from a IHCP solution depending on the temperature measurement accuracies. These results are summarized in Table 3.12. It is concluded from this summary that CGM gives, however slightly, more accurate results than SDM, as was expected from the discussion of the different test cases. The largest error occurs for the linearly varying h_i along the fin height, and is not larger than 1%. Thus it can be concluded that the accuracy of the fin effectiveness determination using the IHCP solution method with CGM is 1% for a temperature measurement accuracy of 0.5°C.

CGM		σ = 0		σ = 0.05		σ = 0.25	
	ζ_{ex}	ζ	error (%)	ζ	error (%)	ζ	error (%)
Uniform	4.5206	4.5167	0.08	4.5097	0.24	4.5099	0.24
Linear along length	4.5735	4.5724	0.02	4.5654	0.18	4.561	0.27
Linear along height	4.4548	4.4124	0.96	4.4154	0.89	4.4111	0.99
Exponential along length	4.6779	4.6556	0.02	4.6497	0.15	4.6383	0.4
SDM		σ = 0		σ = 0.05		σ = 0.25	
	ζ_{ex}	ζ	error (%)	ζ	error (%)	ζ	error (%)
Uniform	4.5206	4.5114	0.2	4.5086	0.26	4.5081	0.28
Linear along length	4.5735	4.5718	0.04	4.561	0.27	4.556	0.38
Linear along height	4.4548	4.414	0.92	4.4127	0.95	4.4113	0.97
Exponential along length	4.6779	4.6717	0.13	4.6715	0.14	4.6706	0.16

Table 3.12: Summary of fin effectiveness and its accuracy for all different test cases

3.3 Estimation of a thermal contact resistance

The same model of fin and primary surface was used to investigate the accuracy of the IHCP solution for a thermal resistance. For this test case a known heat transfer coefficient profile h_i is assumed at the boundary surfaces S_1 – S_7. The linearly varying h_i profile along the length was imposed on these surfaces. The heat flux at the bottom surface S_8 is also known ($2000\mathrm{W/m^2}$). In the previous test cases there was no contact resistance at surface S_{13}. The contact surface was shown in Fig. 2.15 in Chapter 2. The measured temperatures Y_m on S_1 – S_7 for the minimizing functional J were determined by solving the direct problem with the given heat transfer coefficient profile as boundary conditions on S_1 – S_7 and a given contact resistance on S_{13}. This contact resistance profile is shown as a 3-D plot in Fig. 3.55(a). It has a parabolic profile with the lowest resistance at the outer edges (6.67×10^{-5} $\mathrm{m^2K/W}$) and the highest resistance in the center (1.33×10^{-4} $\mathrm{m^2K/W}$). The first estimation of the contact resistance was set as a uniform value of (3×10^{-4} $\mathrm{m^2K/W}$). The minimization functional J contains all the temperature measurements Y_m on S_1 – S_7. These measured temperatures are assumed to be exact. Therefore the convergence criterion was set at 0.1. This convergence criterion corresponds with an error on the estimated temperatures of $0.001\mathrm{K}$. CGM was used to solve this IHCP, and a converged solution was obtained in 81 iterations. The estimated thermal contact resistance is shown in Fig.3.55(b) and the relative errors in Fig. 3.55(c).

The estimated value is constant at the bottom of the resistance surface and has a relative error of 15% (Fig. 3.55(c)). The relative error varies along the side walls of the resistance from 15% to -30%. These errors seem high, but this is mainly due to the limited value of cells on the resistance surface: it contains 5300 cells, but only 7 along the height of the side walls and 5 along the width of the bottom face. The accuracy can be improved by increasing the number of cells, but this will also influence the number of cells in the fin and primary surface and lead to longer calculation times. Moreover, it is not important to accurately estimate the spatial variation of the contact resistance, but to determine the contact so that the error in the estimated temperatures on the fin and primary surface becomes negligible. If these temperatures are accurate, the heat flux distribution on the fin and primary surface are also accurate, as the convection coefficients on these walls are given. The error in the estimated temperatures was only 0.1% (due to the stopping criterion), which is very accurate. These small temperature errors are much smaller than errors that will be introduced by estimating the heat transfer coefficient on the side walls which will dominate the error on the heat flux distribution.

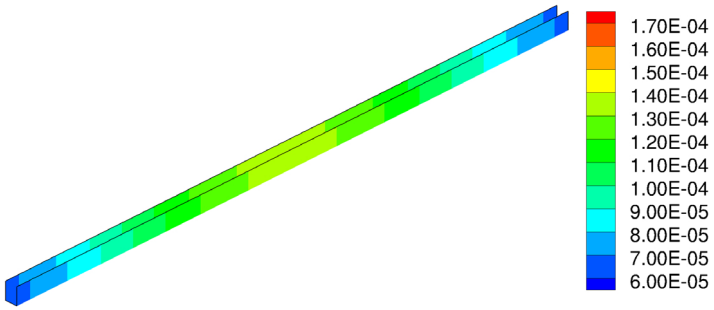

(a)

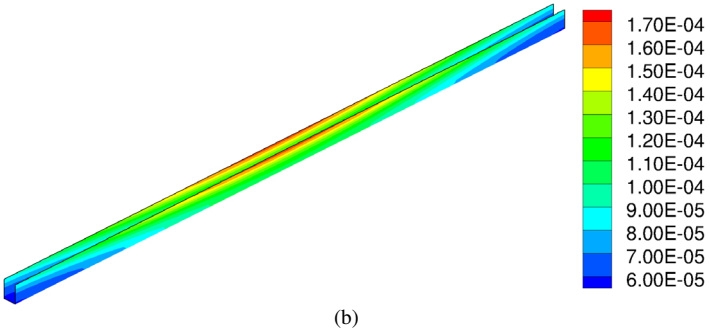

(b)

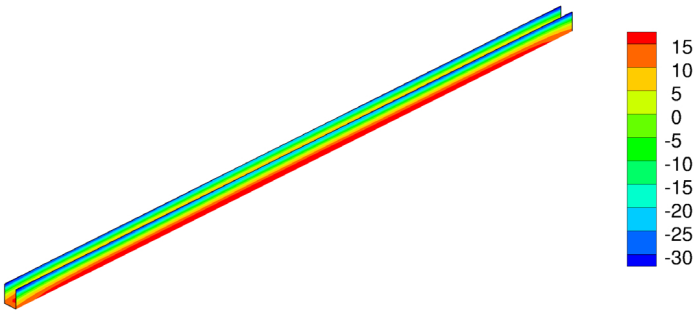

(c)

Figure 3.55: 3-D plots of the thermal resistance at S_{13} with σ=0K. (a) exact contact resistance (in $\mathrm{m}^2\mathrm{K/W}$) ; (b) estimated contact resistance (in $\mathrm{m}^2\mathrm{K/W}$); (c) relative error (%) on estimated contact resistance

3.4 Conclusions

The test cases discussed in this chapter lead to the following conclusions:

- CGM converges much faster than SDM, especially for more complicated heat transfer coefficient distributions
- CGM and SDM give comparable results for the estimation of local heat transfer coefficients. Accurate values are obtained for the majority of the cells, except:
  - near the edges, especially if there is a variation of the heat transfer coefficients in the direction normal to this edge
  - for steep gradients in heat transfer coefficients (such as the exponential profile)
  - CGM gives more accurate estimations on the primary surfaces than SDM
- the error in the estimates of the average heat transfer coefficients are:
  - less than 1% on the fin side surfaces, except if there is a steep gradient on these surfaces. The error can increase to 7% in this case, which is still acceptable
  - less than 1% on the fin tip unless there is a considerable variation of the heat transfer coefficients along the fin height. In this case it can increase up to 20%. The surface area of the fin tip is usually very small compared to the total surface area, which makes it difficult to accurately estimate this heat transfer coefficient. For the same reason, a larger error on the fin tip does not influence the total heat tranfer rate significantly.
  - the average heat transfer coefficient on the primary surface is always lress accurate than the average heat transfer coefficients on the other surfaces. A maximum error of 8% was found. CGM gives more accurate results than the SDM
- the determination of the fin effectiveness is very accurate: smaller than 1% for all test cases

4

Experimental Setup, Calibration and Measurement

In this chapter, a test rig is presented in which both fin effectiveness and local heat transfer coefficients for different fin forms can be determined. In order to experimentally determine fin effectiveness, heat fluxes through the primary surface and the fin need to be known. This information is obtained by measuring surface temperatures and calculating the heat fluxes from these measurements by using the inverse heat conduction technique discussed in Chapter 2. The necessary input for the inverse conduction problem is surface temperature measurements of the fin and primary surface. The subject of this chapter is limited to these measurements, the used techniques and the experimental setup. First, the used measurement techniques and the importance of calibration are explained. Secondly, the fin dimensions of the longitudinal fin and primary surface are determined. Different types of fins with the same basic dimensions of length, height and width are studied. The studied fin types differ in the number of perforations (=heat transfer enhancers) present in the fin (0-1-2). The construction of the test rig in which these fins are investigated, is described, as well as its range of applications.

4.1 Infrared Thermography

The goal of the experimental investigation is to determine local heat transfer coefficients and fin effectiveness. Temperature measurements are indispensable in heat

transfer investigations. Thermocouples are the most commonly used temperature measurement instruments. But the use of infrared thermography is also blooming in recent years.

4.1.1 Infrared radiation

Each object at a temperature above absolute zero (0K) emits radiation in the infrared spectrum, which lies between 1 and 1000 μm. The radiated thermal energy depends on the surface temperature. An important concept in heat radiation is a blackbody, which is an ideal body that absorbs all incident radiation, independent of the wavelength or angle of incidence. So there is no reflection or transmission through the blackbody. A blackbody emits the maximum radiant energy for each wavelength and direction, and is thus used as a reference for emitted radiation from real bodies. Planck's law gives the spectral distribution of hemispherical emissive power and radiant intensity in vacuum, for a blackbody. For a blackbody, this is only function of wavelength λ and temperature [119], [120]:

$$e_{\lambda,b} = \frac{C_1}{\lambda^5 \cdot (e^{\frac{C_2}{\lambda \cdot T}} - 1)} \tag{4.1}$$

C_1 and C_2 are the first and second radiation constants. One talks about hemispherical emissive power, because the radiation emitted from a point on a surface is emitted in the hemisphere as seen from that point. At a given temperature, the emissive power $e_{\lambda,b}$ has a maximum at a certain wavelength λ_{max}, as seen in Figure 4.1 [121]. The maximum spectral radiation is less pronounced for lower object temperatures. λ_{max} can be calculated by differentiating Planck's law to λ. This results Wien's displacement law, stating that the maximum spectral emitted radiation is found for the wavelength (in μm):

$$\lambda_{max} = \frac{2897.76}{T} \tag{4.2}$$

Figure 4.1 also shows that most radiation energy is found near the wavelength λ_{max}. This is a useful guide for the infrared camera selection: the camera has to be able to capture the wavelengths associated with the range of object temperatures. The infrared spectrum is normally divided in four zones or bands [120]:

- near infrared: 0.75-3 μm
- middle infrared: 3-6 μm
- far infrared: 6-15 μm
- extreme infrared: 15-1000 μm

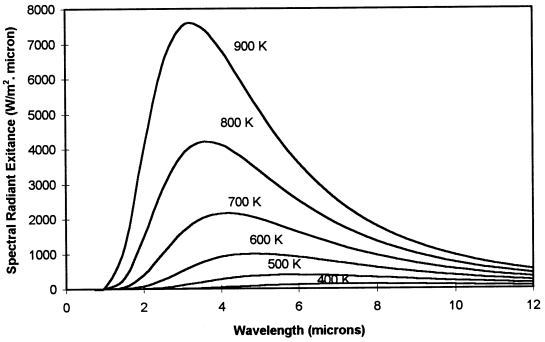

Figure 4.1: Spectral radiation according to Planck's law

For thermography, only the range of 1-15μm is of interest, because of the sensitivity of suitable detectors and the transmittance of the atmosphere. Depending on the detector, infrared cameras are divided into two classes, according to their wavelength range [121]:

- short wave camera (SW): 3-5 μm
- longwave camera (LW): 8-14 μm

Figure 4.2 clarifies the choice for these two specific bands: air has a high transmission in those wavelength bands. Outside these two bands, there is a high absorption and thus energy loss of the infrared radiation.

According to Wien's law, the highest spectral energy band for radiation at ambient temperature (300K) is found at a wavelength of 10 μm, and this peak shifts to shorter wavelengths for higher temperatures. This means that LW cameras should be better suited for temperature measurements of objects at moderate temperature, and SW cameras for temperatures above 100°C. Although this is a good general rule, it does not always indicate the best camera type for a certain application. Maldague stated [122], based on the work of Chrzanowski [123], that a SW and a LW camera give similar results in the temperature range -10°C to 130°C. There is even a slight preference for SW cameras, because the error in temperature measurements is smaller. So although the emitted radiation in the LW range is higher, a SW camera could be more accurate, and this mainly due to the superior detectivity of the detector.

Planck's law in Eq. (4.1) integrated over the total wavelength spectrum gives the total hemispherical radiation flux emitted by the blackbody:

$$e_b = \sigma \cdot T^4 \tag{4.3}$$

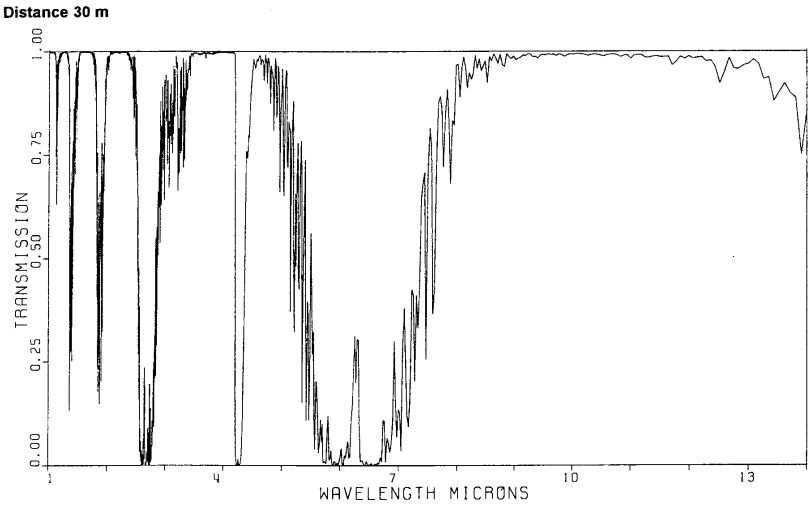

Figure 4.2: Spectral atmospheric transmission over a distance of 30m

where σ is known as the Stefan-Boltzmann constant ($5.67 \times 10^{-8}\mathrm{W/m^2K^4}$).

Emissivity

As mentioned before, a blackbody is an ideal object that absorbs all incident radiation and emits the maximum possible amount of radiation according to Eq. (4.1). The absorption for real objects is limited, and they only emit a portion of the radiation emitted by a blackbody at the same temperature. The ratio of the radiation emitted by a real object to the maximum blackbody radiation (for the same wavelength and object temperature) is called emissivity ϵ:

$$\epsilon = \frac{e_\lambda(T)}{e_{\lambda,b}(T)} \tag{4.4}$$

Notice that emissivity is a surface property: the emissivity of the surface determines the amount of radiation from the object, regardless of the inside properties of the object. Therefore, surface conditions as roughness, oxidation, also influence the emissivity value. Emissivity has a value between 0 and 1. The extreme values are never found in reality but can be approximated. Emissivity is dependent on the monitored wavelength λ, surface temperature and direction. Objects with a constant emissivity (< 1) over the total wavelength spectrum are called greybodies. Because of all these dependencies, a distinction has to be made between different

emissivity terms:

- spectral emissivity: emissivity value at a specific wavelength
- total emissivity: emissivity integrated over all wavelengths
- directional emissivity: emissivity in a specific direction or from a specific viewing angle
- hemispherical emissivity: emissivity integrated over the hemispherical space as seen from the object surface

If one does not know the emissivity of a surface, the exact amount of radiation coming from the surface cannot be determined, and thus the temperature of the surface cannot be measured with an infrared camera. Infrared cameras are sensitive for a specific bandwidth. Nevertheless, they are considered as total radiation cameras, which means that Eq. (4.3) can be used (multiplying the RHS by ϵ for real objects). For most measurements or applications, an infrared camera is placed normal to the measurement surface. So in general, for infrared thermography, the normal total emissivity needs to be known. In literature, values of normal total emissivity are found for most materials [119,121,124]. For materials with a strong wavelength dependent emissivity, a value for SW and LW is given. However, it is not advised to use these literature values as the exact value for an application. First of all, emissivity is a surface property, and surface conditions have a strong influence on the emissivity value. So by using values reported in literature, the uncertainty due to the surface finishing or presence of a thin oxide layer can induce a significant error on the temperature measurement. Secondly, each camera has a certain accuracy on the absolute temperature, which is largely determined by two camera specific errors: offset and response error. These errors vary with camera temperature and construction and are discussed in section 4.1.4.4. So this temperature error varies from camera to camera. If emissivity values from literature are used, these errors can induce a significant error (equal to the camera accuracy) on the absolute temperature value. However, if the emissivity value was determined first with the same camera as used for the final temperature measurement, the camera errors influenced the emissivity measurement and are hence almost completely cancelled in the temperature measurement. Therefore it is advised to determine the emissivity of a specific material with the same infrared camera as will be used for the temperature measurements. Values from literature can be used as a reference to check the obtained emissivity.

Other important parameters

Blackbodies absorb all incident radiation, which means they have an absorptivity $\alpha = 1$. This is not the case for real bodies. Unfortunately, absorptivity is not as

easy to determine as emissivity. However, Kirchhoff's law states that for bodies in thermal equilibrium, spectral absorptivity and spectral emissivity are equal at any temperature and wavelength, or the emissivity is at least a very good approximation for absorptivity [119]. Like emissivity, absorptivity is also dependent on wavelength, direction and temperature and the same definitions of different types are valid.

For real bodies the incident radiation can besides being absorbed, also be reflected or transmitted through the body. The conservation of energy states that al incident radiation on a body is either absorbed, reflected or transmitted. This gives the following equation (4.5), in which E stands for the amount of incident radiation.

$$\begin{aligned} \alpha E + \rho E + \tau E &= E \\ => \alpha + \rho + \tau &= 1 \end{aligned} \tag{4.5}$$

ρ is the reflectivity and τ the transmittance. So the sum of absorptivity, reflectivity and transmittance is always 1. Reflectivity and transmittance are also dependent on wavelength, direction and temperature. With Kirchhoff's law, absorptivity is replaced by emissivity and gives:

$$\epsilon + \rho + \tau = 1 \tag{4.6}$$

For opaque bodies (no transmittance), reflectivity is known if emissivity is determined. If objects are transparent, the transmittance or reflectivity needs to be determined in order to calculate the third property.

4.1.2 Infrared camera parameters

An infrared camera receives radiation and converts this information into temperatures. The radiation incident on the camera lens comes from different sources (see Fig. 4.3). Radiation detected by the camera consists of: energy emitted by the body consistent with ϵ, radiation from the surroundings reflected by the body consistent with ρ, and radiation from the atmosphere.

Radiation from the surroundings depends on the temperature of the surrounding objects in the half sphere seen from the object surface. Those objects could be at different temperatures, which makes it difficult to calculate the incident radiation on the object surface. However, in most cases it is valid to assume that all objects are at the same temperature as the surroundings. It is therefore important to remove all sources of intense radiation from the measurement location, e.g. opaque bodies with a low emissivity, shielding of the optical path,... The simplification that the surroundings is at the same temperature T_{amb} is necessary to construct an equation as input for the infrared camera temperature calculation. Thus T_{amb} is the camera parameter that accounts for reflected radiation. For opaque bodies with

low emissivity, reflection is an important contribution of the radiation received by the camera. Thus T_{amb} must be measured accurately. The emissivity from the surroundings is assumed to be 1. If the complete surroundings is considered, according to Kirchhoff's law, all radiation incident on the surrounding objects will eventually be absorbed by these objects, thus $\alpha = \epsilon = 1$.

Radiation emitted or reflected by an object, travels some distance through atmospheric air before reaching the infrared camera. Air is an attenuating medium, that absorbs infrared radiation, depending on the wavelength, as shown in Fig.4.2. The longer the traveling distance, the more radiation is absorbed, which reduces transmittance τ. A transmission lower than 1 for air indicates there also is emission by the air since there can be no reflection. Thus radiation is emitted with an emissivity of $1-\tau$, as given in Fig.4.3. For high transmittance values, the radiation emitted by air is negligible.

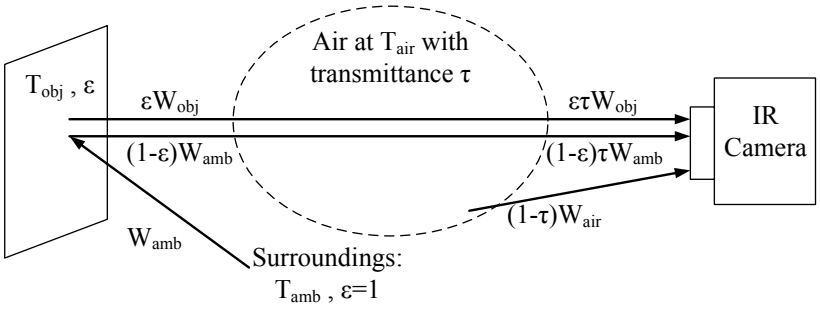

Figure 4.3: Three possibilities of radiation: conservation of energy

If there is a window in the optical path between object and camera, this window will also act as an attenuating medium with a certain transmittance. This is taken into account by adjusting the τ value in Figure 4.3. Radiation energy is denoted as E. If the measurement object is a blackbody at temperature T_{obj}, it emits radiation E_{obj} according to the object temperature. However, in reality, the measurement object is not a blackbody. If the object is assumed to be a greybody with emissivity ϵ, it emits radiation energy $\epsilon \cdot E_{obj}$. If the object is opaque, it reflects an amount of radiation energy from the surroundings $(1-\epsilon) \cdot E_{amb}$. In Figure 4.3, radiation from three sources reaches the camera:

- radiation emitted by the object attenuated by air (τ) between object and camera: $\epsilon \cdot \tau E_{obj}$
- radiation from the surroundings at temperature T_{amb} is reflected by the

opaque object with a reflectivity of $1-\epsilon$ and air transmittance τ: $(1-\epsilon)\cdot \tau E_{amb}$

- radiation emitted by the atmospheric air at temperature T_{air}: $(1-\tau)\cdot E_{air}$

So the total radiation the camera receives is:

$$E_{tot} = \epsilon\cdot\tau\cdot E_{obj} + (1-\epsilon)\cdot\tau\cdot E_{amb} + (1-\tau)E_{air} \tag{4.7}$$

The camera detects the total amount of radiation E_{tot} and needs to convert it into the correct object temperature T_{obj}. To this end the camera is calibrated: the camera output signal was measured for incident radiation received from a blackbody set at accurately known temperatures. This results in a calibration function which relates the camera output signal U to the object temperature T_{obj}:

$$U = \frac{R}{e^{B/T} - F} \tag{4.8}$$

R, B and F are calibration constants. The calibration algorithm has the same form as Planck's law (Eq. (4.1)). If a power linear camera is assumed, the received radiation from equation (4.7) can be written in corresponding camera signals U [121]:

$$\begin{array}{rcl} U_{tot} & = & \epsilon\cdot\tau\cdot U_{obj} + (1-\epsilon)\cdot\tau\cdot U_{amb} + (1-\tau)U_{air} \\ \Rightarrow U_{obj} & = & \frac{1}{\epsilon\cdot\tau}\cdot U_{tot} - \frac{1-\epsilon}{\epsilon}\cdot U_{amb} - \frac{1-\tau}{\epsilon\cdot\tau}\cdot U_{atm} \end{array} \tag{4.9}$$

So in order to determine the camera output signal connected with the emitted object radiation, accurate values are necessary for object emissivity ϵ, transmittance τ of air and any windows and ambient temperature T_{amb}. Then, using the calibration function 4.8, the corresponding object temperature can be determined.

4.1.3 Camera specifications

There are different types of infrared cameras. The difference between a LW and a SW camera was explained before. Next to the wavelength sensitivity range, cameras are also divided in two categories based on the infrared detector type: a scanner or a focal plane array (FPA).

A scanner has only a single detector and uses a mechanical system consisting of mirrors and prisms to scan the field of view (FOV) of the camera. So the different pixels on an infrared image are not simultaneous temperature measurements, but there is a (negligible) time delay between them. FPA cameras have a matrix of detector elements that are scanned electronically, and the different detectors measure simultaneously. Each infrared image pixel of the FOV corresponds with a detector. Scanners with a single detector are more reliable for accuracy because the radiation for each pixel is measured with the same detector. FPA systems use

much more detectors and they could have differing responses, which makes the signal processing more complicated.

For accurate measurements infrared detectors have to be cooled. Often a cooling liquid, like liquid nitrogen, is used to cool the detectors of static cameras, which can have an external cooling circuit. This makes it impossible to place the camera horizontally. But the detector temperature is kept very stable, so the response of the detector shows no great variations. Also the camera only heats up moderately during operation which minimizes the influence of internal camera radiation incident on the detector. For obvious reasons, detectors in portable cameras are not cooled with liquid nitrogen, but are equipped with a thermoelectric cooling. The detector temperature is not as stable as with liquid nitrogen cooling, and thus the response of the detector is less stable.

The infrared camera used in this work is a DIAS Midas LW camera, with a thermoelectrically cooled microbolometer FPA detector, with 320 x 240 detectors. The scan rate is 30 full frames per second. The spatial resolution, also called the instantaneous field of view (IFOV) is 1.6mrad, which corresponds with $0.8\mathrm{mm}$ for the minimal focus distance of $0.5\mathrm{m}$, which is the smallest distance between two points that the camera can detect. Further, the noise equivalent temperature difference (NETD) of the camera is $0.1\mathrm{K}$ at 30°C. This camera specification is explained later. Finally, the measurement uncertainty is 2°C or 2% for temperature > 100°C. This is a rather large uncertainty, but it can be improved by calibration as will be shown in the following section.

4.1.4 Camera calibration

4.1.4.1 Emissivity calibration

Surfaces are often painted to increase the emissivity and improve the measurement accuracy. This also has the big advantage that only the emissivity of the paint needs to be calibrated to measure objects of different materials. Two layers of paint are normally thick enough make the object opaque [121], so the camera sees only the paint. A thin paint layer induces only a small thermal resistance, which has a negligible impact on the heat flux through an object. Different paints are calibrated in this work according to the standard test method of the ASTM standard E1933-99a [125]. This method is based on simultaneously measuring the surface temperature with a thermocouple and the IR camera. To minimize the temperature difference (and thus emissivity error) between thermocouple and thermography measurement, it is important to have an isothermal surface near the measurement area. As there is often a temperature gradient present on objects, and as the emissivity is temperature dependent, emissivity should be constant in that temperature interval in order to do accurate measurements with thermography. The emissivity should be calibrated in the temperature range attained during experiments. So, two

important properties of an emissivity calibration surface are:

- isothermal
- adjustable temperature

Calibration setup and procedure

The calibration setup is shown in Figure (4.4). A thermostat keeps water at a desired constant temperature between 20°C and 90°C. The setup is equipped with a circulation pump that pumps water towards an aluminum vessel and back. The vessel contains 3 liters of water and the circulation provides good mixing, which results in a nearly uniform and constant temperature. The highest temperature variation over a surface of $1\mathrm{cm}^2$ is 0.3°C, partly due to RMS noise on the signal. However, the mean temperature value of a $1\mathrm{cm}^2$ area varies with less than 0.05°C if this area is moved over some centimeters. So the isothermal property is satisfied. For an expected ϵ value of 0.95, an uncertainty of 0.05°C corresponds with an uncertainty of 0.3% on ϵ at 40°C and only 0.1% on ϵ at 80°C.

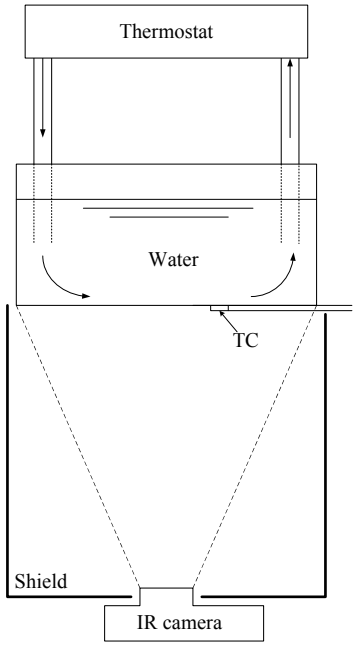

Figure 4.4: Calibration setup

length between camera and calibration surface is shielded from the environment by a wooden casing coated with high emissivity paint. This eliminates errors

induced by nearby heat sources in the surroundings that influence T_{amb}.

Preliminary tests indicated that the surface temperature during experiments would vary between 45°C and 80°C, so the emissivity of the paint is calibrated in this temperature range. The following calibration procedure is executed:

1. A stick-on thermocouple is taped on the calibration surface

2. The infrared camera is placed right underneath the calibration surface and focused until the focal plane coincides with the calibration surface

3. The water temperature is set at the desired temperature using the thermostat

4. Ten thermocouple scans are taken, and at the same time a sequence of infrared images of a $1\mathrm{cm}^2$ area next to the thermocouple (where the surface is visible) is recorded

5. The time averages of both measurements are compared. The emissivity parameter of the camera is adjusted till both temperature values are equal. The obtained emissivity in the camera is the emissivity of the paint at the given temperature

6. Step 3 and 4 are repeated 3 times

7. A new temperature value is set, 5°C higher than the previous one. Steps 3-6 are repeated for the new temperature setting

Three important factors introduce an uncertainty on the measured emissivity:

- camera accuracy and isothermal property of calibration surface

- thermocouple measurement accuracy

- influence of infrared camera parameter uncertainties on the temperature measurement

This maximum temperature difference defines the uncertainty on the emissivity measurement, which can be calculated from the camera measurement equation (Eq. (4.7)). These three uncertainties, as well as the total temperature uncertainty or, better said, the largest possible temperature difference between thermocouple and thermographic camera are calculated in Appendix A. This results in the maximum uncertainty on the measured emissivity value, which varies with object temperature.

Emissivity calibration results

The calibration procedure was executed two times, with two thermocouples at different spots on the surface. Different kind of paints were calibrated. Only the results for the paint with highest emissivity, i.e matt white Krylon paint, are given in Figure 4.5. As seen from these results, the use of a value of $\epsilon = 0.94 \pm 0.007$ is acceptable for surface temperatures > 50°C. At lower surface temperatures, the second measurement data set shows a deviation larger than the calculated emissivity error. A possible reason for this deviation is the temperature dependency of the paint emissivity, which would make it impossible to do accurate temperature measurements without accurate knowledge of this variation.

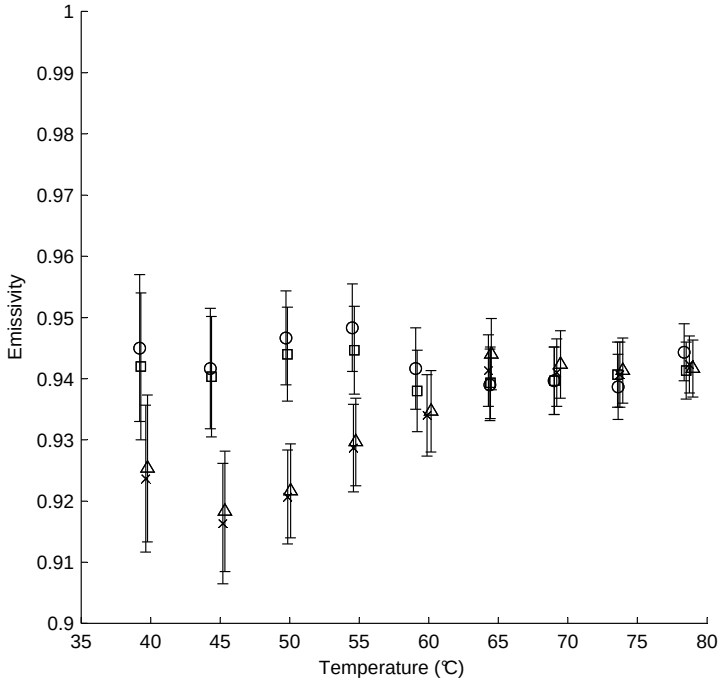

Figure 4.5: Measured emissivity values with error bars (□ TC1, set1 ; ○ TC2, set1 ; Δ TC1, set2 ; × TC2, set2

A possible temperature dependency is checked with a comparative test. The calibration surface is painted with two different paints: one half with the matt white Krylon paint, the other half with a paint of a different composition and manufacturer. This test is executed two times: once with black chalkboard paint as

reference, and once with carbon paint. The calibration surface is set at different temperatures between 45°C and 80°C, and is measured with the infrared camera near the division of both halfs. The emissivity of the paint that gives the highest temperature is set at 1, the emissivity for the other paint is lowered till both temperatures are equal. The results are shown in Figure 4.6. The three different paints have a constant ratio over the investigated temperature range. Two conclusions can be drawn from these results:

- The three paints have either the same temperature dependency for emissivity, which seems highly unlikely, due to the different composition and manufacturers. So it is reasonable to say that all three paints are temperature independent in this temperature range
- The matt white Krylon paint has the highest emissivity and is thus the best paint for accurate measurements. The emissivity of the Krylon paint is 0.94 ± 0.007 in the temperature range [60°C-80°C].

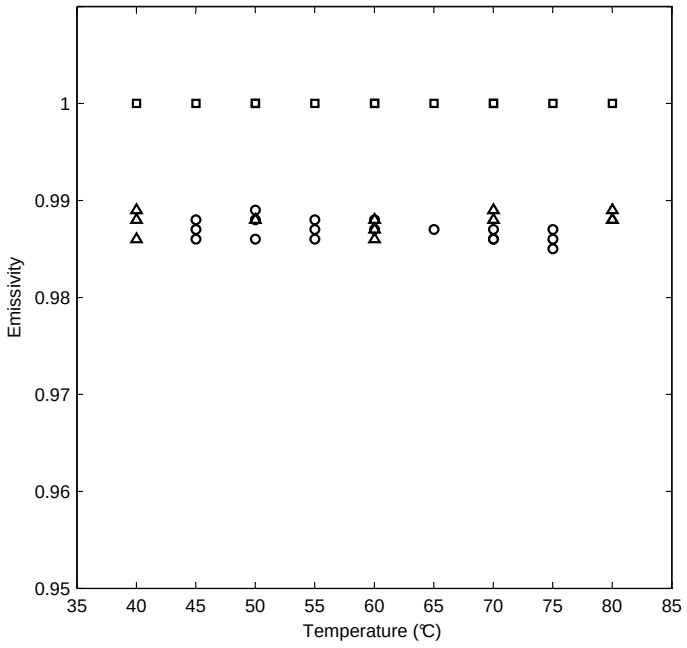

Figure 4.6: Emissivity comparison between matt white Krylon paint (□) (set at $\epsilon = 1$), black chalkboard paint (○) and black carbon paint (△)

As the deviation in Fig.4.5 for surface temperatures < 60°C is not introduced by temperature dependency of the emissivity, the following possible sources of error were investigated:

- temperature drop over the kapton tape, which provides an extra thermal resistance and increases the surface temperature under the tape. This temperature rise does not exceed 0.01°C, which is lower than the thermocouple accuracy.

- the impact of radiation from the surroundings (by E_{amb}) is too large at these lower temperatures. This explanation seems more likely. The condition of a minimal temperature difference $T_{obj} - T_{amb} > 30$°C, as proposed by Öhman [121] is exaggerated as shown by these results.

It can be concluded that the matt white Krylon paint has the highest emissivity: $\epsilon = 0.94 \pm 0.007$ in the temperature interval 60°C- 80°C. The value can probably be extrapolated to lower temperatures till 40°C as proven by the comparative test, however, the second emissivity measurement does not support this. In order to do accurate measurements, the surface temperatures are kept between 60°C and 80°C during experiments.

4.1.4.2 Ambient temperature calibration

Next to emissivity, T_{amb} is also an important data reduction value, especially for low emissivities or objects at temperatures close to ambient, as shown above. Most of the surrounding heat sources that can distort the measurements are eliminated by placing a shield around the optical path between measurement object and camera. The shield is painted with high emissivity paint. Such a shield was used in the emissivity calibration setup as shown in Fig.4.4. The shield temperature equals the air temperature, so the only heat source which can influence the measurement is the IR camera itself as it emits radiation which reflects on the measurement surface. There are two types of reflection: diffuse and specular reflection. More information on these two types of reflections is given in Appendix A. In Appendix A is also explained that an object should be a diffuse reflector for accurate temperature measurements with the camera perpendicular to the measurement surface.

An analytical calculation of T_{amb} is difficult considering the different environmental sources contributing to the ambient radiation. However, there is a direct measurement method for the reflected ambient temperature, based on an ASTM norm [126]. A special tool is required to perform this method: an infrared mirror with reflectivity $\rho = 1$. Real materials will never attain $\rho = 1$. Some metals with a smooth surface finish have a reflectivity close to 1. The closer the ρ value of the mirror lies to one, the smaller the error on the T_{amb} measurement. If the

measured object is a specular reflector, the mirror should also be specularly reflecting. For a diffuse reflector, a diffusely reflecting mirror is necessary. Specular mirrors are relatively easy to find, but diffuse mirrors are not that common. According to the ASTM standard [126] and Öhman [121], a good approximation for a diffuse mirror is wrinkled aluminum foil. Aluminum foil has a very high reflectivity ($\rho \approx 0.96$). By wrinkling the foil, cavities are formed which result in a more diffuse reflectance. But these cavities also have a downside: the reflectance decreases substantially due to repeated reflections inside the cavities. The best solution is gold plated sandpaper [121], but this is of course expensive. Therefore a diffuse mirror of wrinkled aluminum foil was created. The calibration procedure for T_{amb} according to the ASTM standard was adapted and executed as follows:

1. The diffuse aluminum window was placed just in front of the measured surface
2. The infrared camera is placed perpendicular to the mirror at the same position as during measurements and emissivity calibration. The camera is focused till its focal plane coincides with the mirror
3. The emissivity parameter of the camera is set to 1
4. A sequence of infrared images is recorded during 5 seconds. The sequence is time averaged to reduce the influence of RMS noise.
5. The spatial average of the time averaged image is calculated with a built-in analysis tool. This averaged temperature is T_{amb}
6. Step 4 and 5 are repeated till 3 measurements are done

An infrared image for T_{amb} calibration with an analysis surface is shown in Fig.4.7.

The calibration procedure gives a value of T_{amb} = 20.7°C. The uncertainty on this value depends on two factors:

- The standard deviation of the average value of spatial temperature distribution. This is the standard deviation of the histogram in Fig.4.7(b)
- Uncertainty due to the imperfection of the mirror: $\rho < 1$

The error analysis is reported in Appendix A. The uncertainty by spatial averaging (which is the standard deviation for a 95% interval) is 0.5°C. The second uncertainty due to an imperfect mirror is estimated as follows. The reflectance of aluminum foil is normally $\rho \approx 0.96$. However, the reflectance of wrinkled aluminum foil will be lower. If this value is assumed at 0.9, thus emissivity $\epsilon = 0.1$, a corresponding error can be calculated with the emissivity uncertainty calculation

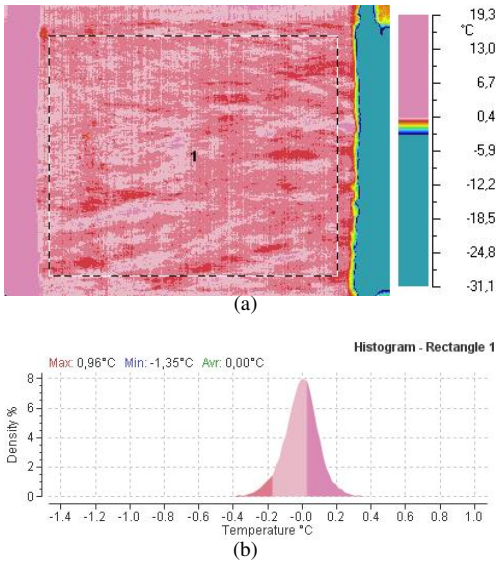

Figure 4.7: Infrared image of the diffuse aluminum mirror with histogram from the square analysis tool

from Appendix A. The emissivity is set to 1 during calibration, as if the mirror was perfect and all radiation incident on the camera is ambient reflected radiation by the mirror. The mirror imperfection can be seen as an error on the ϵ value. So the error on T_{amb} can be estimated by calculating the temperature error by an emissivity error equal to the reflectant error of the mirror. The ambient temperature is set at the expected value (value measured for $\epsilon = 1$) and the object temperature is set at air temperature. For a standard situation with an air temperature of 20°C and T_{amb} varying between 21°C and 30°C (warm camera is the most important heat source from the surroundings), a reflectivity error of 0.1 would give a T_{amb} error between 1.5°C and 1°C. This error is larger than the standard deviation of the measurement image. A total error dT_{amb} = 1.5°C is a good estimation.

4.1.4.3 Window transmittance calibration

A third calibration parameter is transmittance. The calibration parameter is actually meant for adjusting the air transmittance. Air molecules, especially CO_2 and H_2O absorb infrared radiation at specific wavelengths, so the transmittance of air is not always 1. This transmittance varies with the traveled distance, relative humidity and wavelength. However, the transmittance can be assumed equal to 1 in the LW spectrum for short distances (< 10m). This is shown in Figure 4.8, where

the transmittance through air is given in function of wavelength for a distance of 1m. The distance between camera and measured objects in this work is never > 1 meter.

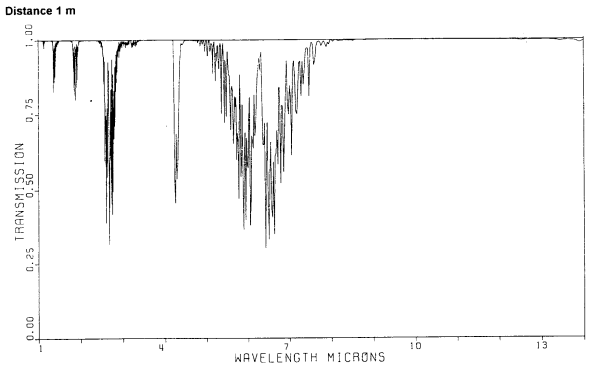

Figure 4.8: The air transmittance in function of wavelength for travel distance of 1 meter through air at 30°C and 50 % relative humidity

Most solid objects are opaque, i.e. the transmittance $\tau = 0$. Some objects are semi-transparent for infrared radiation and are used as windows. For infrared measurements through such a window, the window transmittance has to be known and set as transmittance parameter in the camera. As the measurement object will be placed in a windtunnel, as will be discussed later in this chapter, the use of a window is necessary when using infrared thermography. Most windows are only transparent in limited wavelength intervals and are made of exotic materials (zinc selenide, germanium, zinc sulfide,), which are very expensive and mostly brittle. Of course, there are also commonly used materials that are infrared transparent, such as most plastics. Generally, transmittance is inversely proportional to material thickness. Most common materials have an unpredictable transmittance curve in function of wavelength, where peaks of high transmittance alternate with zones of total absorption. The window for the LW camera should have a high transmittance in the interval $8\mu\mathrm{m}$ – $14\mu\mathrm{m}$, without zones of total absorption. Not many common plastics fulfill this requirement, but polyethylene (PE) does. High density polyethylene (HDPE) even has a higher transmittance than plain PE. It is stronger and more air tight, which is not unimportant for a window in a wind tunnel. Therefore HDPE was chosen as window material.

HDPE foil of $10\mu\mathrm{m}$thickness is used as window. The transmittance of this HDPE foil was calibrated according to the ASTM standard E1897-97 [127]. Transmittance is temperature dependent, yet as the window is placed in the wall of a wind tunnel that operates at room temperature, calibration only has to be done for

a window at room temperature. The ASTM standard was adapted to these conditions and gave the following calibration procedure:

1. Set a blackbody simulator at the desired temperature. A blackbody simulator should have an emissivity ϵ of ± 0.95. The emissivity calibration surface from Fig.4.4 was used, painted with the matt white Krylon paint (with a measured $\epsilon = 0.94 \pm 0.007$)

2. The infrared camera is placed perpendicular to the blackbody simulator. The camera is focused so that his focal plane coincides with the blackbody surface

3. The emissivity parameter of the camera is set to 1 and a sequence of infrared images of the blackbody simulator is recorded during 5 seconds. The sequence is time averaged to reduce the influence of RMS noise.

4. The HDPE window is placed between the camera and the blackbody simulator.

5. A new sequence of infrared images of the blackbody simulator is recorded during 5 seconds. The sequence is time averaged to reduce the influence of RMS noise.

6. The time averages of both measurements are compared and the emissivity parameter is adjusted till both temperature values are equal. The obtained emissivity is the transmittance of the window at the given blackbody simulator temperature

7. Step 3-6 are repeated till 3 measurements are done

8. The blackbody simulator temperature is set 5°C higher. Steps 3-7 are repeated for the new temperature setting

9. A transmittance curve in function of the measured object temperature (and thus the corresponding wavelengths) is obtained for the window transmittance

Time averaged images of the blackbody simulator at 55°C with and without window are shown in Fig.4.9

The following transmittance for HDPE in the temperature interval 50°C-80°C is found: $\tau = 0.9 \pm 0.008$. The transmittance is constant in this temperature interval, and thus independent of the temperature of the measured object. However, Fig. 4.9 indicates that thermography through a HDPE window needs an extra adjustment for camera reflection on the window. Fig.4.9(b) recorded through the window, shows a hot spot in the centre of the image. This hot spot is absent in Fig.4.9(a)

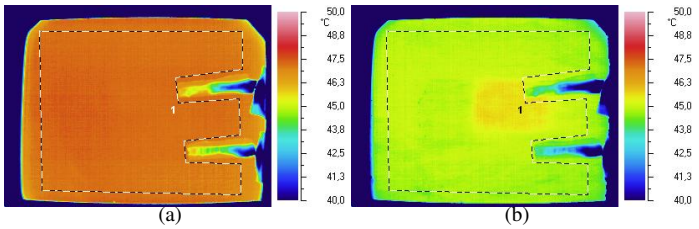

Figure 4.9: Infrared image of the calibration surface with (b) and without (a) window

without window. The hot spot creates an increase of ± 0.8°C compared to the rest of the image. This local temperature increase is not negligible and gives a deformed image of the temperature distribution. This extra error is introduced by reflection of the camera. This could be expected, because plastics are not really diffuse reflectors, but more specular. Reflection from other surrounding objects and walls could also induce such an error, but these are avoided by using a shield. So in order to correct infrared images recorded through a window, one should not only correct for transmittance, but also for camera reflection. Therefore the transmittance of the window has to be determined first. The transmittance calibration is performed on a part of the infrared images outside the camera reflection, which gives in the correct τ value. The correction for the reflection is made with the following procedure:

1. The blackbody simulator is set at a fixed temperature. A time averaged temperature image is made from a recorded sequence of the blackbody simulator in absence of the window. This is the original image

2. The window is placed and again a sequence is recorded from which the time average is taken. This temperature image is the transmitted image

3. The transmitted image is adjusted with the built-in camera program for the calculated τ value. Now, transmitted and original image should be the same (except for some RMS noise) if it was not for the camera reflection in the transmitted image

4. The original image is subtracted from the transmitted image (with camera software). This gives an image where most pixels have a temperature value between -0.1°C and 0.1°C, except for the pixels in the hot spot. This image is the correction image

5. The correction image is used for other images recorded with window, even for a different blackbody simulator temperature. Images are first adjusted for

the window transmittance and secondly, the correction image is subtracted. This gives the actual temperature values within some uncertainty margin.

During the procedure, the camera needs to be at a fixed place in relation to the window.

The fact that a correction image created at 55°C is also applicable for images of objects at different temperatures in the calibration range is not that obvious, even if τ is constant in this range. A small variation of the reflected image is expected is expected, because although the reflected radiation is constant, the radiation from the object going through the window varies with object temperature. The error induced by using a correction image at one temperature for images at other temperatures can be calculated by comparing the corrected images with measurements without window. The comparison is made by subtracting one image from the other. Values around 0°C are expected for the resulting image. The average of the pixel values should be 0°C and the 95% standard deviation gives the error. These errors are all of the same order (±0.2°C), and the histograms of the resulting images do not show any large aberrations. The use of a single correction image for reflection is thus acceptable because its associated error does not exceed the error introduced by the uncertainty on the emissivity. The calibrated transmittance value (τ = 0.9) is involved in the verification of the camera reflection correction: the calculated error for the reflection correction of the images uses the error on the calibrated transmittance parameter τ.

4.1.4.4 Uncertainties due to the IR camera

The Midas LW infrared camera has an absolute temperature error of 2°C. However, the combined error due to emissivity ϵ, ambient temperature T_{amb} and transmittance τ hardly exceeds 0.5°C. So the camera accuracy is not only determined by object and environmental uncertainties. There are also errors induced by camera imperfections. The two main ones are: camera offset error and camera response error. A short explanation of both errors is given.

Camera offset

An infrared camera receives radiation and produces an output (voltage or digital value) that is converted into the real object temperature. The incident radiation on the detector is coming from different sources: the measured object, reflection from surrounding objects, atmospheric radiation, camera optics and internal camera surfaces. The first three sources are external sources that pass through the camera lens and are separated by correct calibration of the three camera parameters ϵ, T_{amb}, and τ, as explained previously. The latter two sources are unwanted and have nothing to do with the radiation incident on the camera lens. They disturb

the radiation power from object and surroundings and add an offset component to the detector output signal. This offset component can be of the same magnitude as the useful signal. As it is related to the internal camera surfaces and optics, it varies with camera temperature. It is obvious that this offset component has to be removed from the output signal. In FPA cameras the clamping method is used combined with a compensation procedure. For the clamping method, an internal reference surface is placed as close as possible to the camera lens and, on demand, turns rapidly in front of the camera lens. The temperature of the reference surface is measured and the output signals of all detectors are stored as a reference image. This reference image is the offset bitmap and is used to remove the influence of internal radiation and thus the offset. This method is very exact, but removes only one offset component: radiation energy coming from the lens itself and the optics and surfaces between lens and reference body are not removed. This last offset component also varies with camera temperature and is reduced with a compensation system. The temperatures of these components are measured with temperature sensors and a camera output signal is calculated based on these temperatures. This output signal is the compensation output and is subtracted from the actual camera output to eliminate this offset [121]. The latter compensation procedure is less accurate than the clamping method and will leave a fraction, varying with camera temperature, of the offset component in the output signal. The influence of this component also varies with the measured object temperature, because, although the offset signal remains constant for a stable camera temperature, it relative importance in the total camera signal varies and thus also the final error on the calculated object temperature. An upper value for this offset error for the object temperature is determined and used in the error calculation in Appendix A. It varies between 1°C at 40°C and 0.7°C at 80°C as shown in Appendix app:error. A final offset error which should be considered is the drift of electronic amplifiers. This drift is eliminated by clamping, after the reference body has turned in front of the detector. After clamping, the drift restarts, so in order to eliminate drift errors in measurements, clamping should be done just before each measurement.

Camera response

A camera response function describes the relative spectral response of the camera as a function of the wavelength. A stable detector temperature is necessary to have a stable camera response. Thermoelectrically cooled cameras cannot keep the detector temperature stable enough [121], which results in a temperature error. This error varies with camera temperature as the dominant wavelength shifts with temperature. To correct for this error, a second reference body, at a high stabilized temperature, is installed in the camera. The camera response is clamped to a certain value corresponding to the temperature difference between the two reference bodies. The response error is calculated in Appendix A.

Influence of camera offset and response

The description of the offset and response error shows that they can result in a significant uncertainty on the measured surface temperature. The offset error seems relatively high (1°C at 40°C object temperature), and the response error is even higher (1.5°C at 40°C object temperature). The sum of the response and offset error is almost constant over the range 40°C-80°C (only 0.1°C variation). The actual influence of these errors during measurements is decreased remarkably by calibration.

When the camera offset error is taken into account for the emissivity determination, the emissivity changes significantly (0.7°C at 40°C is an error of 3% at the emissivity value). However, the calculated offset value is a maximum, so it could well be smaller. The offset error and the fact that it can become relatively large, affects the emissivity determination significantly. However, an exact value of the emissivity is not important in this work, but the real absolute temperature value is important. So, even if the emissivity determined with the camera would have an error of more than 3%, this does not mean that there is a correspondent error on the temperature value. The camera is calibrated by adjusting the emissivity value for a known surface temperature (thermocouple value). The offset and response error cause the calibrated emissivity to differ from the real emissivity value. This does not induce a temperature error in future temperature measurements with the same camera, if it is assumed that the camera temperature is the same as during calibration (after a warm-up period) when the surroundings are at room temperature. So even if the real emissivity value is higher or lower than the measured one, the offset and response errors correct the temperature value to the real temperature value within an error margin as calculated before (error on ϵ, τ and T_{amb}). The offset and response error are hence no longer important after calibration with a temperature sensor. Of course, the camera temperature will not exactly be the same for each measurement, but if the room temperature is more or less stable, it can be assumed that this difference will be small, once the camera has warmed up. The error induced by small variations of camera temperature will be smaller than temperature errors induced by the camera parameters ϵ, τ and T_{amb} and therefore this influence is neglected. Two important conclusions can be drawn from this discussion:

- the calibrated emissivity value is only useable for the camera type it was measured with, and is not an absolute value. One has to be careful with emissivity values found in literature. The use of such values in an infrared camera induces significant errors in the temperature measurement, since the offset and response value are dominant. This explains why the camera accuracy in the specifications is set so high (2°C or $\pm 2\%$, whichever is the highest).

- measurements should only be executed after the camera warmed up, otherwise the camera temperature differs from the temperature during calibration and offset and response errors influence the object temperature. This is a possible explanation for the deviation of the measured emissivity at temperatures < 55°C during the second calibration measurement (Fig.4.5), because these were measured first.

4.1.4.5 Total temperature error after calibration

The previous discussion showed that only the errors on ϵ, τ and T_{amb} are significant for the total temperature calculation. Camera errors such as offset and response error only have an influence on the real emissivity value, but are negligible for the temperature errors after calibration of the camera parameters for a certain material and measurement setup, and at a stable room temperature. The error induced by air temperature is also negligible. The total temperature error is calculated in Appendix app:error. A maximum temperature error of 0.5°C was found.

4.1.5 Advantages of infrared thermography

The camera calibration indicates that it is not so straightforward to do accurate measurement using infrared thermography. It is not just taking pictures with a camera, but different parameters have to be set in the camera in order to obtain correct temperature values. These parameters need careful calibration. This is more labor-intensive than for the widely used thermocouples. However, infrared thermography has some advantages to other measurement techniques:

- no contact: there is no contact between measurement surface and measurement apparatus. The temperature and heat flux field is thus not influenced by the measurement. Often objects are placed in a fluid flow, where the fluid flow also affects the heat transfer. Contact thermometers would disturb the fluid flow and measurement environment. This is not the case for infrared thermography. Note however that infrared thermography cannot be used for to measure surface temperatures of objects in liquids, because liquids are not transparent for infrared thermography.

- temperature profiles: contact thermometers can only measure temperatures in one point. Infrared cameras measure the temperature at a surface, thus in multiple points simultaneously. It is impossible to measure temperature profiles accurately with thermocouples, the temperature field would be disturbed significantly.

These two advantages make infrared thermography an ideal measurement technique for this work.

4.2 Longitudinal fin

A test rig was developed to investigate longitudinal rectangular fins. This fin type is an ideal test case to develop a method for the determination of local heat transfer and fin effectiveness for extended surfaces. So this experimental study is limited to longitudinal rectangular fins, which are commonly used in heat sinks for the cooling of electronics. An extensive literature survey on experimental, numerical and analytical studies on longitudinal rectangular fins was made in Chapter 1. Although there are numerous studies dedicated to this fin type, it was concluded that depending on the fin dimensions, thermal boundary conditions and thermal conductivity of the material (actually Biot number), a two-dimensional model is necessary to do accurate predictions on the real heat dissipation of the fin, while most models are only one-dimensional. If longitudinal fins are limited in length, edge effects also influence the heat transfer in a third dimension. There is thus still need for extra experimental data on this fin type, especially if the studied fin is limited in length (as for fins in heat sinks) since the one-dimensional analytical fin model becomes less accurate for this case. The distribution of local heat transfer coefficients gives an insight in the heat transfer enhancement of fins, especially if these fins feature extra heat transfer enhancers. The rectangular longitudinal fin has also the advantage that it can be constructed relatively easy at a low cost. This increases the possibility of adding heat transfer enhancers to this fin type and investigate their influence experimentally. The large flat fin surfaces are ideal for temperature measurements with infrared thermography over the complete fin. So the choice for the rectangular longitudinal fin as test case are motivated as follows::

- common fin for cooling of electronics
- comparison with numerous analytical and some experimental studies
- provide new experimental data and expand to three-dimensional study
- ease of construction, low cost
- good test case for heat transfer enhancements
- large flat fin surfaces: ideal for infrared thermography measurements

The use of fin effectiveness as a performance indicator is also to be studied in this work. Hence, besides the fin itself , but also a part of the primary surface on which the fin is placed has to be considered. So the test case should consist of both fin and primary surface. Fins are made from metals with a high thermal conductivity. Aluminum was chosen as fin material, because of its high thermal conductivity and because it can be easily processed to different shapes.

4.2.1 Fin Dimensions

The studied fin type is based on fins used in heat sinks for electronics cooling. An example of such a heat sink with rectangular fins and its associated dimensions is shown in Fig. 4.10.

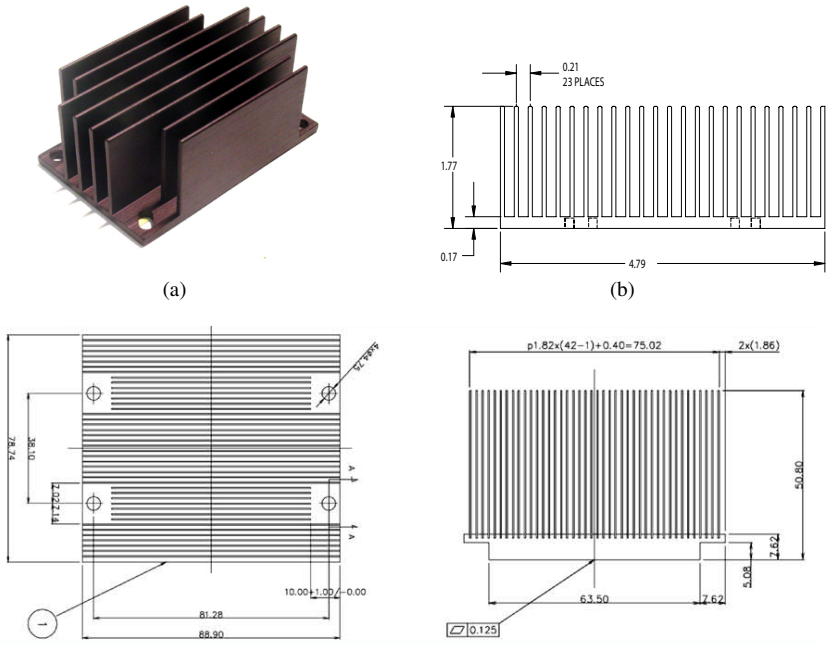

(a) (b) (c)

Figure 4.10: Examples of heat sinks with longitudinal rectangular fins

There is a wide variety in the dimensions of longitudinal fins used for heat sinks, but they are always very thin compared to the height and the length, as can be seen in Fig.4.10. The determination of the dimensions of the fin test case was based on two factors:

- dimensions commonly used in practice
- field of view of the infrared camera

Dimensions from literature

Deans et al. [128] studied the thermal resistance of parallel plate heat sinks (which are rectangular longitudinal fins). The investigated heat sink fin had a length

	d/H	L/H	I/d
Deans et al. [128]	0.025	1.07	2.4
Shaeri et al. [26]	0.33	2	
Sikka et al. [7]	0.12	2.5	4
Elshafei [33]	0.04	4.4	7.5

Table 4.1: Fin dimension ratios for some studies in literature

of $70\mathrm{mm}$, height of $65\mathrm{mm}$ and a thickness of $1.6\mathrm{mm}$. The fin spacing was $3.8\mathrm{mm}$, thus almost two and a half times the fin thickness. Shaeri and Yaghoubi [26] studied perforated parallel plate heat sinks with dimensions $24\mathrm{mm}\times$ $12\mathrm{mm}\times$ $4\mathrm{mm}$. The wavy fins in the heat sinks studied by Sikka et al. [7] had a length of $63.5\mathrm{mm}$and a height of $25.4\mathrm{mm}$, thickness of $3.175\mathrm{mm}$. Fin spacing is $12.7\mathrm{mm}$. Elshafei [33] investigated the flow bypass in longitudinal fin arrays, with fin length $225\mathrm{mm}$, height of $51\mathrm{mm}$ and fin thickness $2\mathrm{mm}$ to a fin spacing of $15\mathrm{mm}$. These are just a few examples of the various dimensions studied in literature. Yet, more important are the dimensionless ratios: thickness to height ratio (d/H), length to height ratio (L/H) and fin spacing to thickness ratio (I/d). These ratios are given in Table 4.1.

In practical heat sinks, the thickness to height ratio is often smaller than 0.1. The ratio of 0.33 as used by Shaeri and Yaghoubi is not common. These fins are probably made thicker because they are perforated. An important ratio for heat sinks is the fin spacing to fin thickness ratio, which is usually between 1 and 4, as confirmed by the examples from literature. This ratio is especially important for flow bypass, which increases for a smaller ratio due to increasing pressure drop. However, a lower ratio means more fins for the same surface area, and thus a better heat dissipation. The fin spacing in the work of Elshafei [33] is not very common, as it was chosen to study the bypass effect. Finally, the length to height ratio is also mentioned here, not because it is an important parameter for the thermal performance, but rather because this ratio is used first to determine the fin dimensions of the test case.

Dimensions based on measurement equipment

As mentioned in paragraph 4.1 an infrared camera will be used to measure surface temperatures. The way this is done, is explained in paragraph 4.3. The camera's spatial resolution of 1.6mrad corresponds to a minimal distance of $0.8\mathrm{mm}$ between two points that the camera can detect for the minimal camera focus distance of $0.5\mathrm{m}$. In order to do temperature measurements as accurate as possible, the choice was made to use as many measurement points as possible. This improves the temperature accuracy and the accuracy for the local heat transfer coefficient

determination increases also, as a more accurate temperature profile can be measured. As the dimensions of fins of heat sinks are normally small, (in the order of centimeters), the studied fin is an upscaled model of heat sink fins. The upper limit on the fin dimensions is determined by the field of view (FOV) of the camera. The largest fin surfaces are the side surfaces, determined by the fin length and height. This would mean that the further the camera is placed from the fin, the larger the fin could be. However, to minimize the disturbing influence from the surrounding on the measurement, the choice was made to place the camera as close as possible to the measurement object, thus $0.5\mathrm{m}$(minimal focus distance). The FOV of the MIDAS camera is 29°(H) × 22°(V). The corresponding FOV expressed in m can be approximated from this, according to Fig. 4.11, with the following expressions:

$$X_{FOV} = 2\tan(\frac{\theta_{H,FOV}}{2}) \cdot L_{focus} \tag{4.10}$$

$$Y_{FOV} = 2\tan(\frac{\theta_{V,FOV}}{2}) \cdot L_{focus} \tag{4.11}$$

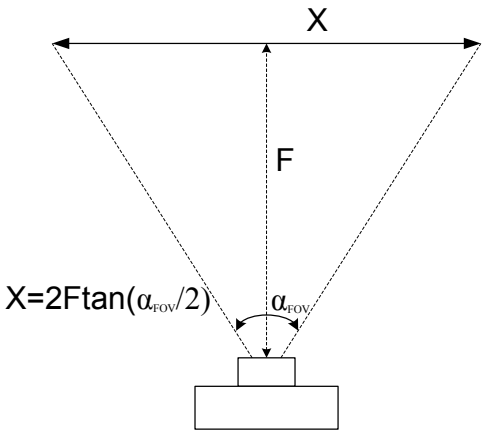

Figure 4.11: The field of view (FOV) recalculation to object dimensions

For the minimal focus distance, the FOV is $0.259\mathrm{m}$(H) × $0.194\mathrm{m}$(V). Thus the maximal fin length is $0.259\mathrm{m}$. For reasons of availability of equipment (i.e. the heat source, explained in paragraph 4.3), the fin length was set at $0.254\mathrm{m}$(10 inches). The maximum fin height is $0.194\mathrm{m}$, but a length to height ratio closer to two is preferred. The height was chosen at $0.142\mathrm{m}$, which gives a L/H ratio of 1.8. A fin thickness of $0.005\mathrm{m}$ gives a d/H ratio of 0.035, so smaller than 0.1. This thickness is standard for aluminum plates. These dimensions are obviously much larger than the standard dimensions used in heat sinks. A more realistic fin for

heat sinks with the same dimensional ratios could have the following dimensions: $51\mathrm{mm}\times$ 28 $\mathrm{mm}\times$ $1\mathrm{mm}$. So the fin is scaled five times.

4.2.2 Primary surface

The fin model not only consists not only of the fin, also a part of the primary surface is modeled. This is necessary in order to determine the fin effectiveness. For heat sinks, the primary surface is actually the base plate, but it could be generalized to any kind of flat primary surface. A stand alone fin is investigated, and can be observed as cut from a series of fins in a heat sink (Fig. 4.12). The primary surface then consists of the base plate for half the fin spacing at both sides of the fin. Again, it is preferred to have the largest possible primary surface area for the measurement accuracy. Therefore the fin spacing was chosen at four times the fin thickness, which is still common in actual heat sinks.

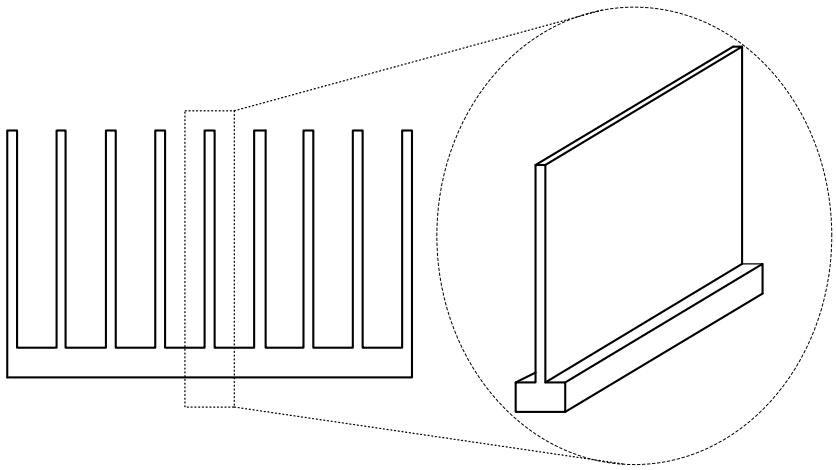

Figure 4.12: The studied fin as cut out off a heat sink

4.3 Experimental setup

The definition of fin effectiveness was already given in Chapter 1 (Fig.1.17). As a reminder, it is the ratio of heat exchange by the fin (Q_f) to that of the primary surface that is covered by the fin's base in absence of the fin (Q_b). So in order to experimentally determine fin effectiveness, a primary surface has to be heated and the heat flux through this surface has to be known. In a second phase, a fin is placed on a part of this heated primary surface and the heat flux through the

fin is determined. The experiment itself is designed as follows. A rectangular aluminum primary surface is heated at the bottom. A second primary surface of the same dimensions is constructed, but with an aluminum cooling fin on top. A heat source provides a constant heat flux to the bottom of the primary surface, and the heat losses sideways from the primary surface and especially downwards from the heat source are minimized in order to force all heat flux upwards through the aluminum primary surface and fin. This is necessary to accurately impose the amount of heat dissipated by the primary surface and fin accurately. Therefore a guard heater assembly is constructed around the primary surface. This guard heat will be explained later. The is entire setup is placed in a wind tunnel

4.3.1 Fin forms

Rectangular longitudinal fins of $0.254\mathrm{m}$ long, $0.144\mathrm{m}$ high and $0.005\mathrm{m}$ thick are studied. A fin is placed centrally on a primary surface of $0.254\mathrm{m}$ long and $0.025\mathrm{m}$ wide. In a first case, the primary surface without fin is measured at seven setpoints of Re, ranging from 9130 to 62115 with the fin surface length as characteristic length. Secondly, a plain rectangular fin is studied. There is no contact resistance between fin and primary surface, as it is made out of one piece. The same geometry is also made with contact resistance. This has the advantage that the primary surface and fin are decoupled, so that different fin forms can be placed on the same primary surface which can stay in place in the experimental setup. A groove of $7\mathrm{mm}$ deep and $5\mathrm{mm}$ thick is made in the primary surface, in which a fin is placed (Fig.4.13). The contact surface S_c (Fig.4.14) introduces a contact resistance for the heat flow. A thermal paste is applied in the groove to reduce this resistance and the heat flow disturbance. This contact resistance can be determined by comparing the measurements of the fin with and without resistance.

All other studied fins are made without primary surface and are placed in the grooved primary surface. The other fin types that are measured are perforated fins, as studied by Shaeri et al. [26]. These are longitudinal fins with lateral square perforations, ranging from one to 20 perforations. The fins with one and two perforations are adapted in this study, with the exact same placement of the perforations. Figure 4.13 shows such a fin, and a scheme with dimensions is given in Fig.4.15 for a fin with two perforations.

4.3.2 Wind tunnel

The fin with primary surface is placed in a wind tunnel to study the influence of the air flow speed on the fin effectiveness, local heat transfer coefficients and average heat transfer coefficient. The latter value can be compared with value from literature on forced convection along a flat plate. The air speeds commonly used

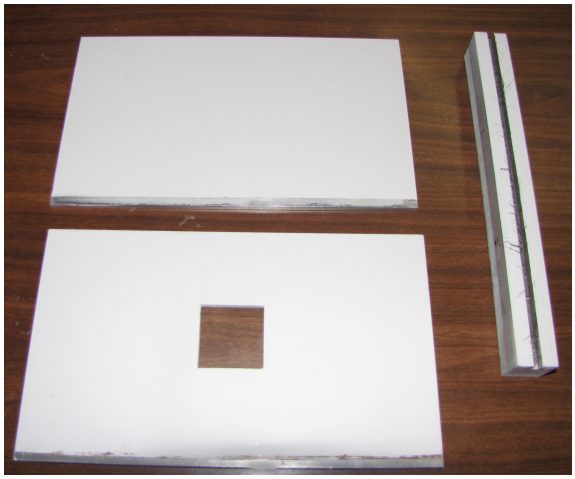

Figure 4.13: The rectangular fin, fin with one perforation and the grooved primary surface

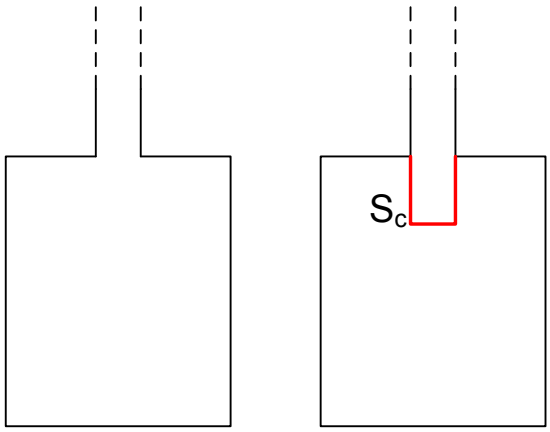

Figure 4.14: The contact resistance surface

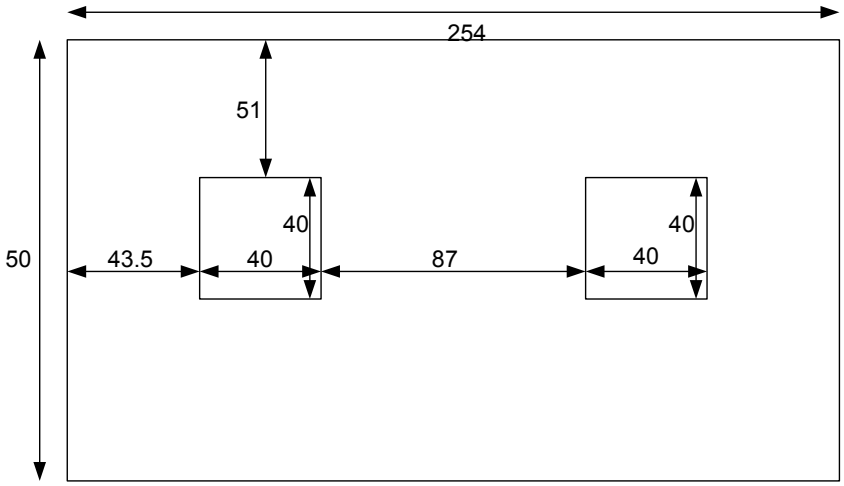

Figure 4.15: Scheme of a perforated fin

in cooling of electronics and heat sinks varies between $1\mathrm{m/s}$ and $6\mathrm{m/s}$ (examples from literature are [26] and [128]), but can go up to higher speeds such as 10 $\mathrm{m/s}$. On average the air speed is situated between $3\mathrm{m/s}$ and $6\mathrm{m/s}$. Normally, the Reynolds number range is specified for experimental research, but the definition of this number varies from author to author. Some authors use the fin thickness as characteristic length [26], others the fin length or the fin spacing [7]. In text books the hydraulic diameter of the flow section is commonly used as characteristic length. The fin and air temperatures in the experiment are assumed to be comparable to the temperature normally reached in heat sinks. Thus the thermal properties of air used in the Reynolds number definition (4.12) (i.e. ρ and μ) are the same as in real applications of these heat sinks.

$$Re = \frac{\rho L v}{\mu} \tag{4.12}$$

So, if the case of a heat sink fin with real dimensions is labeled with the subscript 1, and the test case which is scaled five times bigger with the subscript 2, then the following equation is obtained for equal Re-numbers:

$$Re_1 = Re_2$$
$$\frac{L_1}{L_2} = \frac{v_2}{v_1}$$

So the characteristic length is inversely proportional to air velocity, which

means that the air velocity should be five times smaller for a fin that is five times larger. This gives a Re-range of 0.2 to $2\mathrm{m/s}$ for the wind tunnel. The results for a perforated fin type are compared with data from Shaeri et al. [26], thus their Re-range should be reached in the wind tunnel. They used the fin length as characteristic length, which gave a Re-range of 12.000-30.000. For the fin length of $0.254\mathrm{m}$, this implies a velocity range of $0.8\mathrm{m/s}$-$2\mathrm{m/s}$. This coincides with the same range as calculated previously. So the wind tunnel needs to be a low speed wind tunnel, which operates in the range of 0.2-$2\mathrm{m/s}$. A low speed wind tunnel was available in the department from the PhD work of Leon Patino [129]. Figure 4.16 gives a view of the wind tunnel setup and inlet with honeycomb. This honeycomb is used to achieve a spatially uniform steady air flow over the wind tunnel section. Behind the honeycomb, a turbulence screen is placed that smooths non-uniformities in flow speed. The working range of this wind tunnel is plotted in Fig.4.17, together with the turbulence intensity at various air velocities. The air velocity and turbulence intensity are plotted against the fan speed in rotations per minute. So the air velocity in the wind tunnel can be set by setting the fan speed with a frequency controller.

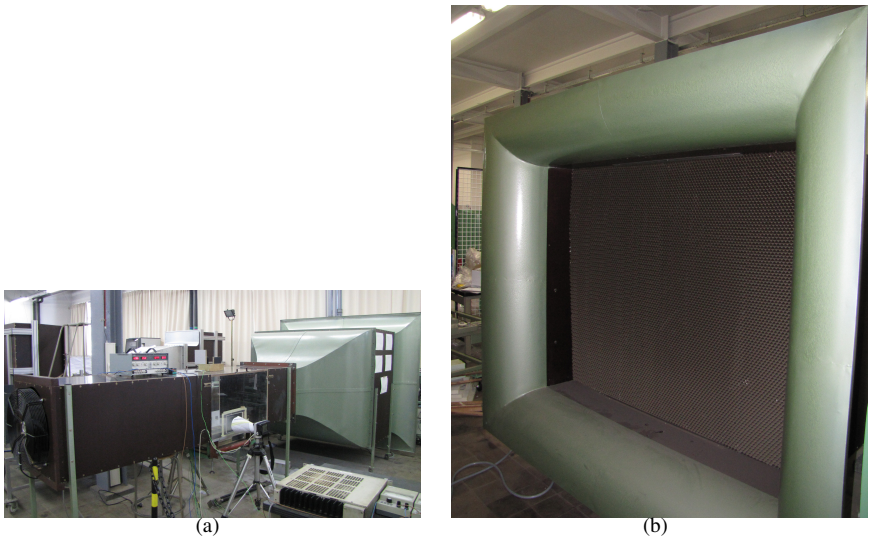

(a) (b)

Figure 4.16: View of the wind tunnel (a) and the inlet of the wind tunnel with honeycomb (b)

The turbulence intensity drops to 2% for an air speed $0.61\mathrm{m/s}$. The maximum air speed is $4.15\mathrm{m/s}$, with a turbulence intensity of 1%. By using the Re-analogy, the corresponding air velocity range for real fin dimensions is $3\mathrm{m/s}$- $20\mathrm{m/s}$.

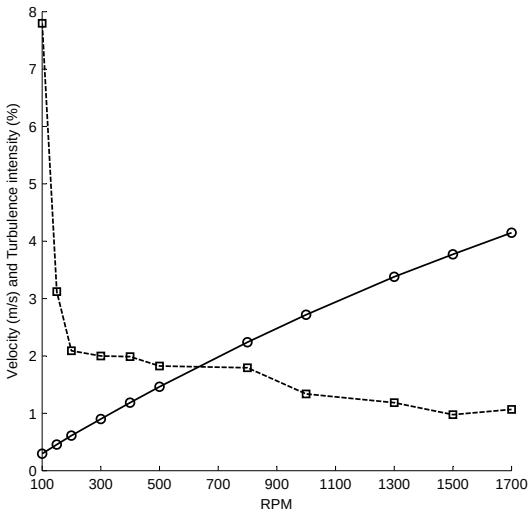

Figure 4.17: Working range and turbulence intensity of the wind tunnel (∘: velocity ; □: turbulence intensity

The wind tunnel has a rectangular test section of 600 mm width and 500 mm height. Every fin type is investigated at seven air velocities varying from 0.61 m/s to 4.15 m/s which corresponds to the following Reynolds numbers ranges at 20°C ambient temperature:

- hydraulic diameter of the test section: Re_{D_h} = 19590 - 133280
- fin length: Re_L = 9130 - 62115
- fin thicknes: Re_d = 180 - 1220

The fin base is set at the same height as the bottom plate of the wind tunnel to avoid disturbance of the air flow and to be able to build a guard heat round the fin base plate. A part of the base plate of the wind tunnel is made adjustable in height. The fin is placed on this base plate, which is adjusted in height so that the insulation surface and primary surface are at the same level as the bottom wall of the wind tunnel, or can be placed higher into the wind tunnel if necessary.

4.3.3 Guard Heater

The fin and primary surface are heated at the bottom, so a heat source is necessary. It is important to have a heat source that is constant in time, so the heat generation at the primary surface is known and constant during the whole experiment.

Therefore, the choice was made to use an electrically powered heat source. If an electric current I flows through a resistance R, the produced amount of heat in the resistance is defined as RI^2. If the resistance is constant, the heat generation will be constant if a power source at a stable voltage is used. First, the required amount of heat has to be determined to chose an appropriate power source and resistance.

Amount of power

The larger the power of the source, the higher the fin temperature. This temperature depends on the thermal conditions at the fin surfaces, i.e. the convection in the wind tunnel. In section 4.1, it was found that temperature measurements with the infrared camera gave more accurate results for temperatures higher than 55°C. The emissivity of the high emissivity paint is more accurately determined for temperatures > 55°C, as is also the case for the transparency of the IR-window material. Therefore, a fin temperature around 70°C, which is also common in heat sink applications, was set as desired temperature. Depending on the air velocity, the amount of convective heat transfer varies, and thus also the fin temperature. This amount of convective heat transfer Q_{conv} is defined as:

$$Q_{conv} = hA(T_{fin} - T_{amb}) \tag{4.13}$$

In Eq.(4.13), A is the total surface of fin and primary surface in the wind tunnel, h is the average convection coefficient over this surface and T_{fin} is the average fin temperature. T_{amb} was set at 20°C. Because infrared thermography was used, the fin and primary surface were painted with high emissivity paint This also means that for surface temperatures 10°C higher than the ambient temperature, radiated heat transfer becomes important. The amount of radiated heat for the fin and primary surface is calculated as:

$$Q_{conv} = \sigma\epsilon A(T_{fin}^4 - T_{amb}^4) \tag{4.14}$$

So, the total heat transfer from the surface of fin and primary surface to the wind tunnel is determined as

$$Q_{tot} = hA(T_{fin} - T_{amb}) + \sigma\epsilon A(T_{fin}^4 - T_{amb}^4) \tag{4.15}$$

All these terms are known, except the average convection coefficient h, which is determined from the equation of laminar convective heat transfer over a horizontal flat plate [130]:

$$Nu = 0.664 \cdot Pr^{1/3} \cdot \sqrt{Re} \tag{4.16}$$

The characteristic length for Nu and Re is the plate length. For the studied fin with length $0.254\mathrm{m}$ and thermal properties of air taken at the average temperature

of 45°C, the Nu range corresponding to the velocity range 0.6-4.15$\mathrm{m/s}$ is Nu = 55 - 148, which makes the range of the heat transfer coefficient h = 6 - 16 $\mathrm{W/m^2K}$. With these values, the heat exchanged from a fin at 70°C in the wind tunnel to its surroundings, is situated in the range:

$$Q_{tot} = 49.89 - 88.57W \tag{4.17}$$

The amount of heat transferred by radiation is 26.68W, which is not negligible. For the accuracy and ease of the experiment, the heat source generates the same amount of power for all different Re-numbers. At 70W, the average fin temperature at low air velocities will be higher than 70°C, which is not a problem for the measurement accuracy. However, at higher air speeds, the fin temperature will drop below 70°C. In order to maintain good accuracy for the infrared temperature measurements, this temperature should stay above 55°C. At 4.15$\mathrm{m/s}$ the fin temperature for a heat source at 70W is still 60°C.

Guard heater construction

A flexible silicone rubber heat foil of Watlow is used as heat source. It is a wire wound heat foil, that can produce up to 100Wof heat, and can withstand temperatures up to 250°C. The heat flux is divided relatively equally over the foil surface, so there are no hot spots that could influence the heat distribution in the fin. The electrical power dissipated by the heat foil is converted entirely into heat. The heat foil is powered by an adjustable electrical power source. The amount of electrical power is measured with an analogue power meter and a digital multimeter. The accuracy of the multimeter on a DC voltage measurement is 0.1%. In order to force all heat flux upwards from the heat source through the aluminum block, heat losses sideways from the primary surface and especially downwards from the heat source have to be minimized. Therefore a guard heater assembly is constructed (Fig. 4.18). The guard heater consists of a second heat foil that is placed beneath the first one with a 10 mmthick layer of promatect type K insulation (k = 0.2 $\mathrm{W/mK}$) between both heat foils. Another layer of promatect is placed under the guard heat foil. A promatect case of 4mm thick is built around the primary surface with the two heat foils. Two wire-wounded heaters consisting of resistance wire are situated on the outside of this casing. One heater is placed along the total height of the primary surface to limit the heat losses from the side surfaces. The second heater is situated between the two heat foils to impede possible heat loss between from the bottom of the source heat foil, through the side walls of the promatect insulation layer, which were found not negligible from numerical simulations.

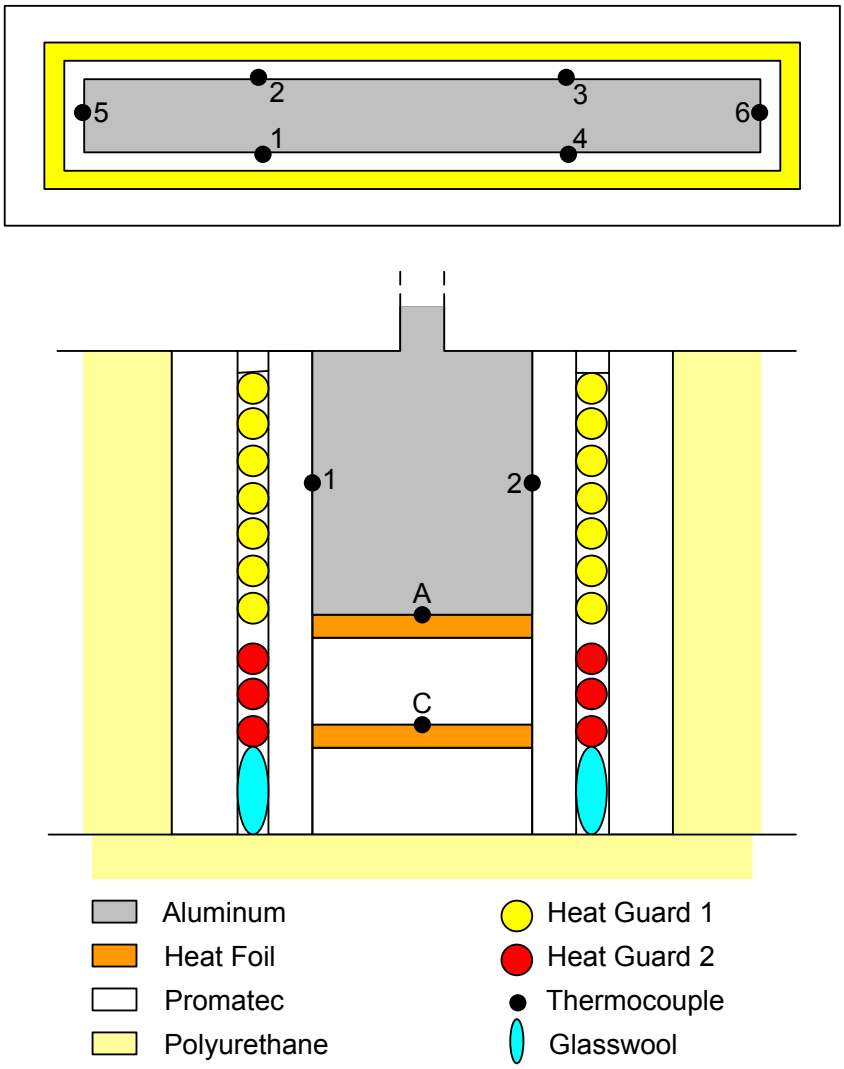

Figure 4.18: The guard heater composition

Heat losses

The temperatures on both heat foils are measured with two thermocouples at each foil. The temperature of the second heat foil is tuned by controlling the amount of dissipated electrical power with a regulating transformer. This temperature is set at the same temperature as the heat source foil. The temperature at the wire-wound guard heater around these heat foils is also measured with a thermocouple, which is connected to a PID-controller. The setpoint of this controller is equal to the heat foils temperature, and the wire-wound heater is kept at this temperature by the PID-controller. The same technique is used for the wire-wound heater around the primary surface. The side wall temperatures of the aluminum primary surface are measured at six points with thermocouples. At the same position, but on the outside of the promatect casing another six thermocouples are placed. The positioning of the thermocouples is indicated in Fig.4.18. The thermocouples are situated halfway the height of the primary surface. The temperature variation along this height is limited: about 0.5°C. The guard heater is controlled by a second PID regulating device that adjusts the voltage until the temperatures on primary surface and guard heater are equal. Only one of the six thermocouples 1-6 can be used as setpoint for this PID-controller, yet the measured temperature is not equal for all thermocouples: thermocouples 1-4 measure similar temperatures (only 0.1°C difference), but thermocouples 5-6 at the end walls are at lower temperatures: the difference with thermocouples 1-4 can be up to 2°C (see Fig. 4.18). All thermocouples 1-6 are constantly monitored, as well as the thermocouples 7-12. The highest temperature for thermocouples 7-12 was always kept as close to but just below the temperature of the corresponding thermocouple on the primary surface (thermocouple 1-6).This is done to prevent that the guard heater induces extra heat flux into the primary surface. Thus the thermocouple at the highest temperature in the guard heater is used to control the voltage in the guard heater. The maximum difference between thermocouples 1-6 and 7-12 is limited to 1°C. This is the maximal temperature difference between the side wall of the primary surface and the guard heater, thus the temperature difference that stands over the $4\mathrm{mm}$ promatect. At the end walls (thermocouples 5-6), this temperature difference can go up to 2°C. So the maximum heat loss along the primary surface side walls is estimated as:

$$\begin{aligned} Q_{loss1} &= \frac{k_{prom}}{d_{prom}}(A_{side} \cdot (1K) + A_{end} \cdot (2K) \\ &= 0.84\mathrm{W} \end{aligned} \tag{4.18}$$

The heat loss through the side walls is maximum 0.84W, which is 1.2% of the total dissipated heat. The same calculation is done for the heat loss at the bottom of the heat foil. The measured temperature difference between thermocouples

A-C and B-D can vary, but the maximum difference is limited to 2°C for all measurements. This corresponds to a heat loss of 0.25W, or 0.4%. This error on the imposed heat flux is used in Chapter 5 for the error estimation.

This guard heater system was placed in an insulation box of polyurethane (k = 0.028 $\mathrm{W/mK}$) to further limit the heat losses and improve the warming up time of the system. Polyurethane is a much better insulator than promatect, nevertheless it was not used to construct the guard heater, because it has a melting temperature of 100°C, and it already becomes weak at temperatures of 70°C. Promatect can withstand much higher temperatures and is more robust. The insulation box has dimensions of $600 \times 400 \times 90\mathrm{mm}$, and is placed in the adjustable base plate of the wind tunnel test section. This assures that the top of the box and primary surface coincide with the base plate of the wind tunnel.

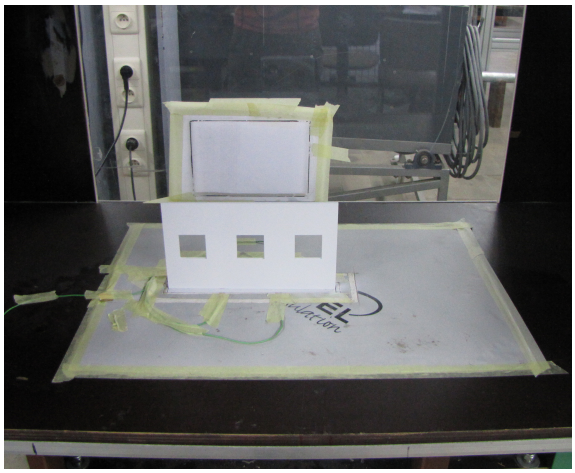

Figure 4.19: The guard heater with perforated fin in the insulation box

4.3.4 Material

The fins and primary surface were made out of aluminum, which has a high thermal conductivity. Two types of aluminum were used: duralumin and aluminum of type EN-AW-6060. The duralumin is used to construct a longitudinal fin connected to the primary surface, thus made out of one piece to avoid contact resistance between fin and primary surface. This is not possible with EN-AW-6060 aluminum, because it has a lower tensile strength and would bend when milled out of one block aluminum. All other fins, without primary surface, are made out of EN-AW-6060 aluminum, which is cheaper. The thermal properties of both types of aluminum were determined with a laser flash diffusivity apparatus. These was

done at the Belgian Ceramic Research Centre (BCRC) and at the Applications Laboratory of Netzsch-Gerätebau. The laser flash method measures the thermal diffusivity a and specific heat c_p of the aluminum, from which the thermal conductivity is calculated as:

$$k = \rho \cdot a \cdot c_p \tag{4.19}$$

The thermal conductivity was determined at three temperatures for each kind of aluminum. Five tests were performed at each temperature from which the average was taken. The results are plotted in Fig. 4.20. The value at 70°C is 190 $\mathrm{W/mK}$ for duralumin, and $218\mathrm{W/mK}$ for EN-AW-6060 aluminum.

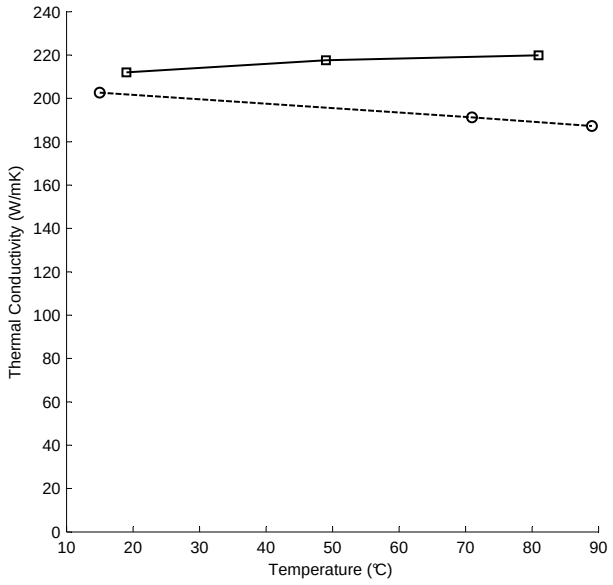

Figure 4.20: The thermal conductivity of aluminum (○: duralumin ; □: EN-AW-6060)

Thermal paste was also used during the experiments to reduce the thermal contact resistance: the a resistance between the heat foil and the primary surface, and between the primary surface and the fin base. At both contact surfaces, a thin layer of Arctic Silver 5 is applied. This has a thermal conductivity of $8.9\mathrm{W/mK}$ and reduces the contact resistance by replacing air cavities (thermal conductivity of air: $0.03\mathrm{W/mK}$ at 80°C) with the better conducting arctic silver.

4.3.5 Measurement setup

To accurately control the airflow around the fin, it is placed inside a wind tunnel section, with wooden and plexiglass walls. The thermpographic camera cannot be placed inside the wind tunnel in order not to disturb the air flow. Otherwise the advantage of thermography as a non-contact measurement technique, which does not disturb the measured process, would be lost. Therefore the camera is placed outside the wind tunnel, and an optical access has to be made in the wind tunnel to view the fin sides and top of the primary surface with the infrared camera. This optical acces is made in the form of windows, made out of HDPE, which has a transparency of 90% in the temperature range of interest [55°C- 80°C]. The use of HDPE as a window material was discussed in section 4.1.4.3.Three windows are placed in the wind tunnel section walls (Fig. 4.21:

- at the front side to measure the front fin surface
- at the top to measure the fin tip and primary surface
- at the back side for the back fin wall temperature measurement, however, this window is only necessary for fins where there is no symmetry anymore (such as the perforated fins)

The camera is placed in front of these windows at $0.5\mathrm{m}$, the minimum focal distance, of the measured surface. As explained in section 4.1, reflections from surroundings and camera on the window interfere with the measurements. The same technique as for the window transmittance calibration was applied to minimize the disturbance from the surroundings and correct the measurements for camera reflectance. First, the influence of radiation from surrounding objects was minimized by placing a shield round the optical path between camera and window (Fig. 4.21). The shield is made from paper ($\epsilon = 0.9$) and has a conical form. It is attached at the camera lens, and extends to the window. This way, radiation from the surroundings cannot interfere with optical path and reflect on the window into the camera lens. The only disturbance during measurements comes from the reflectance of the camera lens on the window. This reflectance is compensated for by using calibration images, as explained in section 4.1, at the start and end of each measurement. A schematic view of the measurement setup is shown in Fig. 4.21, and a picture of the setup in Fig. 4.22.

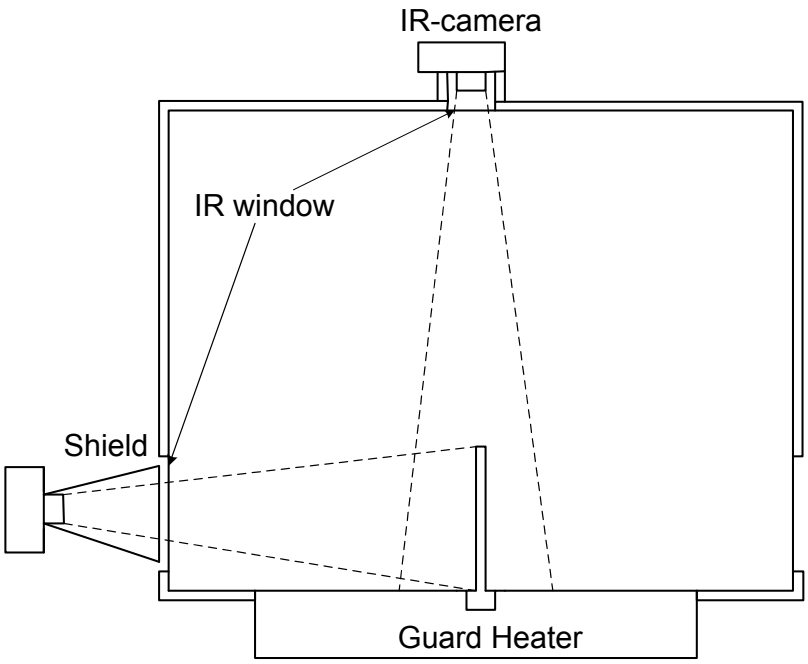

Figure 4.21: Schematic view of the measurement setup

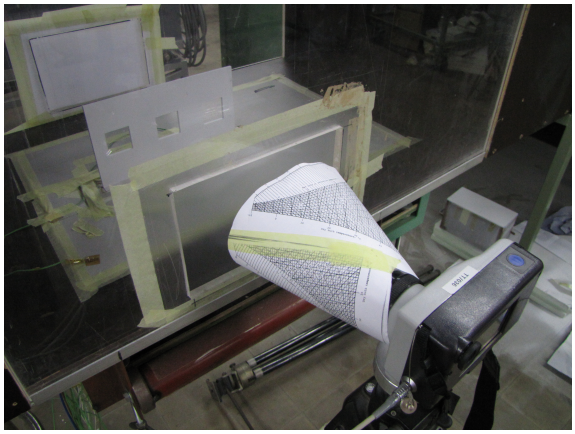

Figure 4.22: The camera with shield for HDPE window in test section

5 Results Experimental Test Case

In this chapter, the results of the experimental test case are presented. First, the data processing and reduction of the temperature measurements are explained. In a second part, the results for the local heat transfer coefficient estimates for a plain rectangular fin and perforated fins are presented and discussed. The fin effectiveness was also determined.

5.1 Data Reduction

The temperature profiles measured using infrared thermography are used as input for the IHCP, in which they are imposed as boundary conditions. The processing of the measurement data is shown in Fig. 5.1.

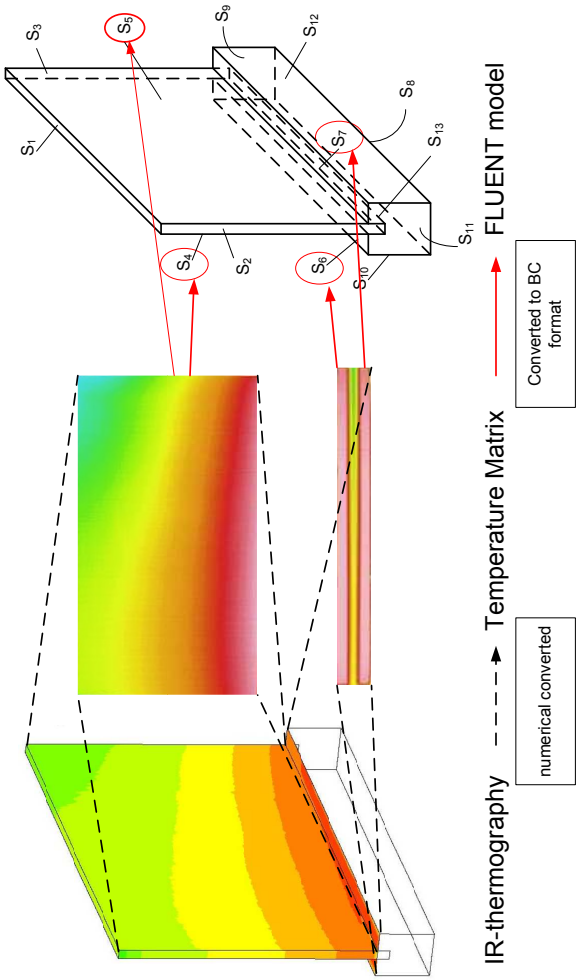

Figure 5.1: Processing of the measurement data to IHCP input

5.1.1 From infrared image to temperature matrix

An infrared image consists of 320 × 240 pixels. Each pixel is a separate measurement point, and contains a numerical value for the corresponding temperature. The IR-camera software makes it possible to export these temperature values in other forms than images, such as text files or excel tables. All the data from one image is written to those files, but only a part of it is useful, i.e. the temperatures of the pixels corresponding to the fin, represented by the dashed rectangle in Fig. 5.2. The boundary data points of the fin were carefully detected, because interference occurs in the pixels at the fin edges (Fig. 5.3). Pixels situated at the edges (high temperature gradient) receive radiation from both parts of the edge and will give an average temperature. It has to be prevented that these boundary pixels are admitted to the temperature matrix, as they are no physically existing fin temperatures. The number of pixels in which this interference occurs depends on the distance between camera and measurement object. In Fig. 5.3 two to three pixels near edges are affected by this. The camera focus also influence this interference effect, because a bad focus causes unsharp boundaries. A procedure was written to detect the edges and reduce the excel file to a rectangular matrix only containig the fin temperature data.

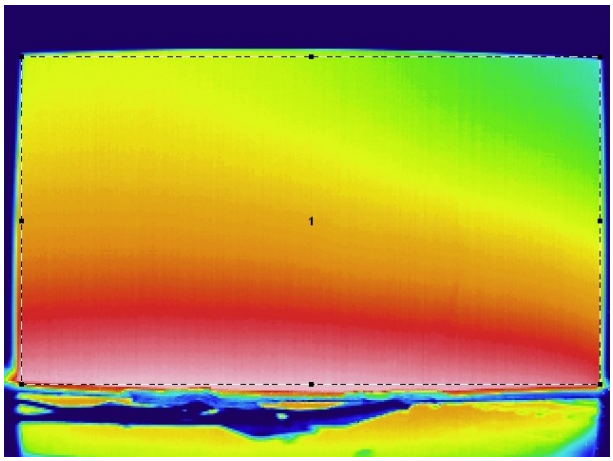

Figure 5.2: View of an IR-image for a fin as seen in the IR-camera software. Only the temperature data in the dashed rectangle us useful

5.1.2 From temperature matrix to IHCP boundary conditions

The temperature matrix has to be converted so that it can be used in FLUENT as a boundary condition for the model of the fin and primary surface. This FLU-

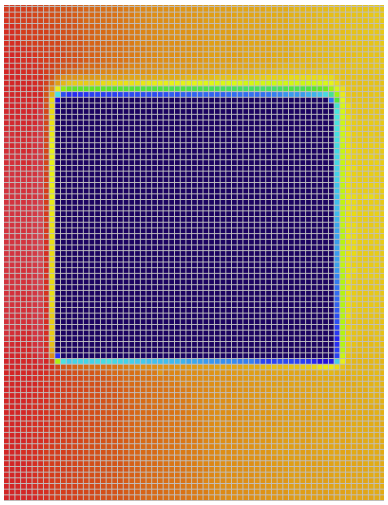

Figure 5.3: Interference of temperature measurements near edges with infrared thermography

ENT model is built based on the number of measurement points. It was explained in Chapter 2 that the number of measurement points in the temperature image is equal to the number of cells on the corresponding boundary surface of the FLUENT model. Thus the number of elements in the temperature matrix defines the grid size. A program is written that automatically generates a grid based on the number of matrix elements. FLUENT cannot use excel files as input for boundary conditions. External data can be written to a FLUENT grid by using profile files: text files containing the spatial coordinates and data values for each data point that is imported into FLUENT. The spatial coordinates of each measurement point are calculated and a program developed in this work, converts the measured temperature matrix to a profile file. These profile files are read into FLUENT and imposed as boundary condition on the boundary surfaces $S_1 - S_7$ (as named in Fig. 2.14). Once these boundary conditions are imported in FLUENT, one calculation iteration is performed to transfer these temperature values to cell centers and to a user-defined memory (UDM). The measured temperature values are now available in FLUENT and in the IHCP solution procedure. This is necessary as the measured temperatures are used to calculate the minimizing functional J (Eq.2.13) and are the boundary condition on surfaces S_1 – S_7 for the IHCP. Now the IHCP can be solved using CGM, as was done previously in Chapter 2. The stopping criterion of the CGM is determined by the uncertainty on the temperature measurements.

5.1.3 Fin effectiveness

The fin effectiveness was previously defined as:

$$\zeta = \frac{Q_f}{Q_p rim} \tag{5.1}$$

In order to determine fin effectiveness, two IHCP solutions are necessary:

- a solution for *unfinned* primary surface: this determines the denominator of ζ. It is the reference case, which is the same for all fin forms and has to be calculated only once.
- a solution for *finned* primary surface: this is fin specific and is solved for each fin type and at each Reynolds number.

Reference case: unfinned surface

The reference case consists only of the primary surface. The same experiment is similar to the case of a fin on a primary surface: the heat foil is placed at the bottom of the primary surface, the side walls are kept adiabatic with the guard heater and the surface temperatures at the top wall are measured. These conditions are also imposed as boundary conditions for the IHCP. The primary surface is measured at different Re-numbers. The heat source at the bottom surface has to be limited compared to the experimental test case of a finned primary surface: a heat source of 70W would result in top surface temperatures of more than 200°C. It was concluded in section 4.1 that temperatures between 55°C and 80°C are measured more accurately due to the camera calibration. Therefore, a smaller heat generation rate was used. Calculation results indicated a required heat source of 7W only. This is much lower than the 70W dissipated by the primary surface with fin. The question can be raised how the fin effectiveness is determined if different heat fluxes are imposed for the case of an unfinned primary surface. The heat flux distribution at the top surface of the unfinned primary surface is not influenced by the dissipated amount of heat, but only by the fluid flow over the top surface as the side surfaces are assumed adiabatic. The heat flux distribution at the primary surface will only vary along the length due to the air flow. It is expected that the heat flux imposed at the bottom will have the same distribution along the width at the top of the primary surface. The primary surface is divided in three parts $S_1 - S_3$ (Fig.5.4) along the width. The central surface S_2 has the width of the thickness of the fin that will be placed on the primary surface. The surface area is divided as follows: $A_{S_1} = A_{S_3} = 2A_{S_2}$, which means that the surface area of S_2 is $1/5$ of the total top surface area. It is expected that the amount of heat transfer through S_2 is also $1/5$ of the total dissipated heat in the primary surface. The solution of the IHCP for the primary surface with the measured temperature profiles confirms this. The amount of heat going through S_2 is:

$$Q_{S_2} = \frac{7\text{W}}{5} = 1.4\text{W}$$

Tt is assumed that the same distribution form is attained if a heat source of 70W is used. Then the amount of dissipated heat through S_2 is **14**W. This is the same value at all Re, and is used as nominator in the fin effectiveness definition (Eq.(5.1))

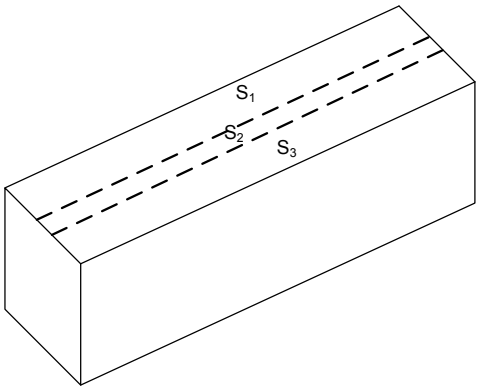

Figure 5.4: Three parts S_1 – S_3 on the primary surface

Solution for finned primary surface

The IHCP is solved for all different fin forms and at all Re from the measured temperature profiles. By solving the IHCP, the local heat flux distribution through the fin and the primary surface is estimated, and thus also the total heat Q_f dissipated by the fin is calculated. This value is then used as denominator in the fin effectiveness definition (Eq. (5.1)).

5.1.4 Local heat transfer coefficients

The IHCP is solved for local heat transfer coefficients, so it is expected that no post-processing of the IHCP solution is necessary. However, this is a dangerous misconception. In a IHCP, conductive heat fluxes are calculated in the fin and these are passed on to the boundaries. However, once at the surface, this heat flux consists of two parts:

- a convective heat flux
- a radiative heat flux

The radiative heat flux is not accounted for in the boundary condition reconstruction of the local convection coefficients $\tilde{h}(S_i)$. So in order to obtain the correct heat transfer coefficient directly from the IHCP, the boundary condition of the direct problem at surfaces $S_1 - S_7$ should have included a radiation term:

$$-k \cdot \frac{\partial T}{\partial n} = h(S_i) \cdot (T - T_\infty) + \sigma\epsilon \cdot \left(T^4 - T_\infty^4\right) \quad \text{on } S_i (i = 1 - 7) \tag{5.2}$$

However, this would complicate the solution of the inverse problem for the construction of the adjoint and sensitivity problem. It is better to solve the IHCP with the convective boundary condition only. Keep in mind that the resulted $\tilde{h}(S_i)$ is then actually a heat transfer coefficient containing both convection and radiation. To obtain the heat transfer coefficient for convection only, the heat flux in each point has to be separated in the two parts. The total heat flux $\tilde{q}(S_i)$ is calculated in each point as a result of the estimated $\tilde{h}(S_i)$.

$$\tilde{q}(S_i) = \tilde{h}(S_i) \cdot (T - T_\infty) \quad \text{on } S_i (i = 1 - 7) \tag{5.3}$$

To obtain the convective heat flux, the radiative heat flux has to be subtracted from the total estimated heat flux $\tilde{q}(S_i)$. This radiative heat flux is relatively large and definitely not negligible, due to the high emissivity ($\epsilon = 0.94$) of the fin and primary surfaces as they are coated with a high emissivity paint to increase the temperature measurement accuracy with the infrared camera. This could be seen as a drawback of thermography. But the upside is that this augments the radiative heat flux, which can then be determined more accurately, as the emissivity is known more precisely as for uncoated surfaces. To calculate the radiative heat flux, view factors have to be accounted for, especially for the measurement points on the primary surface, and those on the fin surface near the fin base. Because of the mutual irradiation between those orthogonal surfaces, the cells near the junction experience the largest influence. A view factor V_f is a calculated for each cell on the fin and primary surfaces $S_4 - S_7$ based on equations found in the work of Siegel and Howell [119]. With the notations from Fig. 5.5, Eq.(5.4) is used to calculate the view factor of each cell. In Fig. 5.5, dA_1 is a cell surface. For cells on the primary surface A_2 is the fin surface, and for cells on the fin surface, A_2 is the primary surface. It was found that only the lower half ot the fin cells are influenced by the radiation from the primary surface. For the calculation of the form factors according to Fig. 5.5 it is assumed that A_2 is at a uniform temperature. In our calculations this is not the case, and a mean surface temperature is used instead. For the primary surface this is a good assumption as there is only a small temperature variation over the total surface area (max 2°C). There is a much larger temperature variation over the fin surface. As radiation will be mainly influenced by the closest fin surface cells, the mean temperature of the lower half of the fin

surface was used instead of the mean temperature of the total surface. The view factor from cell dA_1 to surface A_2 in Fig. 5.5 is given by the following equation:

$$V_f = \frac{1}{2\pi}\left(tan^{-1}\frac{1}{Y_1} - \frac{Y_1}{\sqrt{X_1^2+Y_1^2}}tan^{-1}\frac{1}{\sqrt{X_1^2+Y_1^2}}\right) + \frac{1}{2\pi}\left(tan^{-1}\frac{1}{Y_2} - \frac{Y_2}{\sqrt{X_2^2+Y_2^2}}tan^{-1}\frac{1}{\sqrt{X_2^2+Y_2^2}}\right) \quad (5.4)$$

The radiative heat flux on $S_4 - S_7$ is calculated as:

$$\begin{aligned} q_{rad}(S_i) &= (1-V_f)\cdot\sigma\epsilon\left(T^4 - T_\infty^4\right) + \\ &\quad V_f\cdot\sigma\epsilon\left(T^4 - T^4(S_{avg})\right) \text{ on } S_i(i = 4-7) \end{aligned} \quad (5.5)$$

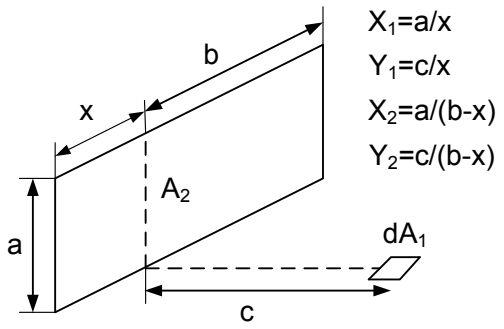

Figure 5.5: View factor from a cell (dA_1) to a surface

The convective heat flux for surfaces $S_4 - S_7$ is determined as:

$$\begin{aligned} q_{conv}(S_i) &= \tilde{q}(S_i) - (1-V_f)\cdot\sigma\epsilon\left(T^4 - T_\infty^4\right) \\ &\quad -V_f\cdot\sigma\epsilon\left(T^4 - T^4(S_{avg})\right) \text{ on } S_i(i = 4-7) \end{aligned} \quad (5.6)$$

For surfaces $S_1 - S_3$ the convective heat flux is:

$$q_{conv}(S_i) = \tilde{q}(S_i) - \sigma\epsilon\left(T^4 - T_\infty^4\right) \text{ on } S_i(i = 1-3) \quad (5.7)$$

The radiative heat flux is calculated for each surface cell using an UDF in FLUENT. The radiative heat flux is calculated for each surface cell using an UDF in FLUENT, and the resulting convective heat flux is stored as a new UDM-value.

The heat transfer coefficient is determined from this heat flux in each boundary surface cell on $S_1 - S_7$ as:

$$h_{conv}(S_i) = \frac{q_{conv}(S_i)}{(T - T_\infty)} \quad \text{on } S_i (i = 1 - 7) \tag{5.8}$$

5.1.5 Reynolds range

As mentioned in Chapter 4, the range of Reynolds numbers Re_L (with fin length as characteristic length) that can be studied in the windtunnel is $Re_L = 9000 - 62000$. For lower Re-numbers there could be an influence of natural convection. This is indicated by the Richardson number ($Ri = Gr/Re^2$): if $Ri > 0.1$ there is mixed convection, if $Ri < 0.1$ only forced convection is considered. The Richardson number was evaluated for all setpoints of the air speed in the wind tunnel. Mixed convection only occurred at the lowest possible set point ($Re = 9000$). There were no measurements done for this lowest Re-number, so mixed convection is not considered in this work. So the range of Re-numbers studied is limited to $Re_L = 13400 - 62000$ for the experimental measurements. The experiments were performed at six different set point for Re in this range.

5.2 Local heat transfer coefficients

5.2.1 Accuracy consideration

First some general remarks are made on the accuracy and interpretation of these results. The interpretation of the results of local heat transfer coefficients is a delicate matter. The results of the numerical test cases from Chapter 3 illustrate this. The solution of an IHCP gives a good idea of the profile of local heat transfer coefficients over a fin, but the absolute values can have a large error for certain cases such as steep gradients in heat transfer coefficients. An IHCP is capable of reconstructing a steep gradient and this at its correct location, but it has difficulties in estimating the correct absolute value at the peak of this gradient. This value will be largely underestimated for exact ($\sigma = 0$) temperature measurements. If there is an error on the temperature measurements, the error on the estimated $\tilde{h}_i$ will increase but not significantly. The result of the numerical test case with exponentially varying h_i (paragraph 3.1.4) is used to give an idea of this error. There is a peak value of $100\mathrm{W/m^2K}$ for the heat transfer coefficient near one of the edges, followed by a steep (exponential) drop from 100 to $6\mathrm{W/m^2K}$. This low value of h_i occurs over the largest part of the fin surface. The IHCP solution manages to reconstruct this profile but finds a peak value of $60\mathrm{W/m^2K}$ (40% error) for exact temperature measurements, and a peak value of $40\mathrm{W/m^2K}$ (60% error) for a temperature measurement error of 0.5°C. These large errors occur only for this

peak value. The error on the small local h_i is maximum 10% for the exact temperature measurements and 15% for a temperature measurement accuracy of 0.5°C. Thus the accuracy of the temperature measurements plays an important role. Note however that the introduction of a temperature measurement error decreases the accuracy of the estimated local $\tilde{h}_i$, but the decrease in accuracy for an increasing temperature measurement error from 0.1°C to 0.5°C is not significant: the reconstructed local h_i profiles are more or less the same. The main difference is that there is more scattering in the estimated $\tilde{h}_i$ for a temperature error of 0.5°C.

The accuracy of the temperature measurements with infrared thermography was determined at a maximum of 0.5°C after camera calibration (Chapter 4). This temperature accuracy determines the stopping criterion for the residual J of the IHCP solution. This was defined as:

$$J\left[h(S_i)\right] < M \cdot \sigma^2 \tag{5.9}$$

The standard deviation σ is 0.25 for an accuracy of 0.5°C. The number of measurement points depends on the number of camera pixels for the fin temperature measurement. Depending on the test case, this number varies between 105000 and 111000. This gives a stopping criterion $J = 7000$. This stopping criterion is monitored during the iterative solution procedure of the IHCP. This stopping criterion is never reached, except for two cases. The results of these two cases clearly give unphysical solutions in the variation of the heat transfer coefficient. This indicates that overregularization appears in these solutions. The other cases stagnate at a residual J value between 20000 and 60000, depending on the test case. This stagnation at a higher residual J as well as the overregularized solutions indicate that the temperature measurement error is higher than the determined 0.5°C. The extreme case with a residual of 60000 corresponds with a standard deviation of $\sigma = 0.75$ and a temperature measurement accuracy of 1.5°C! This is a very high value, close to the camera accuracy of 2°C as found in the camera specifications (see section 4.1.3). However, camera calibration reduced this error to 0.5°C, so these high residuals have to be caused by other errors.

The IHCP solution for a solid rectangular fin is studied at different iterations. The estimated heat transfer coefficients $\tilde{h}_i$ are investigated for unexpected variations, as this is an indication for the presence of overregularization: a large error in temperature measurements introduces a variation in the estimated $\tilde{h}_i$. As mentioned in the literature survey of Chapter 2, the low frequency structure of the heat flux and heat transfer coefficients is revealed after only a few iterations, the high frequency components are recovered much later. This is due to the diffusive nature of the equations of the CGM. Low frequency structure looks at the global structure of the temperature field in the fin and the global temperature gradient over the fin. This is caused by physical phenomena and will lead to the reconstruction of the local heat transfer coefficients. After a few iterations in the solution procedure,

CGM takes the high frequency components into account, i.e. fast variations in temperatures over small distances. This is typically introduced by noisy data and these high frequency temperature variations are not caused by physical phenomena but are introduced by the temperature measurement inaccuracy. The larger the temperature measurement error, the faster these unphysical effects appear in the solution. This is why the stopping criterion is the regularization parameter and it depends on the temperature measurement accuracy. If variations in the solution of the local $\tilde{h}_i$ appear to be not physical, these could be introduced by larger temperature measurement errors.

The solution of the IHCP is investigated for each iteration, and after 20 iterations a variation in the heat transfer coefficient profile that was not expected, occurred for most measurements. The residual J drops below 40000 after 10 iterations. The results for the local heat transfer coefficients along the fin length are shown for two sets of measurement data for Re_L = 50587 in Figures 5.6-5.7 and this at different iterations. This evaluation is done along the fin length halfway the fin height (Fig. 5.6) and along the fin height halfway the fin length (Fig. 5.7) to exclude the influence of possible edge effects. After 15 iterations, the IHCP solution gave a local heat transfer coefficient variation as could be expected from the boundary layer theory (Fig. 5.6(a)). The air flow goes from right to left over the fin surface. The heat transfer coefficient is the highest at the right side where the boundary layer starts to build up. During the development of the boundary layer, the heat transfer coefficient decreases rapidly along the fin length. Once the boundary layer is fully developed, the heat transfer coefficients decrease slowly. This is the expected heat transfer coefficient profile and there is no reason why a different $\tilde{h}_i$ pattern would occur. However, after 25 iterations a small variation occurs for one set of measurement data (□ in Figures 5.6-5.7), which becomes clearly visible after 35 iterations (Fig. 5.6(c)) and becomes extremely large after 45 iterations (Fig. 5.6(d)). There is still a high $\tilde{h}_i$ at the right side, followed by a fast decrease. However, in stead of steadily decreasing to the end of the fin, a small increase of $\tilde{h}_i$ suddenly appears. This was not expected: there is no reason why the boundary layer should be interrupted or become thinner along the fin length. So this increase could be introduced by temperature measurement errors. If the IHCP solution procedure is continued, this sudden increase $\tilde{h}_i$ becomes very large and gives a $\tilde{h}_i$ variation along the fin length which seems very unnatural (Fig. 5.6(d)). However, this increase in $\tilde{h}_i$ does not appear for the second set of measurement data (∘ in Figures 5.6-5.7). So there has to be a reason for this different resulting $\tilde{h}_i$ between both temperature measurement data sets. Therefore the measured temperature field was investigated for both sets. Figure 5.8 shows the relative error between the measured and calculated temperature field for the first data set. The temperature field calculated with the IHCP was taken after 15 iterations. At the location where the sudden increase occurs, there is a larger area of negative tem-

perature errors. After investigation of the measured temperature field, it was found that this was caused by the reflection of the camera lens. It was explained in Chapter 4 that the camera and camera lens are reflected by the HDPE window in the wind tunnel. This reflection caused a significant error (> 1°C) in the temperature field, but it was corrected for (see section 4.1.4.3). It seems that this correction procedure is not accurate enough. This is possibly due to the fact that the camera is not at the exact same position as it was during calibration of the window. Even a shift of the image over two to three pixels is critical. Also, the camera temperature is not stable, so there is a difference in camera temperature between calibration and measurements. This causes an error in the correction for camera reflection. It was found that there could still be a temperature error varying between 0.1°C and 0.5°C. This temperature error varies from case to case.

The error due to camera reflection is not a random error, but a systematic error. It causes a temperature drop or rise over a large part of the fin surface (indicated in red in Fig. 5.8). As this is a systematic error over a significant area, this cannot be seen as a high frequency component anymore and will influence the IHCP solution earlier than the random temperature measurement errors. This systematic error causes a temperature variation over a part of the fin area. As this temperature gradient is small (of 0.1°C-0.5°C) compared to the temperature gradient over the entire fin, this influences the IHCP solution only after a few iterations, if a certain residual is reached. This is clearly illustrated in Fig. 5.6: the influence of this error became only noticeable after 20 iterations. The residual had already dropped below 15000. However, this is not a fixed rule. Depending on the case, this systematic error can be smaller or larger. The residual value from which the systematic error influences the solution varies from case to case. Thus this is studied for each case separately to prevent that nonphysical solutions are obtained.

For the second temperature data set this systematic error was very small: 0.1°C. This is of the order of the temperature measurement noise and will influence the IHCP solution at a lower residual J than the first temperature data set. Therefore, this second data set gives more accurate results than the first one, as it can converge further without any influence of the systematic error. The solutions obtained from temperature data containing the systematic error lack accuracy because a higher stopping criterion is used, mostly between 30000 and 60000. This corresponds to temperature measurement errors situated between 1°C and 1.5°C. The corresponding error on local $\tilde{h}_i$ was estimated at 15%-25% from numerical experiments. The numerical experiments showed that this error is even larger if there is a steep gradient in $\tilde{h}_i$. So the global heat transfer coefficient profiles and variations over the fin surface are correct in the following results, but the absolute values of $\tilde{h}_i$ have a significant error. The solution with the camera reflection error of 0.1°C reaches a residual J of 10000 when the influence of the camera reflection starts to influence the solution. A residual J of 10000 corresponds to a temperature measurement

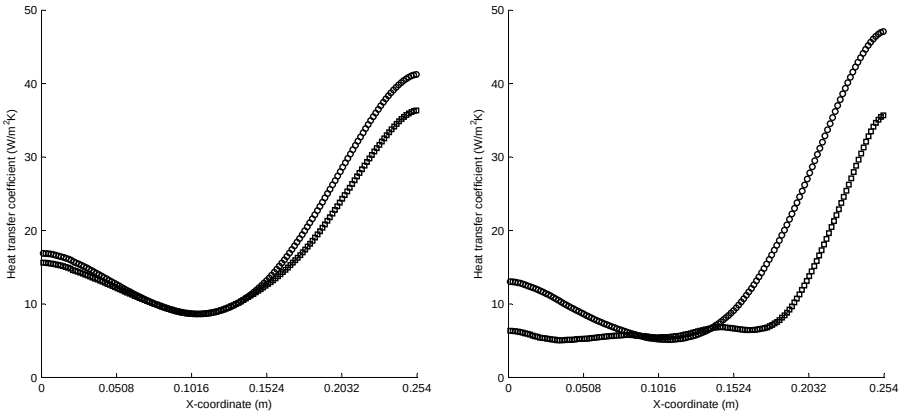

(a) 15 iterations

(b) 25 iterations

(c) 35 iterations

(d) 45 iterations

Figure 5.6: Plots of the estimated heat transfer coefficients $\tilde{h}_i$ for Re = 50587 for a solid fin along the fin length. □: result with camera reflection ; ∘: result without camera reflection

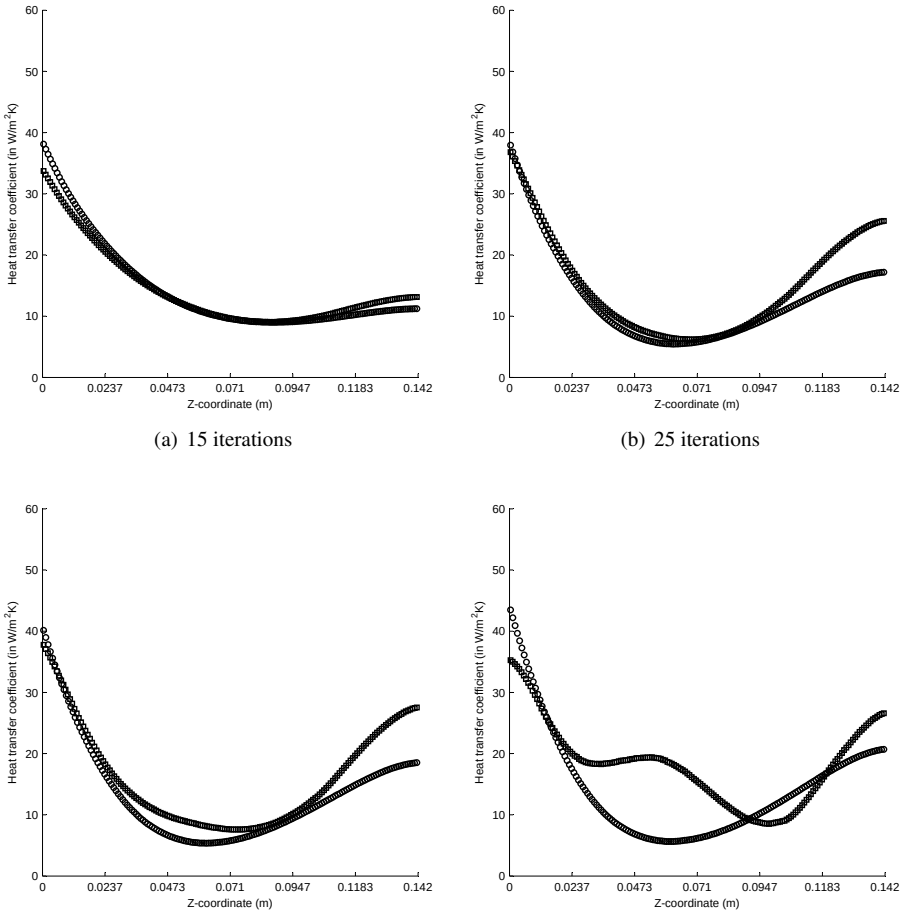

(a) 15 iterations

(b) 25 iterations

(c) 35 iterations

(d) 45 iterations

Figure 5.7: Plots of the estimated heat transfer coefficients $\tilde{h}_i$ for Re = 50587 for a solid fin along the fin height. □: result with camera reflection ; ∘: result without camera reflection

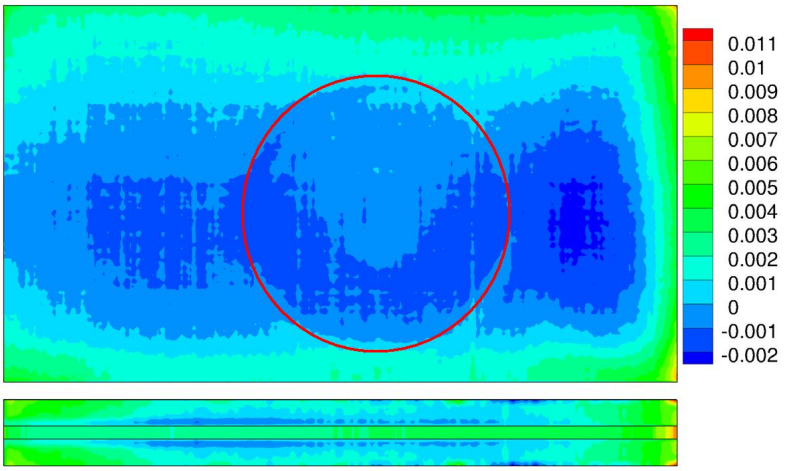

Figure 5.8: 2-D plot of the relative error between measured and calculated temperature for the first measurement data set

accuracy of 0.6°C which is comparable to the calculated accuracy of 0.5°C used in the numerical experiments. This temperature data will give relatively accurate results and is used in the following discussion of the experimental results.

It was very time consuming to obtain a solution without the systematic error from camera lens reflection as it requires an in-situ calibration of the infrared window for camera reflection. This means that the calibration has to be done after each measurement. The windtunnel is opened for this calibration method, which causes an interruption of the steady flow in the windtunnel and thus in the heat transfer. Hence the calibration can only be executed for a short time. After each calibration, the flow has to be stabilized again and a steady state condition has to be attained, which is very time consuming. So this is not the best measurement method. In the following discussion, this calibration method is used for the solid longitudinal fin, but not for the perforated fins. The results for the longitudinal solid fin are thus more accurate than the results for perforated fins which still contain a systematic error.

5.2.2 Results

Three different fins are investigated: a solid longitudinal fin, a longitudinal fin with one perforation and a fin with two perforations. The results for local heat transfer coefficients are evaluated in a similar way as the results of the numerical test cases in Chapter 3. This means that 2-D plots of the front fin surface S_5 and

primary surfaces S_6 – S_7 are used, as well as line plots along evaluation lines. Five evaluation lines along the fin length are used, and two along the fin height. There is also still one evaluation line along the length on the primary surface. The location and numbering of evaluation lines L_1 – L_5 is shown in Fig. 5.9. Evaluation line L_6 is situated on the primary surface along the length.

The three cases are studied at six different Re_L in the range of Re_L = 13400 – 62000. The $\tilde{h}_i$ variation is very similar for different Re_L, but the absolute values differ: local $\tilde{h}_i$ are higher for higher Re_L, and the gradients of $\tilde{h}_i$ are also steeper at higher Re_L. Because of the similarity for different Re_L, the local $\tilde{h}_i$ are only discussed at one Re_L for the three different fins. The discussion is done for the results of Re_L = 50587. The air flows over the fin from right to left.

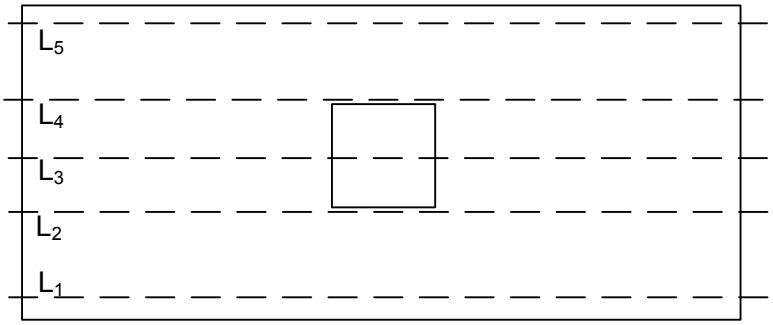

Figure 5.9: The five evaluation lines L_1 – L_5 along the fin length

Solid fin

The 2-D plot for $\tilde{h}$ is shown in Fig. 5.10. The line plots for $\tilde{h}_i$ along evaluation lines L_1 – L_6 are shown in Fig. 5.11. The heat transfer coefficient profile along the fin length follows, as expected, the boundary layer development: the heat transfer coefficient is the largest at the right side where there is no boundary layer. The boundary layer develops over the first half of the fin length. During development, the boundary layer builds up rapidly, which explains the steep gradient for $\tilde{h}_i$ along the fin length over the first fin half. Once the boundary layer is fully developed, the heat transfer coefficients decrease slowly, and there is even a small increase near the end of the fin. Stachiewicz [3] states that for a flat plate of finite width, as the trailing edge is approached, the boundary layer thickness decreases and secondary flows are established. These edge vortices and boundary layer thinning tend to cause an increase in heat transfer coefficients near the edges of the fin. This explains the small increase in $\tilde{h}_i$ near the trailing edge. This increase appears at

the last part of the fin, 4cm from the traling edge of the fin. The accuracy of the IHCP solution is determined from the numerical experiments (Figures 5.12-5.13). The residual J has dropped just below 10000 for this solution, which corresponds to a temperature error of 0.6°C, comparable to the numerical experiments with an accuracy of 0.5°C. The error on $\tilde{h}_i$ along the fin length is determined from the numerical experiment with an exponential profile (paragraph 3.1.4.2), which indicates that the largest error appears near the steep gradient in $\tilde{h}_i$, but this error is much smaller than the peak in $\tilde{h}_i$. This indicates that there is in fact a peak value at the leading edge.

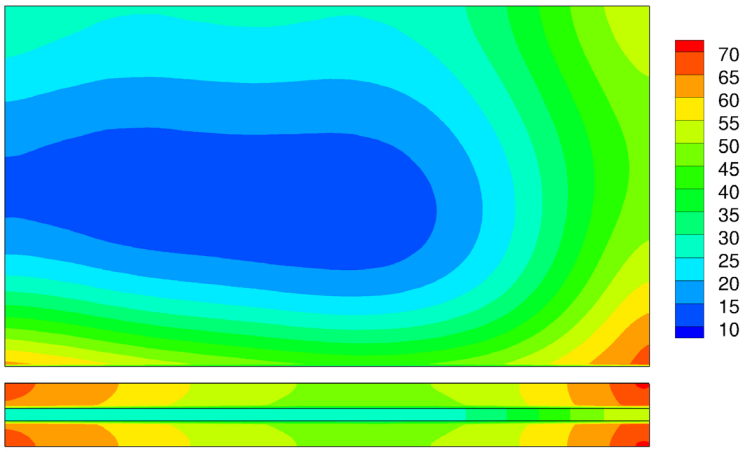

Figure 5.10: 2-D plot of the estimated heat transfer coefficient $\tilde{h}_i$ (in $\mathrm{W/m^2K}$) for Re_L = 50587 for a solid fin

The heat transfer coefficient is higher at the fin base than at the fin tip. Figures 5.10 and 5.11(b) show that $\tilde{h}_i$ has a much higher value at the primary surface. This large $\tilde{h}_i$ occurs also near the base of the fin, but decreases exponentially along the fin height to a minimum halfway the fin height, and then increases again slowly till the fin tip. The maximum value near the fin base is much larger than the maximum near the fin tip, which is also shown by the error bars. The error bars along the fin height (Fig. 5.13) are based on the numerical experiments with varying heat transfer coefficients along the fin height. The maximum value near the fin base is in contradiction with the heat transfer coefficient variation along the fin height found by Stachiewicz [3] (Fig. 5.14). According to Stachiewicz [3] the heat transfer coefficient increases from the base to halfway the fin height and than h_i decreases to 75% of the fin height, after which it increases again to the fin tip. The increase near the fin tip corresponds with the experimental results, but the lower values near

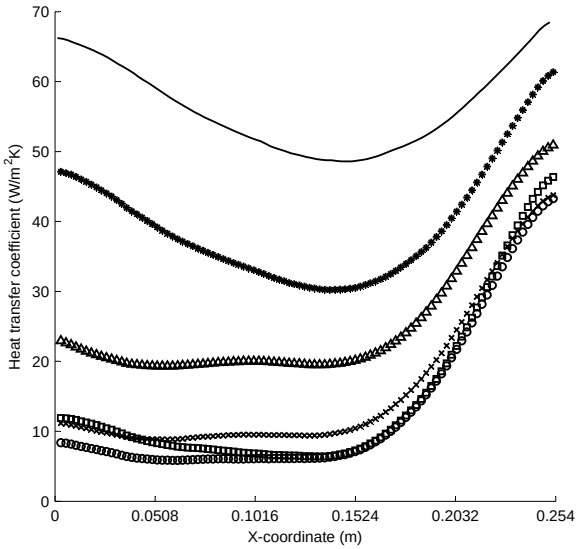

(a) $*$: L_1, $\square$: L_2, $\circ$:L_3, Δ:L_4,$\times$: L_5, $-$:L_6

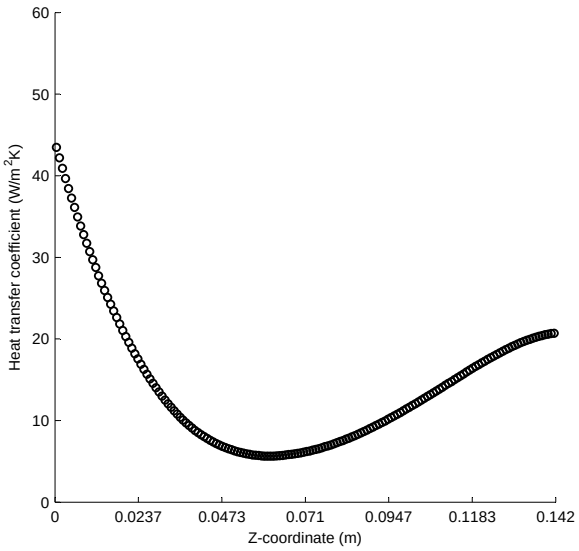

(b)

Figure 5.11: Plots of the estimated heat transfer coefficients $\tilde{h}_i$ along the evaluation lines $L_1 - L_6$ (a) and along the fin height in the middle of the fin (b) for Re_L = 50587 for a solid fin

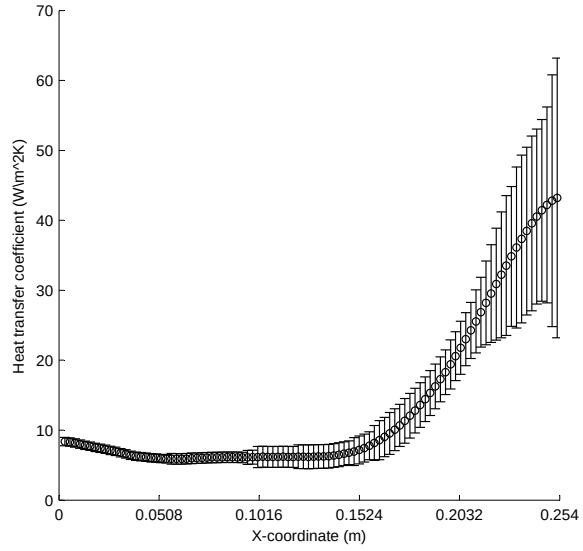

(a)

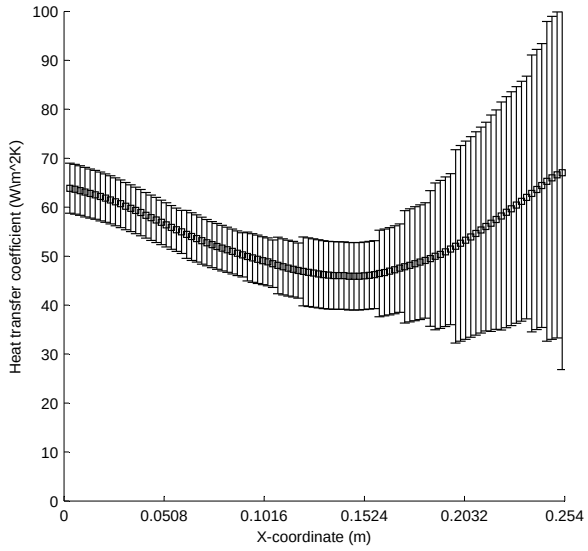

(b)

Figure 5.12: Plots of the estimated heat transfer coefficients $\tilde{h}_i$ with error bars (a) along L_3; (b) along L_6 for Re_L = 50587 for a solid fin

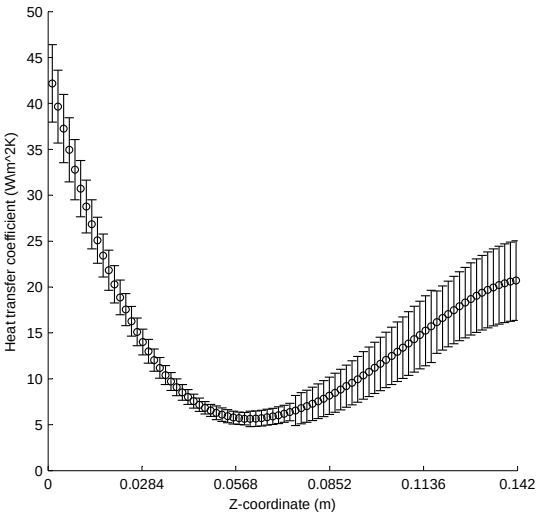

Figure 5.13: Plot of the estimated heat transfer coefficients $\tilde{h}_i$ with error bars along the fin height for Re_L = 50587 for a solid fin

the fin base are a contradiction with these experimental results. Note however that Stachiewicz's results were obtained for a longitudinal fin in a fin matrix and thus the proximity of other fins influences the air flow and thus heat transfer coefficient distribution. In this work a stand-alone fin is studied, which results in another flow pattern over the fin surface. The largest heat transfer coefficient is found near the fin base, which is introduced by a horse-shoe vortex. This flow phenomenon occurs at the leading edge of the fin, at the junction of fin and primary surface. At that position the boundary layer on the fin and the boundary layer on the primary surface get mixed with each other. These boundary layers are orthogonally orientated to each other and create the so called horse-shoe vortex. An example of a horse-shoe vortex is shown in Fig. 5.15. This horse-shoe vortex consists of a longitudinal set of vortices, created at the junction of fin and primary surface, which rolls over the plate and fin surface and causes a locally thinning of the boundary layer [131]. This leads to an increase of the local heat transfer coefficient. The horse-shoe vortex only occurs at the base of the fin and thus causes the increase in local heat transfer coefficients at the base of the fin. This also explains the higher heat transfer coefficient found on the primary surface and near the bottom of the fin (Fig. 5.11(a)). Stachiewicz [3] did not find this effect because the studied fin was placed in a fin array. If the spacing is small enough, the naturally occurring horse-shoe vortex can be completely eliminated, and other flow effects will

determine the heat transfer coefficient variation. However, in the current case the results clearly show the presence of a horse-shoe vortex. This result was confirmed by investigating the flow around the longitudinal solid fin. The flow visualization was performed in two ways: experimental flow visualization in a watertunnel (Fig. 5.16) and CFD simulations (Fig. 5.17).

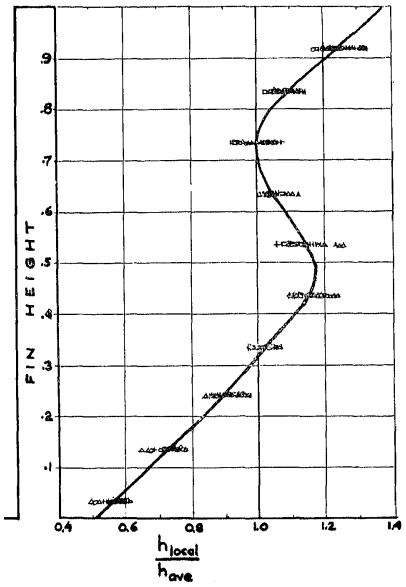

Figure 5.14: The local heat transfer coefficient variation, normalized with respect to the average coefficient, along the fin height as found by Stachiewicz [3]

The experimental flow visualization is performed in a watertunnel using ink to visualize stream lines. A scaled model of the fin is placed in the water tunnel: the Re-number with the fin thickness as characteristic length is the same for the fin in the water tunnel as for the fin in the windtunnel at Re_L = 50587. This Reynolds number is Re_d = 995. The fin in the watertunnel is three times thicker than the actual fin to obtain the same Re_d and the water velocity is 8 $\mathrm{cm/s}$. The boundary layer has built up for only $4\mathrm{cm}$ on the base plate before it reaches the fin front. This boundary layer will be smaller than the boundary layer on the windtunnel base plate before it reaches the fin, and thus the horse-shoe vortex will also be smaller. But the goal of the flow visualization images is to show the presence of a horse-shoe vortex near the bottom of the fin and this is clearly visible in Fig. 5.16. The flow around the fin was also simulated using CFD (FLUENT) in order to visualize the horse-shoe vortex. A dense grid near the base plate wall and fin walls is necessary in order to capture the boundary layer and the starting horse-shoe

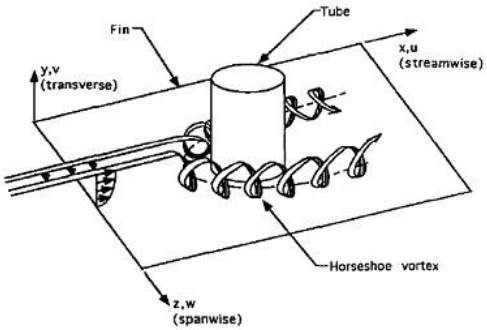

Figure 5.15: Example of a horse-shoe vortex

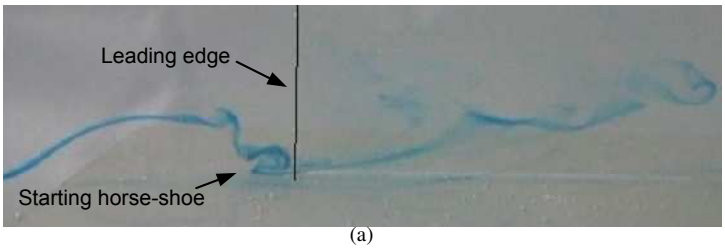

(a)

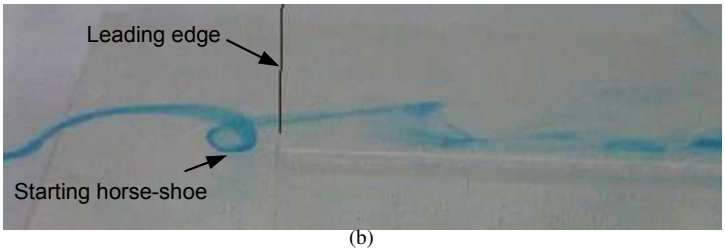

(b)

Figure 5.16: Visualisation of the horse-shoe vortex at the leading edge of the fin in a watertunnel

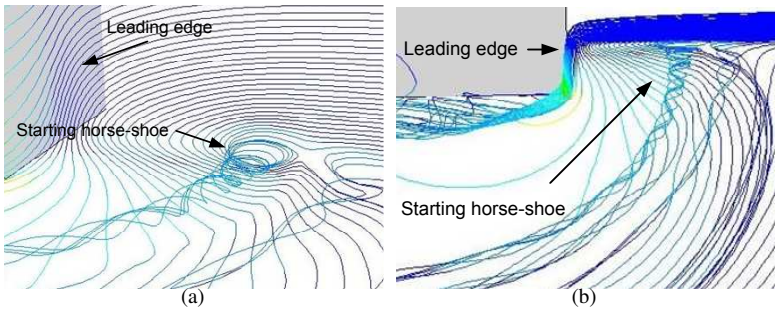

Figure 5.17: Visualisation of the horse-shoe vortex from CFD-simulation. (a) isometric view; (b) top view

vortex. This demands large amounts of computer memory. It is only possible to create a grid that is dense enough near the leading edge of the fin where the horse-shoe vortex is created. A dense grid along the whole fin length demands too much computer memory. The grid consists of 10 million cells. The boundary conditions are chosen in such a way that the results are independent of the boundary positions. This is already described in paragraph 3.1.5. A horse-shoe vortex was found near the foot of the fin, as shown in Fig. 5.17. This vortex can only be seen for the first part of the fin, and seems to be dissipated relatively fast, but this is mainly due to a lack of grid resolution. However, the most important conclusion is that a horse shoe vortex is initiated at the leading edge of the fin, which causes an increase in the heat transfer coefficient near the bottom of the fin.

The local heat transfer coefficient estimated by solving the IHCP gives good results for the solid fin. The $\tilde{h}_i$ variations are explained, except for the increase in $\tilde{h}_i$ on the primary surface and near the fin base from halfway the fin length. This is probably due to a secondary flow pattern resulting from the horse-shoe vortex. This flow pattern cannot be visualized in the water tunnel as the visualization would interrupt the flow pattern. It was also impossible to visualize this using CFD due to a lack of available computer memory.

Fin with one perforation

The line plots along the fin length are shown in Fig. 5.18. The 2-D plots for $\tilde{h}$ are shown in Fig. 5.19. The influence of the boundary layer thickness is again clearly noticeable, as is the large heat transfer coefficient near the bottom of the fin due to the horse-shoe vortex. It is remarkable that the values of the local heat transfer coefficients have increased compared to the case of a solid fin. The variation of $\tilde{h}$ along the central evaluation line L_3 is also plotted in Fig. 5.18 (the

dashed line). If this is compared with the variation of $\tilde{h}$ along L_3, the values of $\tilde{h}$ for the perforated fin are significantly higher. At the leading edge the difference is still smaller (7% or $2\mathrm{W/m^2K}$) than the estimated error on $\tilde{h}$ of 20%. This was expected as the heat transfer only depends on the development of the boundary layer at the leading edge. However it increases along the fin length to 40% or $6\mathrm{W/m^2K}$. This difference is significant, because it is much larger than the estimated $\tilde{h}$ accuracy of 20%. This increase is thus caused by the perforation in the fin. The large constant $\tilde{h}$ behind the perforation on the evaluation lines L_2 – L_4 is remarkable (Fig. 5.18. This is caused by the presence of the perforation, as L_3 runs over the perforation, L_2 is right below it and L_3 just above the perforation. The constant large $\tilde{h}$ is probably caused by a thinning of the boundary layer after the perforation. This thinning of the boundary layer is caused by a negative pressure gradient in the perforation. The increase of the local heat transfer coefficient directly beneath the perforation (L_2 in Fig. 5.18) also suggests a thinning of the boundary-layer due to a negative pressure gradient in the perforation. This effect is not noticeable anymore on a larger distance of the perforation (L_1 in Fig. 5.18). This explanation of the thinning of the boundary layer due to a negative pressure gradient in the perforation is based on the work of Shaeri et al. [5]. They showed in their numerical simulations that a recirculation zone appears in the perforation and that the distance between the streamlines becomes smaller at the location of the perforation (Fig.5.20). This indicates a thinning of the boundary layer and thus higher heat transfer coefficients. The results from the IHCP solution confirm the result of Shaeri et al. [5].

The mean heat transfer coefficient $\tilde{h}_{avg}$ of the perforated fin is also larger than the $\tilde{h}_{avg}$ of the solid fin. These mean heat transfer coefficients are listed in Tables 5.1-5.3. For $Re_L > 40000$ the difference in mean heat transfer coefficient on the side fin surface is significantly larger (> 20% error) for a perforated fin than for a solid fin, which indicates an improvement of the heat transfer for a perforated fin.

Fin with two perforations

The line plots along the fin length are shown in Fig. 5.21. The 2-D plots for $\tilde{h}$ are shown in Fig. 5.22. The influence of the boundary layer thickness is again clearly noticeable, as is the large heat transfer coefficient near the bottom of the fin due to the horse-shoe vortex. The values of the local heat transfer coefficients have increased even more than for a fin with one perforation, compared to the case of a solid fin. The variation of $\tilde{h}$ along the central evaluation line L_3 is also plotted in Fig. 5.21 (dashed line). The difference between $\tilde{h}$ for the fin with two perforations and the solid fin is $7.5\mathrm{W/m^2K}$ (or 50%) at the trailing edge. This is a significant increase introduced by the two perforations.

The increase of the local heat transfer coefficient behind the first perforation and directly beneath and above this perforation shows no noticeable increase

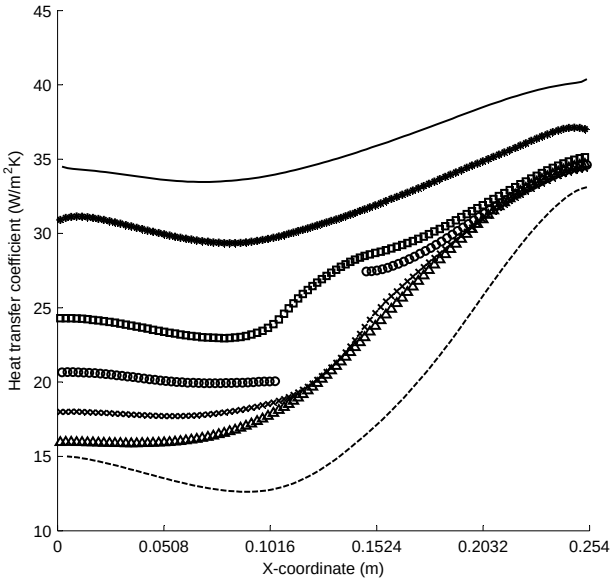

Figure 5.18: Line plots of the estimated heat transfer coefficients $\tilde{h}_i$ along the evaluation lines $L_1 - L_6$ for Re = 50587 on a fin with one perforation. $\diamond$: L_1, $\square$: L_2, $\circ$:L_3, Δ:L_4,$\times$: L_5, $-$:L_6, $--$: L_3

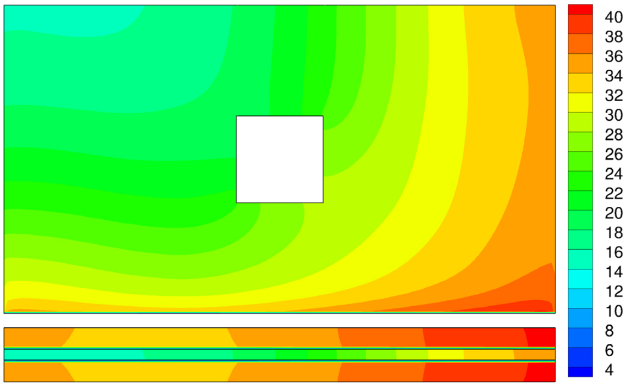

Figure 5.19: 2-D plot of the estimated heat transfer coefficient $\tilde{h}_i$ (in $\mathrm{W/m^2K}$) for Re_L=21861 for a fin with one perforation

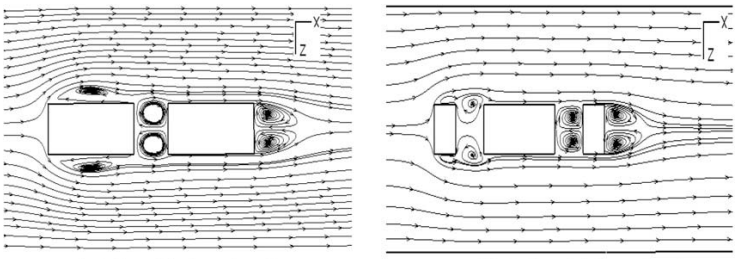

Figure 5.20: Numerical simulation results of fluid flow round perforated fins found by Shaeri et al. [5]

($L_2 - L_4$ in Fig. 5.21). However, over the second perforation is significant. The $\tilde{h}$ on L_3 behind the second perforation is much higher than it was before the perforation which indicates a thinning of the boundary layer. The increase of $\tilde{h}$ along L_2 and L_4 also suggest a thinning of the boundary layer, due to a negative pressure gradient in over the second perforation. This conclusion is also confirmed by the results of Shaeri et al. [5] (Fig.5.20). The boundary layer is still developing when it reaches the first perforation. There is only a small recirculation in the first perforation, and thus no negative pressure gradient or thinning of the boundary layer. At the second perforation the recirculation in the perforation occurs again and a thinning of the boundary-layer due to a negative pressure gradient in the perforation occurs.

The mean heat transfer coefficient $\tilde{h}_{avg}$ of the perforated fins is larger than the $\tilde{h}_{avg}$ of the solid fin. These mean heat transfer coefficients are listed in Tables 5.1-5.3. For $Re_L > 40000$ the difference in mean heat transfer coefficient on the side fin surface is significantly larger (> 20% error) for the perforated fins than for a solid fin, which indicates an improvement of the heat transfer from a perforated fin. At $Re_L < 40000$ the increase in heat transfer coefficient on the front fin surface is not significant anymore: the difference for $\tilde{h}_{avg}$ on the fin front surface is smaller than the accuracy. This indicates that the benefit of a perforated fin decreases for $Re_L < 40000$, probably because a smaller negative pressure gradient is caused by the perforation at lower air velocities.

5.3 Fin effectiveness

The fin effectiveness is also determined at each Re_L-value for the three different fins. There is an important difference between the case for the solid fin and the cases with perforated fins: a thermal contact resistance between primary surface and fin base. This will influence the fin effectiveness. The thermal resistance has to

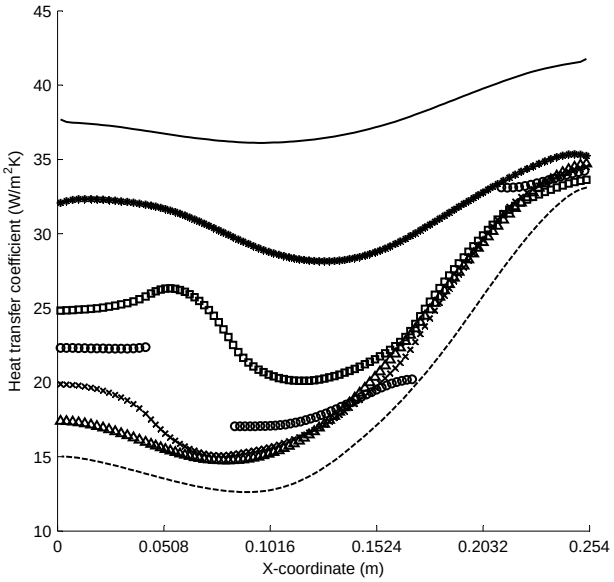

Figure 5.21: Line plots of the estimated heat transfer coefficients $\tilde{h}_i$ along the evaluation lines $L_1 - L_6$ for Re = 50587 on a fin with two perforations. $\diamond$: L_1, $\square$: L_2, $\circ$:L_3, Δ:L_4,$\times$: L_5, $-$:L_6, $--$: L_3

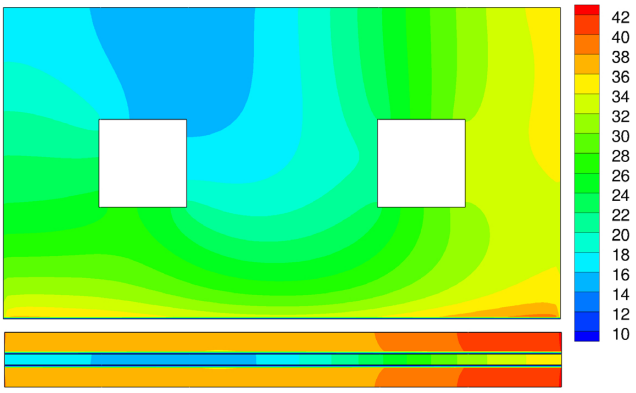

Figure 5.22: 2-D plot of the estimated heat transfer coefficient $\tilde{h}_i$ (in $\mathrm{W/m^2K}$) for Re_L=21861 for a fin with two perforations

Re	solid	1 perforation	2 perforations
21862	10.04	11.80	12.68
33485	14.89	17.54	18.55
40635	17.83	21.08	20.76
50587	21.56	26.40	24.43
62073	25.13	29.13	28.05

Table 5.1: Average heat transfer coefficients for the fin front

Re	solid	1 perforation	2 perforations
21862	5.40	8.11	9.80
33485	11.98	13.08	16.66
40636	13.64	17.41	17.70
50587	17.48	22.70	21.13
62074	19.93	24.81	25.00

Table 5.2: Average heat transfer coefficients for the fin tip

be determined in order to determine fin effectiveness, but it was also necessary to calculate the local heat transfer coefficient on the perforated fins discussed in the previous paragraph. This thermal contact resistance was determined by solving another IHCP as explained in Chapter3. The thermal contact resistance in the experimental test cases consists of a thin layer of thermal conductive paste between fin base and primary surface. The larger this resistance, the less heat is dissipated by the fin, and thus the lower the effectiveness. Thus the thermal conductive paste needs to have a high conductivity. Arctic silver was used which has a thermal conductivity of $8.9\mathrm{W/mK}$. The thermal contact resistance is experimentally determined with the following method. The local heat transfer coefficients on the fin walls and primary surface were determined for the solid fin without contact resistance (fin and primary surface in one piece) by solving the IHCP. These results were reported in section 5.2.2. The estimated heat transfer coefficient profile was

Re	solid	1 perforation	2 perforations
21862	22.06	21.81	20.67
33485	30.28	30.21	24.81
40636	32.54	30.74	31.49
50587	36.64	35.82	37.80
62074	41.33	42.44	43.42

Table 5.3: Average heat transfer coefficients for the primary surface

used as boundary conditions for the solid fin with thermal contact resistance to estimate the contact resistance by solving the IHCP defined in section 2.4.5. The contact resistance varying between 3.33×10^{-4} and 5×10^{-4} $\mathrm{m^2K/W}$was obtained (Fig. 5.23.

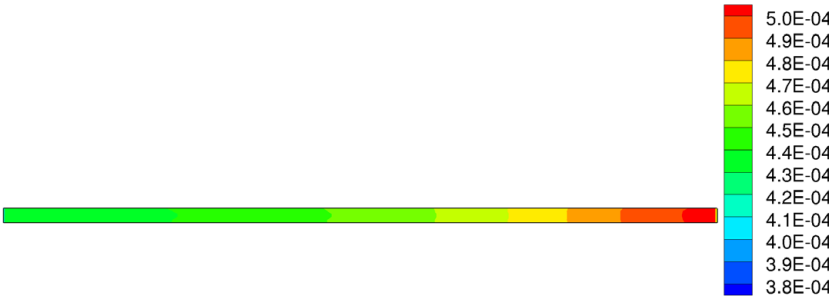

Figure 5.23: Estimated thermal contact resistance in $\mathrm{m^2K/W}$

The fin effectiveness in function of Re_L and local convection coefficients for the perforated fins were determined using this estimated thermal resistance. As the contact resistance influences the fin effectiveness, fin effectiveness was also determined for a solid fin with contact resistance. The result for the solid fins is plotted are in Fig.5.24. A decreasing fin effectiveness for increasing Re_L is expected according to literature, but this is not noticeable. This is due to the large error on the absolute values of $\tilde{h}$: an accuracy of 20% was estimated for the high residuals J of the IHCP solutions. In Chapter 3 the error on the fin effectiveness was determined at a maximum of 1% for a temperature accuracy of 0.5°C, which is a slight overestimation. For the higher residuals of J correspoding with temperature measurement errors between 1°C and 1.5°C, this error was estimated at 2% (error bars in Figures 5.24-5.26). Comparison of the results for fin effectiveness of solid fins with perforated fins (Figures 5.24-5.26) showed that the fin effectiveness is almost the same for al these fins. The contact resistance introduces a small increase in fin effectiveness for the solid fin (5.24). However, the variation is so small and is situated in the error range, so that no conclusion can be drawn from this result. The same conclusion is made for the fins with perforations: there is a small increase in fin effectiveness, but this increase is not significant and is smaller than the error range. The decreasing fin effectiveness with Re_L is not found. The results for fin effectiveness lack accuracy and no useful conclusion can be drawn. To detect the sensitivity of fin effectiveness as function of geometric and flow parameters, a more accurate temperature measurement is necessary. Cancelling the systematic error for the thermography measurements would result in such an increase in

accuracy.

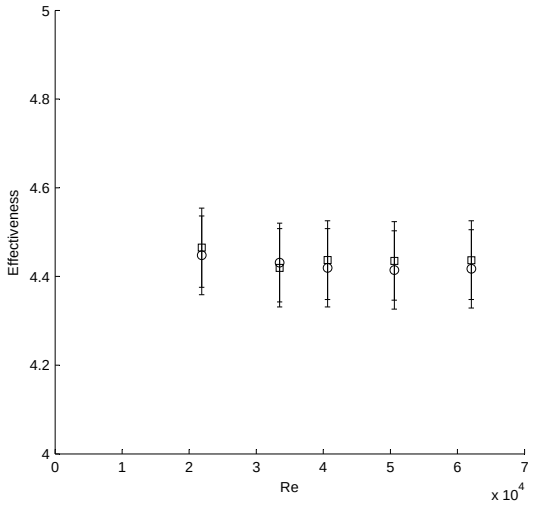

Figure 5.24: Fin effectiveness in function of Re_L for a solid fin. □: without contact resistance; ∘: with contact resistance

5.4 Conclusion

The IHCP solution procedure was applied to an experimental test case. The test cases consisted of three longitudinal fins: a solid fin, a fin with one and a fin with two perforations. The fin surface temperatures were measured and used as boundary conditions for the IHCP. Although the temperature measurement accuracy was determined at 0.5°C, the corresponding residual J for the IHCP solution could not be attained, except for the solid for which good results were obtained. It was found that a systematic error appeared in the temperature measurements for the other fin types due to camera lens reflection on the IR-window. This systematic error introduces nonphysical solutions if the CGM solution procedure converges beyond the point where regularization becomes the dominant factor compared to the physical constraints. As a consequence the accuracy of the IHCP solution is limited. Despite this, the estimated heat transfer coefficient profiles correspond with the expected values for the studied flow regimes, certainly for the solid fin. This means that they can be used to qualitatively predict the effect of modifications to the fin.

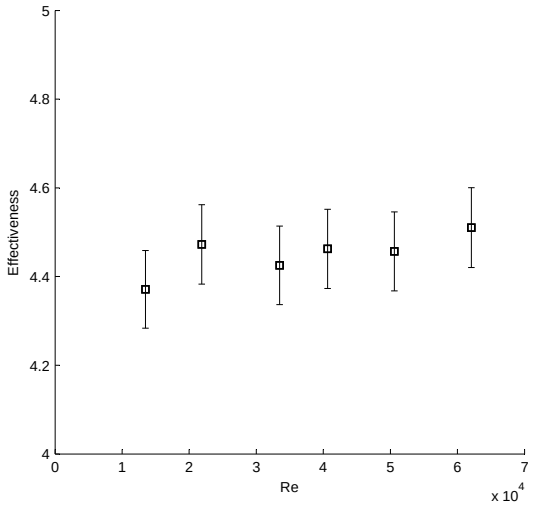

Figure 5.25: Fin effectiveness in function of Re_L for a fin with one perforation and contact resistance at the base

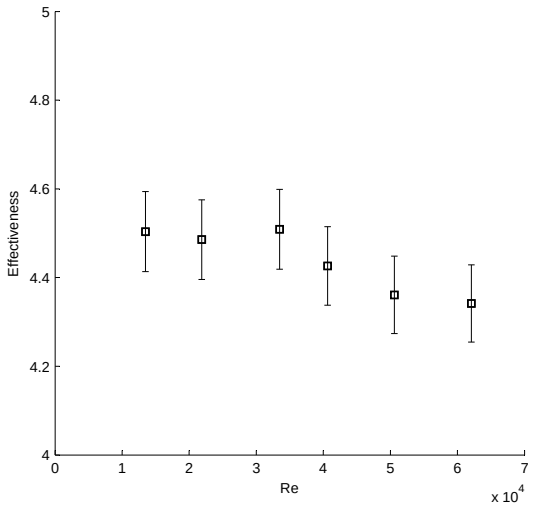

Figure 5.26: Fin effectiveness in function of Re_L for a fin with two perforations and contact resistance at the base

6 Conclusions

6.1 Conclusions

A measurement methodology to determine fin effectiveness and local heat transfer coefficients on longitudinal fins is developed in this work. This methodology consists of two parts: first the fin surface temperatures are measured with thermography, and secondly these temperature measurements are numerically processed to calculate the corresponding heat transfer coefficients at these measurement points. Thus a numerical method is coupled to experimental measurements. The determination of heat fluxes from temperatures is obtained by solving the inverse heat conduction problem (IHCP). The IHCP described in this work, in which heat transfer coefficients on both a longitudinal fin and primary surface have to be determined, is a three-dimensional, steady state, linear problem. In a first stage, possible solution methods for IHCPs are studied. Methods based on the Conjugate Gradient Method (CGM) or the Steepest Descent Method (SDM) appeared to be suitable for solving linear three-dimensional IHCPs. These methods are mathematically developed for the studied case of a longitudinal fin placed on a primary surface. The CGM is implemented into a program that communicates with FLUENT, in which the actual direct heat conduction calculations are done. The developed solution method is applied to various three-dimensional numerical test cases. Four different cases of varying local heat transfer coefficients are studied on a model of rectangular longitudinal fin: an uniform heat transfer coefficient profile, a linearly varying profile along the fin length, a linearly varying profile along the fin height

and an exponentially varying profile along the fin length. These cases are studied for different temperature measurement accuracies to examine the sensitivity of the solution method to measurement noise. It was concluded from these test cases that CGM gives accurate results for these three-dimensional cases, but larger deviations occur near the edges and for steep gradients of the heat transfer coefficients. These deviations are limited to a small amount of calculation points, which is acceptable, since the general trend is still reconstructed. The deviations at the edges increase if there are uncertainties on the measured temperatures, but the results remain in an acceptable error range. Also, by increasing the the measurement error, these deviations do not increase significantly. It was concluded that CGM is a good solution method for three-dimensional IHCPs based on experimentally measured temperatures.

In a second phase, the experimental measurement technique based on infrared thermography was developed. An error analysis is applied on the parameters (emissivity, transmittance and reflection) that influence the measurement accuracy for thermography. The infrared camera is calibrated and the correct application is illustrated to attain the highest possible accuracy. A test rig is designed in which different fin forms of longitudinal fans can be studied at various Reynolds numbers. The fin dimensions of the longitudinal fin and primary surface are determined for accurate temperature measurements. The fin surface temperature profile is measured, as welll as the primary surface temperature profile. Different types of fins are studied: plain rectangular longitudinal fins and preforated longitudinal fins. The measured temperature profiles are processed with the developped numerical solution method for IHCP. This solution method estimates the local heat transfer coefficients. It was found from these results that a systematic error appeared in the measured temperature profile due to camera lens reflection on the IR-window. The temperature measurement uncertainty is thus higher than 0.5°C for which the camera was calibrated. The IHCP stopping criterion indicated a temperature uncertainty between 1°C and 1.5°C with the exception of the solid fin for which some measurements without systematic error were obtained. Those measurements gave a measurement uncertainty of 0.6°C. Hence the results for the solid fin are accurate and the estimated heat transfer coefficients correspond well with the expected flow regimes. For the perforated fins, the systematic error introduces nonphysical solutions if the CGM solution has iterated beyond the point where regularization becomes the dominant factor compared to the physical constraints. As a consequence the accuracy of the IHCP solution is limited. Despite this, the estimated heat transfer coefficient profiles correspond with the expected distribution for the studied flow regimes. The results for the perforated fins show the influence of the perforations and a thinning of the boundary layer in the vicinity of these perforations.It was also found that the average heat transfer coefficient over the fin is higher than for solid fins. It was concluded from the result that the

developed method can qualitatively predict the effect of modifications to the fin. However, the solution lacks accuracy on the absolute values of the heat transfer coefficients due to the large temperature uncertainty which is mainly caused by the systematic error due to camera reflection. For the same reason the error on the fin effectiveness is too large to draw conclusions for the fin effectiveness of the different fin types. Despite the systematic error in the temperature measurements, the developed method still gave good results for the local heat transfer coefficients. This shows the potential of this method. An increase in temperature measurement accuracy will also give quantitavely good results, as indicated by the results of the numerical test cases. The IHCP proved to be a powerful method in estimating local heat transfer coefficients.

6.2 Future recommandations

The main goal for future work should be the increase in accuracy of the developed method. Two recommandations are made to obtain a higher accuracy:

- more accurate temperature measurements: this can be achieved by removing the systematical error in these measurements. As the systematical error was introduced by reflectance of the camera lens on the IR-window, the best way to remove this error is the use of non-reflecting windows. Such windows should have a transmittance of almost 100%. Zinc selenide windows with an anti-reflection coating can have a transmittance of over 99%. If such a window were used, the systematic error disappears in the measurements, and the measurement accuracy of 0.5°C due to camera calibration is obtained. Materials with a high transmittance and an antireflective coating are expensive, especially for larger windows. These materials are often very brittle and soluble in water, which limits their application.

- IHCP solution procedure with less measurement points: an IHCP can also be solved if less measurement points are used without a significant loss in accuracy. If this solution procedure could be implemented in the developed method, the presence of a systematic error would not cause a problem as the IHCP can be solved only with measurement data that is not subjected to this systematic error. The most accurate measurement data can be chosen for as boundary condition for the IHCP which increases the accuracy of the final solution. The grid would also become independent of the number of measurement points. Hence, the grid can be denser near steep gradients of heat transfer coefficients which increases the accuracy of the local heat transfer estimates. A solution procedure with fewer measurement points has also other advantages such as a significant decrease in calculation time. First steps were already made to a solution procedure with fewer, but there are

some problems with using FLUENT to solve the adjoint problem because of the unnatural boundary conditions for this problem with less measurement points. If this problem can be solved, the developed method becomes much more accurate.

A

Uncertainty on infrared measurements

A.1 Emissivity uncertainty

The uncertainty in the emissivity during calibration was induced by three uncertainties

A.1.1 Camera reading uncertainty and isothermal surface

The signal of the infrared camera contains noise. The RMS noise creates an error called NETD: Noise Equivalent Temperature Difference. The NETD is 0.1K at 30°C and decreases with increasing temperature (0.07K at 80°C). Errors due to noise are decreased by time averaging multiple measurements. The NETD decreases with a factor $\sqrt{N}$ where N is the number of images in a sequence. The same applies for the RMS noise error og thermocouple measurements.

There is however a second, more important camera reading error: a built-in spatial analysis function is used to determine a surface temperature next to the thermocouple. The function is applied to the time-averaged infrared image. Spatial averaging induces an error of two times the standard deviation of the measurement points in the analysis tool. This value varies between 0.1°C and 0.15°C, which indicates a good isothermal property for the calibration surface. Also notice that the influence of the RMS noise is further reduced by the spatial averaging. The error induced by RMS noise is ten times smaller than the error on the spatial averaged temperature and thus can be neglected.

A.1.2 Thermocouple uncertainty

It is important to keep this uncertainty as small as possible. Therefore careful calibration as well as attachment of the thermocouple is necessary. The stick-on thermocouples are all calibrated in a temperature calibrator, where a certified PT100 was used as reference temperature value. An absolute uncertainty of 0.1°C was attained after calibration.

It is critical to have a good thermal but electrically insulated contact between thermocouple and surface. An uninsulated thermocouple decreases the thermal resistance between the thermocouple and the measurement point, however, also the electrical insulation is lost. The type-K thermocouples are made of Ni-NiCr junctions, and a direct contact with metals can create an extra thermocouple junction and thus incorrect temperature values. Also current loops can be induced and cause noise in the measurement signal. In order to eliminate these problems, direct contact between the aluminum calibration surface and thermocouple junction is avoided. It was found from tests that a thin paint layer is not insulating enough. Therefore a thin layer of kapton tape is applied to parts of the calibration surface to guarantee an electrical insulation between the thermocouple and the aluminum surface. Both surface and tape are painted. Analysis of infrared images shows that there is no change in the emissivity value of the paint depending on the underlying materials. The temperature uncertainty introduced by this attachment method is of the order of 0.01°C. This error is negligible compared to the 0.1°C accuracy of the thermocouple itself.

A.1.3 Infrared parameter uncertainties

The influence on the IR temperature measurements of different camera parameters such as T_{amb}, T_{air} and the transmittance τ is discussed. An incorrect air temperature value T_{air} leads to negligible temperature measurement errors as was found in a sensitivity analysis of this parameter. The distance between camera and calibration surface is kept as small as possible: the minimal camera focal distance is 0.5m. For distances smaller than 1 meter, there is no atmospheric absorption in the long wave infrared spectrum: τ = 1. A small error on τ has a negligible influence on the measured object temperature. The influence of T_{amb} however is not negligible if the object temperature is close to the ambient temperature. The ASTM standard E1933-99a [125] states that the difference between a measured surface and T_{amb} should be at least 10°C in order to do accurate emissivity measurements. Other sources [121] mention a temperature difference of 30°C. A 10°C difference is not the same for a calibration surface at 40°C or at 80°C. This can be reasoned by using the Stefan-Boltzmann law (Eq. (4.3)). Both T_{obj} and T_{amb} are elevated to the fourth power to calculate the associated radiation energy. Thus, a temperature difference $T_{obj} - T_{amb}$ of 10°C at an object temperature of 80°C will give a larger

difference between T_{obj}^4 and T_{amb}^4 than at 40°C. So at lower temperatures, the difference has to be large enough to reduce the impact of the uncertainty in T_{amb}. A summary of the sensitivity and error analysis on the measured temperature and emissivity by an inaccurate T_{amb} is given in Tables A.1-A.2.

	ϵ = 0.95		ϵ = 0.9	
	dT_{amb} = −1°C	dT_{amb} = −3°C	dT_{amb} = −1°C	dT_{amb} = −3°C
dT_{obj} (°C)	0.04	0.125	0.09	0.27
$d\epsilon$ (%)	0.25	0.75	0.5	1.5

Table A.1: Uncertainty on object temperature T_{obj} caused by an ambient temperature uncertainty dT_{amb} and the forthcoming uncertainty on the ϵ determination. Values calculated at T_{obj} = 40°C and different ϵ

	ϵ = 0.95		ϵ = 0.9	
	dT_{amb} = −1°C	dT_{amb} = −3°C	dT_{amb} = −1°C	dT_{amb} = −3°C
dT_{obj} (°C)	0.03	0.09	0.07	0.19
$d\epsilon$ (%)	0.05	0.2	0.15	0.4

Table A.2: Uncertainty on object temperature T_{obj} caused by an ambient temperature uncertainty dT_{amb} and the forthcoming uncertainty on the ϵ determination. Values calculated at T_{obj} = 80°C and different ϵ

A.2 Ambient temperature uncertainty

The ambient temperature influences the infrared temperature measurements, as radiation from the surroundings and the camera itself is detected by the camera, either directly or indirectly through reflection on the measurement surface. The reflected radiation depends on the type of reflection, and radiation coming from the camera itself can influence the temperature measurement. The two types of reflection are:

- Diffuse reflecting objects reflect radiation coming from all directions and reflect it in all directions. Diffuse means that reflection, emissivity and absorptivity do not depend on direction. So radiation from the camera is reflected in all directions. Theoretically, it would be possibly to calculate the reflected radiation into the camera and the corresponding T_{amb} but practically this is difficult.

- For specularly reflecting objects, the reflected radiation comes from limited directions. In the case a camera is placed right in front of a specular reflector, heat coming from the camera reflects back to the camera. This disturbs the infrared image drastically. For specular reflection, the infrared image cannot be corrected with a single value for T_{amb}, because a correction is applied to all pixels, and a specular reflection influences all pixels differently, as seen in Fig.A.1. Thus if the camera is placed in front of a specularly reflecting measurement object, it is impossible to do accurate temperature measurements because the camera reflection disturbs the thermal image of the object differently for various pixels.

In most cases, one prefers to place the camera perpendicular to the measurement surface to get the best image. In this case the measurement object is a diffuse reflector. An example of the camera reflectance is given in Figures A.1(a)-A.1(b) for a specular reflector. A specular reflector gives a significant error on the infrared temperature measurement: 0.4°C for an emissivity of ±0.9 (Fig.A.1(a)). This results in a wrong emissivity determination. The temperature images used to determine the emissivity shows no specular camera reflection when the krylon paint was used, so the paint is a diffusive reflector. This is a very important property for a high emissivity coating for infrared measurements. Thus by coating a specular reflector with a diffusely reflecting paint, measurements with an infrared camera normal to the object can be done.

A.3 Total temperature uncertainty by infrared thermography

An error analysis was performed on the temperature measurement accuracy with the infrared camera after calibration. The temperature measurement accuracy depends on the accuracy of different parameters: emissivity ϵ, ambient temperature T_{amb}, transmittance τ, atmospheric temperature T_{atm}, camera offset and camera response. The influence of an error in each of these parameters induces an error in the measured object temperature with the thermographic camera. The partial errors on the measured object temperature related to a certain parameter can be calculated with the following equations.

Partial temperature error due to emissivity uncertainty:

$$\Delta T_{obj}(\epsilon) = \frac{T_{obj}^2}{B}\left(1 - \frac{U_{amb}}{U_{obj}}\right) \cdot \frac{\Delta\epsilon}{\epsilon} \tag{A.1}$$

Partial temperature error due to uncertainty in ambient temperature T_{amb}:

$$\Delta T_{obj}(T_{amb}) = \frac{1-\epsilon}{\epsilon} \cdot \frac{T_{obj}^2}{T_{amb}^2} \cdot \frac{U_{amb}}{U_{obj}} \cdot \Delta T_{amb} \tag{A.2}$$

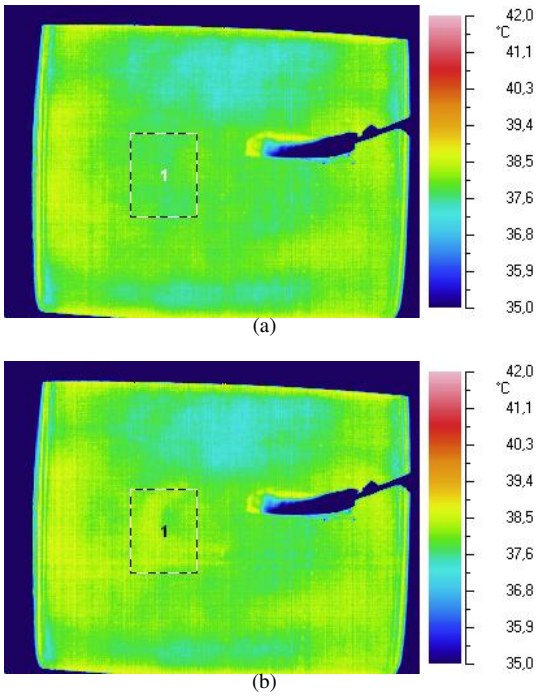

Figure A.1: Infrared picture of the calibration surface with and without hand around the camera lens. The difference at the marked section is a 0.4°C increase in temperature

Partial temperature error due to transmittance uncertainty:

$$\Delta T_{obj}(\tau) = \frac{T_{obj}^2}{B}\left(1 - \frac{U_{amb}}{U_{obj}} + \frac{U_{amb} - U_{atm}}{U_{obj} \cdot \epsilon}\right) \cdot \frac{\Delta\tau}{\tau} \tag{A.3}$$

Partial temperature error due to uncertainty in atmosphere temperature T_{atm}:

$$\Delta T_{obj}(T_{amb}) = \frac{1-\tau}{\epsilon \cdot \tau} \cdot \frac{T_{obj}^2}{T_{atm}^2} \cdot \frac{U_{atm}}{U_{obj}} \cdot \Delta T_{atm} \tag{A.4}$$

Partial temperature error due to the camera offset:

$$\Delta T_{obj}(T_{offset}) = \frac{1}{\epsilon \cdot \tau} \cdot \frac{T_{obj}^2}{T_{speclow}^2} \cdot \frac{U_{speclow}}{U_{obj}} \cdot \Delta T_{specabs} \tag{A.5}$$

Partial temperature error due to the camera response:

$$\Delta T_{obj}(R) = \frac{T_{obj}^2}{B}\left(1 + \frac{1-\epsilon}{\epsilon} \cdot \frac{U_{amb}}{U_{obj}} + \frac{1_\tau}{\epsilon \cdot \tau}\frac{U_{atm}}{U_{obj}}\right) \cdot \frac{\Delta R}{R} \tag{A.6}$$

R and B are camera calibration constants and U is the camera output signal which is determined by Eq. (4.8).$U_{speclow}$ is the camera output corresponding to the lower temperature limit of the measurement range of the camera. $\Delta T_{specabs}$ is the absolute temperature error corresponding to this temperature limit. The total uncertainty on the object temperature without the uncertainty due to camera imperfections (offset and response):

$$\Delta T_{obj}(tot, cal) = \sqrt{\Delta T_{obj}^2(\epsilon) + \Delta T_{obj}^2(T_{amb}) + \Delta T_{obj}^2(\tau) + \Delta T_{obj}^2(T_{atm})} \tag{A.7}$$

And the total uncertainty with camera imperfections is determined as:

$$\Delta T_{obj}(tot) = \sqrt{\Delta T_{obj}^2(tot, cal) + \Delta T_{obj}^2(offset) + \Delta T_{obj}^2(R)} \tag{A.8}$$

This error analysis was performed for the following determined parameter values and their uncertainties:

- ϵ=0.94
- $d\epsilon$=0.007
- dT_{amb}=1.5°C
- τ=0.9
- $d\tau$=0.008

- T_{atm}=20°C

The camera calibration errors are: R=762546 ; B=1503,11 and F=1,1645. The total temperature error was determined for the object temperature range of 40°C to 80°C. The influence of a variation of T_{amb} was also checked by performing the error analysis for both T_{amb}=20°C and T_{amb}=25°C. The error analysis values are reported in TablesA.3-A.4. It was found that the maximal total error occurs at the highest temperatures, thus 80°C and is 0.54°C if the influence of the camera imperfections is neglected due to calibration, and it is 2.28°C if camera imperfections are important.

	Fouten							
T_{obj} (°C)	$\Delta T_{obj}(d\epsilon)$ (°C)	$\Delta T_{obj}(dT_{amb})$ (°C)	$\Delta T_{obj}(d\tau)$ (°C)	$\Delta T_{obj}(T_{atm})$ (°C)	$\Delta T_{obj}(offset)$ (°C)	$\Delta T_{obj}(R)$ (°C)	$\Delta T_{obj}(tot)$ (°C)	$\Delta T_{obj}(tot,cal)$ (°C)
40	0.137	0.079	0.147	0.097	1.038	1.722	2.024	0.236
50	0.197	0.072	0.212	0.089	0.951	1.804	2.063	0.311
60	0.255	0.066	0.273	0.082	0.878	1.892	2.121	0.388
70	0.309	0.062	0.332	0.076	0.815	1.985	2.195	0.464
80	0.362	0.058	0.389	0.071	0.761	2.083	2.282	0.539

Table A.3: Error analysis for T_{amb}=20°C

	Fouten							
T_{obj} (°C)	$\Delta T_{obj}(\epsilon)$ (°C)	$\Delta T_{obj}(T_{amb})$ (°C)	$\Delta T_{obj}(\tau)$ (°C)	$\Delta T_{obj}(T_{atm})$ (°C)	$\Delta T_{obj}(offset)$ (°C)	$\Delta T_{obj}(R)$ (°C)	$\Delta T_{obj}(tot)$ (°C)	$\Delta T_{obj}(tot, cal)$ (°C)
40	0.105	0.083	0.149	0.097	1.038	1.728	2.028	0.222
45	0.137	0.079	0.182	0.093	0.993	1.768	2.044	0.258
50	0.168	0.076	0.214	0.089	0.951	1.810	2.066	0.296
55	0.199	0.073	0.245	0.085	0.913	1.853	2.093	0.335
60	0.228	0.070	0.275	0.082	0.878	1.897	2.124	0.373
65	0.256	0.067	0.305	0.079	0.845	1.943	2.158	0.412
70	0.284	0.065	0.334	0.076	0.815	1.990	2.197	0.450
75	0.312	0.063	0.362	0.074	0.787	2.038	2.238	0.488
80	0.339	0.061	0.390	0.071	0.761	2.087	2.283	0.525

Table A.4: Error analysis for T_{amb}=25°C

References

[1] International Energy Agency. *Worldwide Trends in Energy Use and Efficiency*. http://www.iea.org/Textbase/Papers/2008/Indicators_2008.pdf.

[2] Intel. *Moore's law 40th anniversary*. http://www.intel.com/technology/mooreslaw/.

[3] Stachiew.Jw. *Effect of Variation of Local Film Coefficients on Fin Performance*. Journal of Heat Transfer, 91(1):21–26, 1969.

[4] P. Razelos. *A critical review of extended surface heat transfer*. Heat Transfer Engineering, 24(6):11–28, 2003.

[5] M. R. Shaeri, M. Yaghoubi, and K. Jafarpur. *Heat transfer analysis of lateral perforated fin heat sinks*. Applied Energy, 86(10):2019–2029, 2009.

[6] N. K. Burgess and P. M. Ligrani. *Effects of dimple depth on channel nusselt numbers and friction factors*. Journal of Heat Transfer-Transactions of the Asme, 127(8):839–847, 2005.

[7] K. K. Sikka, K. E. Torrance, C. U. Scholler, and P. I. Salanova. *Heat sinks with fluted and wavy plate fins in natural and low-velocity forced convection*. Ieee Transactions on Components and Packaging Technologies, 25(2):283–292, 2002.

[8] M. A. Almogbel. *Constructal tree-shaped fins*. International Journal of Thermal Sciences, 44(4):342–348, 2005.

[9] P. J. Heggs and I. M. Somasundram. *Fin performance ratios greater than unity: Not just a theoretical aspiration*. Applied Thermal Engineering, 27(5-6):951–961, 2007.

[10] A. Pourshaghaghy, F. Kowsary, and A. Behbahaninia. *Comparison of four different versions of the variable metric method for solving inverse heat conduction problems*. Heat and Mass Transfer, 43(3):285–294, 2007.

[11] W. L. Chen and Y. C. Yang. *Estimation of the Transient Heat Transfer Rate at the Boundary of an Electronic Chip Packaging*. Numerical Heat Transfer Part a-Applications, 54(10):945–961, 2008.

[12] T. Loulou and E. P. Scott. *Estimation of 3-Dimensional heat flux from surface temperature measurements using an iterative regularization method*. Heat and Mass Transfer, 39(5-6):435–443, 2003.

[13] H. T. Chen, J. P. Song, and Y. T. Wang. *Prediction of heat transfer coefficient on the fin inside one-tube plate finned-tube heat exchangers*. International Journal of Heat and Mass Transfer, 48(13):2697–2707, 2005.

[14] A. J. S. Neto and M. N. Ozisik. *2-Dimensional Inverse Heat-Conduction Problem of Estimating the Time-Varying Strength of a Line Heat-Source*. Journal of Applied Physics, 71(11):5357–5362, 1992.

[15] C. H. Huang, I. C. Yuan, and H. C. Ay. *A three-dimensional inverse problem in imaging the local heat transfer coefficients for plate finned-tube heat exchangers*. International Journal of Heat and Mass Transfer, 46(19):3629–3638, 2003.

[16] C. H. Huang and H. C. Lo. *A three-dimensional inverse problem in predicting the heat fluxes distribution in the cutting tools*. Numerical Heat Transfer Part a-Applications, 48(10):1009–1034, 2005.

[17] P. J. Heggs. *Fin effectiveness is a better performance indicator than fin efficiency*. Sixth Uk National Conference on Heat Transfer, 1999(7):3–12, 1999.

[18] G.E. Moore. *Cramming more components onto integrated circuits*. Electronics, 38(8), 1965.

[19] B. Guenin. *Packaging Challenges For High Heat Flux Devices*. Electronics Cooling, 12(3), 2006.

[20] ITRS. *International Technology Roadmap for Semiconductors, 2005 Edition*. `http://www.itrs.net/Links/2005itrs/Home2005.htm`.

[21] Y.C. Cengel. *Heat Transfer: A Pratical Approach*. Tata Mcgraw Hill Publishing Company Limited, New Delhi, 2002.

[22] S. S. Anandan and V. Ramalingam. *Thermal management of electronics: A review of literature*. Thermal Science, 12(2):5–26, 2008.

[23] The Heatsink Guide. *Maximum CPU temperature and maximum CPU power usage*. `http://www.heatsink-guide.com/`, 2004.

[24] S. A. El-Sayed, S. M. Mohamed, A. M. Abdel-latif, and A. E. Abouda. *Investigation of turbulent heat transfer and fluid flow in longitudinal rectangular-fin arrays of different geometries and shrouded fin array*. Experimental Thermal and Fluid Science, 26(8):879–900, 2002.

[25] A. F. Mills. *Heat Transfer*. Prentice-Hall, Upper Saddle River, 2nd edition, 1999.

[26] M. R. Shaeri and M. Yaghoubi. *Thermal enhancement from heat sinks by using perforated fins*. Energy Conversion and Management, 50(5):1264–1270, 2009.

[27] H. J. Lane and P. J. Heggs. *Extended surface heat transfer - the dovetail fin*. Applied Thermal Engineering, 25(16):2555–2565, 2005.

[28] A. Aziz and V. J. Lunardini. *Multidimensional Steady Conduction in Convecting, Radiating, and Convecting-Radiating Fins and Fin Assemblies*. Heat Transfer Engineering, 16(3):32–64, 1995.

[29] A. H. Al-Essa and F. M. S. Al-Hussien. *The effect of orientation of square perforations on the heat transfer enhancement from a fin subjected to natural convection*. Heat and Mass Transfer, 40(6-7):509–515, 2004.

[30] A. D. Kraus, A. Aziz, and J. Welty. *Extended Surface Heat Transfer*. Wiley Interscience, New York, 2001.

[31] C. J. M. Lasance. *The need for a change in thermal design philosophy*. Electronics Cooling, 1(2), 1995.

[32] D. W. Copeland. *Fundamental performance limits of heatsinks*. Journal of Electronic Packaging, 125(2):221–225, 2003.

[33] E. A. M. Elshafei. *Effect of flow bypass on the performance of a shrouded longitudinal fin array*. Applied Thermal Engineering, 27(13):2233–2242, 2007.

[34] D.R. Harper and W.B. Brown. *Mathematical equations for heat conduction in the fins of air-cooled engines*. Technical Report NACA Report No. 158, NACA, 1922.

[35] K.A. Gardner. *Efficiency of Extended Surface*. ASME Journal of Heat Transfer, 67:621–631, 1945.

[36] P. Razelos and E. Georgiou. *2-Dimensional Effects and Design Criteria for Convective Extended Surfaces*. Heat Transfer Engineering, 13(3):38–48, 1992.

[37] W. Lau and C. W. Tan. *Errors in One-Dimensional Heat-Transfer Analysis in Straight and Annular Fins*. Journal of Heat Transfer-Transactions of the Asme, 95(4):549–551, 1973.

[38] L. J. Huang and R. K. Shah. *Assessment of Calculation Methods for Efficiency of Straight Fins of Rectangular Profile*. International Journal of Heat and Fluid Flow, 13(3):282–293, 1992.

[39] D. C. Look. *Two-Dimensional Fin Performance - Bi (Top Surface) Greater-Than-or-Equal to Bi (Bottom Surface)*. Journal of Heat Transfer-Transactions of the Asme, 110(3):780–782, 1988.

[40] B. Kundu and P. K. Das. *Performance analysis and optimization of straight taper fins with variable heat transfer coefficient*. International Journal of Heat and Mass Transfer, 45(24):4739–4751, 2002.

[41] C. Casarosa and A. Franco. *On the optimum thermal design of individual longitudinal fins with rectangular profile*. Heat Transfer Engineering, 22(1):51–71, 2001.

[42] P. Razelos and R. N. Krikkis. *Two-dimensional fin performance: Bi (top surface) ¿= Bi (bottom surface)*. International Communications in Heat and Mass Transfer, 31(2):203–210, 2004.

[43] A. G. A. Nnanna, A. Haji-Sheikh, and D. Agonafer. *Effect of variable heat transfer coefficient, fin geometry, and curvature on the thermal performance of extended surfaces*. Journal of Electronic Packaging, 125(3):456–460, 2003.

[44] S. W. Ma, A. I. Behbahani, and Y. G. Tsuei. *2-Dimensional Rectangular Fin with Variable Heat-Transfer Coefficient*. International Journal of Heat and Mass Transfer, 34(1):79–85, 1991.

[45] Ghai M.L. *Heat transfer in straight fins*. In Proc. Gen. Disc. Heat Transfer, Institute of Mechanical Engineers, page p 180, London, 1951.

[46] K.A. Gardner. *Discussion on paper by M.L. Ghai*. In Proc. General discussion on Heat Transfer, Institute of Mechanical Engineers, London, 1951.

[47] K. Laor and H. Kalman. *Performance and optimum dimensions of different cooling fins with a temperature-dependent heat transfer coefficient*. International Journal of Heat and Mass Transfer, 39(9):1993–2003, 1996.

[48] E. M. Sparrow and S. Acharya. *A Natural-Convection Fin with a Solution-Determined Non-Monotonically Varying Heat-Transfer Coefficient*. Journal of Heat Transfer-Transactions of the Asme, 103(2):218–225, 1981.

[49] H. C. Unal. *Determination of the Temperature Distribution in an Extended Surface with a Non-Uniform Heat-Transfer Coefficient*. International Journal of Heat and Mass Transfer, 28(12):2279–2284, 1985.

[50] R. H. Yeh. *Optimization of Longitudinal Fins with Temperature-Dependent Thermal Parameters*. Heat Transfer Engineering, 15(3):25–34, 1994.

[51] C. G. Advani and S. P. Sukhatme. *Analysis of a Vertical Rectangular Cross-Sectioned Fin Losing Heat by Laminar Free Convection*. Indian Journal of Technology, 11(3):105–109, 1973.

[52] E. M. Sparrow and D. K. Hennecke. *Temperature Depression at Base of a Fin*. Journal of Heat Transfer, 92(1):204–206, 1970.

[53] P. C. S. Juca and A. T. Prata. *2-Dimensional Fins Attached to a Thick Wall - Effect of Nonuniform Root Temperature*. International Journal of Heat and Mass Transfer, 36(1):233–236, 1993.

[54] N. V. Suryanarayana. *2-Dimensional Effects on Heat-Transfer Rates from an Array of Straight Fins*. Journal of Heat Transfer-Transactions of the Asme, 99(1):129–132, 1977.

[55] P. J. Heggs and P. R. Stones. *The Effects of Dimensions on the Heat Flow-Rate through Extended Surfaces*. Journal of Heat Transfer-Transactions of the Asme, 102(1):180–182, 1980.

[56] A. D. Snider and A. D. Kraus. *The Quest for the Optimum Longitudinal Fin Profile*. Heat Transfer Engineering, 8(2):19 – 25, 1987.

[57] B. Kundu and P. K. Das. *Optimum profile of thin fins with volumetric heat generation: A unified approach*. Journal of Heat Transfer-Transactions of the Asme, 127(8):945–948, 2005.

[58] P. Razelos and X. Kakatsios. *Optimum dimensions of convecting-radiating fins: Part I - longitudinal fins*. Applied Thermal Engineering, 20(13):1161–1192, 2000.

[59] Q.D. Kern and D.A. Kraus. *Extended surface heat transfer*. McGraw-Hill, New York, 1972.

[60] D. C. Look and H. S. Kang. *Optimization of a Thermally Nonsymmetrical Fin - Preliminary Evaluation*. International Journal of Heat and Mass Transfer, 35(8):2057–2060, 1992.

[61] B. T. F. Chung and J. R. Iyer. *Optimum Design of Longitudinal Rectangular Fins and Cylindrical Spines with Variable Heat-Transfer Coefficient*. Heat Transfer Engineering, 14(1):31–42, 1993.

[62] H. S. Kou, J. J. Lee, and C. W. Chen. *Optimum thermal analysis of a heat sink with various fin cross-sections by adjusting fin length and cross-section*. Heat Transfer Engineering, 29(6):537–545, 2008.

[63] B. Sahin and A. Demir. *Performance analysis of a heat exchanger having perforated square fins*. Applied Thermal Engineering, 28(5-6):621–632, 2008.

[64] H. Wee, Q. Zhang, P. M. Ligrani, and S. Narasimhan. *Numerical predictions of heat transfer and flow characteristics of heat sinks with ribbed and dimpled surfaces in laminar flow*. Numerical Heat Transfer Part a-Applications, 53(11):1156–1175, 2008.

[65] O. Braunshtein, H. Kalman, and A. Ullmann. *Performance and optimization of composed fin arrays*. Heat Transfer Engineering, 25(4):4–12, 2004.

[66] Fluent Inc. *Fluent user's guide Version 6.2*, 2005.

[67] P. J. Heggs and T. H. Ooi. *Design charts for radial rectangular fins in terms of performance ratio and maximum effectiveness*. Applied Thermal Engineering, 24(8-9):1341–1351, 2004.

[68] T. Wu and K. Vierow. *A local heat flux measurement technique for inclined heat exchanger tubes*. Experimental Heat Transfer, 19(1):1–14, 2006.

[69] C. H. Huang, U. C. Jan, R. Li, and A. J. Shih. *A three-dimensional inverse problem in estimating the applied heat flux of a titanium drilling - Theoretical and experimental studies*. International Journal of Heat and Mass Transfer, 50(17-18):3265–3277, 2007.

[70] C. H. Huang and H. C. Lo. *A three-dimensional inverse problem in estimating the internal heat flux of housing for high speed motors*. Applied Thermal Engineering, 26(14-15):1515–1529, 2006.

[71] O. M. Alifanov and A. V. Nenarokomov. *Three-dimensional boundary inverse heat conduction problem for regular coordinate systems*. Inverse Problems in Engineering, 7(4):335–362, 1999.

[72] P. Wikstrom, W. Blasiak, and F. Berntsson. *Estimation of the transient surface temperature and heat flux of a steel slab using an inverse method*. Applied Thermal Engineering, 27(14-15):2463–2472, 2007.

[73] T. C. Chen, C. C. Liu, H. Y. Jang, and P. C. Tuan. *Inverse estimation of heat flux and temperature in multi-layer gun barrel*. International Journal of Heat and Mass Transfer, 50(11-12):2060–2068, 2007.

[74] Hukseflux Thermal Sensors. *PU series, heat flux sensors and specials*. http://www.hukseflux.com/products/heatFlux/PUseries.html.

[75] T. Tszeng and V. Saraf. *A study of fin effects in the measurement of temperature using surface-mounted thermocouples*. Journal of Heat Transfer-Transactions of the Asme, 125(5):926–935, 2003.

[76] H. C. Ay, J. Y. Jang, and J. N. Yeh. *Local heat transfer measurements of plate finned-tube heat exchangers by infrared thermography*. International Journal of Heat and Mass Transfer, 45(20):4069–4078, 2002.

[77] T. Orzechowski. *Determining local values of the heat transfer coefficient on a fin surface*. Experimental Thermal and Fluid Science, 31(8):947–955, 2007.

[78] S. Freund and S. Kabelac. *Measurement of local convective heat transfer coefficients with temperature oscillation IR thermography and radiant heating*. In ASME Summer Conference 2005, pages HT2005–72855, San Francisco, 2005.

[79] M. R. G. Haghighi, M. Eghtesad, P. Malekzadeh, and D. S. Necsulescu. *Three-dimensional inverse transient heat transfer analysis of thick functionally graded plates*. Energy Conversion and Management, 50(3):450–457, 2009.

[80] J. V. Beck, B. Blackwell, and C. R. jr. St. Clair. *Inverse heat conduction*. Wiley-Interscience, New York, 1985.

[81] M. N. Oezisik and H. R. B. Orlande. *Inverse heat transfer : fundamentals and applications*. Taylor and Francis, London, 2000.

[82] S. Kaka and Y. Yener. *Heat conduction*. Taylor and Francis, Washington, 3rd edition, 1993.

[83] W. M. Rohsenow, J. P. Hartnett, and Y. I. Cho. *Handbook of heat transfer*. McGraw-Hill, New York, 3rd edition, 1998.

[84] F. P. Incropera. *Introduction to heat transfer*. Wiley, Hoboken, 5th edition, 2007.

[85] S. Deng and Y. Hwang. *Solution of inverse heat conduction problems using Kalman filter-enhanced Bayesian back propagation neural network data fusion*. International Journal of Heat and Mass Transfer, 50(11-12):2089–2100, 2007.

[86] O. M. Alifanov and E. A. Artyukhin. *Regularized numerical solution of nonlinear inverse heat-conduction problem*. Journal of Engineering Physics and Thermophysics, 29(1):934–938, 1975.

[87] G. P. Deidda, E. Bonomi, and C. Manzi. *Inversion of electrical conductivity data with Tikhonov regularization approach: some considerations*. Annals of Geophysics, 46(3):549–558, 2003.

[88] M. Hanke. *The Minimal Error Conjugate-Gradient Method Is a Regularization Method*. Proceedings of the American Mathematical Society, 123(11):3487–3497, 1995.

[89] T. Luttich, A. Mhamdi, and W. Marquardt. *Design, formulation, and solution of multidimensional inverse heat conduction problems*. Numerical Heat Transfer Part B-Fundamentals, 47(2):111–133, 2005.

[90] O. M. Alifanov. *Application of the regularization principle to the formulation of approximate solutions of inverse heat-conduction problems*. Journal of Engineering Physics and Thermophysics, 23(6):1566–1571, 1972.

[91] J. V. Beck, B. Blackwell, and A. HajiSheikh. *Comparison of some inverse heat conduction methods using experimental data*. International Journal of Heat and Mass Transfer, 39(17):3649–3657, 1996.

[92] O. M. Alifanov and N. V. Kerov. *Determination of external thermal load parameters by solving the two-dimensional inverse heat-conduction problem*. Journal of Engineering Physics and Thermophysics, 41(4):1049–1053, 1981.

[93] D. Lesnic, L. Elliott, and D. B. Ingham. *Application of the boundary element method to inverse heat conduction problems*. International Journal of Heat and Mass Transfer, 39(7):1503–1517, 1996.

[94] M. Prud'homme and T. H. Nguyen. *On the iterative regularization of inverse heat conduction problems by conjugate gradient method*. International Communications in Heat and Mass Transfer, 25(7):999–1008, 1998.

[95] Y. C. Yang and W. L. Chen. *An iterative regularization method in simultaneously estimating the inlet temperature and heat-transfer rate in a forced-convection pipe*. International Journal of Heat and Mass Transfer, 52(7-8):1928–1937, 2009.

[96] A. Behbahani-nia and F. Kowsary. *A direct transformation matrices method for solution of inverse heat conduction problems*. Numerical Heat Transfer Part B-Fundamentals, 46(4):371–386, 2004.

[97] M. J. Cialkowski, A. Frackowiak, and K. Grysa. *Solution of a stationary inverse heat conduction problem by means of Trefftz non-continuous method*. International Journal of Heat and Mass Transfer, 50(11-12):2170–2181, 2007.

[98] S. Gross, M. Somers, A. Mhamdi, F. Al Sibai, A. Reusken, W. Marquardt, and U. Renz. *Identification of boundary heat fluxes in a falling film experiment using high resolution temperature measurements*. International Journal of Heat and Mass Transfer, 48(25-26):5549–5562, 2005.

[99] M. M. Heydari and B. Farhanieh. *An Inverse Problem Method for Gas Temperature Estimation in Partially Filled Rotating Cylinders*. Scientia Iranica, 15(5):584–595, 2008.

[100] J. M. Mulcahy, D. J. Browne, K. T. Stanton, F. R. C. Diaz, L. D. Cassady, D. F. Berisford, and R. D. Bengtson. *Heat flux estimation of a plasma rocket helicon source by solution of the inverse heat conduction problem*. International Journal of Heat and Mass Transfer, 52(9-10):2343–2357, 2009.

[101] S. K. Kim, J. S. Lee, and W. I. Lee. *A solution method for a nonlinear three-dimensional inverse heat conduction problem using the sequential gradient method combined with cubic-spline function specification*. Numerical Heat Transfer Part B-Fundamentals, 43(1):43–61, 2003.

[102] J. Taler. *Determination of local heat transfer coefficient from the solution of the inverse heat conduction problem*. Forschung Im Ingenieurwesen-Engineering Research, 71(2):69–78, 2007.

[103] J. Z. Wang, A. J. S. Neto, F. D. M. Neto, and J. A. Su. *Function estimation with Alifanov's iterative regularization method in linear and nonlinear heat conduction problems*. Applied Mathematical Modelling, 26(11):1093–1111, 2002.

[104] H. M. Park and O. Y. Chung. *Comparison of various conjugate gradient methods for inverse heat transfer problems*. Chemical Engineering Communications, 176:201–228, 1999.

[105] W. L. Chen, Y. C. Yang, and S. S. Chu. *Estimation of heat generation at the interface of cylindrical bars during friction process*. Applied Thermal Engineering, 29(2-3):351–357, 2009.

[106] H. T. Chen and J. Y. Lin. *Simultaneous estimations of temperature-dependent thermal conductivity and heat capacity*. International Journal of Heat and Mass Transfer, 41(14):2237–2244, 1998.

[107] S. Kim, M. C. Kim, and K. Y. Kim. *An integral approach to the inverse estimation of temperature-dependent thermal conductivity without internal measurements*. International Communications in Heat and Mass Transfer, 29(1):107–113, 2002.

[108] C. Y. Yang. *Estimation of the temperature-dependent thermal conductivity in inverse heat conduction problems*. Applied Mathematical Modelling, 23(6):469–478, 1999.

[109] C. H. Huang and J. Y. Yan. *An Inverse Problem in Simultaneously Measuring Temperature-Dependent Thermal-Conductivity and Heat-Capacity*. International Journal of Heat and Mass Transfer, 38(18):3433–3441, 1995.

[110] C. H. Huang and Y. L. Tsai. *A transient 3-D inverse problem in imaging the time-dependent local heat transfer coefficients for plate fin*. Applied Thermal Engineering, 25(14-15):2478–2495, 2005.

[111] C. H. Huang and S. P. Wang. *A three-dimensional inverse heat conduction problem in estimating surface heat flux by conjugate gradient method*. International Journal of Heat and Mass Transfer, 42(18):3387–3403, 1999.

[112] C. H. Huang and W. C. Chen. *A three-dimensional inverse forced convection problem in estimating surface heat flux by conjugate gradient method*. International Journal of Heat and Mass Transfer, 43(17):3171–3181, 2000.

[113] C. H. Huang and B. H. Chao. *An inverse geometry problem in identifying irregular boundary configurations*. International Journal of Heat and Mass Transfer, 40(9):2045–2053, 1997.

[114] C. H. Huang and C. W. Chen. *A boundary-element-based inverse problem of estimating boundary conditions in an irregular domain with statistical analysis*. Numerical Heat Transfer Part B-Fundamentals, 33(2):251–268, 1998.

[115] A.J. Snyman. *Practical mathematical optimization: an introduction to basic optimization theory and classical and new gradient-based algorithms*. Springer, New York, 2006.

[116] O. M. Alifanov. *Solution of an inverse problem of heat conduction by iteration methods*. Journal of Engineering Physics, 26(4):471–476, 1974.

[117] L. S. Lasdon, S. K. Mitter, and A. D. Waren. *Conjugate Gradient Method for Optimal Control Problems*. Ieee Transactions on Automatic Control, Ac12(2):132–135, 1967.

[118] Y. C. Yang. *Estimation of thermal contact resistance and thermally induced optical effects in single-coated optical fibers*. Optics Communications, 278(1):81–89, 2007.

[119] R. Siegel and J.R. Howell. *Thermal Radiation Heat Transfer*. Taylor & Francis, Washington, USA, third edition edition, 1992.

[120] C. Meola and G. M. Carlomagno. *Recent advances in the use of infrared thermography*. Measurement Science & Technology, 15(9):R27–R58, 2004.

[121] C. Öhman. *Measurement In Thermography*. FLIR, Danderyd, 2001.

[122] X. Maldague. *Basic Thermography: Part - A+B*. In QIRT: Quantitative Infrared Thermography, Brussels, 2004.

[123] K. Chrzanowski. volume 7 of *Research & Development Treatises*. www.inframet.pl, 2001.

[124] NN. *Non-Contact Temperature Measurement*, volume 1. Putman Publishing Company and Omega Press LLC, 1998.

[125] ASTM Standard E1933. *Standard Test Methods for Measuring and Compensating for Emissivity Using Infrared Imaging Radiometers*. ASTM International, 2005.

[126] ASTM Standard E1862. *Standard test methods for measuring and compensating for reflected temperature using infrared imaging radiometers*. ASTM International, 2002.

[127] ASTM Standard E1897. *Standard Test Methods for Measuring and Compensating for Transmittance of an Attenuating Medium Using Infrared Imaging Radiometers*. ASTM International, 2002.

[128] J. Deans, J. Neale, W. Dempster, and C. K. Lee. *The use of effectiveness concepts to calculate the thermal resistance of parallel plate heat sinks*. Heat Transfer Engineering, 27(5):56–67, 2006.

[129] O.A. Leon Patino. *Optimisation of Heat Sinks by Computational Flow Dynamics Techniques*. PhD thesis, Ghent University - UGent, 2003.

[130] NN. *VDI Warmeatlas*. VDI, Berlin, 1980.

[131] C. T'Joen. *Thermo-Hydraulic Study of Inclined Louvered Fins*. PhD thesis, Ghent University-UGENT, 2008.